Title
Seismic Earth Pressures on Retaining Structures and Basement Walls in Cohesionless Soils

Author
Geraili Mikola, Roozbeh

Publication Date
2012

Peer reviewed|Thesis/dissertation

Seismic Earth Pressures on Retaining Structures and Basement Walls in Cohesionless Soils

By

Roozbeh Geraili Mikola

A dissertation submitted in partial satisfaction of the

requirements for the degree of

Doctor of Philosophy

in

Engineering - Civil and Environmental Engineering

in the

Graduate Division

of the

University of California, Berkeley

Committee in charge:

Professor Nicholas Sitar, Chair

Professor Jonathan D. Bray

Professor Douglas S. Dreger

Fall 2012

Seismic Earth Pressures on Retaining Structures and Basement Walls in Cohesionless Soils

by

Roozbeh Geraili Mikola

Abstract

Seismic Earth Pressures on Retaining Structures and Basement Walls
in Cohesionless Soils

by

Roozbeh Geraili Mikola

Doctor of Philosophy in Engineering - Civil and Environmental Engineering

University of California, Berkeley

Professor Nicholas Sitar, Chair

Observations of the performance of basement walls and retaining structures in recent earthquakes show that failures of basement or deep excavation walls in earthquakes are rare even if the structures were not designed for the actual intensity of the earthquake loading. Failures of retaining structures are most commonly confined to waterfront structures retaining saturated backfill with liquefaction being the critical factor in the failures. Failures of other types of retaining structures are relatively rare and usually involve a more complex set of conditions, such as sloping ground either above or below the retaining structure, or both. While some failures have been observed, there is no evidence of a systemic problem with traditional static retaining wall design even under quite severe loading conditions. No significant damage or failures of retaining structures occurred in the recent earthquakes such as Wenchuan earthquake in China (2008) and, or the large subduction zone earthquakes in Chile (2010) and Japan (2011). Therefore, this experimental and analytical study was undertaken to develop a better understanding of the distribution and magnitude of seismic earth pressures on cantilever retaining structures.

The experimental component of the study consists of two sets of dynamic centrifuge model experiments. In the first experiment two model structures representing basement type setting were used, while in the second test a U-shaped channel with cantilever sides and a simple cantilever wall were studied. All of these structures were chosen to be representative of typical designs. Dry medium-dense sand with relative density on the order of from 75% to 80% was used as backfill. Results obtained from the centrifuge experiments were subsequently used to develop and calibrate a two-dimensional, nonlinear, finite difference model built on the FLAC platform.

The centrifuge data consistently shows that for the height of structures considered herein, i.e. in the range of 20-30 ft, the maximum dynamic earth pressure increases with depth and can be reasonably approximated by a triangular distribution This suggests that the point of application of the resultant force of the dynamic earth pressure increment is approximately 1/3H

above the base of the wall as opposed to 0.5-0.6 H recommended by most current design procedures. In general, the magnitude of the observed seismic earth pressures depends on the magnitude and intensity of shaking, the density of the backfill soil, and the type of the retaining structures. The computed values of seismic earth pressure coefficient (ΔK_{ae}) back calculated from the centrifuge data at the time of maximum dynamic wall moment suggest that for free standing cantilever retaining structures seismic earth pressures can be neglected at accelerations below 0.4 g. While similar conclusions and recommendations were made by Seed and Whitman (1970), their approach assumed that a wall designed to a reasonable static factor of safety should be able to resist seismic loads up 0.3 g. In the present study, experimental data suggest that seismic loads up to 0.4 g could be resisted by cantilever walls designed to an adequate factor of safety. This observation is consistent with the observations and analyses performed by Clough and Fragaszy (1977) and Fragaszy and Clough (1980) and Al-Atik and Sitar (2010) who concluded that conventionally designed cantilever walls with granular backfill could be reasonably expected to resist seismic loads at accelerations up to 0.4 g.

Finally, numerical models using FLAC finite difference code were quite successful and able to produce a reasonably good agreement with the results of the centrifuge experiments. However, while the finite difference models were able to capture the main aspects of the seismic response observed in the centrifuge experiments, the results of the analyses were highly sensitive to the selection of soil and interface parameters. Therefore, numerical models used for future designs should be carefully calibrated against experimental data to provide reliable results.

Professor Nicholas Sitar
Dissertation Committee Chair

To my wife, Athena

Table of Contents

List of Figures

List of Tables

Acknowledgments

I am grateful to my doctoral advisor, Professor Nicholas Sitar, for his invaluable guidance and support throughout the course of my studies and research at the University of California, Berkeley. He really trusted me and gave me freedom throughout my research. He always was there for me whenever I needed him. He listened to me and asked my opinion. I've learned a lot from him just simply by watching him while interacting with other people. Indeed it was a great pleasure for me to work with Prof. Sitar.

Gabriel Candia "GA", another smart PhD candidate, practically took a lead on data processing. Without GA's substantial help, this dissertation would not have been possible. We complement each other's strengths and weaknesses. We conducted five centrifuge tests together and truly had a great run and I look forward to working with him for many years to come.

I would like to thank Nathaniel Wagner and Jeff Zayas. The experimental program carried out in this research could not have been executed without their able assistance.

I would like to thank all the staff at the Center for Geotechnical Modeling at the University of California, Davis, especially Chad Justice, Ray Gerhard, Lars Pederson and Dan Wilson for their support and technical input during the experimental phase of this study.

My special thanks go to my teachers at University of California at Berkeley, Professor Jonathan D. Bray, Professor Ray Seed, Professor Juan Pestana and Professors Michael Riemer for their continuous mentorship and support.

I would like thank Professor Peter Byrne and Doctor Naesgaard for generously providing the UBCHYST's FISH source code during the numerical phase of this study.

Importantly, I was extremely fortunate to have the friendship and support of a number of fellow PhD students such as Joe Weber, Hamed Hamedifar, Tonguc Deger, Julian Waeber, Mike George, Justin Hollenback, Josh Zopan, Matt Over, Katherine Jones, Margaret C. Parks. I thank them for providing such friendly environment at Davis Hall.

Finally, I would like to thank my family and friends for supporting me through this period. Particularly, my wife, Athena, has been with me every step of this way. Her strength and love made me strong and her trust in my abilities supported me through difficult times. This work wouldn't have been possible without her. My mom, Pari, dad, Dariush, and my sisters, Donya and Nabat have sacrificed much to make sure that I follow my dream and I owe them everything that I have ever done and will ever do.

The research funding was provided in part by a grant from the California Geotechnical Engineering Association (CalGeo), the State of California Department of Transportation (Caltrans) Contract No. 65N2170 and NSF-NEES-CR Grant No. CMMI-0936376:" Seismic Earth Pressures on Retaining Structures", and Itasca Consulting Group Inc. Programs FLAC^{2D} and FLAC^{3D} were generously made available by Itasca Consulting Group Inc. under collaborative research agreements (IEP loan).

Any opinions, findings, and conclusions or recommendations expressed in this material are those of the author(s) and do not necessarily reflect the views of the National Science Foundation or the California Department of Transportation.

Chapter 1
Introduction

1.1. Purpose of the study

The first analytical solution of the problem of lateral static earth pressures on retaining structures is attributed to Coulomb (1776). He used force equilibrium to determine the magnitude of the soil thrust acting on the wall for the minimum active and maximum passive conditions. Since the problem is indeterminate, a number of potential failure surfaces must be analyzed to identify the critical failure surface. Later, Rankine (1857) developed a simpler procedure for computing minimum active and maximum passive static earth pressures. By assuming general shear failure in the soil behind the wall, Rankine was able to reduce the lateral earth pressure problem so as to be able to compute the static earth pressure for cohesionless soils in a single step. The work of Rankine and Coulomb forms the basis of static earth pressure analyses and design procedures for static lateral loading on retaining structures are well developed and accepted.

However, even under static conditions, the prediction of actual forces and deformations on retaining walls is a complicated soil-structure interaction problem. The dynamic response of even the simplest type of retaining wall is, therefore, even more complex. In general, the dynamic response depends on the mass and stiffness of the wall, the backfill and the underlying ground, the interaction among them and the nature of the input motions.

The seminal work on the analysis of seismic forces on retaining walls was performed in Japan following the Great Kanto Earthquake of 1923 by Okabe (1926) and Mononobe and Matsuo (1929). The method proposed by these authors and currently known as the Mononobe-Okabe (M-O) method is based on Coulomb's theory of static earth pressures. The M-O method was originally developed for gravity walls retaining cohesionless backfill materials and it has become the most commonly used approach to determine seismically induced lateral earth pressures even though there have been extensive studies of the problem over the intervening years.

Significant reviews and analyses of the problem were presented by numerous investigators, including Seed and Whitman (1970). Nazarian and Hadjian (1979), Prakash et al. (1969), Prakash (1981), and Aitken (1982); however, these studies had relatively little impact on design and engineering practice until relatively recently. Moreover, while many theoretical, experimental and analytical studies have been conducted on the subject of seismic earth pressures in the last eighty years, to date, there seems to be no general agreement on a seismic design method for retaining structures or whether seismic provisions should be applied at all (see Chapter 2).

1.2. Motivation of the study

A review of the performance of basement walls in past earthquakes by Lew et al. (2010a) shows that failures of basement or deep excavation walls in earthquakes are rare even if the structures were not explicitly designed for earthquake loading. Failures of retaining structures are

most commonly confined to waterfront structures retaining saturated backfill with liquefaction being the critical factor in the failures. Failures of other types of retaining structures are relatively rare (e.g. Whitman, 1991; Al-Atik ; and Sitar, 2010; Sitar et. al. 2012) and usually involve a more complex set of conditions, such as sloping ground either above or below the retaining structure, or both.

While some failures have been observed, there is no evidence of a systemic problem with traditional static retaining wall design even under quite severe loading conditions (see e.g. Gazetas et al., 2004). Most recently, no significant damage or failures of retaining structures occurred in the 2008 Wenchuan earthquake in China, or in the recent great subduction zone generated earthquakes in 2010 in Chile (Verdugo et a. 2012) and in 2011 in Japan (Sitar et al. 2012). These observations are consistent with the conclusion reached by Seed and Whitman (1970) who noted that gravity retaining structures designed for adequate factor of safety under static loading should perform well under seismic loading for PGA up to about 0.3 g.

Probably, the most challenging aspect of documenting and interpreting field performance is the fact that well documented case histories with actual design and performance data for modern retaining structures are very sparse. Clough and Fragaszy (1977) present a rare, well documented case history of the performance of flood channel walls in the Los Angeles basin during the 1971 San Fernando earthquake. They concluded that reinforced concrete cantilever structures, well designed and detailed for static loading, performed without any sign of distress at accelerations up to about 0.4 g. A similar conclusion was reached by Seed and Whitman (1970), as already mentioned.

1.3. Research objectives

Given the paucity of observed failures of modern retaining structures in recent earthquakes it is of interest to evaluate the adequacy of the current design approaches that are mostly built on the work of Mononobe and Okabe (1929). Thus, the objective of the research presented herein was to evaluate the dynamic behavior of retaining structures with granular, dry sand backfill.

1.4. Scope of work

This study included an extensive literature review of previous analytical, numerical and experimental work related to dynamic earth pressures. Results of this literature review along with a review of the available case histories of retaining structures under seismic loading are presented in Chapter 2 of this dissertation.

The experimental phase of this study consisted of performing a series of two dynamic centrifuge experiments to measure the magnitude and distribution of seismic earth pressures on both basement and non-displacing and displacing cantilever retaining structures. A detailed description of the experimental design and setup is presented in Chapter 3. Results of the two centrifuge experiments are presented in terms of acceleration, displacement, moment and pressure responses in Chapter 4.

After performing the dynamic centrifuge experiments and analyzing the experimental results and observations, a two-dimensional (2-D) nonlinear finite difference (FD) code FLAC was used to study the behavior of basement and retaining walls and backfill under seismic

loading. The 2-D numerical models were calibrated against the recorded data and observations from the two centrifuge experiments. Through comparison between the computed and centrifuge-recorded responses, the FD model was evaluated for its ability to capture the essential features and soil-structure interaction of the retaining wall backfill system during earthquakes. A detailed description of the development and calibration of the FD model is presented in Chapter 5. Conclusions and design recommendations are presented in Chapters 6&7.

1.5. References

- Aitken, G.H. (1982). Seismic Response of Retaining Walls, MS Thesis, University of Canterbury, Christchurch, New Zealand.
- Al-Atik, L. and Sitar, N. (2010), "Seismic Earth Pressures on Cantilever Retaining Structures," Journal of Geotechnical and Geoenvironmental Engineering, October, (136) 10, pp. 1324-1333.
- Clough, G.W. and Fragaszy, R.F. (1977). "A Study of Earth Loadings on Floodway Retaining Structures in the 1971 San Fernando Valley Earthquake," Proceedings of the Sixth World Conference on Earthquake Engineering, Vol. 3.
- Coulomb, CA. "Essai sur une application des regies des maximis et minimis a quelques problemes de statique relatifs a 1'architecture," Memoires de I'Academie Royale pres Divers Savants, Vol. 7, 1776.
- Gazetas, G, Psarropoulos, PN, Anastasopoulos, I. and Gerolymos, N. (2004). "Seismic Behaviour of Flexible Retaining Systems Subjected to Short-Duration Moderately Strong Excitation," Soil Dynamics and Earthquake Engineering, (24), 537-550.
- Lew, M., Sitar, N., Al-Atik, L., Pourzanjani, M. and Hudson, M.B. (2010b). "Seismic Earth Pressures on Deep Building Basements." Structural Engineers Association of California, Proceedings of the Annual Convention, 2010.
- Mononobe, N, and Matsuo M. "On the Determination of Earth Pressures during Earthquakes," Proceedings, World Engineering Congress, Vol. 9, 179-187, 1929.
- Nazarian, H.N. and Hadjian, A.H. (1979). "Earthquake Induced Lateral Soil Pressures on Structures," Journal of Geotechnical Engineering Division, ASCE, (105) GT9: 1049-1066.
- Okabe S. "General Theory of Earth Pressure," Journal of the Japanese Society of Civil Engineers, Tokyo, Japan, Vol. 12 , No. 1, 1926. Prakash, S. and Basavanna, B.M. (1969). " Earth Pressure Distribution behind Retaining Wall during Earthquakes," Proceedings of the Fourth World Conference on Earthquake Engineering, Santiago, Chile.
- Prakash, S. and Basavanna, B.M. (1969). "Earth Pressure Distribution behind Retaining Wall during Earthquakes," Proceedings of the Fourth World Conference on Earthquake Engineering, Santiago, Chile.
- Prakash, S. (1981). "Dynamic Earth Pressures," State of the Art Report – International Conference on Recent Advances on Geotechnical Earthquake Engineering and Soil Dynamics, St. Louis, Missouri, Vol. III, 993-1020.
- Rankine, W. "On the Stability of Loose Earth," Philosophical Transactions of the Royal Society of London, Vol. 147, 1857.

- Seed, H.B. and Whitman, R.V. (1970). "Design of Earth Retaining Structures for Dynamic Loads," ASCE Specialty Conference, Lateral Stresses in the Ground and Design of Earth Retaining Structures, Cornell Univ., Ithaca, New York, 103‑147.
- Sitar, N., Geraili Mikola, R., and Candia, G. "Seismically Induced Lateral Earth Pressures on Retaining Structures and Basement Walls", Keynote Lecture, Geotechnical Engineering State of the Art and Practice, Keynote Lectures from GeoCongress 2012, GSP 226, ASCE, 2012.
- Verdugo, R., Sitar, N, Frost, J.D., Bray, J.D., Candia, G., Eldridge, T., Hashash, Y., Olson, S.M., and Urzua, A., (2012), "Seismic Performance of Earth Structures: Dams, Levees, Tailings Dams and Retaining Walls," Earthquake Spectra, Volume 28, Issue S1, Page S75-S96, June, ISSN: 8755-2930.
- Whitman, R.V. (1991). "Seismic Design of Earth Retaining Structures," Proceedings, Second International Conference on Recent Advances in Geotechnical Earthquake Engineering and Soil Dynamics, ASCE, St. Louis, MO., 1767-1778.

Chapter 2
Literature Review

2.1. Introduction

Since the pioneering work of Mononobe and Matsuo (1929) and analytical work of Okabe (1926), there have been numerous experimental, analytical and numerical studies of the dynamic behavior of retaining walls in order to provide a methodology for rational design. The different approaches used to study dynamic earth pressures can be divided into analytical, numerical, and experimental methods. While a vast amount of literature exists on the topic of seismically induced lateral earth pressures, this chapter summarizes previous research performed highlighting only selected works of relevance to this study.

2.2. Analytical Methods

For the purposes of analysis, retaining walls have been traditionally divided into two categories (e.g NEHRP 2010): “yielding” walls that can move sufficiently to develop minimum active earth pressures and “non-yielding” walls that do not satisfy this movement condition. Note that in this context, yielding refers to permanent displacement of the wall as a result of the seismic event and does not mean that stresses within the structural system were exceeded. In this dissertation in order to avoid this confusion the terms “displacing” and “non-displacing” are used instead of “yielding” and “non-yielding”, respectively. The amount of movement to develop minimum active pressure is very small. A displacement at the top of the wall of 0.002 times the wall height is typically sufficient to develop the minimum active pressure state. Generally, free-standing gravity or cantilever walls are considered to be yielding walls (except massive gravity walls founded on rock), whereas building basement walls restrained at the top and bottom often are considered to be non-yielding.

2.3. Displacing Walls

2.3.1. The Mononobe-Okabe (1926-1929)

Following the great Kanto Earthquake of 1923 in Japan, Mononobe and Matsuo (1929) performed a series of higly original experiments using a shaking table. Their original shaking table design consisted of a rigid base box mounted on rails and driven with an ingenious conical drum winch connected through a crankshaft to the base of the box (Figure 2.1). This arrangement allowed for simple application of sinusoidal excitation with linearly varying frequency, i.e. a frequency sweep. The ends of the box were trap doors, spring mounted at the base, with pressure gauges mounted at the top to measure the load as the “wall” tilted outward. As shown in the figure, the box dimensions were 9 ft long, 4 ft wide and 4 ft deep, with one door, door A, spanning the whole width of the box and the other door, door B, spanning only one half of the width of the box. Although, the box was quite substantial in size, the depth of the medium dense sand fill was only 4 ft and the sides of the box were rigid.

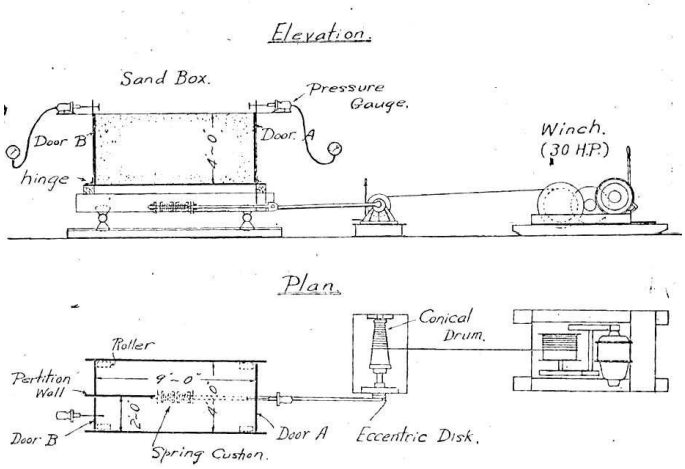

Figure 2.1. Shaking table arrangement used by Mononobe and Matsuo (1929).

The results of these experiments and Okabe's (1926) and analytical work then led to the development of what is now often referred to as the Mononobe-Okabe (M-O) method. This methodology was originally developed for gravity walls retaining cohesionless backfill materials, however, since then it has been extended to a full range of different soil properties.

The method is an extension of Coulomb's sliding wedge theory and for active conditions the M-O analysis incorporates the following assumptions:

1. The backfill soil is dry, cohesionless, isotropic, homogenous and elastically undeformable material with a constant internal friction angle.
2. The wall is long enough to make the end effect negligible.
3. The wall yields sufficiently to mobilize the full shear strength of the backfill along potential sliding surface and produce minimum active pressures.
4. The potential failure surface in the backfill is a plane that goes through the heel of the wall.

These assumptions make the problem determinate with respect to force equilibrium and lead to the following expression for the resultant dynamic active thrust P_{ae}:

$$P_{ae} = \frac{1}{2}\gamma H^2(1 - k_v).K_{ae} \tag{2.1}$$

Where

$$K_{ae} = \frac{cos^2(\varphi - \psi - \beta)}{\cos\psi \cos^2\beta \cos(\delta+\beta+\psi)\left[1+\sqrt{\frac{\sin(\varphi+\delta)\sin(\varphi-\psi-i)}{\cos(\delta+\beta+\psi)\cos(i-\beta)}}\right]^2} \tag{2.2}$$

H = height of wall
k_v = coefficient of vertical acceleration of soil wedge
k_h = coefficient of horizontal acceleration of soil wedge
$\psi = \tan^{-1}\left(\frac{k_h}{1-k_v}\right)$
γ = unit weight of backfill
φ = friction angle of backfill
δ = friction angle at wall-backfill interface

i = backfill slope with respect to horizontal
β = angle between inner face of wall and vertical

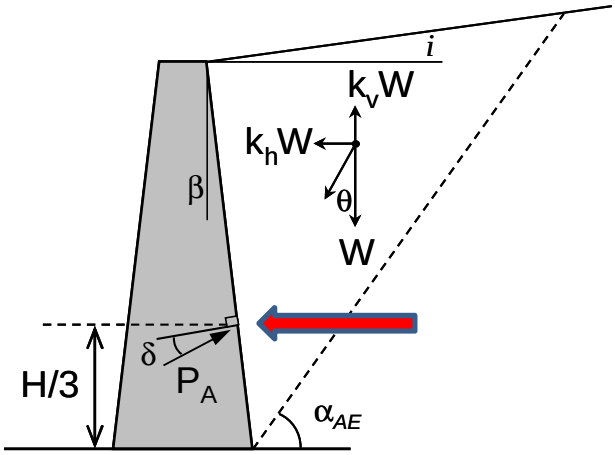

Figure 2.2. Forces considered in Mononobe-Okabe analysis.

The M-O method gives the total active thrust acting on the wall and the point of application of the thrust is assumed to be at $H/3$ above the base of the wall.

2.3.2. Seed and Whitman (1970)

Seed and Whitman (1970) performed a parametric study to evaluate the effects of changing the angle of wall friction, the friction angle of the soil, the backfill slope and the vertical acceleration on the magnitude of dynamic earth pressures. They observed that the maximum total earth pressure acting on a retaining wall can be divided into two components: the initial static pressure and the dynamic increment due to the base motion.

Seed and Whitman (1970) suggested that the static, dynamic increment and total lateral earth pressure can be related as:

$$P_{ae} = P_a + \Delta P_{ae} \quad (2.3)$$

$$K_{ae} = K_a + \Delta K_{ae} \quad (2.4)$$

Seed and Whitman (1970), based on a parametric sensitivity analysis, further proposed that for practical purposes:

$$\Delta K_{ae} \approx (3/4)k_h \quad (2.5)$$

$$\Delta P_{ae} = (1/2)\gamma H^2(3/4)k_h = (3/8)k_h\gamma H^2 \quad (2.6)$$

where k_h is horizontal ground acceleration as a fraction of gravitational acceleration. They observed that the peak ground acceleration occurs for only one instant of time and does not have sufficient duration to cause significant wall movements. Therefore, they recommended using a

reduced ground acceleration of about 85% of the peak value in seismic design of retaining walls. After reviewing the results of experimental work based on small 1g shaking table experiments by Mononobe and Matsuo and later by Prakash (see who else is referenced by Seed), Seed and Whitman (1970) suggested the point of application of the active thrust should be at 0.6H above the base of the wall as show in Figure 2.3. However, Seed and Whitman (1970) concluded that "many walls adequately designed for static earth pressures will automatically have the capacity to withstand earthquake ground motions of substantial magnitudes and in many cases, special seismic earth pressure provisions may not be needed." More recently, NEHRP (FEMA 750) (Building Seismic Safety Council, 2010) recommended that “Unless permanent displacement of the wall is acceptable, k_h should be taken equal to the site peak ground acceleration, PGA”. The basis of this recommendation in not given and cannot be traced to any published information.

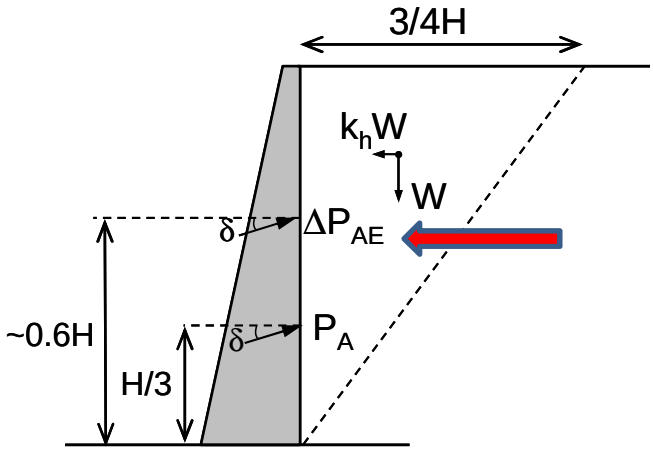

Figure 2.3. Forces considered in Seed-Whitman analysis.

2.3.3. Mylonakis (2007)

A recent alternative to the M-O method for plastic soils was developed by Mylonakis et al. (2007). They proposed a closed-form stress plasticity solution for gravitational and earthquake-induced earth pressures on retaining walls. The presented solution is essentially an approximate yield-line approach, based on the theory of discontinuous stress fields, and takes into account the following parameters: (1) weight and friction angle of the soil material, (2) wall inclination, (3) backfill inclination, (4) wall roughness, (5) surcharge at soil surface, and (6) horizontal and vertical seismic acceleration. Both active and passive conditions are considered by means of different inclinations of the stress characteristics in the backfill.

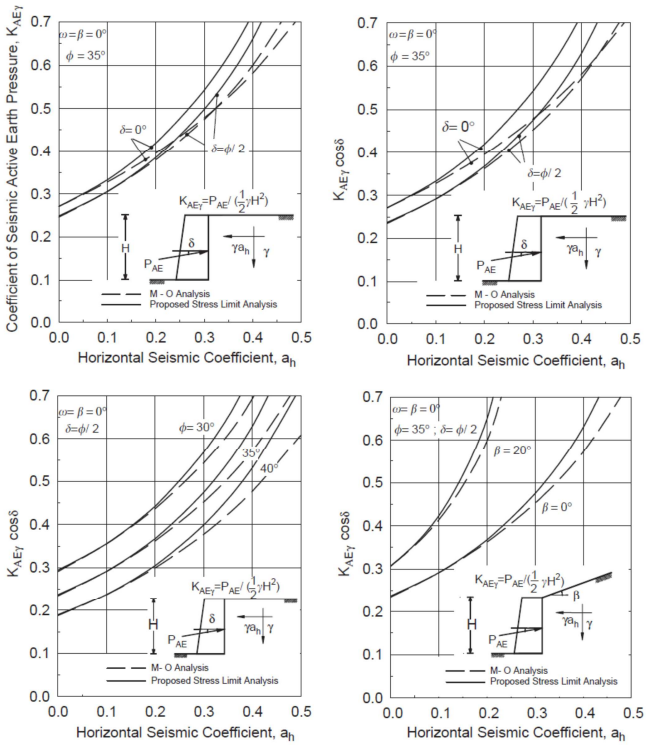

Figure 2.4. Comparison of active seismic earth pressures predicted by the solution proposed by Mylonakis et al. (2007) and from conventional M–O analysis, for different geometries, material properties and acceleration levels; a_v= 0 (from Mylonakiset al., 2007).

Figure 2.4, referring to cases examined in the seminal study of Seed and Whitman (1970), for a reference friction angle of 35°. Naturally, active pressures increase with increasing levels of seismic acceleration and slope inclination and decrease with increasing friction angle and wall roughness. The conservative nature of the proposed analysis versus the M–O solution is evident in the graphs. The trend is more pronounced for high levels of horizontal seismic coefficient a_h>0.25, smooth walls, level backfills, and high friction angles. Conversely, the trend becomes weaker with steep backfills, rough walls, and low friction angles.

2.4. Non-displacing Walls

2.4.1. Wood (1973)

Wood (1973) used elastic and elastic wave propagation theories to develop solutions for an elastic soil stratum on a rigid base with a rigid wall under various forcing conditions.

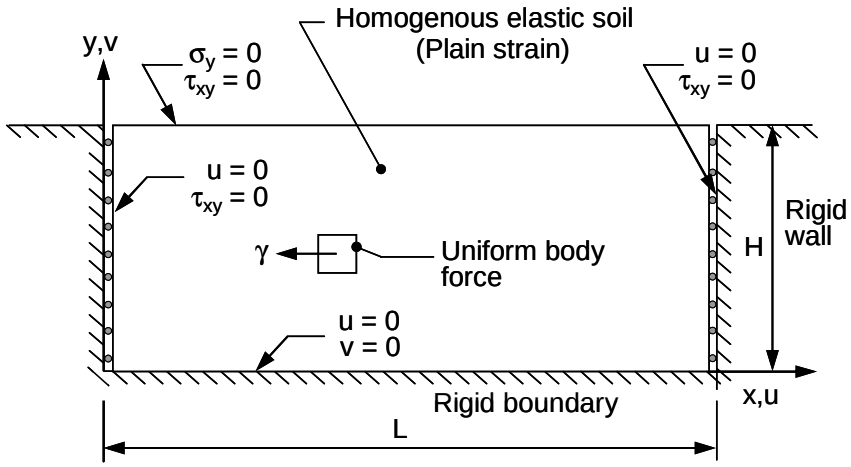

Figure 2.5. Wood (1973) rigid problem.

For a perfectly rigid wall (Figure 2.5), supporting a relatively long layer of soil, he determined that the earthquake force component computed was likely to be greater than twice that estimated by M-O method. Identical horizontal earthquake coefficients k_h were used in the computation. It was thus recommended that for rigid wall embedded in rock or very firm soil, restrained by piles or deeply buried, an elastic analysis should be used instead of the M-O method (Building Seismic Safety Council, 2010). Wood established that the dynamic amplification was insignificant for relatively low-frequency ground motions (i.e., motions at less than half of the natural frequency of the unconstrained backfill), which would include many earthquake problems. For uniform, constant k_h applied throughout the elastic backfill, Wood (1973) developed the dynamic thrust, ΔP_{ae}, acting on smooth rigid non-displacing walls as:

$$\Delta P_{ae} = F k_h H^2 \tag{2.7}$$

The value of F is approximately equal to unity (Whitman, 1991) leading to the following approximate formulation for a rigid non-displacing wall on a rigid base:

$$\Delta P_{ae} = k_h H^2 \tag{2.8}$$

the point of application of the dynamic thrust is taken typically at a height of $0.6H$ above the base of the wall, as shown in Figure 2.6. It should be noted that the model used by Wood (1973) does not incorporate any effect of the inertial response of a superstructure connected to the top of the wall (Building Seismic Safety Council, 2010). This effect may modify the interaction between the soil and the wall and thus modify the pressures from those calculated assuming a rigid wall on a rigid base.

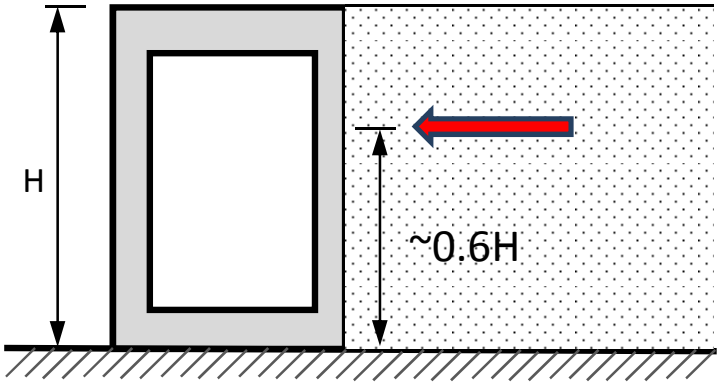

Figure 2.6. The point of application of the dynamic thrust in Wood analysis (Wood 1973).

Although the study performed by Wood included dynamic analysis of a rigid wall with fixed base condition, the solution commonly used and presented in Equations 2.7 and 2.8 is based on static "1g" loading of the soil and wall and does not include the effects of the wave propagation in the soil.

2.5. Experimental Studies

Since the pioneering work of Mononobe and Matsuo (1929) there have been numerous other experimental studies aimed at measuring seismic earth pressuresIn general, the experimental studies fall into two main categories: scaled models on 1-g shaking tables and scaled centrifuge models. Shaking table model experiments have been by far most common, owing to the relative ease of access to shaking tables and the perceived simplicity of model building. Dynamic centrifuge experiments, on the other hand, are relatively recent and less common, since geotechnical centrifuges are a relatively new addition to the experimental infrastructure. Over the years, a wide range of shake table experiments have been performed in order to measure dynamic earth pressure and investigate the retaining wall response (e.g., Mononobe and Matsuo 1929, Jacobsen, 1939; Ishii et al., 1960; Matsuo and Ohara, 1960; Murphy, 1960; Niwa, 1960; Ohara, 1960; Sherif et al. 1982; Nandakumaran and Joshi,1973; Sharif and Fang 1984a, 1984b). Many of these tests were performed on a very small scale, and the results have shown varying levels of agreement with the theoretical predictions (Al-Atik and Sitar 2010).

Some of the early tests suffered from inadequate instrumentation, unrealistic frequencies and amplitudes of input vibrations, and lack of plane strain conditions, which are assumed in most analytical and design methods (Ortiz et. al, 1983). These tests generally indicated that the M-O method gives the magnitude of the total resultant force reasonably well (Ortiz et. al, 1983) and the incremental dynamic earth pressure acts at somewhere between 0.45 and 0.55 H from the base depending on the wall movement (Matsuzawa et. al., 1985), where H is the wall height. However, 1g tests suffer from a lack of similitude of stress levels between small scale models and any realistic large scale structures. Because important static and dynamic soil properties are dependent on effective stress level, the applicability of small scale 1g shaking table tests for

quantitative assessment is limited although their results are useful in examining qualitative behavior (Dewoolkar et. al. 2001).

Dynamic centrifuge tests on model retaining walls with dry and saturated cohesionless backfills have been performed by Ortiz (1983), Bolton and Steedman (1985), Zeng (1990), Steedman and Zeng (1991), Stadler (1996), and Dewoolkar et al. (2001). The majority of these dynamic centrifuge experiments used sinusoidal input motions and pressure cells to measure earth pressures on the walls.

Ortiz et al. (1983) performed a series of dynamic centrifuge experiments on cantilever retaining walls with dry medium dense sand backfill as shown in Figure 2.8. Ortiz et al. (1983) observed a broad agreement between the maximum measured forces and the M-O predictions. Ortiz et al. (1983) commented that the maximum dynamic force acted at about one third the height of the wall above its base. The importance of inertial effects was not considered.

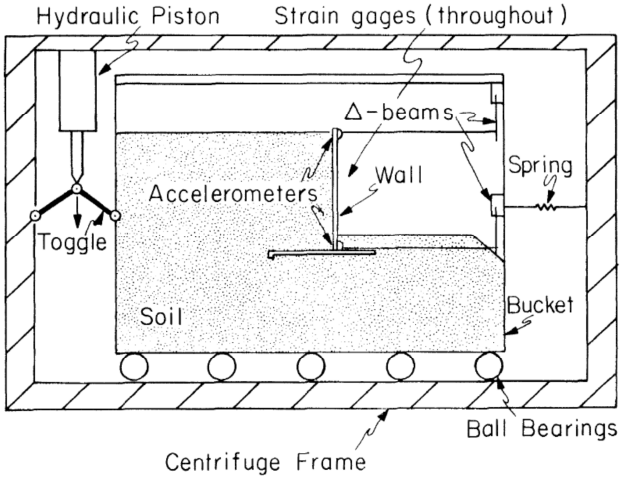

Figure 2.7. Ortiz (1983) experiments setup.

Bolton and Steedman conducted dynamic centrifuge experiments on concrete (1982) and aluminum (1985) cantilever retaining walls supporting dry cohesionless backfill, and their results generally supported the M-O method. Steedman (1984) performed centrifuge experiments on cantilever retaining walls with dry dense sand backfill and measured dynamic forces in agreement with the values predicted by the M-O method, but suggested that the point of application should be located at mid-height of the wall. Based on Zeng (1990) dynamic centrifuge experiments, Steedman and Zeng (1990) suggested that the dynamic amplification or attenuation of input motion through the soil and phase shifting are important factors in the determination of the magnitude and the distribution of dynamic earth pressures.

Stadler (1996) performed fourteen dynamic centrifuge experiments on cantilever retaining walls with dry medium dense sand backfill and observed that the total dynamic lateral earth pressure profile is triangular with depth but that the incremental dynamic lateral earth pressure profile ranges between triangular and rectangular. Moreover, Stadler (1996) suggested that using reduced acceleration coefficients of 20-70% of the original magnitude with the M-O method provides good agreement with the measured forces. Stadler (1996) experimental configuration is presented in Figure 2.9.

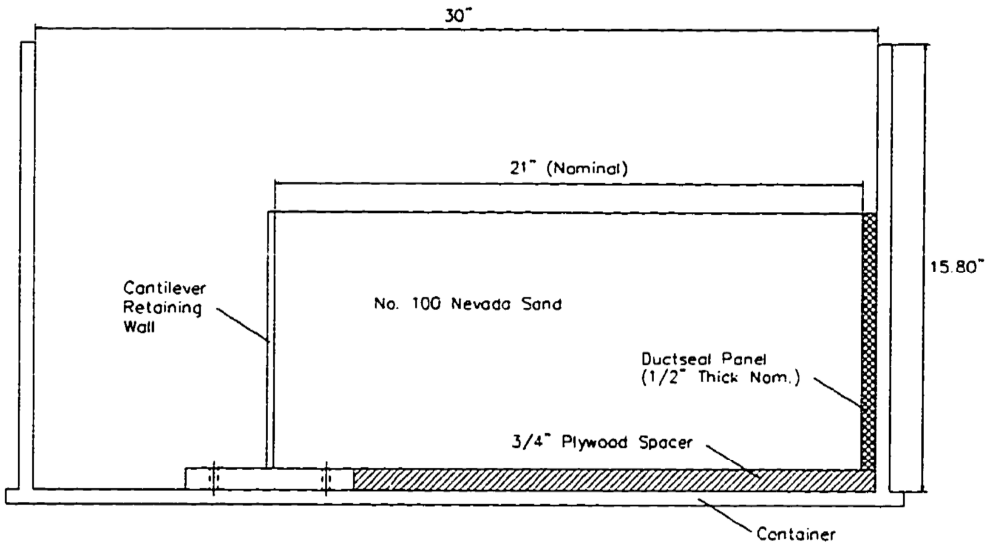

Figure 2.8. Stadler (1996) typical test configuration.

Deewoolkar et al. (2001) performed centrifuge dynamic excitation tests with fixed-base cantilever walls (Figure 2.10) supporting saturated, liquefiable, cohesionless backfills. From those experiments, Deewoolkar et al. (2001) concluded that excess pore pressure generation contributed significantly to seismic lateral earth pressure in the saturated backfill. Deewoolkar et al. (2001) also concluded that the maximum dynamic thrust was proportional to the input base acceleration.

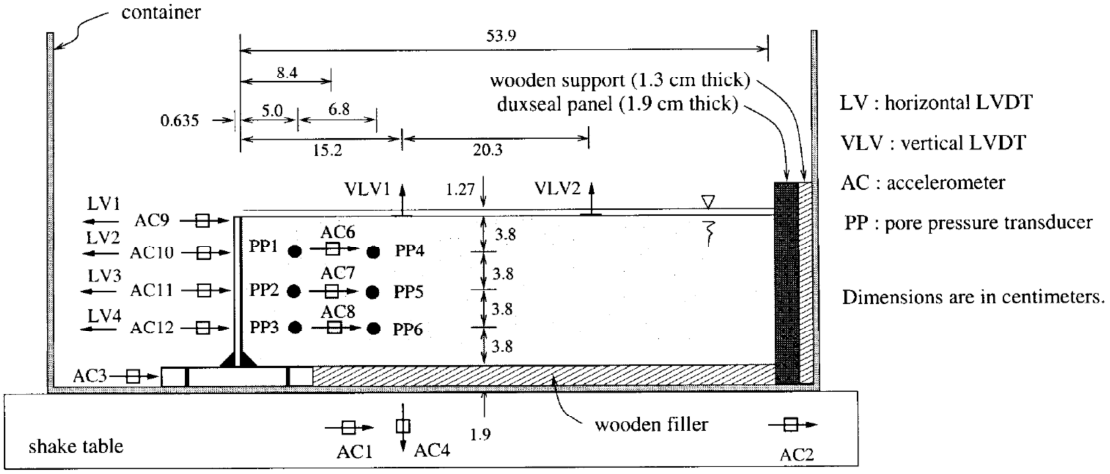

Figure 2.9. Dewoolkar (2001) typical test configuration.

Nakumara (2006) and Al-Atik and Sitar (2008) recently conducted separate shake table tests using centrifuge facilities, and both separately concluded that the measured earth pressure during shaking was lower than the M-O method predictions. Nakamura (2006) also found that the inertial force was not always transmitted to the wall and backfill simultaneously. The configuration of the Nakamura (2006) and Al-Atik and Sitar (2008) centrifuge models are presented in Figure 2.11-2.12 respectively.

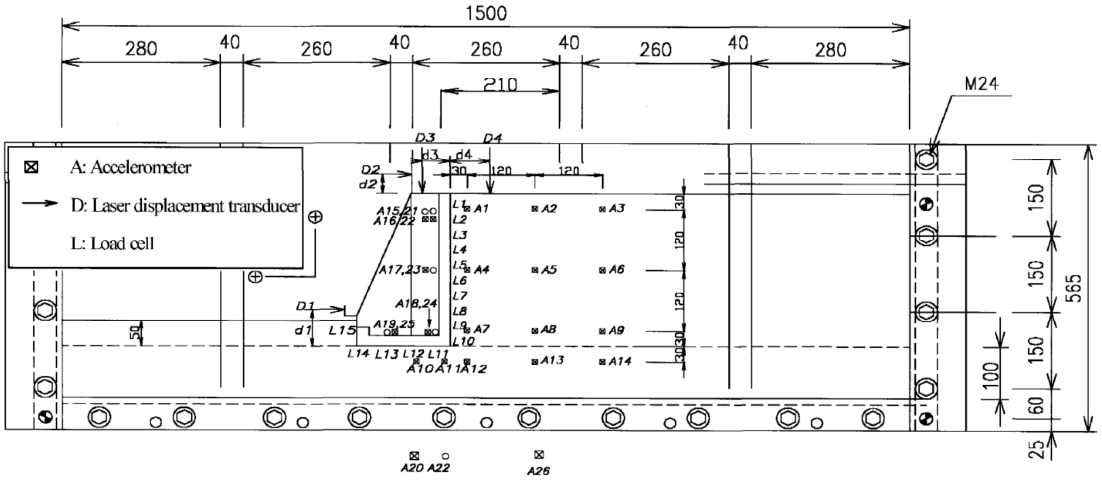

Figure 2.10. Nakamura (2006) test configuration.

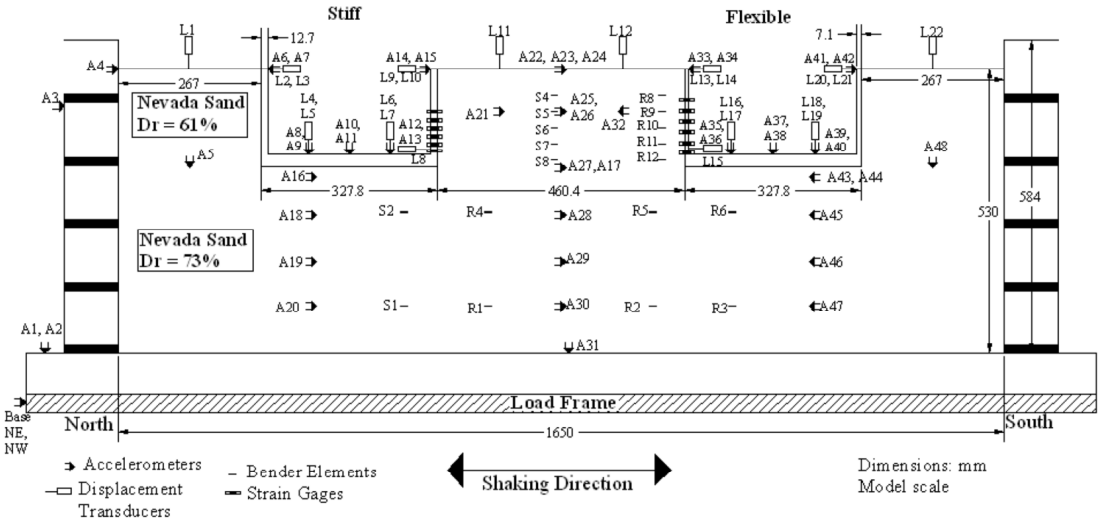

Figure 2.11. Al-Atik and Sitar (2008) test configuration.

2.6. Numerical Studies

Earthquake-induced pressures on retaining walls have been evaluated also using dynamic response-analyses. Simulations of the dynamic wall-backfill interaction using numerical models are important as they can provide additional valuable insights if properly calibrated. Alampalli and Elgamal (1990) developed a numerical model based on the compatibility between mode shapes of the wall and the adjacent backfill soil. Using a model consisting of flexible cantilever wall supporting a semi-infinite uniform visco-elastic layer, Veletsos and Younan (1997) concluded that the magnitude and distribution of wall displacement and pressure can be quite sensitive to the flexibility of the wall and its base. Richards et al. (1999) presented a kinematic

model with springs representing the soil and found that the point of action of the dynamic earth pressure resultant varies with different types of wall movement.

Al-Homoud and Whitman (1999) used a finite element numerical model to analyze gravity walls founded on dry sand. They compared the results with those of tridimensional centrifuge tests and observed that there was a good agreement between both methods for wall displacement.

Green and Ebeling (2002) modeled the dynamically induced lateral earth pressure on the stem portion of a concrete cantilever earth retaining wall with dry medium dense sand using FLAC finite difference code and concluded that at very low levels of acceleration, the seismic earth pressures were in agreement with Mononobe-Okabe predictions; however, as accelerations increased, seismic earth pressures were larger than those predicted by the M-O method.

Gazetas et al. (2004) performed simulations of L-shaped walls, pre-stressed anchored pile walls, and reinforced soil walls, employing both linear and non-linear soil models. Using those models, Gazetas et al. (2004) showed that including realistic effects such as the wall flexibility, foundation soil deformability, material soil yielding and soil wall separation and sliding tends to reduce the effects of dynamic excitations on those walls. Gazetas et al. (2004) also used an FE model to simulate a case history in which a retaining wall performed well during an actual earthquake.

Psarropoulos et al. (2005) carried out a study to validate the assumptions of Veletsos and Younan analytical solution and to define the range if its applicability. The numerical models were developed using the commercial finite-element package ABAQUS. The versatility of the numerical methods, finite-element and finite-difference, permited the treatment of more realistic situations that are not amenable to analytical solutionincluding the heterogeneity of the retained soil, and translational flexibility of the wall foundation.

To investigate the characteristics of the lateral seismic soil pressure on building walls, Ostadan (2005) performed a series of soil-structure-interaction analyses using SASSI. Using the concept of a single degree-of-freedom, Ostadan (2005) proposed a simplified method to predict maximum seismic soil pressures for building walls resting on firm foundation material. This proposed method resulted in dynamic earth pressure profiles comparable to or larger than the Wood (1973) solution, with the maximum earth pressure occurring at the top of the wall.

Pathmanathan (2006) developed a finite element numerical models to understand the dynamic behavior of retaining structures, and, in particular, to find the magnitude and distribution of dynamic lateral earth pressure on the wall, as well as the displacement and forces induced by horizontal ground shaking. Retaining structures considered include a flexible diaphragm wall, a cantilever wall and a gravity wall. In all the analyses, the soil is assumed to act as a homogeneous, elasto-plastic medium with Mohr-Coulomb failure criterion and the walls are assumed to act as linear elastic. He concluded that the dynamic earth pressure induced on the wall corresponded with those predicated by the Mononobe-Okabe method, when the levels of shaking were small. The dynamic earth pressure calculated to be smaller than those predicted by Mononobe-Okabe method, when the levels of shaking were large and the points of application of incremental dynamic forces showed considerable fluctuation about the value (0.6H) as proposed by Seed-Whitman (1970).

Jung and Bobet (2008) added a translational spring to the base of a bending and rotating wall model supporting elastic soil elements, and found that the wall rotational, bending, and translational flexibilities significantly affected the magnitude and distribution of the dynamic pressure. Specifically, Jung and Bobet (2008) found that the dynamic earth pressure behind a rigid wall with a stiff foundation is larger than that for a flexible wall with a soft foundation.

After performing the dynamic centrifuge experiments and analyzing the experimental results and observations, Al-Atik and Sitar (2008) performed a two-dimensional (2-D) nonlinear finite element (FE) model on the OpenSees platform to study the behavior of retaining walls and backfill under seismic loading. The 2-D FE model was calibrated against the recorded data and observations from the two centrifuge experiments and they concluded that the FE model was able to capture the main response features of the retaining wall-backfill system.

2.7. Observed Field Performance of Retaining Walls during Earthquakes

While damage to retaining walls has been observed after some earthquakes, it has often involved a weak (for instance liquefiable) underlying layer (Gazetas et al. 2004, Shirato et al. 2006, Al-Atik and Sitar 2008). In the absence of such a weak layer, many retaining structures have performed well, even in cases where the seismic load was not explicitly a design consideration (Seed and Whitman 1970, Lew et al. 1995, Gazetas et al. 2004, Al-Atik and Sitar 2008).

After the 1971 San Fernando earthquake, Clough and Fragaszy (1977) found that U-shaped channel floodway structures designed only for static Rankine (1857) active pressures, performed well with peak excitation up to about 0.4 g, and sustained damage at above 0.5 g.

Numerous "temporary" anchored walls were subjected to acceleration levels in excess of 0.2 g and in some cases as large as 0.6 g during the 1994 magnitude 6.7 Northridge earthquake. Lew et al (1995) described four such pre-stressed-anchored piled walls in the greater Los Angeles area with excavation depths of 15 to 25 m and supporting relatively stiff soils. The authors reported that the measured deflections of these walls did not exceed 1 cm and that no significant damage was observed.

During the 1995 magnitude 7 Kobe earthquake in Japan, a wide variety of retaining structures most of them located along railway lines were put to test. Gravity-type retaining walls such as masonry and unreinforced concrete were heavily damaged. On the other hand, reinforced-concrete walls experienced only limited damage (Gazetas et al. 2004). Koseki et al (1998) presented preliminary evaluations of the internal and external stability of several damaged retaining walls during the Kobe earthquake. The aim of their study was to improve the current design procedures that are mostly based on the M-O theory. Koseki et al (1998) concluded that a horizontal acceleration coefficient based on a reduced value of the measured peak horizontal acceleration (60 to 100% of peak ground acceleration) is appropriate for use with the M-O method.

During the 1999 magnitude 7.6 Chi-Chi earthquake in Taiwan, flexible reinforced concrete walls and reinforced-soil retaining walls performed relatively well. Ling et al. (2001) studied cases of modular-block geosynthetic-reinforced soil retaining walls and reinforced slopes failures during the Chi-Chi earthquake. They attributed part of these failures to the topography

and geotechnical conditions in Taiwan, whereby many walls were located along slopes and mountains and were constructed with obvious lack of professional design.

The most recent observations (Sitar et. al., 2012) show that no significant damage or failures of retaining structures occurred in the 2008 Wenchuan earthquake in China, or in the recent great subduction zone generated earthquakes in 2010 in Chile (2010) and in 2011 in Japan Overall, the case histories show that retaining structures perform quite well under seismic loading, even if they were not specifically designed to handle dynamic loads.

2.8. References

- Al-Atik, L. and Sitar, N. (2008). Experimental and Analytical Study of the Seismic Performance of Retaining Structures. Pacific Earthquake Engineering Research Center, PEER 2008/104, Berkeley, CA.
- Al-Atik, L. and N. Sitar, 2010. Seismic Earth Pressures on Cantilever Retaining Structures, Journal of Geotechnical and Geoenvironmental Engineering, Vol. 136, No. 10, pp. 1324-1333, doi: 10.1061/(ASCE)GT.1943-5606.0000351.
- Alampalli, S. and Elgamal A. (1990). "Dynamic response of retaining walls including supported soil backfill: A Computational Model," Fourth U.S. National Conference on Earthquake Engineering, Palm Springs, CA, Vol. 3, 623-632.
- Al-Homoud, A. S., and Whitman, R. V. (1999). "Seismic analysis and design of rigid bridge abutments considering rotation and sliding incorporating non-linear soil behavior." Soil Dynamics and Earthquake Engineering, 18(4), 247-277.
- Bolton M. D., and Steedman, R. S. 1985. The behavior of fixed cantilever walls subject to lateral loading. Application of Centrifuge Modeling to Geotechnical Design, Craig (ed.), Balkema, Rotterdam.
- Building Seismic Safety Council. (2010). NEHRP Recommended Provisions for Seismic Regulations for New Buildings and Other Structures (FEMA 750), 2009 Edition, Part 1 – Provisions. BSSC, Washington, DC.
- Clough, G.W. and Fragaszy, R.F. (1977). "A Study of Earth Loadings on Floodway Retaining Structures in the 1971 San Fernando Valley Earthquake," Proceedings of the Sixth World Conference on Earthquake Engineering, Vol. 3.
- Dewoolkar, M. M., Ko, H., and Pak R. Y. S. 2001. Seismic behavior of cantilever retaining walls with liquefiable backfills. Journal of Geotechnical and Geoenvironmental Engineering, ASCE 127(5): 424-435.
- Gazetas, G., Psarropoulos, P., Anastasopolous, I., and Gerolymos, N. (2004). "Seismic behaviour of flexible retaining systems subjected to short-duration moderately strong excitation." Soil Dynamics and Earthquake Engineering (24), Elsevier: 537-550.
- Green, R.A., and Ebeling, R.M., (2002). "Seismic analysis of cantilever retaining walls, Phase I, ERDC/ITL TR-02-3, Information technology laboratory, US army corps of engineers, Engineer research and development center, Vicksburg, MS.
- Ishii, T. Arai, M. Tsuchida, H. 1960. "Lateral Earth Pressures in an Earthquake", Proceedings, Second world conference on Earthquake Engineering, Tokyo, Japan.
- Jacobsen, L.S. 1939. Appendix D of "The Kentucky Project", Technical Report No. 13, Tenessee Valley Authority, 1951.
- Jung, C. and Bobet, A. (2008). "Seismic earth pressures behind retaining walls: effects of rigid body motions," Zeng, D., Manzari, M., and Hiltunen, D., Eds., Proceedings, Geotechnical Earthquake Engineering and Soil Dynamics IV, ASCE., Sacramento, CA.
- Koseki, J, Tatsuoka, F, Munaf, Y, Tateyama, M, and Kojima, K. "A Modified Precoedure to Evaluate Active Earth Pressure at High Seismic Loads," Soils and Foundations, Special Issue on Geotechnical Aspects of the January 17, 1996 Hyogoken-Nambu Earthquake, Vol. 2, 209-216, 1998.
- Lew, M, Simantob, E, and Hudson, ME. "Performance of Shored Earth Retaining Systems during the January 17, 1994, Northridge Earthquake", Proceedings of the Third International

Conference on Recent Advances in Geotechnical Earthquake Engineering and Soil Dynamics, St Louis, Missouri, Vol. 3, 1995.

- Ling, HI, Leshchinsky, D, and Chou, N. "Post-earthquake Investigation on Several Geosynthetic-reinforced Soil Retaining Walls and Slopes during the Chii-Chii Earthquake in Taiwan," Soil Dynamics and Earthquake Engineering," Vol. 21, 297-313, 2001.
- Matsuo, M. Ohara, S. 1960. Lateral Earth Pressures and Stability of Quay Walls during Earthquakes, Proceedings, Second world conference on Earthquake Engineering, Tokyo, Japan.
- Matsuzawa H, Ishibashi I, Kawamuara M. 1985. Dynamic soil and water pressures of submerged soils. Journal of Geotechnical Engineering; 111(10):1161-76.
- Mononobe, N. Matsuo, M. 1929. On the determination of earth pressures during earthquakes, Proceedings, World Engineering Conference, Japan, Vol. 9.
- Murphy, V.A. 1960. The effect of ground characteristics on a seismic design of structures", Proceedings, Second world conference on Earthquake Engineering, Tokyo, Japan.
- Mylonakis, G., Kloukinas, P. and Papatonopoulos, C. (2007). "An Alternative to the Mononobe-Okabe Equation for Seismic Earth Pressures", Soil Dyn. and Earthquake Eng., (27) 10, 957-969.
- Nakamura, S. "Reexamination of Mononobe-Okabe Theory of Gravity Retaining Walls Using Centrifuge Model Tests," Soils and Foundations, Vol. 46, No. 2, 135-146, 2006.
- Niwa, S. 1960. An experimental study of oscillating earth pressures acting on a quay wall, Proceedings, Second world conference on Earthquake Engineering, Tokyo, Japan.
- Nandakumaran P, Joshi VH. Static and dynamic active earth pressures behind retaining walls. Bull Ind Soc Earthquake Technol 1973;10(3).
- Ohara, S. 1960. Experimental Studies of seismic active and seismic passive earth pressure, Proceedings, Second world conference on Earthquake Engineering, Tokyo, Japan.
- Okabe S. "General Theory of Earth Pressure," Journal of the Japanese Society of Civil Engineers, Tokyo, Japan, Vol. 12 , No. 1, 1926.
- Ortiz LA, Scott RF, Lee J. 1983. Dynamic centrifuge testing of a cantilever retaining wall, Earthquake Engineering and Structural Dynamics, vol. 11. New York: Wiley, (p. 251-68).
- Ostadan, F. (2005). "Seismic Soil Pressure for Building Walls – An Updated Approach," Journal of Soil Dynamics and Earthquake Engineering, (25): 785-793.
- Psarropoulos, P.N., Klonaris, G. and Gazetas, G. (2005). "Seismic earth pressures on rigid and flexible retaining walls." Soil Dynamics and Earthquake Engineering, Elsevier, No. 25. pp 795-809.
- Pathmanathan, R. (2006), numerical modelling of seismic behaviour of earth-retaining walls, a dissertation thesis.
- Rankine, W. "On the Stability of Loose Earth," Philosophical Transactions of the Royal Society of London, Vol. 147, 1857.
- Richards, R., Huang, C., and Fishman, K. (1999). "Seismic earth pressure on retaining structures." Journal of Geotechnical and Geoenvironmental Engineering, 125(9), 771-778.
- Seed, HB, and Whitman, RV. "Design of Earth Retaining Structures for Dynamic Loads," ASCE Specialty Conference, Lateral Stresses in the Ground and Design of Earth Retaining Structures, Cornell Univ., Ithaca, New York, 103-147, 1970.

- Sherif MA, Fang YS. Dynamic earth pressures on rigid walls rotating about the base. In: Proceedings of the of eighth world conference on earthquake engineering, vol. 6. San Francisco; 1984a. p. 993–1000.
- Sherif MA, Fang YS. Dynamic earth pressure on walls rotating about top. Soils Found 1984b;24(4):109–17.
- Sherif, M. A., Ishibashi, I., and Lee, C. D. 1982. Earth pressure against stiff retaining walls. Journal of Geotechnical Engineering, ASCE 108: 679-695.
- Stadler A. T. 1996. Dynamic centrifuge testing of cantilever retaining walls. PhD Thesis, University of Colorado at Boulder.
- Steedman, R. S., and Zeng, X. 1991. Centrifuge modeling of the effects of earthquakes on free cantilever walls. Centrifuge'91, Ko (ed.), Balkema, Rotterdam.
- Sitar, N., Geraili Mikola, R., and Candia, G., Seismically Induced Lateral Earth Pressures on Retaining Structures and Basement Walls, Invited Keynote Paper, GeoCongress 2012, ASCE, State of the Art, pp. 335-358.
- Veletsos, A., and Younan, A. (1997). "Dynamic response of cantilever retaining walls," Journal of Geotechnical and Geoenvironmental Engineering, 123(2), 161-172.
- Wood, JH. "Earthquake induced soil pressures on structures," PhD Thesis, California Institute of Technology, Pasadena, CA, 1973.
- Whitman, R.V. (1991). "Seismic Design of Earth Retaining Structures," Proceedings, Second International Conference on Recent Advances in Geotechnical Earthquake Engineering and Soil Dynamics, ASCE, St. Louis, MO., 1767-1778.
- Zeng, X. "Modeling Behavior of Quay Walls in Earthquakes," PhD Thesis, Cambridge University, Cambridge, England, 1990.

Chapter 3
Experimental Approach

3.1. Background

3.1.1. Introduction

Scaled 1-g shaking table test have been used commonly to assess the behavior of soil structure interaction under dynamic loading. However, there is a limitation to these types of models when used to predict the seismic response because the stress levels in the models are less than those found in prototype structures and the behavior of soil is stress dependent. Ideally, prototype scale models would be desirable. Unfortunately, such tests are difficult to perform because of their high costs, extensive time required for model construction, and trouble finding a shaker with the ability to simulate earthquake motions that has the capacity to shake both the structure and enough backfill to allow for the simulation of realistic site response. Alternatively, prototype stress levels can be obtained in small-scale models by using a centrifuge. This is the approach chosen in this study.

3.1.2. Scaling laws

The principal concept behind using the centrifuge models is to use a higher gravitation level to create a stress and a stress distribution in the model which are identical to the stress and the stress distribution in the prototype. Table 3.1 shows scaling relations for the different quantities.

3.1.3. Advantages of Centrifuge Modeling

Dynamic centrifuge testing of scaled models of earth structures has become an invaluable tool to understanding geotechnical earthquake engineering problems that would have been otherwise very hard to study. Discussions of the advantages of dynamic centrifuge modeling have been previously presented by a number of researchers including Kutter (1995) and Dobry and Liu (1994), for example. The principal advantages are as follows:

- Small-scale models can be used to accurately simulate prototypes with realistic soil stress states and depths;
- The results and rests are highly repeatable;
- The modes of failure and deformations can be observed directly;
- The models are efficient and cost-effective alternative to full-scale testing;
- Earthquake motions with a wide range of magnitudes and frequency contents can be reproduced; and
- The models are well suited for the evaluation of empirical methods and validation of numerical modeling techniques.

Table 3.1. Conventional scaling factors used for centrifuge testing.

Quantity Name	Scaling Factor (model/Prototype)
Density	1
Gravity	N
Stress, Pressure, Moduli	1
Length, Displacement	1/N
Mass	$1/N^3$
Force	$1/N^2$
Dynamic Time	1/N
Dynamic Velocity	1
Dynamic Acceleration	N
Dynamic Frequency	N
Diffusion Time	$1/N^2$

3.1.4. Limitations of Centrifuge Modeling

While centrifuge model experiments have many advantages over other experimental approaches, there are also inherent limitations (Hausler 2002, Al-Atik 2010):

- Depending on the radius of the centrifuge there is a slightly nonlinear stress distribution due to the increasing radius of rotation with depth of the model, which results in a small variation in the g level and hence the scaling factors with depth;
- Container side-walls interact with the soil. This effect can be minimized in the centrifuge experiments by using a flexible shear beam container. This type of container is designed such that its natural frequency is much less than the initial natural frequency of the soil (Kutter 1995);
- The container bottom, which is the source of input motion imparted to the soil, represents a rather unnatural and very rigid geologic transition; and
- Experimental errors can be exacerbated by the scaling factors.

3.1.5. Potential Errors in Centrifuge Modeling

No experimental technique in geotechnical engineering is able to reproduce exactly the same conditions as those that exist in the prototype field situation. This is due to the non-homogeneity and anisotropy of soil profiles, both in natural deposits and in man-made earth structures, and to the limitation of the modeling tool. The best we can do is to identify the factors that cause differences between the behavior of the model and the prototype, and asses and minimize their effects. The potential errors that may be present in the set of experiments presented herein are addressed later within the context of the interpretation of the experimental results.

3.2. UC Davis Centrifuge, Shaking Table, and Model Container

Two centrifuge experiments were performed on the dynamic centrifuge at the Center for Geotechnical Modeling (CGM) at the University of California, Davis. The centrifuge has a radius of 9.1 m, a maximum payload of 4,500 kg, and an available bucket area of 4 m^2 as shown in Figure 3.1. The centrifuge capacity in terms of the maximum acceleration multiplied by the maximum payload is 240 g-tonnes. The shaking table has a maximum payload mass of 2,700 kg and a maximum centrifugal acceleration of 75 g. Additional technical specifications for the centrifuge and shaking table are available in Kutter et al. (1994) and Kutter (1995).

Figure 3.1. The large centrifuge payload bucket at the Center for Geotechnical Modeling at U.C. Davis.

The two models were constructed in a rectangular flexible shear beam container, known as FSB2, with internal dimensions of 1.65 m long x 0.79 m wide x approximately 0.58 m deep. The bottom of the container is coated with grains of coarse sand and is uneven. The container consists of a series of stacked aluminum rings separated by neoprene rubber, as shown in Figure 3.2. The flexible model container is mounted on a servo-hydraulic shaking table. The shaker actuators are controlled by a conventional closed-loop feedback control system and have the capacity of producing between 14 and 30 g shaking accelerations at frequencies up to 200 Hz. The maximum absolute shaking velocity is about 1 m/sec and the stroke is 2.5 cm peak to peak.

To minimize boundary effects, the container is designed such that its natural frequency is less than the initial natural frequency of the soil (Kutter 1995). The centrifugal acceleration used in the two experiments was 36 g. All results are presented in terms of prototype units unless otherwise stated.

Figure 3.2. Model container FSB2.

3.3. Model Test Configurations

The first centrifuge experiment, ROOZ01, was performed on a uniform density sand model. The model configuration is shown in Figure 3.3 and 3.4 in model units in profile and plan views. In prototype scale, the ROOZ01 model consisted of two retaining wall structures, stiff and flexible non-displacing basement walls, of approximately 6 m height spanning the width of the container. The structures were designed to have the stiffness, mass, and natural frequency of typical reinforced concrete structures. They sat on approximately 12.5 m of dry medium-dense sand (Dr = 75%) and the backfill soil consisted of dry medium-dense sand (Dr = 75%). Both structures had stiff mat foundations. The second centrifuge experiment, ROOZ02, was performed on a two-layer sand model. The model configuration is shown in Figure 3.5 and 3.6 in model units in profile and plan views. The ROOZ02 model consisted of the non-displacing U-shaped cantilever and displacing retaining wall structures. The structures sat on approximately 12.5 m of dry medium-dense sand (Dr = 80%) and supported a dry medium-dense sand backfill (Dr = 75%).

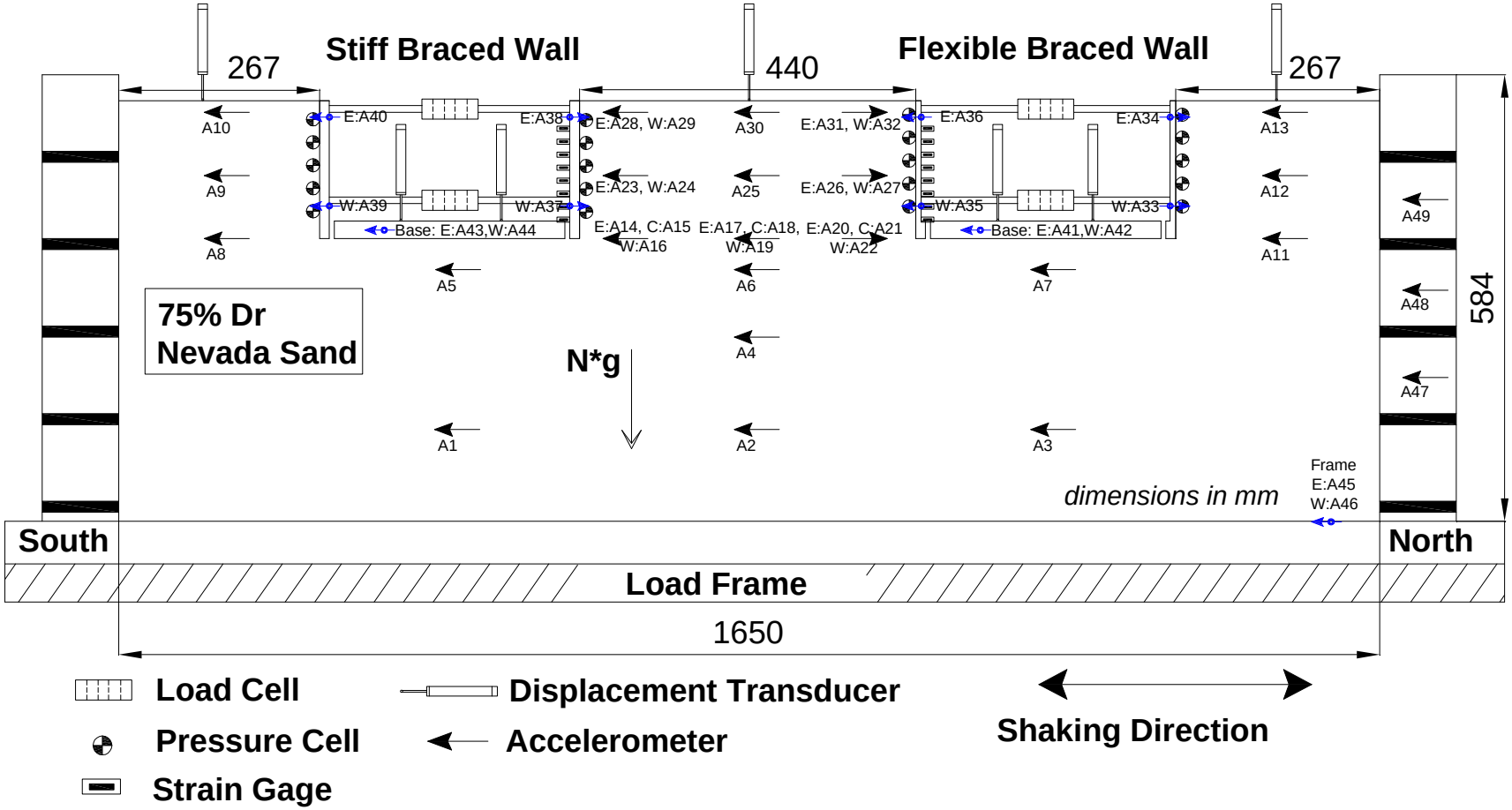

Figure 3.3. ROOZ01 Model configuration, profile view (dimension in mm).

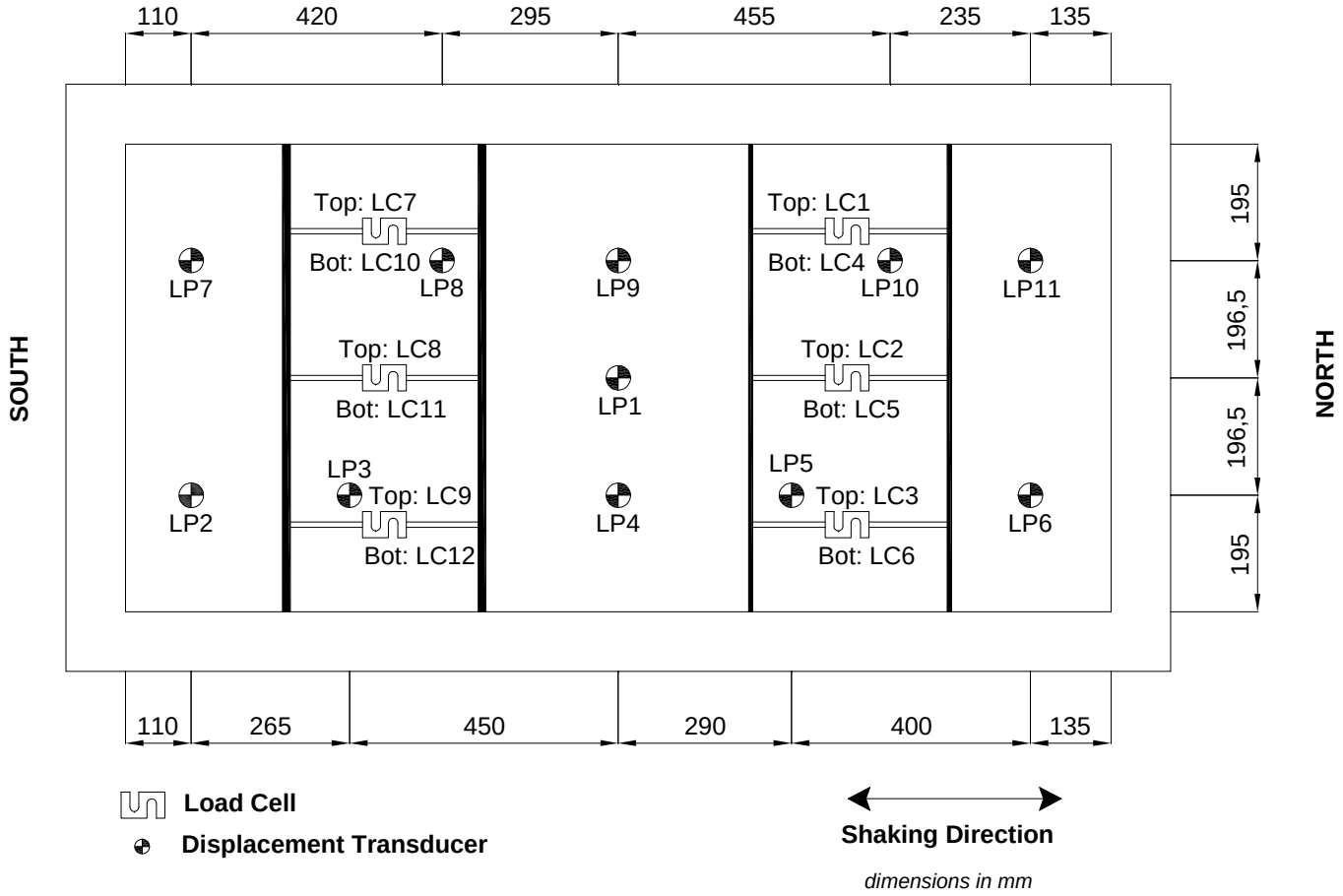

Figure 3.4. ROOZ01 model configuration, plan view (dimension in mm).

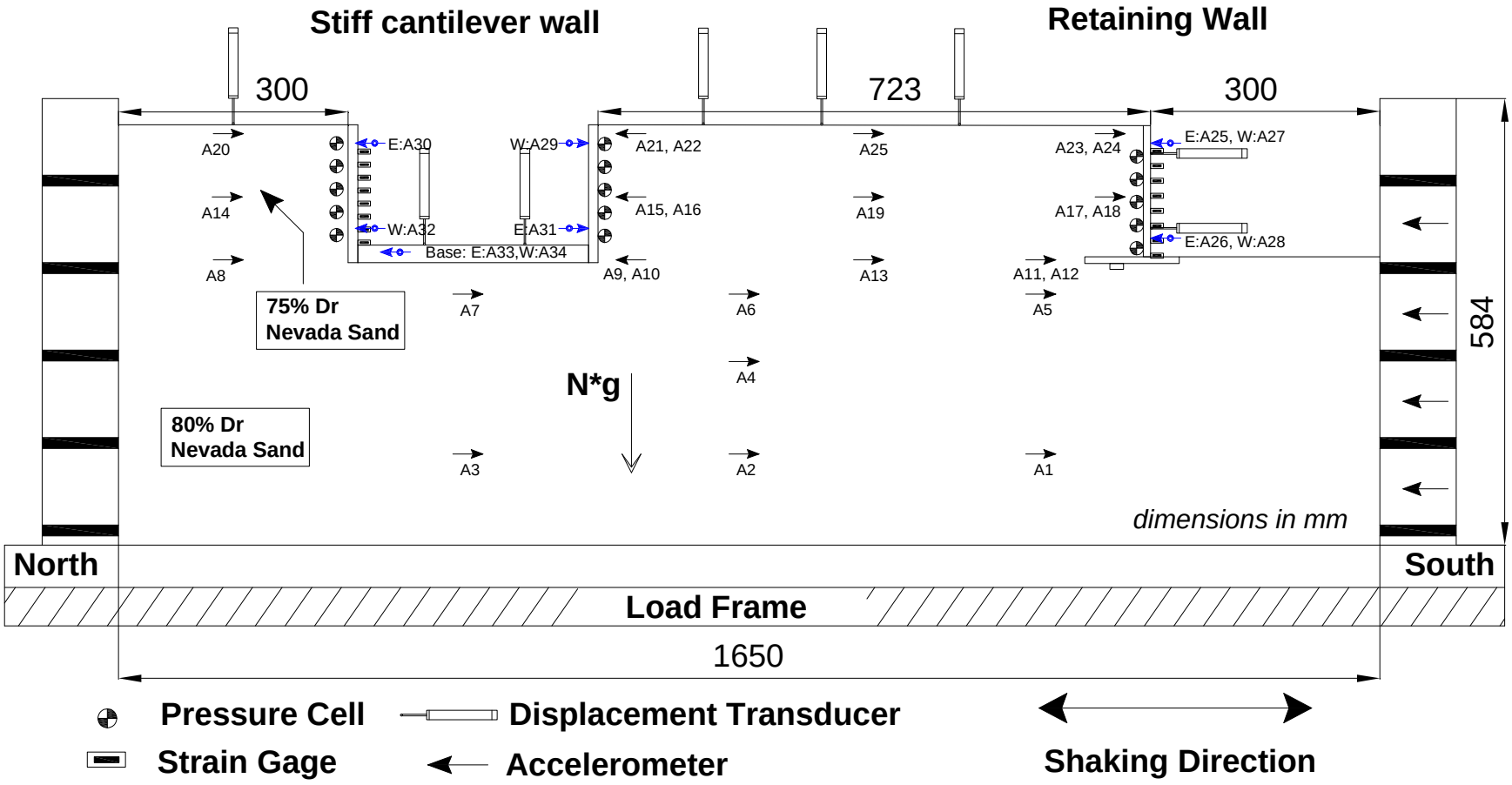

Figure 3.5. ROOZ02 Model configuration, profile view (dimension in mm).

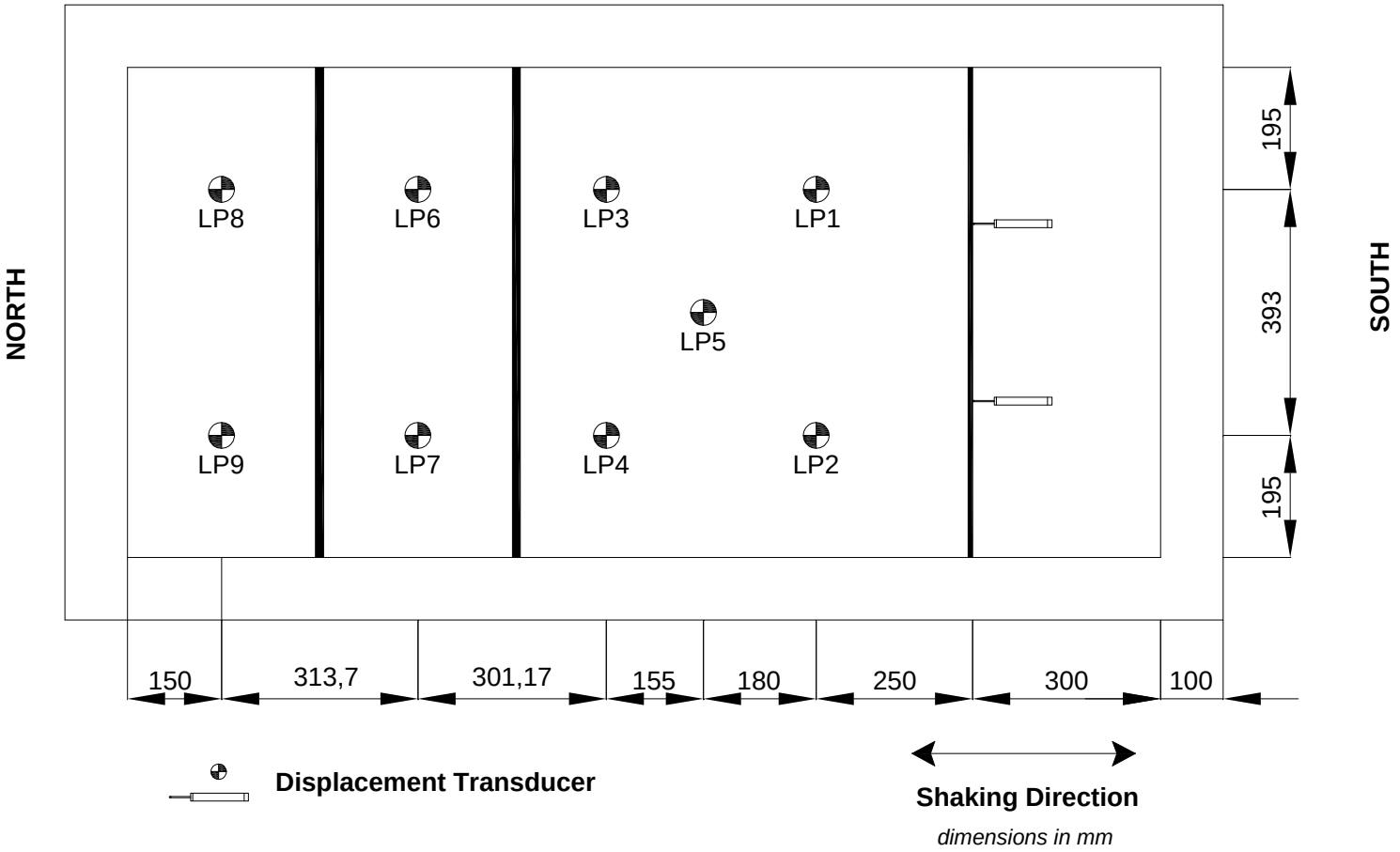

Figure 3.6. ROOZ02 model configuration, plan view (dimension in mm).

3.4. Soil Properties

The model soil was dry Nevada Sand. Nevada Sand is a mined, non-processed, and uniformly graded fine angular sand with a coefficient of uniformity (Cu) of 1.06 and a mean grain diameter (D50) of 0.15 mm. Mechanical grain size analyses of Nevada sand are shown in Figure 3.7. It has a mean grain size of 0.14 - 0.17 mm, a uniformity coefficient of 1.67, a specific gravity of 2.67, and less than 5% fines (Kammerer et al. 2000). It should be noted that the mechanical properties of Nevada Sand vary with each batch delivered to the centrifuge. Table 3.2 summarizes the soil properties of the latest Nevada Sand batch delivered to the CGM and the historical data from various researchers.

Table 3.2. Mechanical Properties of Nevada Sand from Various Tests.

Source	Gs	e_{min}	e_{max}	γ_d, min (KN/m^3)	γ_d, max (KN/m^3)
Arulmoli et al. (1991)	2.67	0.51	0.887	13.87	17.33
Balakrishnan (1997)	-	0.55	0.84	14.21	16.92
Woodward Clyde (1997)	-	-	-	13.97	16.75
Kammerer et al. (2000)	2.67	0.533	0.887	13.87	17.09
UC Davis - Seiji Kano (2007)	2.65	0.486	0.793	14.50	17.49
Cooper Lab (2007)	-	0.52	0.78	14.57	17.05
Cooper Lab (2008)	2.65	0.510	0.748	14.86	17.20

Slight variations in the results can be attributed to the inherent changes in the different sand batches delivered to the CGM facility and to the different testing methods used (ASTM versus Japanese standards). The minimum and maximum dry densities determined by Cooper Labs (2008), yielded 14.86 and 17.20 kN/m^3 respectively. These minimum and maximum dry density values were used in this study. The initial friction angle value for the backfill Nevada sand was estimated to be 34° for ROOZ01 and 36° for ROOZ02 (Arulmoli et al. 1992).

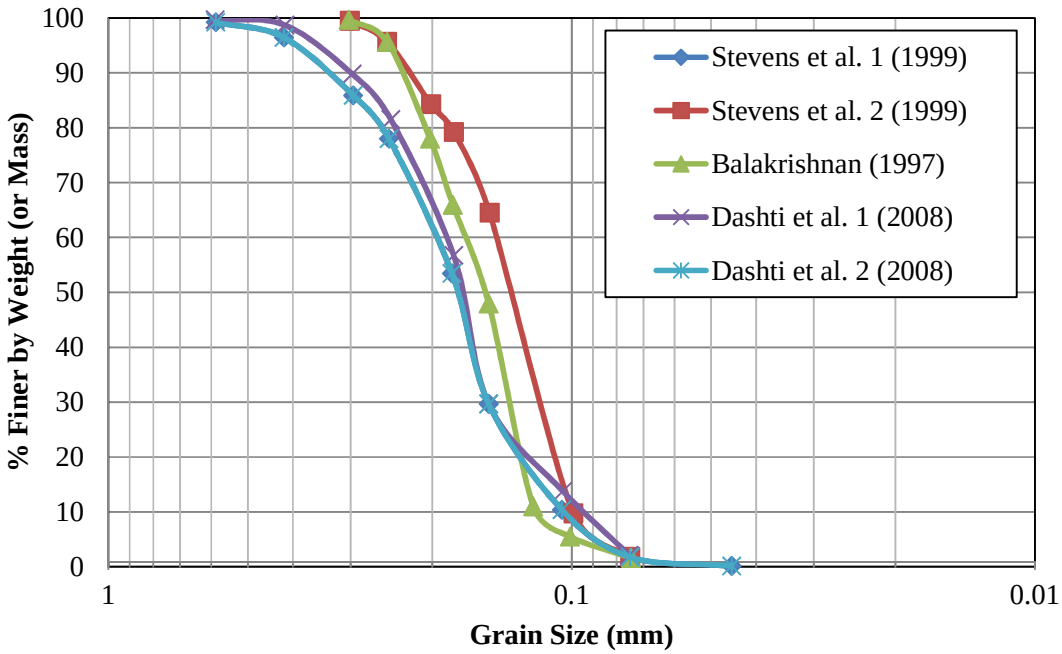

Figure 3.7. Grain size distribution for Nevada Sand.

3.5. Structure Properties

Three different types of retaining prototype structures were modeled in this research effort, as follows: 1) non-displacing cross braced (basement) structure; 2) a non-displacing U-shape cantilever structure and 3) a displacing retaining wall. All the retaining structures were constructed of T6061 aluminum plate. The Young's modulus and Poisson's ratio for this grade of aluminum are 10,000 ksi and 0.32, respectively. Non-displacing basements consisted of two parallel plates braced by six threaded bars (three on top and three on bottom) as well as base plate as shown in Figure 3.8 and 3.9. The base plate was separated from walls using soft damper and its job was simply to prevent the soil from heaving into the opening. The displacing cantilever wall was constructed of two plates, a base plate and wall stem (Figure 3.10). The plates were bolted together in an inverted T configuration. The same materials of non-displacing basement are used to construct non-displacing U-shaped cantilever wall instead plates were bolted to the base plate using five regular 7/8 inch aluminum bolts as shown in in Figure 3.11.

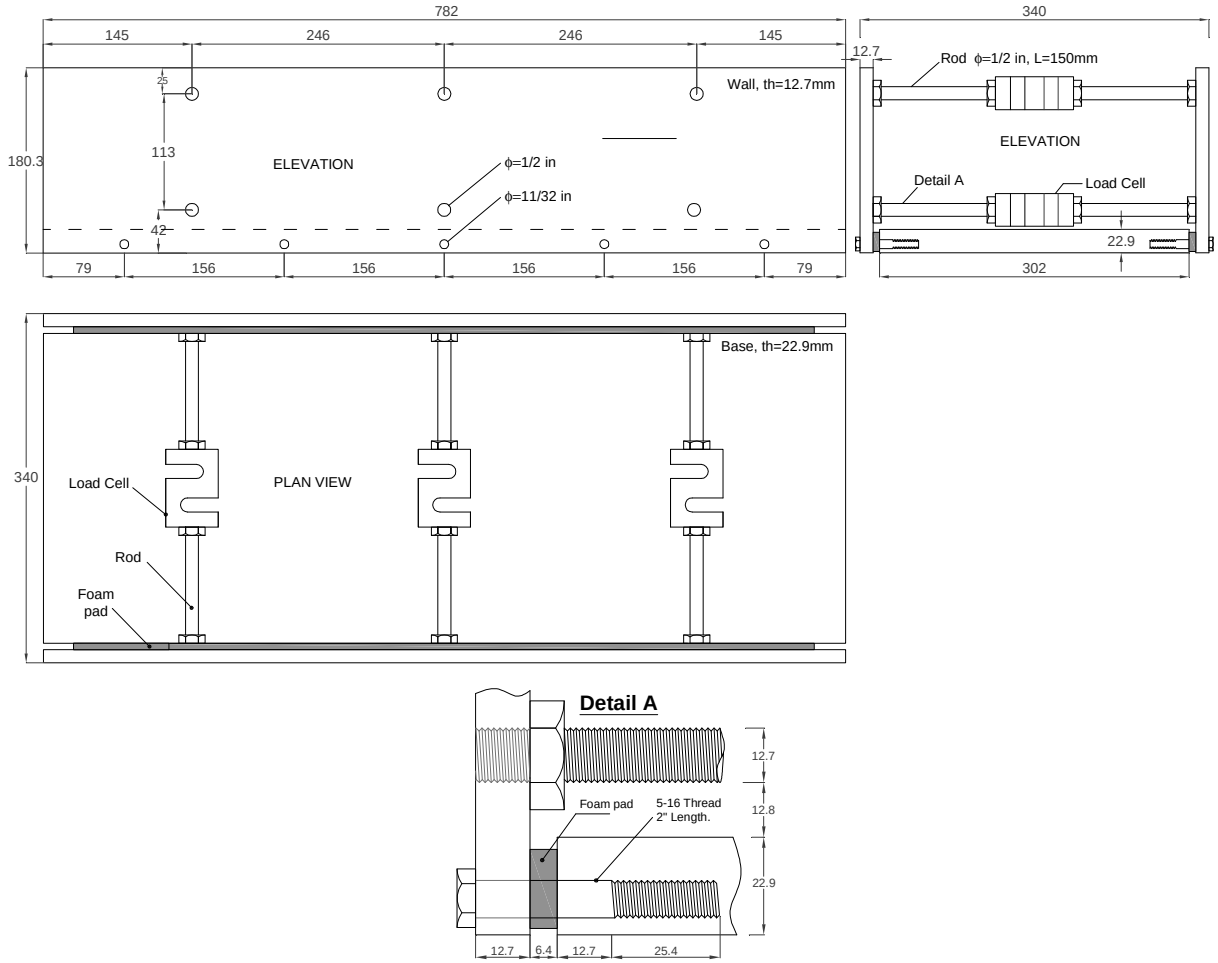

Figure 3.8. Stiff cross braced model structure configuration (dimensions in mm, model scale).

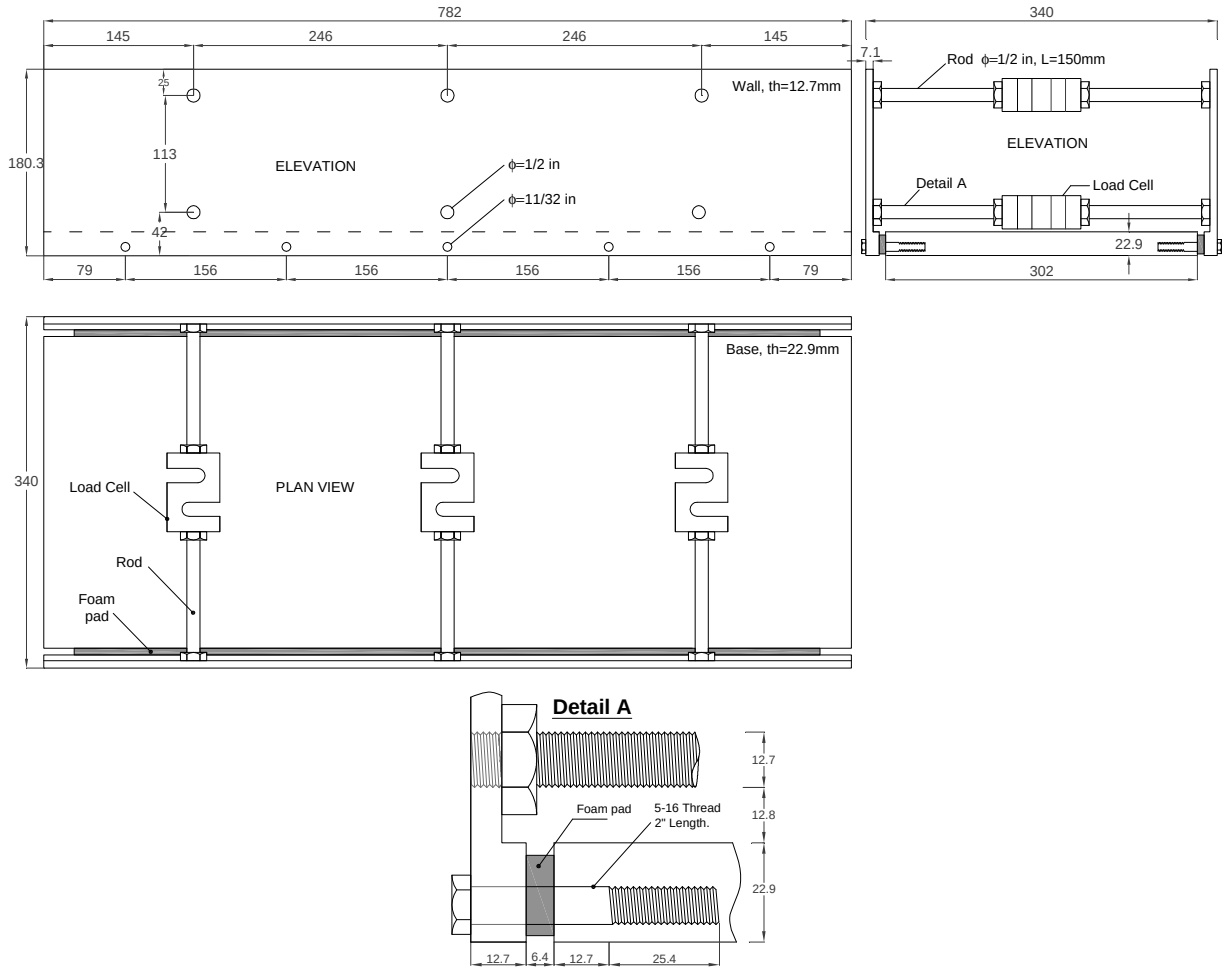

Figure 3.9. Flexible cross braced model structure configuration (dimensions in mm, model scale).

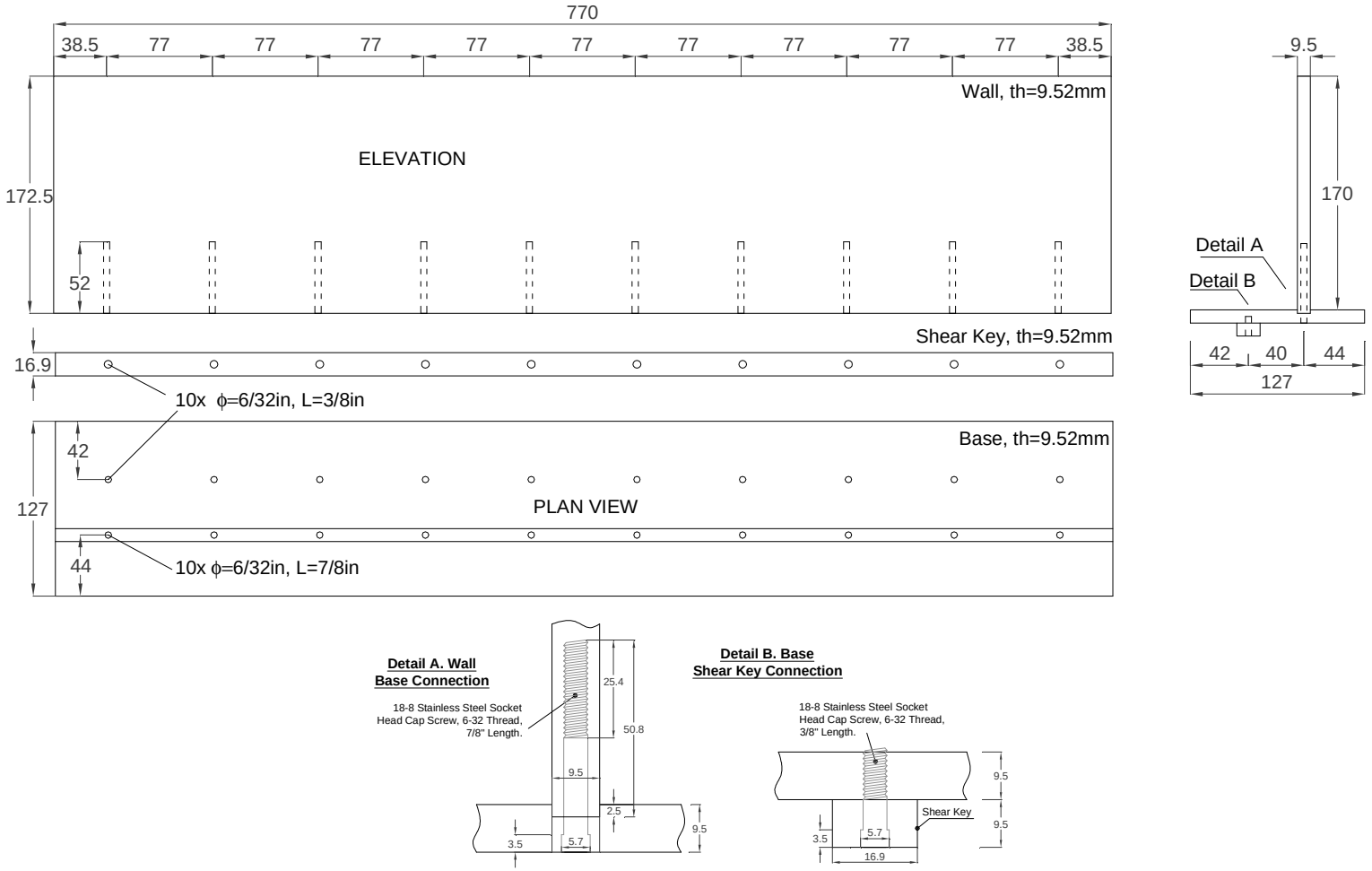

Figure 3.10. Stiff U-shaped model structure configuration (dimensions in mm, model scale).

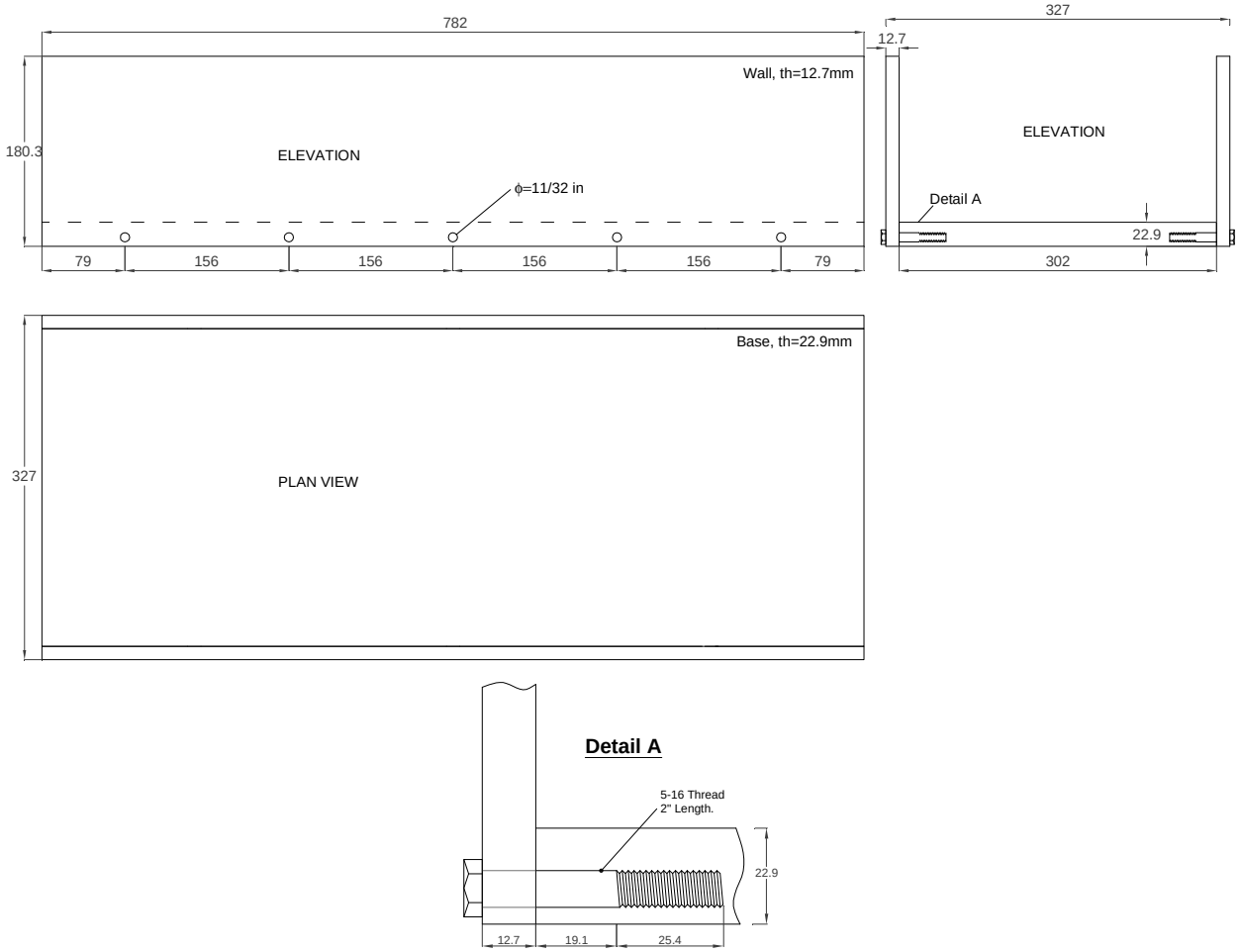

Figure 3.11. Retaining model structure configuration (dimensions in mm, model scale).

All the structures spanned the width of the container and all the structures were designed to represent typical reinforced concrete retaining structures. Thickness of the model walls was determined by matching the stiffness of the reinforced concrete prototypes. The stiffness of the reinforced concrete prototypes was calculated using the effective moment of inertia of the concrete sections rather than the gross moment of inertia $I = (bH^3/12)$. The effective moment of inertia takes into account the cracking of the concrete sections. The mass of the reinforced concrete prototypes was also matched by adding small lead pieces to the model structures, without significantly impacting their stiffness.

3.6. Model Construction

To achieve a uniform deposit with relatively density of 75%, Nevada Sand was first dry-pluviated (Figure 3.12a, b) into a calibration chamber using the large pluviator for calibration. By varying the drop height and the rate of flow of the pluviating sand, different relatively density can be obtained. The model was then constructed in lifts. After each lift, the soil surface is vacuumed down to a desired elevation, where the instruments are placed (Figure 3.13). The model was weighed after each lift to ensure that the soil remained at the desired uniform relatively density of 75% throughout the model construction.

The retaining structures were placed at their corresponding elevations. Finally, the backfill sand was placed behind the walls in several layers. Industrial grease was placed between the structures' walls and the container to provide a frictionless boundary and prevent sand from passing through. Photographs of the model under construction and on the centrifuge arm are shown in Figures 3.12 – 3.15.

(a) **(b)**

Figure 3.12. (a) Calibration of dry-pluviator **(b)** Pluviation of sand inside model container.

Figure 3.13. Placing accelerometers in the corresponding position.

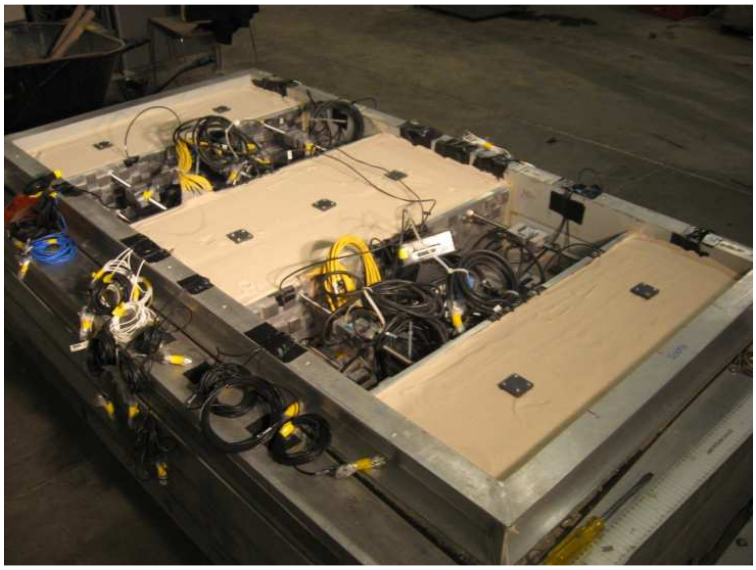

Figure 3.14. Model under construction.

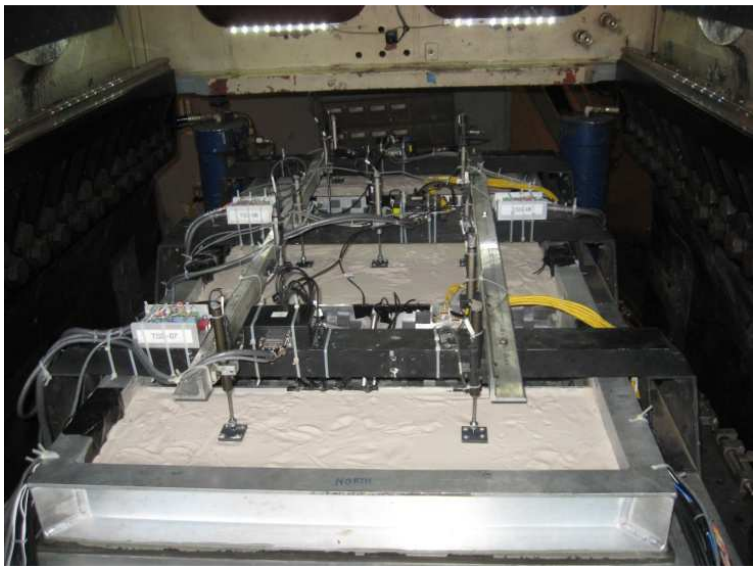

Figure 3.15. Model on centrifuge arm.

3.7. Instrumentation

Six different types of miniature electronic transducers were employed in the experimental program, accelerometers, strain gages, linear potentiometers (LP), linear variable differential transformer (LVDT), pressure transducers and load cells. These devices measured acceleration on the shaking table, retaining wall, and backfill soil; bending strain and deflection of the wall stem; backfill settlement; lateral earth pressure on retaining wall as well as axial force in horizontal strut. Detailed descriptions of the transducers are given in the following section.

3.7.1. ICP Accelerometers

All the ICP accelerometers (Figure 3.16) used in this research were manufactured by PCB Piezotronics, Inc. These are quartz piezoelectric accelerometers designed specifically for high frequency response. The accelerometers are quite rugged and well suited for the extreme condition present in the centrifuge test environment. The ICP accelerometers have ±100 g or ±50 g ranges. The calibration data provided by the manfacturer were used for all accelerometers.

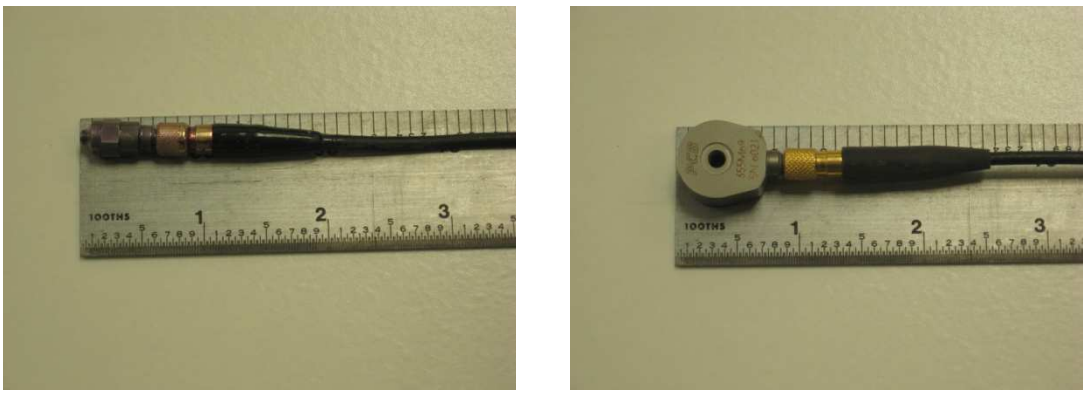

Figure 3.16. PCB Piezotronics acclerometers.

3.7.2. Strain gages

The strain gages employed in this research were manufactured by Vishay Measurements Group. Type J2A-13-S181H-350 gages were used. Moments on the retaining structures are measured directly by the use of these strain gages. The non-displacing and displacing cantilever walls were instrumented with eight pairs of strain gages (Figure 3.17). The strain gage circuits were arranged as Wheatstone Bridge circuits as shown in Figure 3.18. This configuration minimized the number of balancing resistors as well as the number of sliprings taken up since all the pairs of strain gages have but one common ground the excitation voltage is 5 V DC.

Strain gages were manually calibrated specifically for these tests and compared to the manufacturer's specification. To accomplish this, the base of each model retaining wall was rigidly secured and weights hung from the free end of the wall. The load was distributed evenly across the width of the wall. This effectively created a cantilever beam with a concentrated load at the end, moments of which can be readily determined. Weights of 7.5, 15, 22.5, 30 kgf were hung and the output recorded

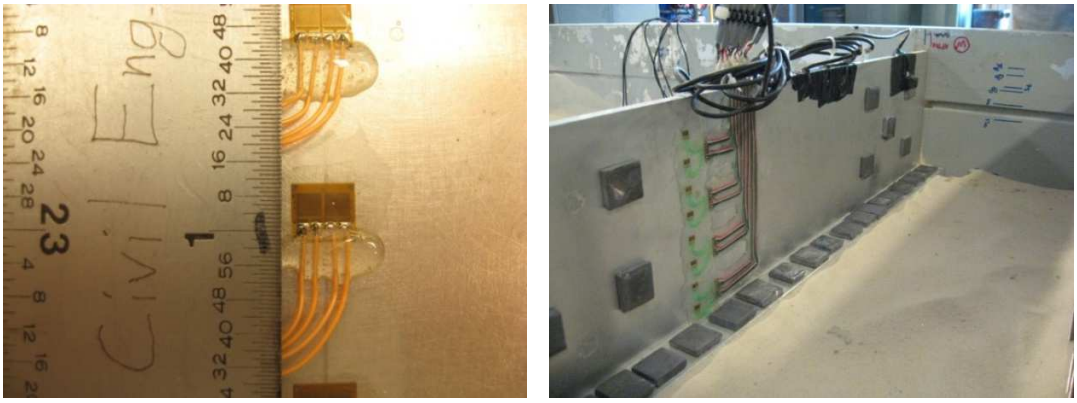

Figure 3.17. Strain gages located at the walls.

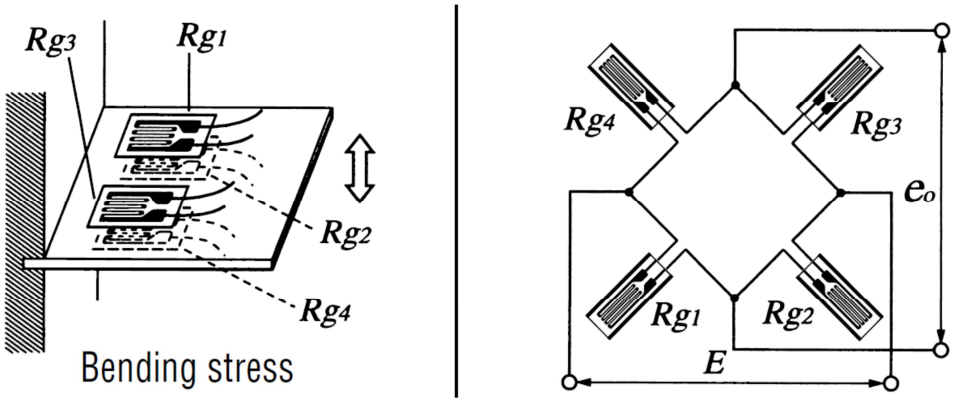

Figure 3.18. Wheatstone Bridge circuit.

3.7.3. Earth Pressure transducers

Direct measurements of lateral earth pressure on the model retaining wall stems were made using miniature pressure transducers. The Tactilus free form sensor system (Figure 3.20a, b) pressure sensors were employed. These have a range of 0 to 25 psi. Earth pressure transduceres specifications are listed in Table 3.3. These pressure transducers were calibrated by placing them on the base of the small container of the small Schaevits, centrifuge which has a 1-m radius (Figure 3.19a, b). Measurements were then taken with the centrifuge stationary (at 1g) and spinning to 65g. The increase in g-acceleration cause an increase in the soil unit weight by the corresponding factor N (see Table 3.1) and thus an increase in pressure, in this manner, a calibration constant in terms of psi/volt was experimentally determined for pressure transducer.

(a) **(b)**

Figure 3.19. (a) UC Davis Schaevits centrifuge (1m radius) **(b)** Tactilus free form sensor placed on the base of small container.

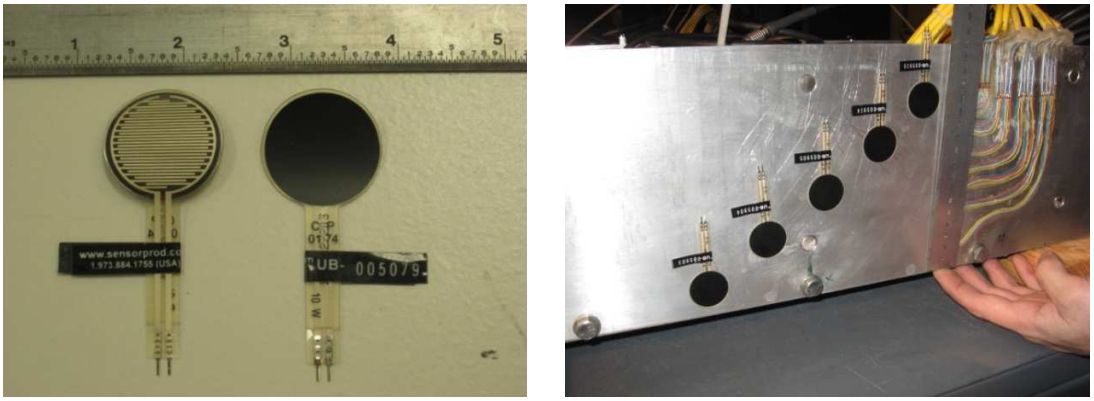

(a) **(b)**

Figure 3.20. (a) The Tactilus free form pressure transducer **(b)** pressure transducers placed on the sides of retaining structures.

Table 3.3. Tactilus free form sensors performance characteristics (Tactilus, 2012)

Sensor Specifications	
Technology	Resistive
Pressure Range	0-15 psi
Dimensions	15 mm
Thickness	From 14 mils
Durability	Up to 1000 uses
Recommend Current	5 mA
Supply Voltage	3-6 VDC
Temperature Range	0° to 113°F (0° to 45°C)
Spatial Resolution	Custom
Scan Speed	100 hertz

The locations of the strain gages, Tactilus free form sensors, on the non-displacing and displacing cantilever structures for experiments ROOZ01 and ROOZ02 are shown in Figures 3.21a, b.

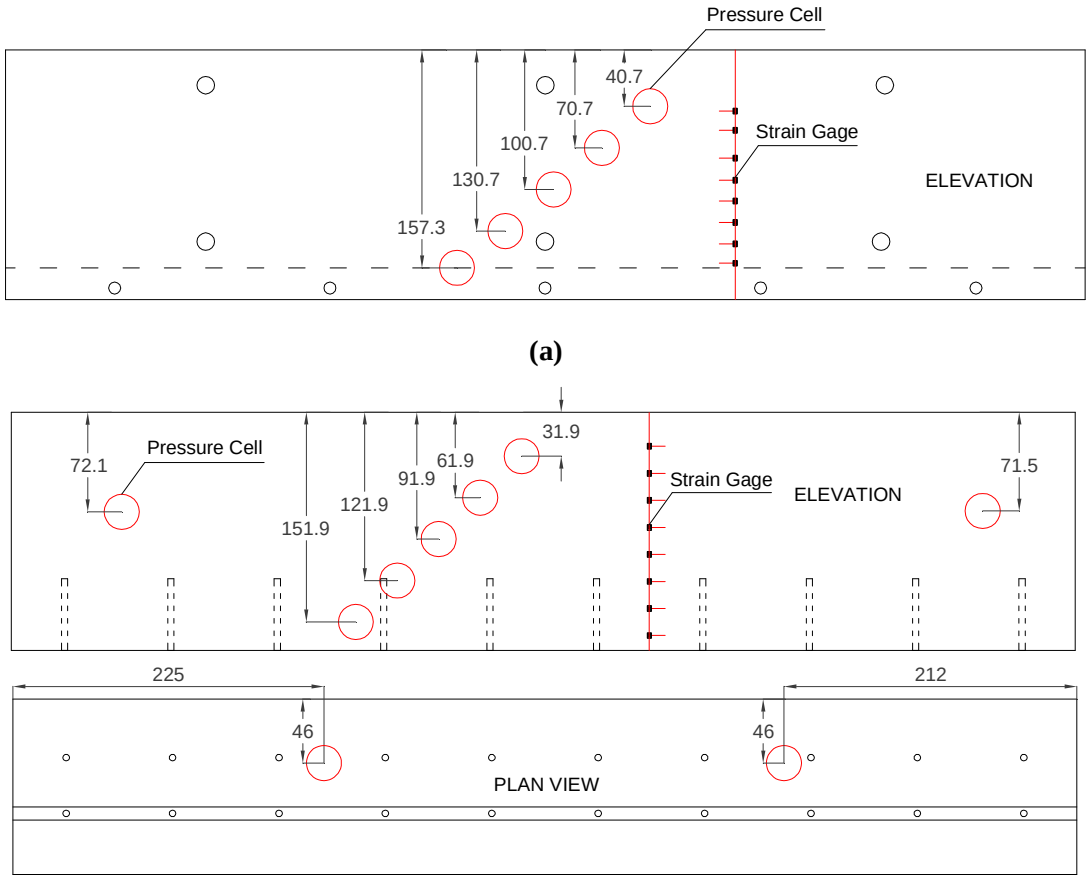

Figure 3.21. Pressure cells and strain gages layout on **(a)** Non-Displacing basement and cantilever walls **(b)** Displacing retaining wall for ROOZ01 and ROOZ02, (dimensions: mm, model scale)

3.7.4. Displacement Transducers (LP and LVDT)

Both linear potentiometer (LP) and linear variable differential transformer (LVDT) were used in this research (Figure 3.22a, b). LP's with nominal linear range of ±2" were used to measure the backfill settlement and LVDT's with nominal linear range of ±1" were used to measure the static and dynamic lateral deformation/deflections of the model retaining wall stems.

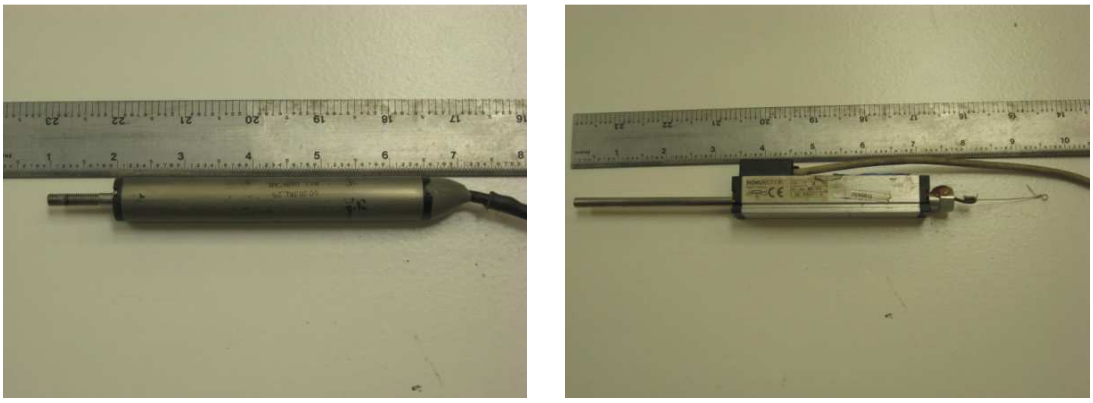

(a) **(b)**

Figure 3.22. Displacement transducers **(a)** LP **(b)** LVDT.

To calibrate, LP's and LVDT's body were placed in a fixed position. The core was then displaced through the entire linear range in small increments using a reference LP with known calibration factor. Voltage changes were recorded by the data acquisition system. In this manner, a calibration constant in terms of inch/volt was experimentally determined for each displacement transducer.

3.7.5. Load Cells (LC)

Six load cells (LC's) (Figure 3.23a) were installed (three at the top and three at the bottom) between struts in the non-displacing braced wall structures (basements) as shown in Figure 3.23b to measure the applied horizontal load. Situated behind the test wall, the load cells provide a measurement of the total lateral force. The LC's employed in this research were manufactured by Interface Inc. Type SSM-AJ-500 was used. Calibration data provided bt the manfacturer was used for all load cells.

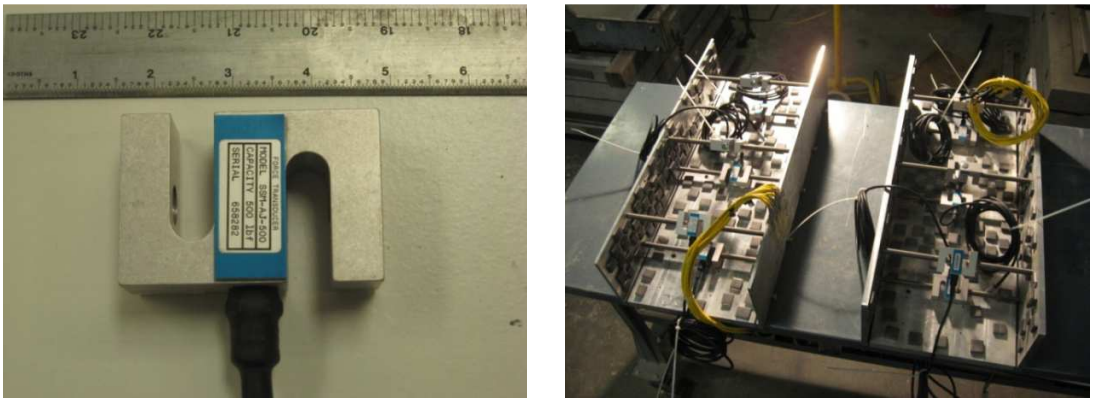

(a) **(b)**

Figure 3.23. (a) Load cells, **(b)** Placed load cells between struts.

3.8. Data Acquisition

The data acquisition infrastructure at the CGM facility consists of several parallel systems that can be operated in combination or independently and allow researchers to record data during all stages of model construction and testing. ICP accelerometers, displacement transducers, strain gages, load cells and earth pressure sensors were routed through different amplifiers for signal conditioning to the main data acquisition system (RESDAQ-Main). Appropriate gain levels were set at the different amplifier channels to ensure good signal quality for the various sensors. RESDAQ-Main allows fast data sampling at a model scale rate of 4096 Hz during simulated seismic events. Slow data sampling at a rate of 1 Hz in model scale was used during spin up, spin down and between shaking events.

Data was saved starting a few seconds before shaking and ending a few seconds after each shaking event. Data was subsequently converted to engineering prototype units using the corresponding channel gain list and centrifuge scaling laws after being zero-referenced. Also, the algebraic sign of the data was adjusted to reflect the conventional coordinate system chosen for the model. All horizontal acceleration and displacement recordings were corrected so that their signs are positive to the south and vertical displacement is positive downward, regardless of the orientation of the instruments themselves. The raw data in voltage obtained from the two experiments was converted to prototype scale engineering units by multiplying by the appropriate instrument calibration factors and adjusting for instruments gains. Details of the data acquisition systems are available at the CGM website (http://nees.ucdavis.edu).

3.9. Shaking Events

Twelve shaking events were applied to the ROOZ01 model in flight at 36g centrifugal acceleration. The shaking was applied parallel to the long sides of the model container and orthogonal to the model structures. The shaking events consisted of a step wave, a ground motion recorded at the Takatori (TAK) stations during the 1995 Kobe earthquake and applied two times, Santa Cruz station during the Loma Prieta 1989 earthquake and applied once, ground motions recorded at the Yarmica (YPT) station during the Kocaeli, Turkey, 1999 earthquake and Saratoga West Valley College (WVC) stations during the Loma Prieta 1989 earthquake. Step waves are usually applied at the beginning of a shaking series in order to test the instruments and the data acquisition system. The shaking events for ROOZ01 along with their prototype base peak accelerations are shown in Table 3.4.

Ten shaking events were applied to the ROOZ02 model in flight at 36 g centrifugal acceleration. The shaking events consisted of step waves, ground motions recorded at the Yarmica (YPT) station during the Kocaeli, Turkey, 1999 earthquake, Santa Cruz station during the Loma Prieta 1989 earthquake, a ground motion recorded at the Takatori (TAK) stations during the 1995 Kobe earthquake and ground motions recorded at the Santa Cruz (SC) station and Saratoga West Valley College (WVC) stations during the Loma Prieta 1989 earthquake. The shaking events for ROOZ02 along with their prototype base peak accelerations are shown in Table 3.5. Input ground

motions for experiments ROOZ01 and ROOZ02 should reasonably reproduce the range of frequencies present in the recorded earthquake motions. However, travel limitations of the shaking table limit the low-frequency content of the input motions and, therefore, affect the overall spectra of the motions.

Table 3.4. Shaking events for ROOZ01.

Shaking Event	Input Peak Acceleration (g)
Step Wave	0.08
Kobe-TAK090-1	0.61
LomaPrieta-SC-1	0.53
Kocaeli-YPT060-1	0.05
Kocaeli-YPT060-2	0.21
Kocaeli-YPT060-3	0.40
Kocaeli-YPT330-1	0.14
Kocaeli-YPT330-2	0.38
Loma Prieta-WVC270-1	0.30
Kocaeli-YPT330-3	0.28
Kobe-TAK090-2	0.61
Loma Prieta-WVC270-2	0.32
Kocaeli-YPT330-4	0.33

Table 3.5. Shaking events for ROOZ02.

Shaking Event	Input Peak Acceleration (g)
Step Wave	0.03
Kocaeli-YPT060-1	0.19
Kocaeli-YPT060-2	0.25
Kocaeli-YPT060-3	0.34
Kocaeli-YPT330-1	0.32
LomaPrieta-SC-1	0.52
Kobe-TAK090-1	0.60
LomaPrieta-SC-2	0.54
Loma Prieta-WVC270-1	0.32
Kocaeli-YPT330-2	0.34
Kobe-TAK090-3	0.64

3.10. Known Limitations and Problems

3.10.1. Overview

The main problems and limitations encountered during centrifuge experiments ROOZ01 and ROOZ02 are the following:

- One load cells the east bottom stiff basement wall failed at the beginning of the experiment ROOZ01. The load carried by this load cell was made equal with load at the bottom west in the same structure.

- Accelerometer A24 and A48 failed during the experiment ROOZ01.
- Linear potentiometer LP2, LP8 and LP11 exceeded maximum during experiment ROOZ01.
- Accelerometer A19 and A33 failed during the experiment ROOZ02.
- Linear potentiometer LP5 failed during experiment ROOZ02.
- SG8 on the non-displacing U-shaped wall failed during the experiment ROOZ02.

3.10.2. Tactilus Free Form Sensor Performance

Direct measurement of lateral earth pressure using pressure transducers was originally intended in order to obtain direct insight into the nature of the static and dynamic lateral earth pressure profiles.

The Tactilus earth pressure transducers have a manufacturer stated frequency response up to 100 Hz, as shown in Table 3.3. This frequency response is sufficient for sampling static earth pressure, but it is under sampling the dynamic earth pressure due to the fact that the scaling in a centrifuge requires a sensor with frequency response of at least up to 500-700 Hz to fully capture the dynamic earth pressure . Consequently, the pressure cell data is used in herein only to identify the shape of the dynamic earth pressure distribution load cells and strain gages are used to obtain the magnitude of the corresponding forces.

3.11. References

- Al-Atik, L. and N. Sitar, 2010. Seismic Earth Pressures on Cantilever Retaining Structures, Journal of Geotechnical and Geoenvironmental Engineering, Vol. 136, No. 10, pp. 1324-1333, doi: 10.1061/(ASCE)GT.1943-5606.0000351.
- Arulmoli, K, Muraleetharan, KK, Hosain, MM, and Fruth, LS. "VELACS Laboratory Testing Program, Soil Data Report," The Earth Technology Corporation, Irvine, California, Report to the National Science Foundation, Washington D.C., March, 1992.
- Dobry, R, and Liu, L. "Centrifuge Modeling of Soil Liquefaction," Proceedings of the Tenth World Conference on earthquake Engineering, Balkema, Rotterdam, 6801- 6809, 1994.
- Kammerer, AM, Wu, J, Pestana, JM, Riemer, M, and Seed, RB. "Cyclic Simple Shear Testing of Nevada Sand for PEER Center Project 2051999," Geotechnical Engineering Report No. UCB/GT/00-01, University of California, Berkeley, CA, 2000.
- Hausler, E. "Influence of Ground Improvement on Settlement and Liquefaction: A Study Based on Field Case History Evidence and Dynamic Geotechnical Centrifuge Tests". PhD Thesis, Fall 2002.
- Kutter, BL, Idriss, IM, Kohnke, T, Lakeland, J, Li, XS, Sluis, W.,Zeng, X, Tauscher, RC, Goto, Y, and Kubodera, I. "Design of a Large Earthquake Simulator at UC Davis," Centrifuge 94, Leung, Lee, and Tan (eds.), Balkema, 169-175, 1994.
- Kutter, BL. "Recent Advances in Centrifuge Modeling of Seismic Shaking," Proceedings., St. Louis, Vol. II, 927-941, 1995.
- Taktilus. "Tactilus Free Form Sensor System", 2012.

Chapter 4

Experimental Results

4.1. Data Reduction Methodology

The initial step in processing the instrument data recorded using the high speed data acquisition system involved filtering to reduce noise and conversion to engineering units. The data were then further processed to interpret various responses of interest. This section describes the methodology used in analyzing and interpreting the recorded data.

4.1.1. Acceleration

All recorded acceleration time series were corrected such that horizontal accelerations are positive towards the south end of the model container regardless of the orientation of the instruments themselves. Acceleration time series were filtered using a fifth order Butterworth low-pass filter with prototype scale corner frequency of 25 Hz for noise reduction, as well as a third order Butterworth high-pass filter with a prototype scale corner frequency of 0.3 Hz to remove the long period drift that would appear in the records after integration to velocity and again to displacement. The disadvantage of such filtering is that any apparent permanent offset of the instrument is also removed. Acceleration time series recorded at the northeast and northwest ends of the load frame were averaged to obtain the input ground motion.

4.1.2. Displacement

Displacement time series measured by the linear potentiometers and the LVDTs were zeroed before shaking by removing the average of the first 50 data points from the records. They were also filtered with a first order Butterworth low pass filter with a prototype scale corner frequency of 10 Hz for noise reduction.

4.1.3. Strain Gage Measurement and Bending Moment Computation

Data recorded by the strain gages on the non-displacing cantilever and displacing retaining walls were converted into strains using the strain gage calibration factors. Strain time series at each strain gage location were converted into stress and then into moment time series using the elastic beam bending theory. The strain time series were filtered using a first order low-pass Butterworth filter with a prototype scale corner frequency of 25 Hz for noise reduction.

Moments interpreted from strain gage measurements include contributions from static earth pressures, dynamic earth pressures and wall inertial moments. In order to evaluate the contribution of these different components to the moment, the following terminology has been adopted:

- Total wall moment refers to moment on the wall due to static earth pressure, dynamic earth pressure increment and wall inertial force;
- Static wall moment refers to moment on the wall due to static earth pressure;
- Inertial wall moment refers to moment on the wall due to wall inertia;

Dynamic wall moments (due to dynamic earth pressure increment and wall inertia) were interpreted by applying a moving average filter to the total wall moment time series. The moving average filter determines the static trend for each moment time series; deducing this trend from the corresponding total wall moment time series results in a dynamic wall moment time series.

4.1.4. Wall Inertia Moment

Strain gages used in the second (ROOZ02) centrifuge experiment recorded total wall moments resulting from wall inertia and earth pressures acting on the walls. Earth pressure sensors measured only total earth pressures. In centrifuge experiment ROOZ02, accelerometers were placed at the top and the base of the non-displacing cantilever (U-shape) and displacing retaining walls. Records obtained from these accelerometers were used to estimate wall inertial moments. The displacement distributions along the wall are then determined by the double integration of the accelerograms. The moment of the cantilever walls were then estimated as follow:

$$M_{base} = (3EI\delta_{max}/H^2) \quad (4.1)$$

In which $M_{base}$is the moment at the base of the wall, E Young's Modulus, I Moment of Inertia, H is the height of the wall and δ_{max} is the maximum deflection at the tip of the wall which can be estimated as below:

$$\delta_{max} = D_{top} - D_{base} \quad (4.2)$$

Where

D_{top} = displacement recorded at the top of the wall,

D_{base} = displacement recorded at the base of the wall.

Therefore the strain at the base of the cantilever wall can be estimated as:

$$\varepsilon_{base} = (t/2) \times (3\delta_{max}/H^2) \quad (4.3)$$

Where t is the thickness of the wall. Wall inertial moment and strain time series were approximated at all times. A cantilever beam can deflect in an infinite variety of shapes, and for exact analysis, it must be treated as an infinite degree of freedom system possessing an infinite number of natural modes of vibration (Chopra, 2007). In this study, it is assumed that the cantilever retaining walls deflect at all times according to the first vibration mode (also known as the fundamental vibration mode).

A cubic (third order) polynomial is fitted to the strain points at each time step. The polynomial fitting, requires at least two boundary conditions, the strain at the top and base of the cantilever wall should be zero and ε_{base}, respectively, and has the form:

$$\varepsilon(z) = Az^3 \quad (4.4)$$

In which *A* is a curve fitting coefficient which is estimated at each time step to give the best fit (i.e. maximum R-square) and *z* is the depth from the top of the wall.

The strain due to inertial moment time series were estimated at any depth of the wall using equations 4.1, 4.2, 4.3 and 4.4. Then the wall inertial moment time series can be approximated as follows:

$$M(z) = (2EI\varepsilon(z)/th) \quad (4.5)$$

4.1.5. Lateral Earth Pressure

Five sensors at experiment ROOZ01 and seven sensors at experiment ROOZ02 were mounted on each side of the walls to directly measure the seismically induced lateral earth pressures at the locations shown in Figures 3.21. Time series recorded by the earth pressure sensors were filtered using a first order low-pass Butterworth filter with a prototype scale corner frequency of 22 Hz to reduce noise. The problems encountered with the pressure sensors along with an evaluation of their performance were discussed in Section 3.10.2.

Total lateral earth pressure profiles (due to static and dynamic earth pressures) were plotted for each wall by choosing the time at which the maximum moment occurred at the lowest strain gage sensor of each wall. Total lateral earth pressure profiles were also interpreted from the total earth pressure moment profiles recorded by the strain gages and corrected to remove the wall inertial effects as will be discussed in Section 4.5.3.

4.2. Input Ground Motions

Tables 4.1 and 4.2 present the ground motion parameters for the different input shaking events for centrifuge experiments ROOZ01 and ROOZ02, respectively. The tables include the following information:

1) The peak ground acceleration (PGA);
2) The Arias intensity (1970), I_a, which is a measure of the total energy released and defined as
   $$I_a = \frac{2\pi}{g}\int a^2(t)dt; \quad (4.6)$$
3) The significant duration $D_{5\text{-}95\%}$ (Trifunac and Brady 1975), defined as the time required for 90% of total energy to be released, i.e. the interval between 5% and 95% of the arias intensity;
4) T_p (predominant period), the period at which the maximum spectral acceleration occurs in an acceleration response spectrum calculated at 5% damping;
5) T_m,a frequency content characterization parameter estimated as (Rathje et al., 1998) :
   $$T_m = \frac{\Sigma\frac{C_i^2}{f_i}}{C_i^2} \quad (4.6)$$
   where C_i, are the Fourier amplitudes and f_i represent the discrete Fourier transform frequencies between 0.25-20 Hz.

Table 4.1. Input ground motions parameters for the different shaking events during ROOZ01.

Shaking Event	PGA(g)	I_a(m/sec)	T_P (sec)	T_m (sec)	D_{5-95}(sec)
Kobe-TAK090-1	0.69	4.13	0.19	0.52	6.27
Loma Prieta-SC-1	0.41	0.97	0.35	0.62	10.79
Kocaeli-YPT060-1	0.02	0.00	0.63	0.61	16.83
Kocaeli-YPT060-2	0.11	0.06	0.62	0.60	6.39
Kocaeli-YPT060-3	0.21	0.23	0.27	0.56	6.09
Kocaeli-YPT330-1	0.07	0.03	0.23	0.62	6.98
Kocaeli-YPT330-2	0.27	0.30	0.15	0.60	6.69
Loma Prieta-WVC270-1	0.24	0.25	0.24	0.63	4.44
Kocaeli-YPT330-3	0.24	0.28	0.27	0.66	7.75
Kobe-TAK090-2	0.50	2.48	1.14	0.80	7.17
Loma Prieta-WVC270-2	0.21	0.22	0.24	0.66	4.59
Kocaeli-YPT330-3	0.24	0.29	0.26	0.65	7.91

The horizontal acceleration, integrated velocity, integrated displacement and Arias intensity time series along with the acceleration response spectra at 5% damping are presented in Appendix A (Figures A-1 to A-22)for the input ground motions applied during both experiments ROOZ01 and ROOZ02.

Table 4.2. Input ground motions parameters for the different shaking events during ROOZ02.

Shaking Event	PGA(g)	I_a(m/sec)	T_P (sec)	T_m (sec)	D_{5-95}(sec)
Kocaeli-YPT060-1	0.13	0.08	0.27	0.60	6.34
Kocaeli- YPT 060-2	0.14	0.10	0.27	0.58	6.45
Kocaeli- YPT 060 -3	0.23	0.27	0.27	0.55	6.27
Kocaeli- YPT 330-1	0.26	0.36	0.23	0.57	6.73
Loma Prieta-SC-1	0.39	1.09	0.35	0.59	10.97
Kobe-TAK090-1	0.65	4.38	0.19	0.53	6.27
Loma Prieta-SC-2	0.39	1.06	0.30	0.59	10.98
Loma Prieta-WVC270-1	0.19	0.22	0.24	0.64	4.91
Kocaeli- YPT 330-2	0.24	0.34	0.23	0.58	6.97
Kobe-TAK090-2	0.64	4.35	0.19	0.54	6.27

4.3. Soil Settlement and Densification

Vertical soil deformations were recorded at the soil surface and at the foundation level of each structure by linear potentiometers and LPs at the locations shown in Figures 3.3 – 3.4 and Figures 3.5 – 3.6 for ROOZ01 and ROOZ02, respectively.

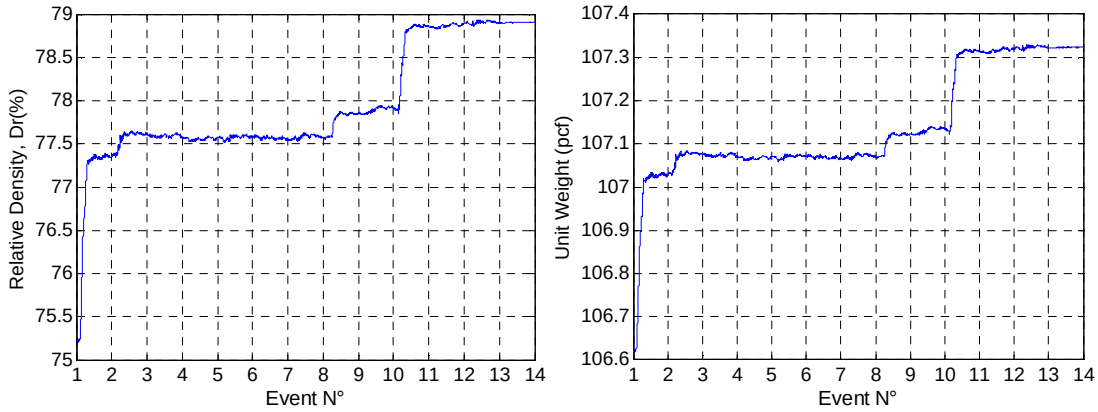

Figure 4.1. Soil settlement and relative density after different shaking events for ROOZ01.

The static offsets measured by the displacement transducers were used to determine the settlement increment of the uniform density soil model after the different shaking events in both experiments. Figures 4.1 and 4.2 show the settlement value along with the relative density (D_r) of the soil after each shaking event for ROOZ01 and ROOZ02, respectively. It is apparent that the maximum settlement occurred during the first Kobe event in both sets of experiments, due to the large magnitude of shaking and the relatively low initial density of the sand.

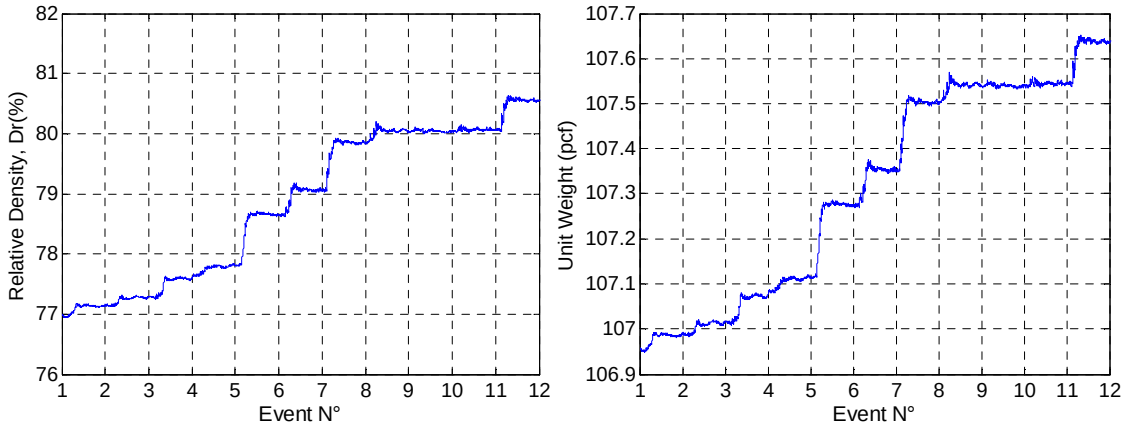

Figure 4.2. Soil settlement and relative density after different shaking events for ROOZ02.

4.4. Seismic Behavior of Retaining Wall-Backfill System

In this section, the seismic behavior of the backfill and retaining walls observed in the centrifuge experiments is presented through an evaluation of the acceleration and inertial responses of the backfill and the retaining walls.

4.4.1. Acceleration Response

Figures 4.3 and 4.4 show the acceleration response spectra (5% damped) at different elevations in the model for Kobe-TAK090-2 event in the experiments ROOZ01 and ROOZ02. This data shows amplification of the base motion between the base and the top of the soil column, especially in the period range around 1.2 s.

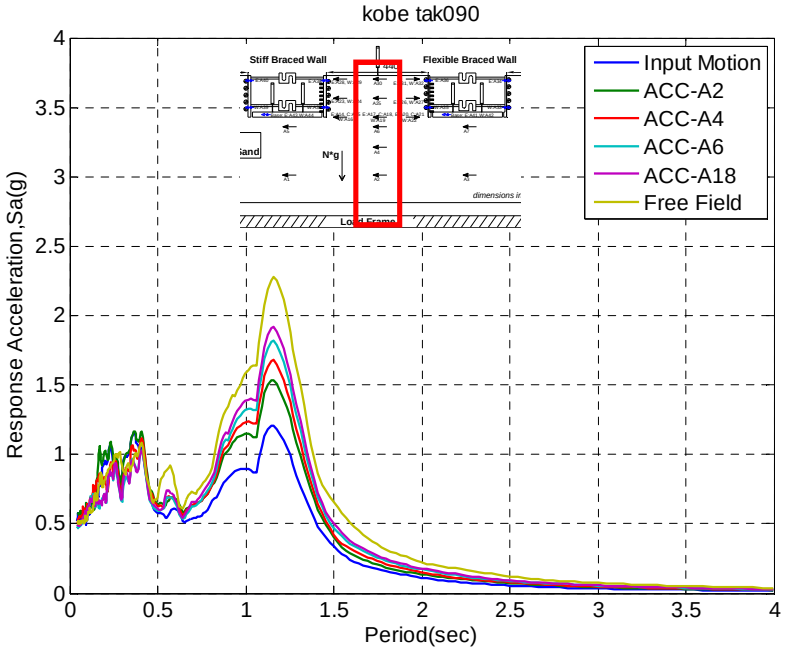

Figure 4.3. (a) Spectral accelerations at different elevations in ROOZ01 for Kobe-TAK090-2 event (5% damped).

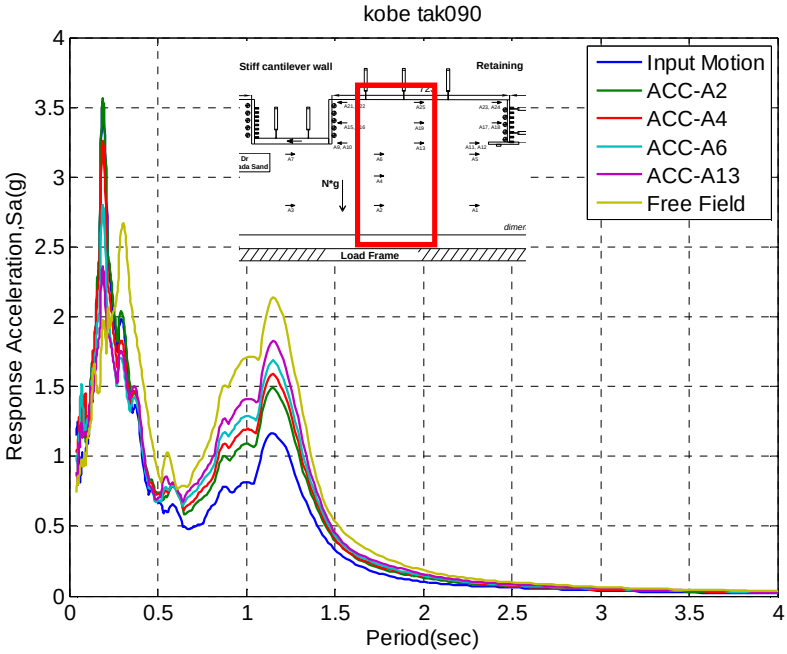

Figure 4.4. (a) Spectral accelerations at different elevations in ROOZ02 for Kobe-TAK090-2 event (5% damped).

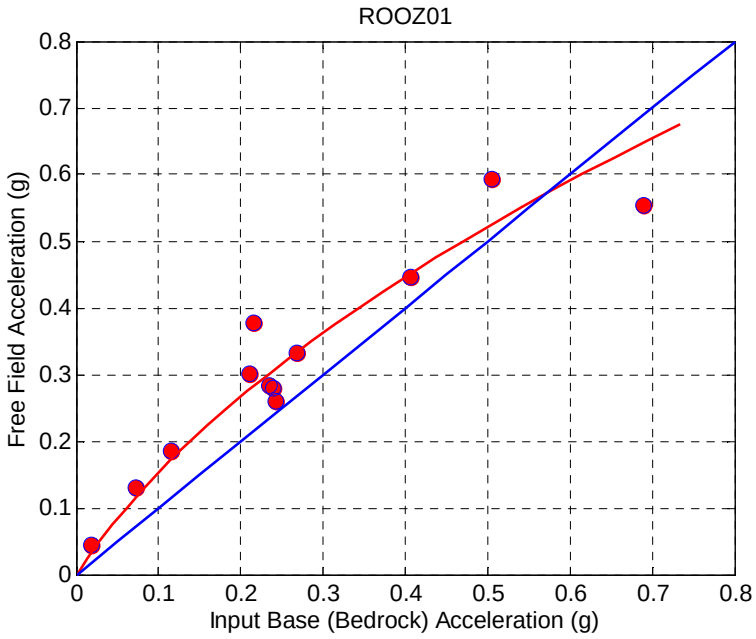

Figure 4.5. Base motion amplification/de-amplification for ROOZ01 experiment.

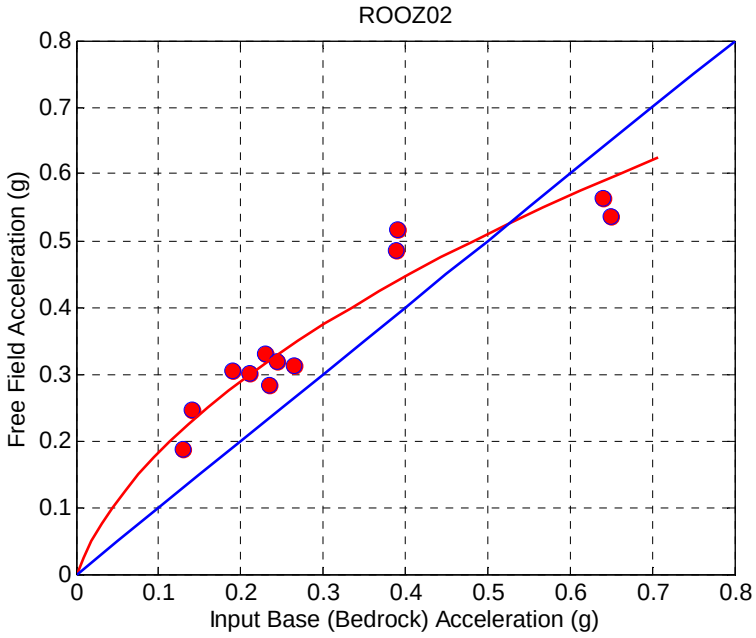

Figure 4.6. Base motion amplification/de-amplification for ROOZ02 experiment.

Figure 4.5 and 4.6 show the peak accelerations measured at the foundation versus those measured at the top of the soil (free field). As can be seen, the ground motions are consistently amplified at the top of the soil up to about 0.5 g and attenuated at accelerations in excess of 0.6g.

4.4.2. Wall and Backfill Response

Figures 4.7 through 4.12 present the acceleration response spectra (5% damped) during Loma Prieta-SC-2 and Kobe-TAK090-2 shaking events for experiment ROOZ01 and ROOZ02. As shown in Figures 4.7 and 4.8, the amplification of soil and non-displacing basement wall is almost similar from bottom to top. The model responded mostly at period around 0.4s when shaken with the Loma Perienta-SC-2 event, and at periods around 0.4s and 1.2s when shaken with Kobe-TAK090-2 event, reflecting the respective input motion characteristics.

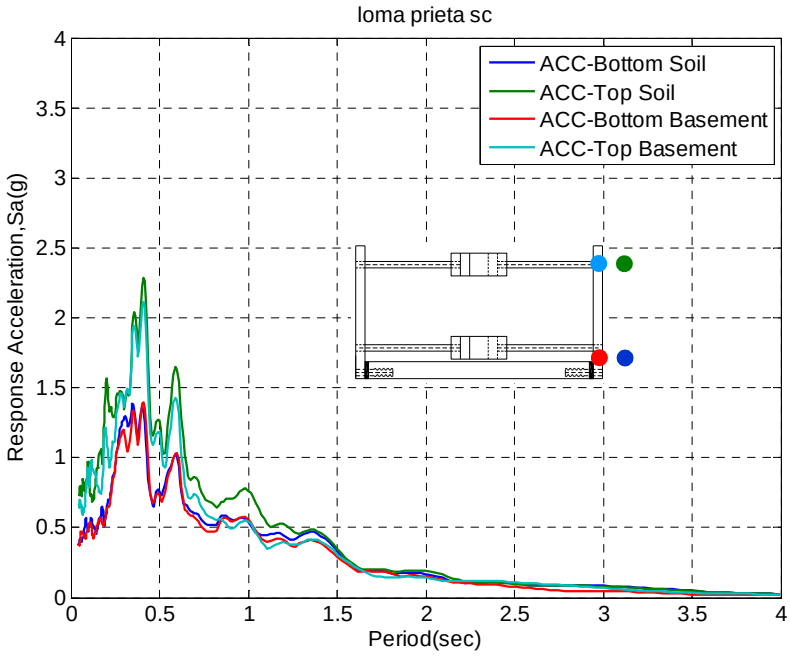

Figure 4.7. Spectral accelerations of top and bottom of the soil and the basement structure for Loma Prieta-SC-2 event (5% damped).

In the Loma Perienta-SC-2 event with the cross-braced, basement wall the amplification between soil and wall is quite similar, as shown in Figure 4.7. In contrast, the Kobe-TAK090-2 event produces slightly higher amplification in the structure with respect to the soil, as shown in Figure 4.8.

Figures 4.9 and 4.10 show that the amplification of ground motions from the base to the top of the non-displacing cantilever wall is greater than that within the soil column. In comparison the amplification of motions from the base to the top of a displacing retaining wall is essentially the same as the amplification in the soil column, as shown in Figures 4.11 and 4.12.

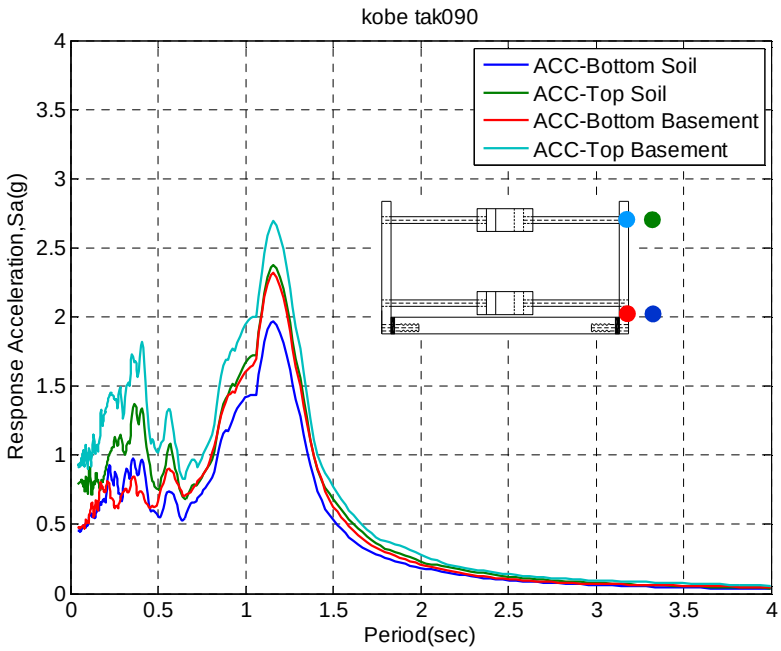

Figure 4.8. Spectral accelerations of top and bottom of the soil and the basement structure for Kobe-TAK090-2 event (5% damped).

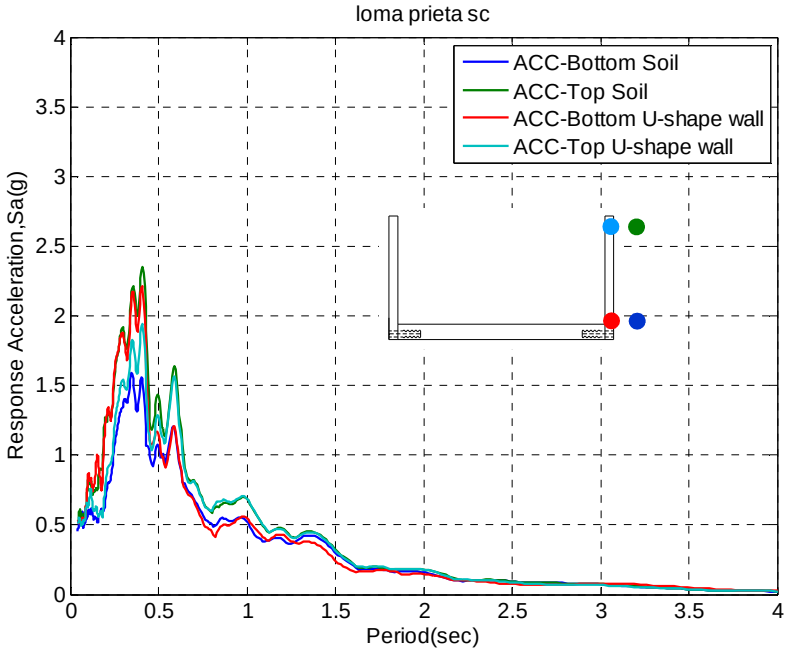

Figure 4.9. Spectral accelerations of top and bottom of the soil and the non-displacing cantilever wall for Loma Prieta-SC-2 event (5% damped).

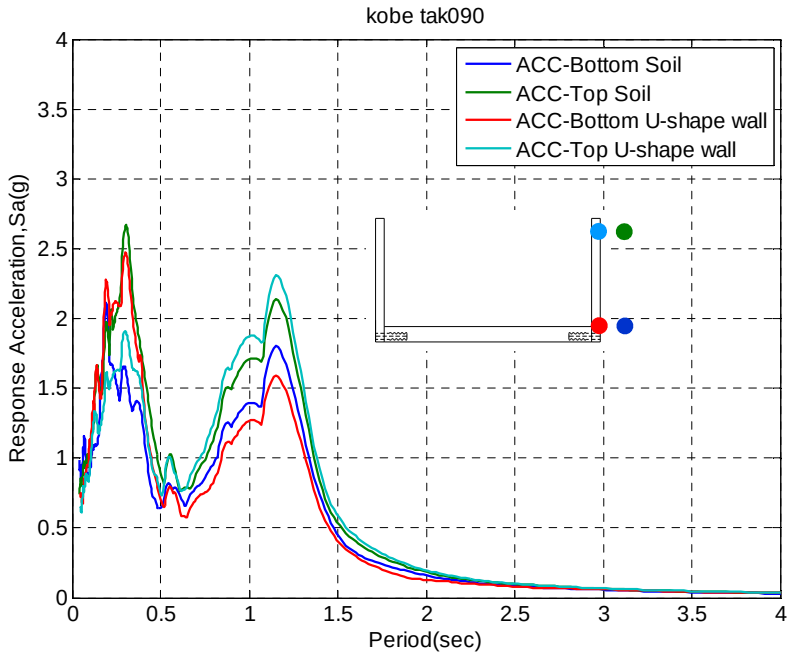

Figure 4.10. Spectral accelerations of top and bottom of the soil and the non-displacing cantilever wall for Kobe-TAK090-2 event (5% damped).

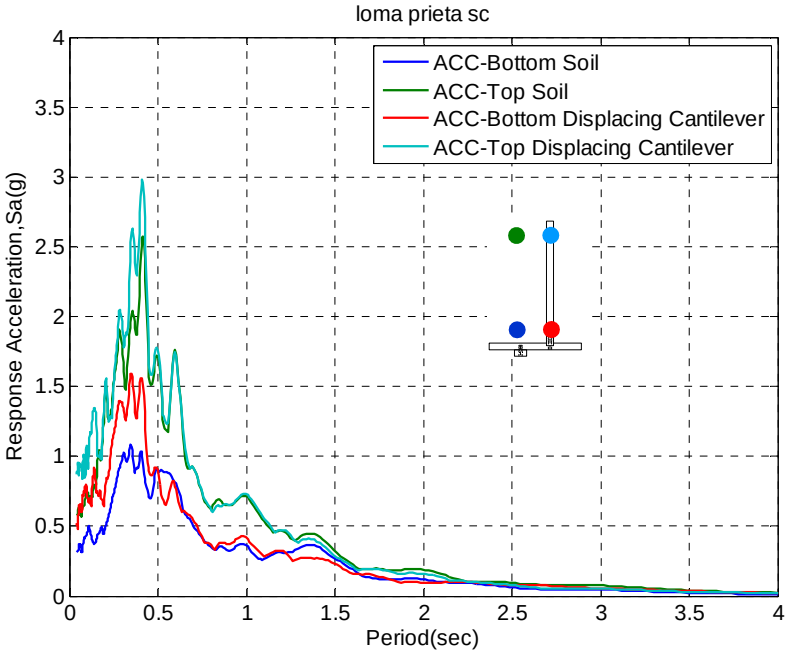

Figure 4.11. Spectral accelerations of top and bottom of the soil and displacing retaining wall for Loma Prieta-SC-2 event (5% damped).

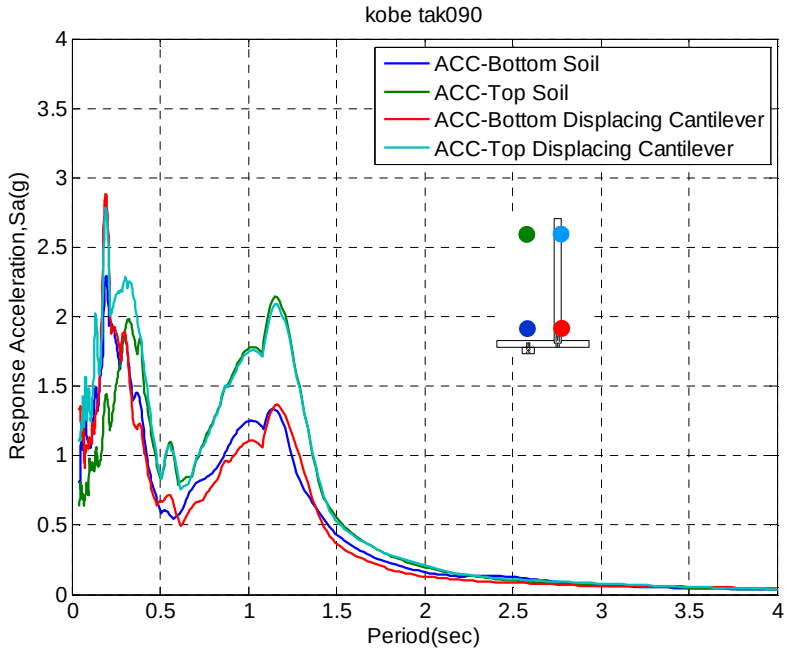

Figure 4.12. Spectral accelerations of top and bottom of the soil and displacing retaining wall for Kobe-TAK090-2 event (5% damped).

As seen in Figures 4.7 through 4.12 the presence of the retaining structure imposes a boundary that alters the response of the backfill. Furthermore, it has been shown that the amplification of the structure alone can be higher than that of soil. In general, the results of this investigation provide a clear indication of the direct dynamic interaction between the wall, the retained soil, and the retained structures. That fact justifies the necessity for a more elaborate consideration of this aspect of soil-structure interaction during the seismic design.

4.5. Bending Moments

4.5.1. Static Moments

Figures 4.13 - 4.14 present the static at-rest and static active moment profiles measured by the strain gages on the non-displacing cantilever and displacing retaining walls before and after Loma Prieta-SC-2 and Kobe-TAK090-2 shaking events in both experiments. The calculated moment profile is based on an assumed triangular lateral earth pressure profile. The theoretical static active moment was estimated using a backfill initial friction angle of 36° using the Coulomb (1776) theory and the static at-rest moment was estimated using K_0=0.5 . As is shown in Figures 4.13 - 4.14, the static moment on the non-displacing cantilever wall before and after earthquake is slightly higher than static moment due to at-rest earth pressure. Most importantly, the initial moments measured on displacing cantilever walls were in good agreement with theoretical moments due to active earth pressure.

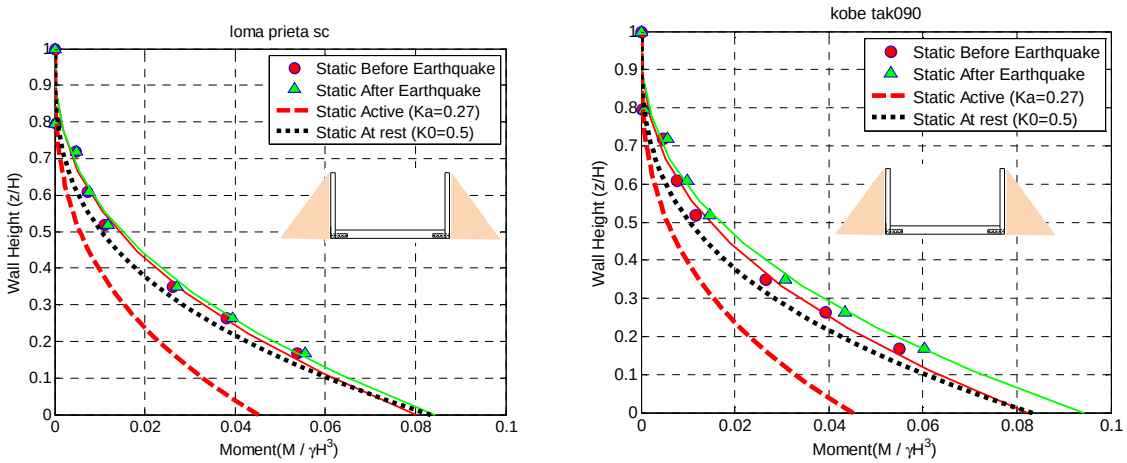

Figure 4.13. Normalized static moment profiles measured by the strain gages and estimated using static at-rest and static active pressure distributions of non-displacing cantilever wall before and after Loma Prieta-SC-2, and Kobe-TAK090-2 for ROOZ02.

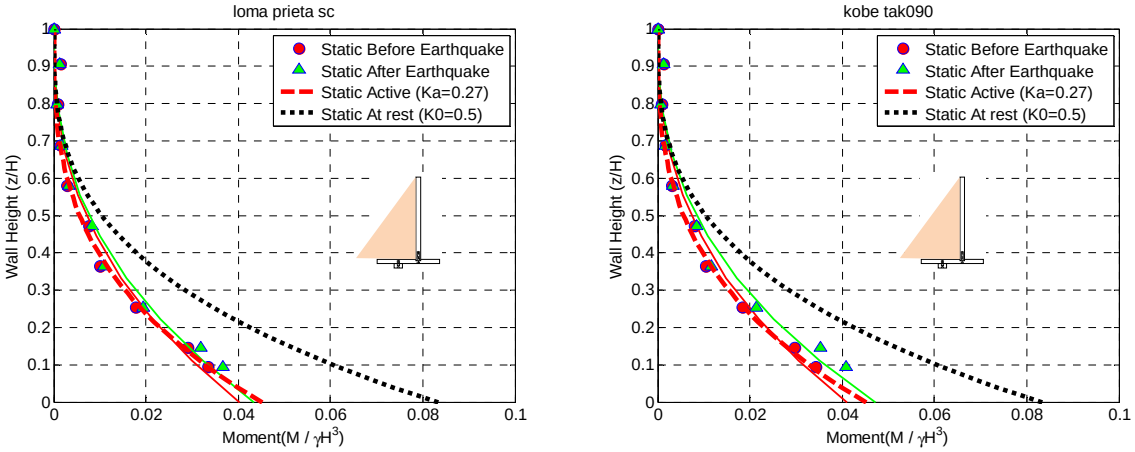

Figure 4.14. Normalized static moment profiles measured by the strain gages and estimated using static at-rest and static active pressure distributions of displacing retaining wall before and after Loma Prieta-SC-2, and Kobe-TAK090-2 for ROOZ02.

4.5.2. Total Dynamic Wall Moments

Figures 4.15 - 4.16 present the maximum total wall moment profiles interpreted from the strain gage measurements on the non-displacing cantilever and displacing retaining walls for Loma Prieta-SC-2, Loma Prieta-WVC270-2, Kocaeli-YPT330-2 and Kobe-TAK090-2 shaking events in centrifuge experiment ROOZ02. Static active and static at rest moment estimates at the base of the walls are also included in the figures for reference. Recall that total wall moments are produced by static earth pressures, dynamic earth pressure increments and wall inertial moments. Cubic polynomial curves generally provide the best least squares fits for the moment data in Figures 4.15 - 4.16 with R-square generally greater than 0.98.

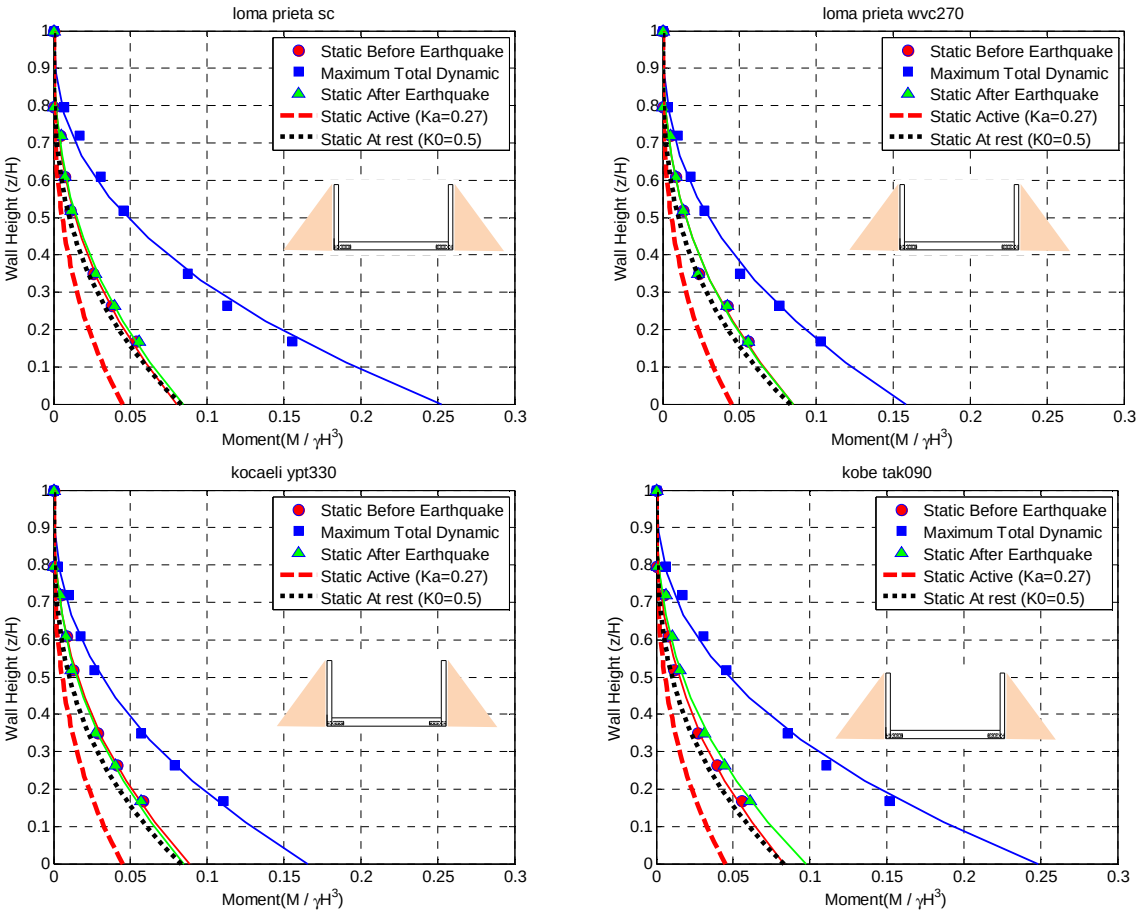

Figure 4.15. Maximum total wall moment profiles measured by strain gages and static active and at rest moment estimates on the non-displacing cantilever wall for Loma Prieta-SC-2, Loma Prieta-WVC270-2, Kocaeli-YPT330-2 and Kobe-TAK090-2 for ROOZ02.

The maximum total wall moments in experiment ROOZ02, occurs during the Kobe motions due to the large intensity of shaking. Moment profiles measured on the non-displacing cantilever walls are generally larger than those recorded on the displacing retaining walls. Moment profiles on both walls are well represented by cubic polynomial fits.

Additional plots of the maximum dynamic wall moment distributions interpreted from the strain gage measurements for both the non-displacing cantilever and the displacing retaining walls are presented in Appendix A (Figures A-23 to A-42) for the different shaking events in experiment ROOZ02.

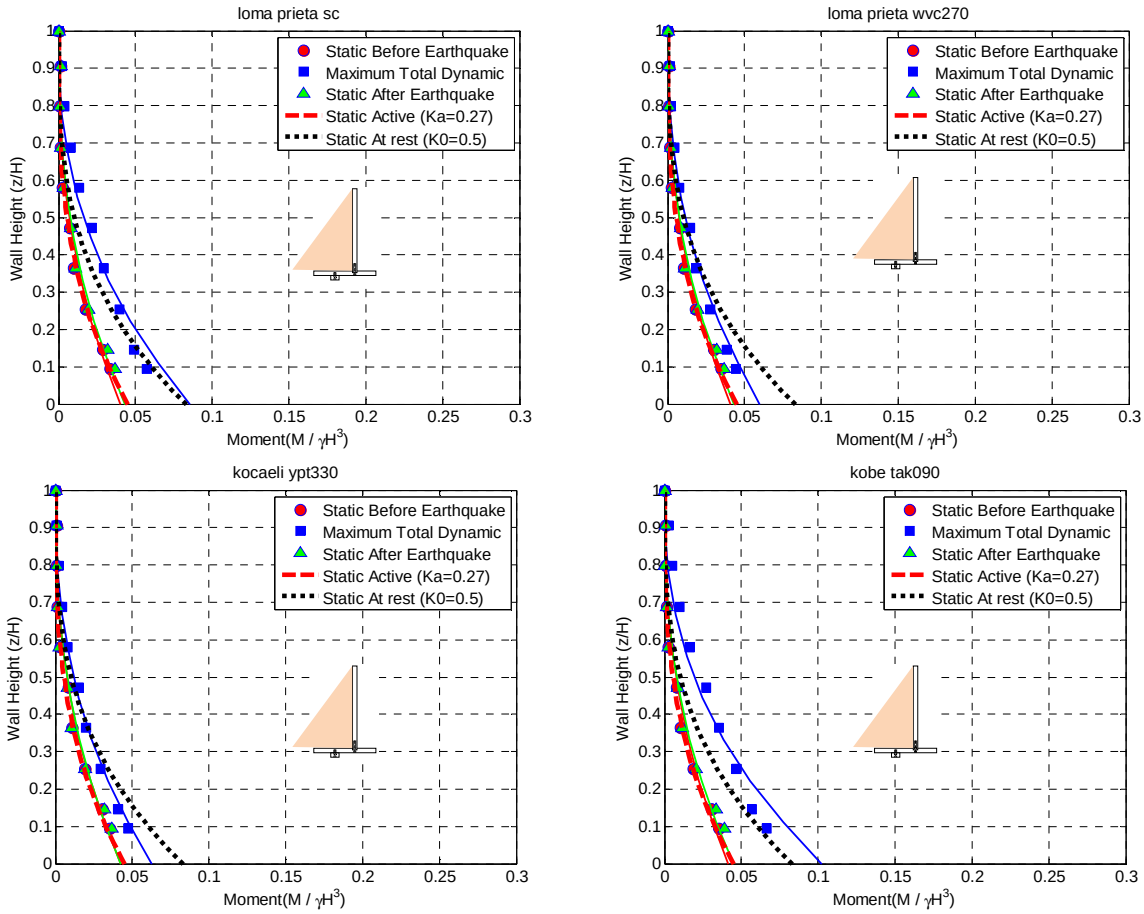

Figure 4.16. Maximum total wall moment profiles measured by strain gages and static active and at rest moment estimates on the displacing retaining wall for Loma Prieta-SC-2, Loma Prieta-WVC270-2, Kocaeli-YPT330-2 and Kobe-TAK090-2 for ROOZ02**.**

4.5.3. Wall Inertial Moments

In the pseudostatic method of analysis, the effect of earthquake loading is modeled by an additional set of static forces representing the inertial forces acting on the retaining wall backfill system. As mentioned in Chapter 2 (Literature Review), inertial forces acting on retaining structures are generally ignored in most seismic earth pressures theories, especially for cantilever retaining walls. Moreover, the literature review revealed several studies whereby the total dynamic moments or forces acting on the cantilever retaining walls were reported as being induced by dynamic earth pressures without any attempt to evaluate the contribution of the wall inertial effects to the total wall forces and moments. It is important to note that the M-O and the Seed and Whitman (1970) methods do not account for wall inertial effects in their dynamic earth pressure estimates. Richards and Elms (1979) observed that wall inertia for gravity retaining walls can be of the same order as that of the dynamic soil pressure computed by the M-O method and should be properly accounted for.

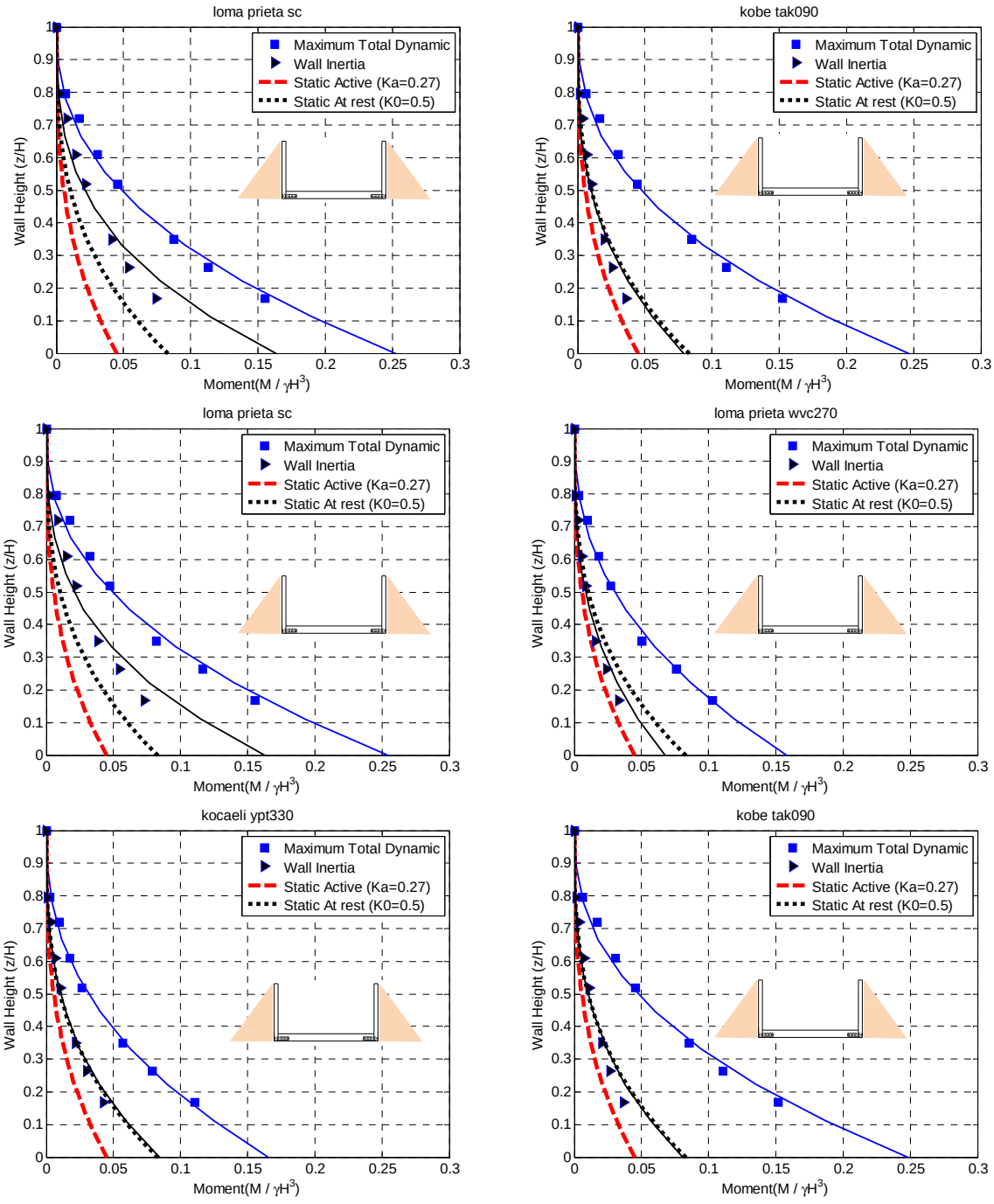

Figure 4.17. Maximum total and inertial wall moment profiles measured by strain gages and accelerometers on the non-displacing cantilever wall for Loma Prieta-SC-1, Kobe-TAK090-1, Loma Prieta-SC-2, Loma Prieta-WVC270-2, Kocaeli-YPT330-2 and Kobe-TAK090-2 for ROOZ02.

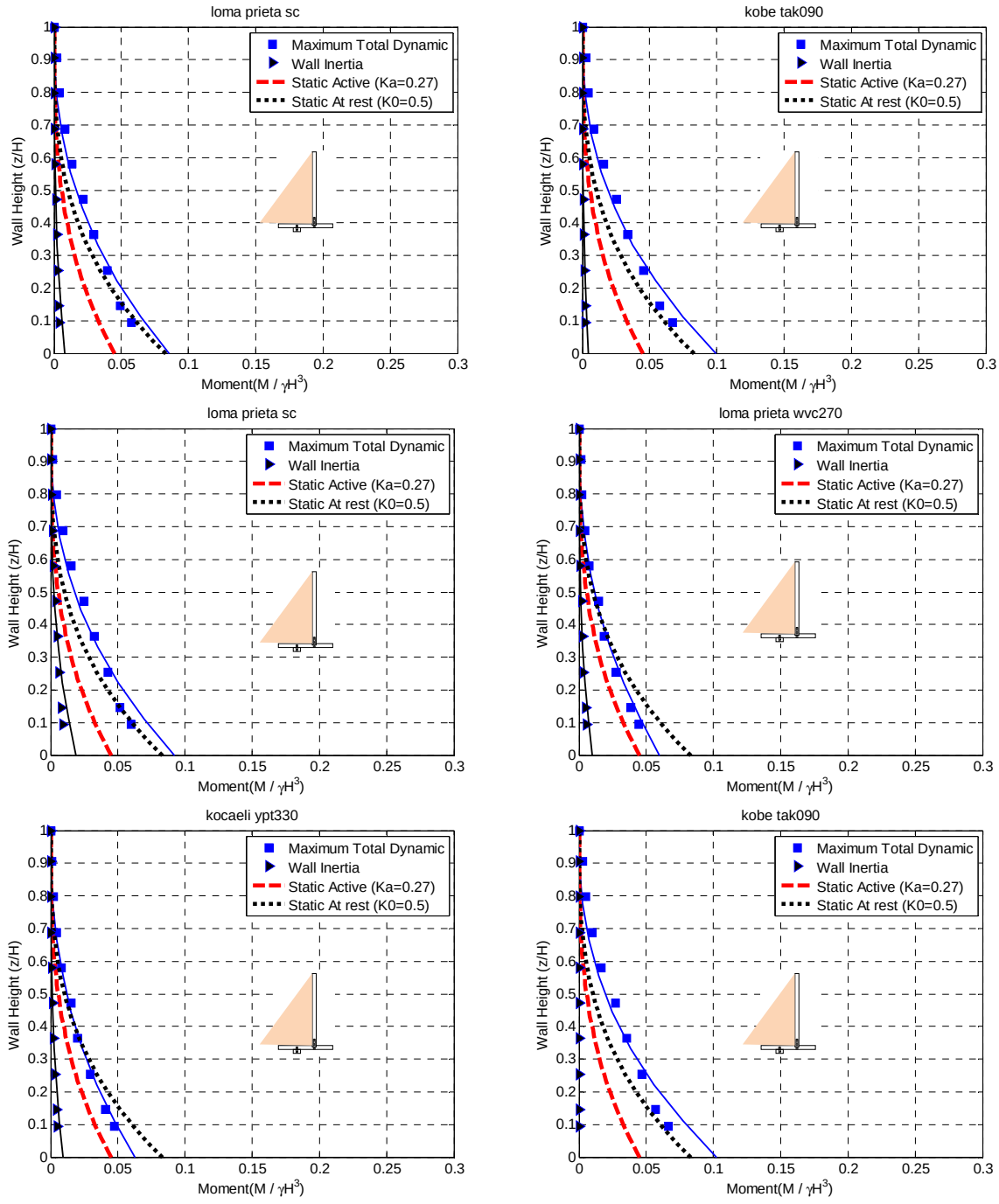

Figure 4.18. Maximum total and inertial wall moment profiles measured by strain gages and accelerometers on the displacing retaining wall for Loma Prieta-SC-1, Kobe-TAK090-1 , Loma Prieta-SC-2, Loma Prieta-WVC270-2, Kocaeli-YPT330-2 and Kobe-TAK090-2 for ROOZ02.

In an attempt to provide a better understanding of the seismic behavior of cantilever retaining walls and an accurate estimate of seismically induced lateral earth pressures, wall inertial effects were evaluated in this study. Their contribution to the dynamic response of the wall was investigated based on data recorded in the dynamic centrifuge experiments. Wall

moments due to wall inertia at different locations on the non-displacing cantilever and displacing retaining walls were estimated for ROOZ02 according to the method outlined in Section 4.1.4. Wall inertia moments were compared to dynamic wall moments interpreted from the strain gage data and include the combined effects of both dynamic earth pressures and wall inertia. Figures 4.17 and 4.18 present the wall inertia moment contributions to the dynamic wall moment profiles interpreted at non-displacing cantilever and displacing retaining walls for the for Loma Prieta-SC-1, Kobe-TAK090-1, Loma Prieta-SC-2, Loma Prieta-WVC270-2, Kocaeli-YPT330-2 and Kobe-TAK090-2 shaking events in ROOZ02. The wall inertia moment contribution to the dynamic wall moment interpreted from the strain gage measurements for both non-displacing cantilever and displacing retaining walls are presented in Appendix A (Figures A-23 to A-42).

Figure 4.17 shows that, the moment of wall due to inertia for non-displacing cantilever wall (U-Shaped wall) from Loma Prieta-SC-1 with PGA 0.39 and T_p=0.35 (predominant period) is almost twice as large as that produced by the Kobe-TAK090 with GPA 0.65 and T_p=0.19, as shown in Table 4.2. Although overall no direct correlation between predominant period of the shaking event and dynamic moment due to wall inertia has been observed in the experiments performed in this study, this potential relationship deserves closer attention in future studies.

Overall, the contribution of wall inertia to the dynamic wall moments is noticeable in non-displacing cantilever wall, but slightly smaller in displacing retaining wall perhaps due to lateral rigid motion displacement of the wall. Wall inertia is therefore important and should be accounted for appropriately in the seismic design of retaining structures.

4.6. Lateral Force Measurements

The total lateral force behind the basement wall are presented as time histories in Figure 4.19a and 4.19b on both stiff and flexible non-displacing basement walls for Loma Prieta-SC-1 and Kobe-TAK090-2 for ROOZ01. As explained in Chapter 3, the load cell (LC) force values represent the lateral earth pressure resultant plus the test wall inertia during shaking, and the static lateral earth pressure resultant before and after the excitation (when the inertia of the wall is zero).

In this case the inertial force due to differential acceleration of the two parallel walls is very small with respect to lateral force and would be negligible. As shown in Figure 4.19, the three load cells on the top of the basements show significantly smaller load as opposed to the rest of the load cells placed on the bottom of the models which is evidence that dynamic earth pressure increases with depth. Additionally the final static load increases slightly during strong excitation, such as produced by the Kobe-TAK090 motion. This observation indicates that the backfill densification occurs throughout strong shaking events, which is consistent with soil settlement and densification sequence presented in Section 4.3.

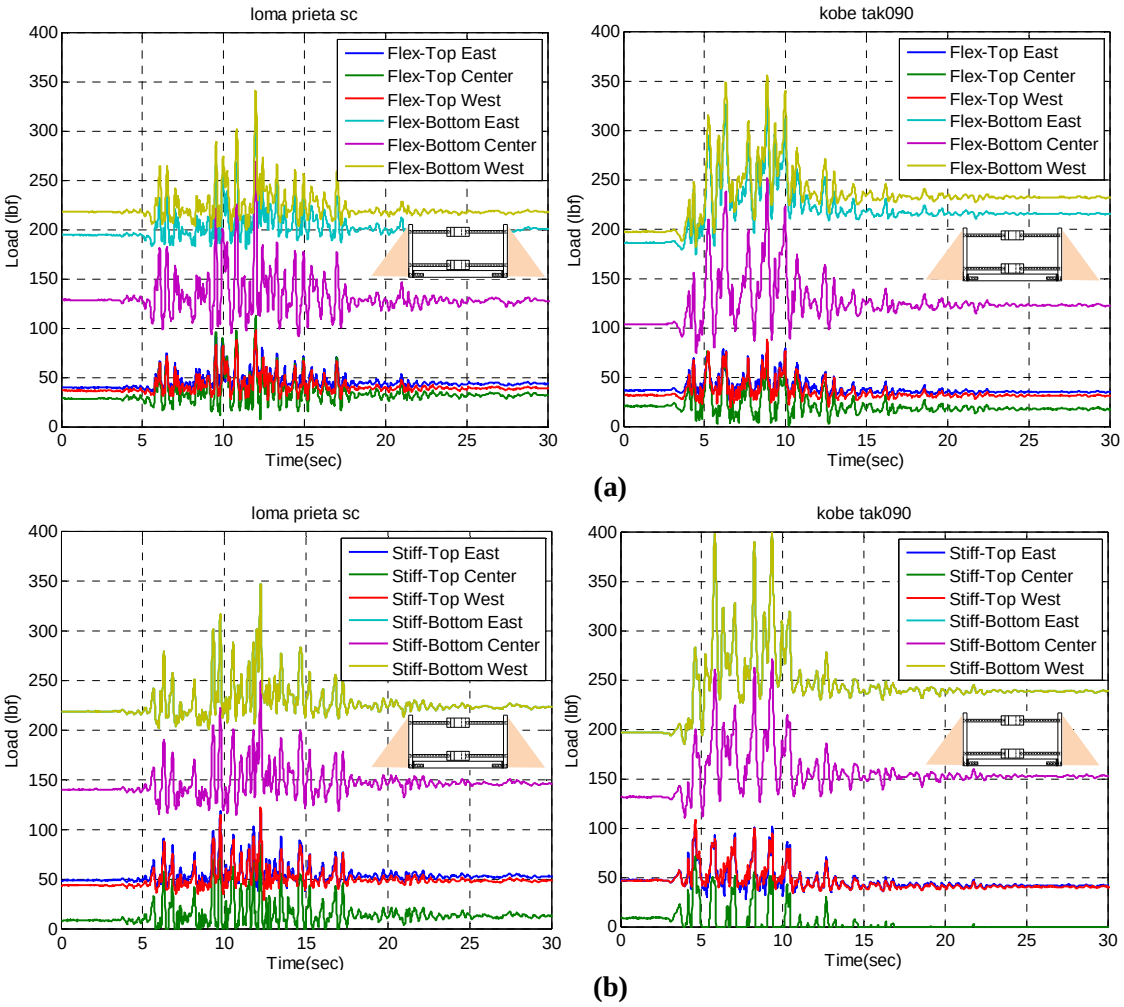

Figure 4.19. Total lateral force time series estimated by load cells on both stiff and flexible non-displacing basement walls for Loma Prieta-SC-1 and Kobe-TAK090-2 for ROOZ01 (a) flexible basement wall (b) stiff basement wall.

4.7. Static and Dynamic Earth Pressures

4.7.1. Static Earth Pressure

Figures 4.20 through 4.22 present static lateral earth pressure profiles directly measured by the earth pressure sensors normalized by γH^2 versus normalized height after the Loma Prieta-SC-2 and Kobe-TAK090-2-2 shaking events, as well as theoretical at-rest and active earth pressure. The static earth pressure was estimated using a backfill initial friction angle of 36° in both experiments using Coulomb theory (1776) and the static at-rest earth pressure was estimated using K_0=0.5. In case of non-displacing basement wall, static earth pressure measured by pressure sensors are slightly higher than at-rest earth pressure. Earth pressure behind the non-displacing cantilever walls falls between at-rest and active earth pressure as shown in Figure 4.20, but in the case of displacing retaining walls the earth pressure measured by pressure sensors shows a really good agreement with active earth pressure as shown in Figure 4.22.

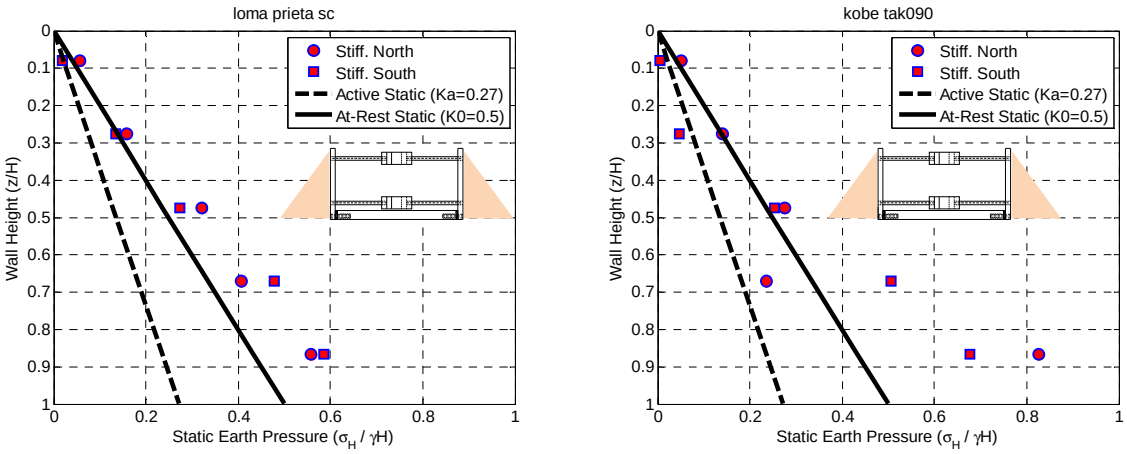

Figure 4.20. Static earth pressure profiles measured by pressure cells on outside and inside of the basement wall for Loma Prieta-SC-2 and Kobe-TAK090-2 for ROOZ01.

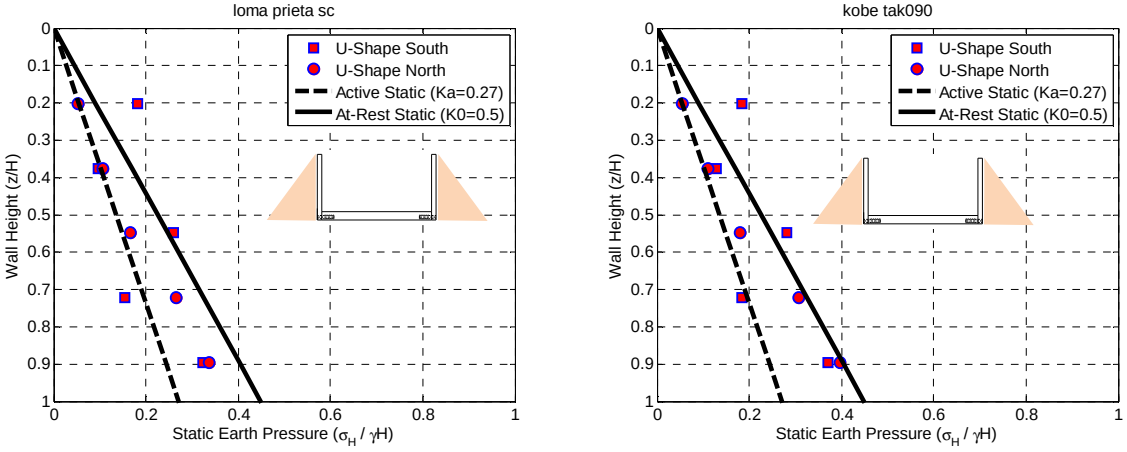

Figure 4.21. Static earth pressure profiles measured by pressure cells on outside and inside of the non-displacing cantilever wall for Loma Prieta-SC-2 and Kobe-TAK090-2 for ROOZ02.

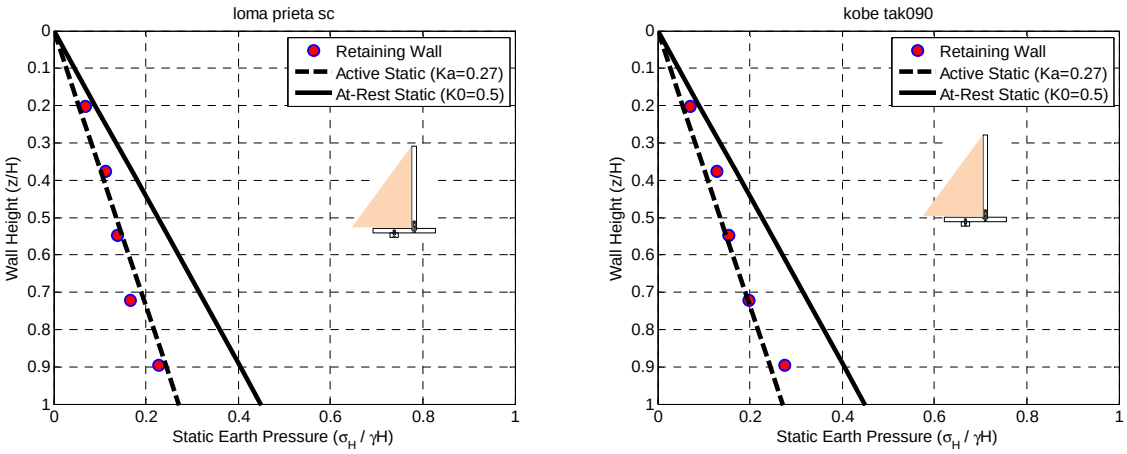

Figure 4.22. Static earth pressure profiles measured by pressure cells on outside and inside of the displacing retaining wall for Loma Prieta-SC-2 and Kobe-TAK090-2 for ROOZ02.

4.7.2. Dynamic Earth Pressure

The dynamic lateral earth pressures measured directly by earth pressure cells during shaking are shown in Figure 4.23 for the Loma Prieta-SC-1 and Kobe-TAK090-2 events on both non-displacing cantilever and displacing retaining walls. These data clearly show an earth pressure increasing with depth.

Direct measurement of lateral earth pressures using miniature pressure transducers was originally intended. However, due to the performance characteristics of the these sensors discussed in Section 3.10.2, in this study their use is restricted to identifying behavioral trends and supporting measurements made by strain gages and load cells, as discussed in the following Section.

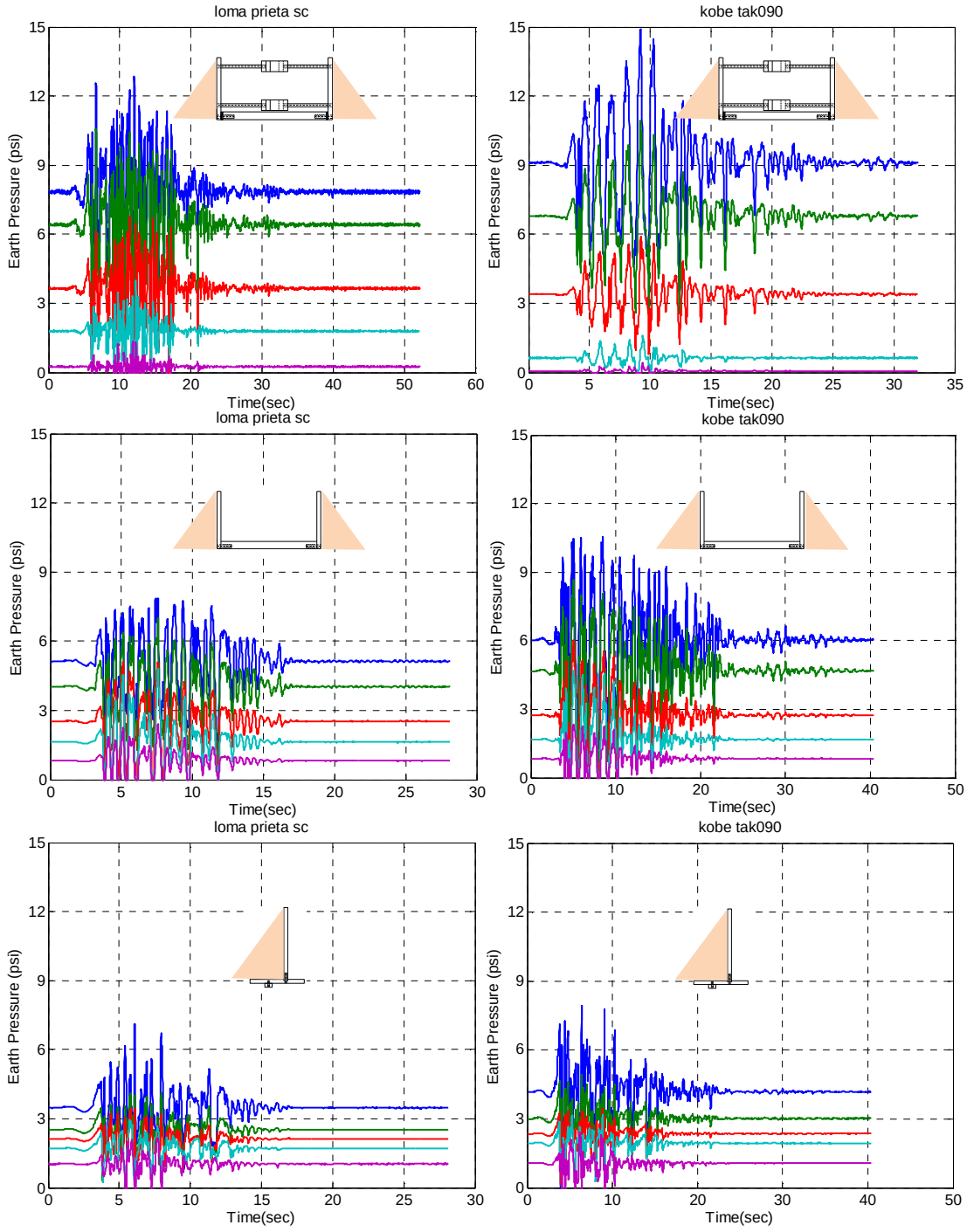

Figure 4.23. Total earth pressure time series estimated by pressure sensors on all walls for Loma Prieta-SC-1 and Kobe-TAK090-2.

4.7.3. Interpreted Dynamic Earth Pressure

For ROOZ01, the area underneath the dynamic pressure distribution given by earth pressure transducers was corrected based on overall load estimated by load cells and the corresponding linear pressure profiles were back calculated (Figure 4.24).

In order to determine the dynamic earth pressure profiles from the strain gage measurements, the strain gage data at maximum moment were fitted with cubic polynomials, as described in Section 3.10.2. Maximum total moments at the base of the walls were extrapolated using the cubic polynomial fit and the corresponding linear pressure profiles that generated these moments were back calculated. The maximum total pressure profiles interpreted from the strain gage data were corrected to remove wall inertial effects for the shaking events in experiment ROOZ02 and, therefore, represent dynamic earth pressure profiles (Figure 4.24).

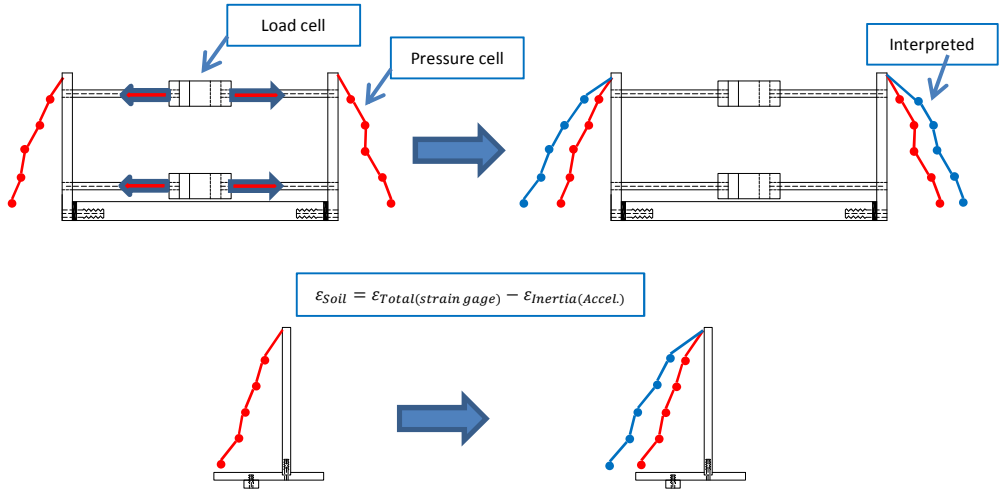

Figure 4.24. Procedure used to interpret the earth pressure measured by pressure transducer.

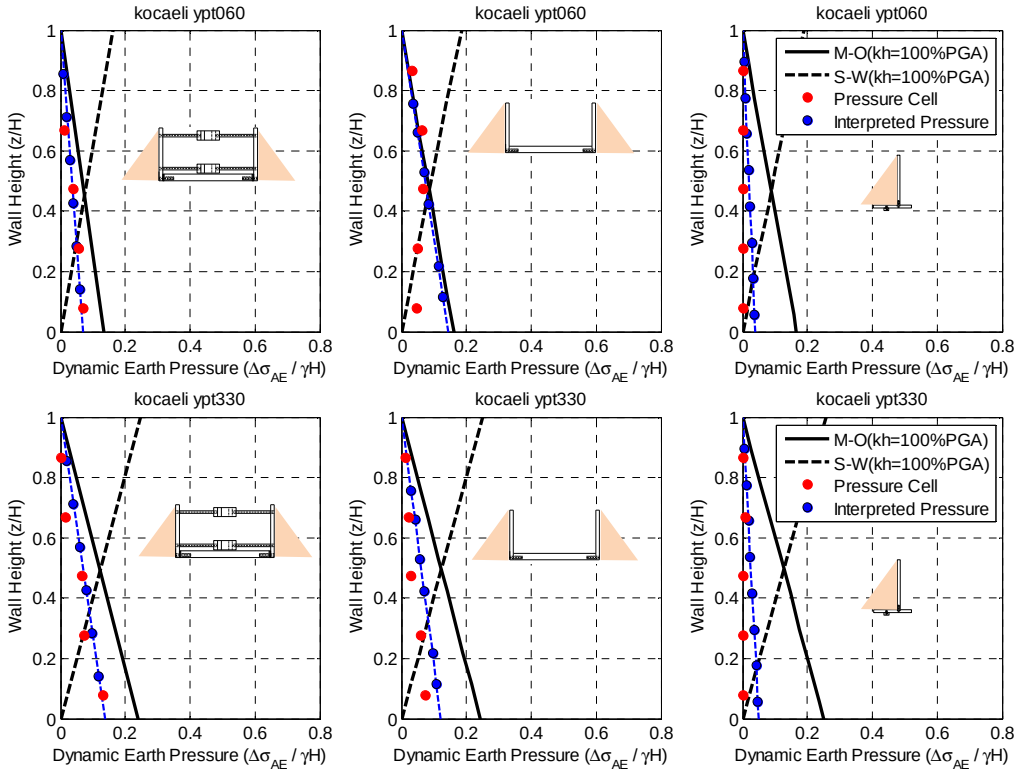

Figure 4.25. Dynamic earth pressure distributions directly measured and interpreted from the pressure sensors and strain gage and load cell data and estimated M-O as well as S-W on walls for Kocaeli-YPT060-3 (PGA_{ff}=0.25), Kocaeli-YPT330-2 (PGA_{ff}=0.34).

Figures 4.25 and 4.26 present the dynamic earth pressure distributions recorded by the earth pressure sensors and interpreted from the load cells as well as strain gage measurements on the non-displacing cantilever wall, non-displacing braced wall as well as the displacing cantilever during the different shaking events for experiments ROOZ01 and ROOZ02. The theoretical pressure distributions using the Mononobe-Okabe (M-O) and Seed and Whitman (S-W) methods are all computed assuming k_h = 100%PGA.

It is important to note, that all of the data represent the earth pressures and earth pressure distributions at the point of maximum dynamic moment, which does not necessarily correspond to the maximum observed earth pressure, as already noted by Al-Atik and Sitar (2010). As shown in the Figures, overall, the earth pressure sensors measured lower pressures than interpreted from the strain gage and load cell measurements. The corresponding dynamic earth pressure time series interpreted from the strain gage measurements and load cells for both non-displacing cantilever and displacing retaining walls are presented in Appendix A (Figures A-43 to A-64).

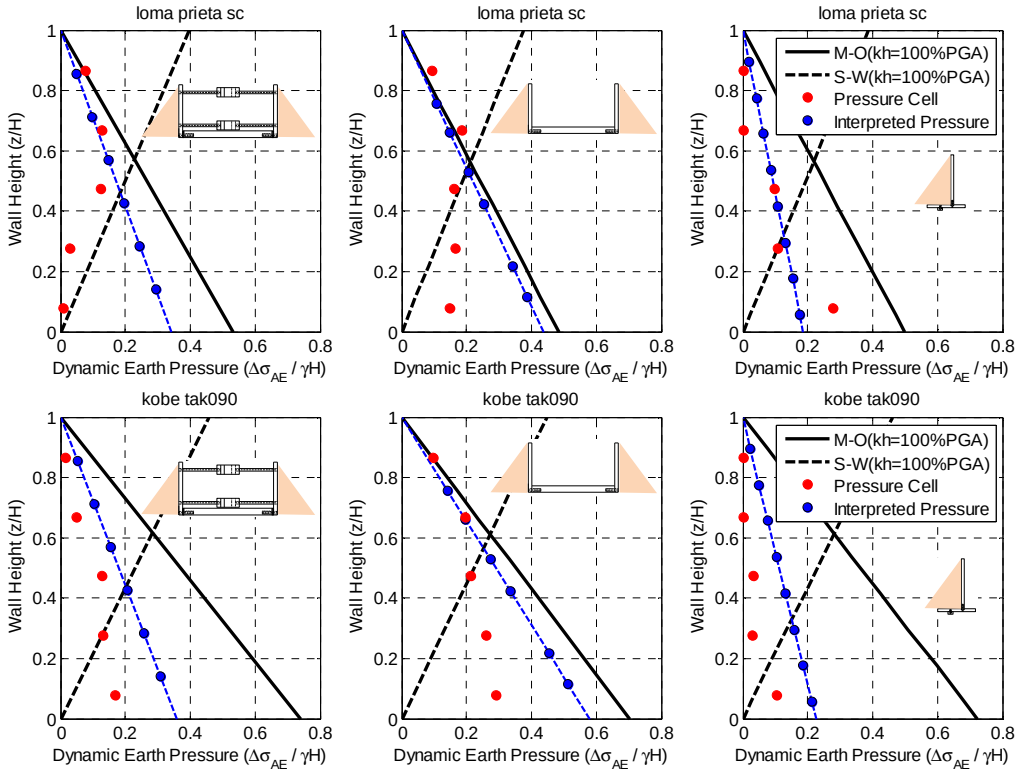

Figure 4.26. Dynamic earth pressure distributions directly measured and interpreted from the pressure sensors and strain gage and load cell data and estimated M-O as well as S-W on walls for Loma Prieta-SC-1 (PGA_{ff}=0.51), Kobe-TAK090-2 (PGA_{ff}=0.61).

4.8. Retaining Wall Rigid Body Motion

Horizontal displacement transducers located at the top of the stiff and flexible walls in both centrifuge experiments were used to measure rigid body motion of the displacing retaining wall during shaking as well as static offsets. The instrument rack to which displacement transducers were attached experienced vibration during spinning and shaking. This vibration resulted in large apparent deflections and its effect is obvious in the recorded displacement time series. As a result, dynamic displacement data recorded by the linear potentiometers and the LVDTs were considered inaccurate and were not used in this study. Data recorded by the displacement transducers were only used to determine static offsets. Figure 4.27 shows the horizontal translation of the displacing retaining wall during shaking events in experiment ROOZ02 in which the x-axis shows the events number and y-axis shows the horizontal translation in model scale. As can be seen, the retaining wall has stopped translating after sixth event (i.e. Loma Prieta-SC-1) due to densification of the sand.

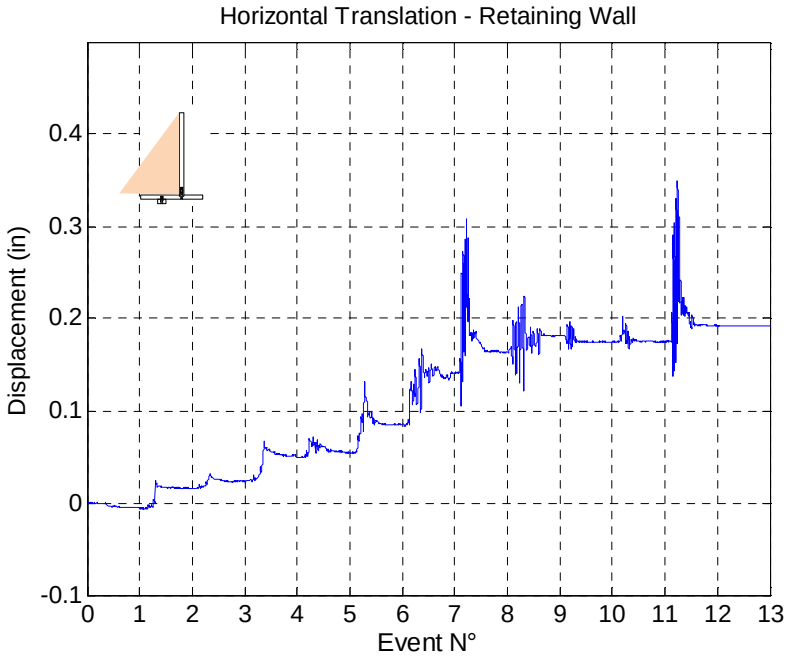

Figure 4.27. Horizontal translation of the displacing retaining wall during shaking evens.

Figure 4.28 shows the rigid body rotation of the displacing retaining wall during shaking events in experiment ROOZ02. The negative rotation means rotation away from the soil backfill. Similar to horizontal translation (Figure 4.27) the retaining wall stopped rotating after sixth event.

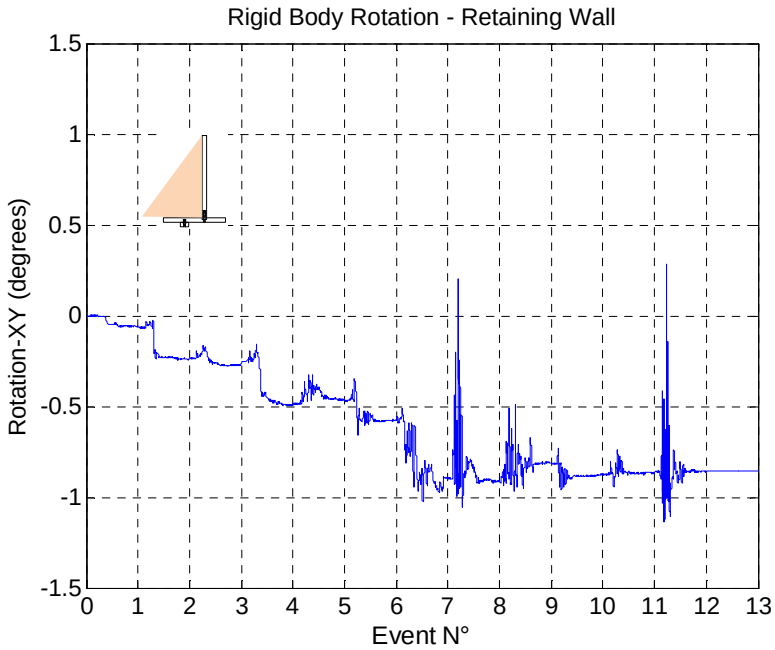

Figure 4.28. Rigid body rotation of the displacing retaining wall during shaking evens.

4.9. Summary

Several comments and observations may be made regarding the information contained in the dynamic profiles. For the horizontal acceleration ratio profiles, the trend of amplification vertically upward through the wall and backfill soil is clearly evident in all the experiments and is a function of the input acceleration. Typically, the magnitude of amplification is approximately similar in the wall and soil.

Direct measurement of lateral earth pressure using pressure transducers was originally intended. However, the erratic behavior of these devices under dynamic loading limited their usefulness. In this study, their use is restricted to identifying behavioral trends and supporting measurements made by, other more reliable, gages such as load cells and strain gages.

As was the case under static loading conditions, the profiles of total and incremental dynamic bending moments are strongly cubic in nature. The measured values are quite well represented by a third degree polynomial fit. The implication of this measured behavior is that the dynamic lateral pressure profile is a linear function. Finally, the experimental measurements show that total earth pressure profiles consistently increase monotonically downward in the manner that is typically observed and assumed under static conditions.

4.10. References

- Al-Atik, L. and N. Sitar, 2010. Seismic Earth Pressures on Cantilever Retaining Structures, Journal of Geotechnical and Geoenvironmental Engineering, Vol. 136, No. 10, pp. 1324-1333, doi: 10.1061/(ASCE)GT.1943-5606.0000351.
- Arulnathan, R, Boulanger, RW, Kutter, BL, and Sluis, WK. "New Tool for Shear Wave Velocity Measurements in Model Tests," Geotechnical Testing Journal, GTJODJ, Vol. 23, No. 4, 444-453, 2000.
- Boardman, T. "Seismic Earth Pressures on Below Grade Retaining Structures," PEER/UC Berkeley Seismic Earth Pressures Workshop, June 8, 2006.
- Chopra, AK. "Dynamics of Structures: Theory and Applications to Earthquake Engineering," Third Edition, Prentice Hall, Upper Saddle River, New Jersey, 2007.
- Coulomb, CA. "Essai sur une application des regies des maximis et minimis a quelques problemes de statique relatifs a 1'architecture," Memoires de I'Academie Royale pres Divers Savants, Vol. 7, 1776.
- Mononobe, N, and Matsuo M. "On the Determination of Earth Pressures during Earthquakes," Proceedings, World Engineering Congress, Vol. 9, 179-187, 1929.
- Okabe S. "General Theory of Earth Pressure," Journal of the Japanese Society of Civil Engineers, Tokyo, Japan, Vol. 12 , No. 1, 1926.
- Rathje, EM, Abrahamson, NA, and Bray, JD. "Simplified Frequency Content Estimates of Earthquake Ground Motions," Journal of Geotechnical and Geoenvironmental Engineering, Vol. 124, No. 2, 150-159, 1998.
- Richards, R, and Elms, DG. "Seismic Behavior of Gravity Retaining Walls," Journal of the Geotechnical Engineering Division, ASCE, 105, (GT4), 449-64, 1979.
- Seed, HB, and Whitman, RV. "Design of Earth Retaining Structures for Dynamic Loads," ASCE Specialty Conference, Lateral Stresses in the Ground and Design of Earth Retaining Structures, Cornell Univ., Ithaca, New York, 103-147, 1970.

Chapter 5

Numerical Simulation

5.1. Introduction of FLAC Algorithm

The FLAC computer program (Fast Lagrangian Analysis of Continua) uses explicit, finite difference (FD) (ITASCA, date) to perform static and dynamic, non-linear, numerical analyses of continuous media and it has been extensively used for analysis of a variety of geotechnical problems. Most importantly, the code is relatively flexible and adaptable in that it allows a user to define problem specific constitutive relationships. Detailed descriptions of the code and its capabilities are described in detail elsewhere (ITASCA, 2011), therefore, only the details of the code implementation specific to the modeling effort performed in this research are addressed herein.

The aim of the Lagrangian explicit solution method is to resolve a static problem (elastoplastic) or quasi-static problem (viscoplastic) by means of the equations of motion. The solution scheme is depicted in Figure 5.1, with reference to a computational step Δt.

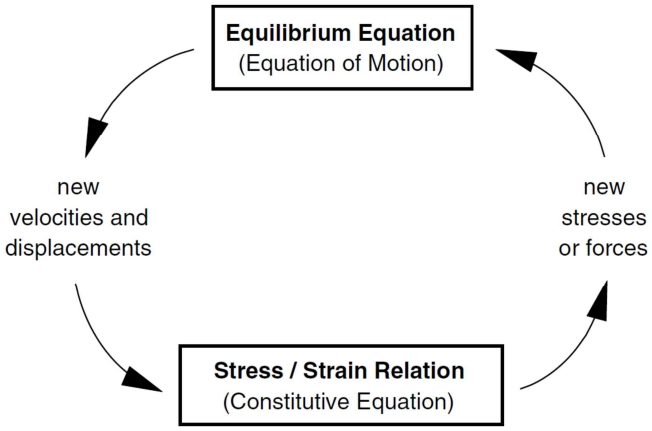

Figure 5.1. Basic explicit calculation cycle (from Itasca 2011).

The solution uses the equations of motion to obtain a new field of nodal velocities at each time step by means of the integration of the accelerations at time $\Delta t/2$, as illustrated in Figure 5.2. A second integration at time $\Delta t/2$ is used to solve for nodal displacements. The respective equations of motion of Newton for a deformable body in a Lagrangian reference system can be expressed as:

$$\rho \frac{\delta \dot{u}_t}{\delta t} = \frac{\delta \sigma_{ij}}{\delta x_j} + \rho g_i \tag{5.1}$$

where ρ is the volumetric weight, $\dot{u}_\iota$ is the nodal velocity, x_j is the spatial coordinate, g_i is the acceleration at that time step, σ_{ij} is the stress tensor, and *t is* the model time. The strain tensor at time Δt can be written as:

$$\dot{\varepsilon_{\iota J}} = \frac{1}{2}\left[\frac{\delta \dot{u}_\iota}{\delta x_j} + \frac{\delta \dot{u}_J}{\delta x_i}\right] \tag{5.2}$$

The stress tensor is then evaluated by means of the constitutive law of the material, which implementation is described in the following section. The new nodal forces, are then calculated from the stress field, and are used to evaluate the new field of acceleration at the end of the computational step Δt. The sequence of iterations is schematically shown in Figure 5.2.

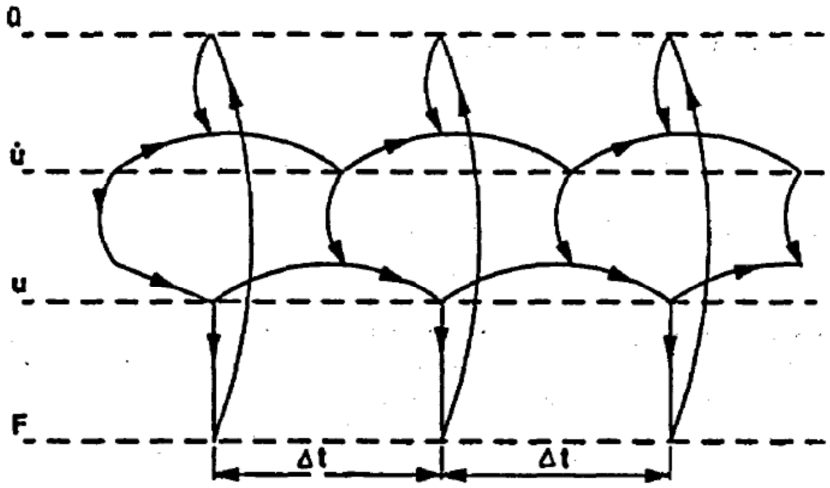

Figure 5.2. Interlaced nature of calculation cycle used in FLAC (from Itasca 2011).

The main assumption in this computational scheme is that the newly computed stresses do not influence the nodal velocities evaluated in the previous step. This hypothesis is true if the computational time step Δt is small enough so that the lack of equilibrium within an element does not propagate to the neighboring elements during the same time interval.

The solution procedure is not unconditionally stable. A critical time step, Δt_c, that cannot be exceeded by the computational time step Δt, must be defined. Cormeau (1975) and Billaux and Cundall (1993) state that the evaluation of the critical time step can be done with the constraint that the velocity of the solution wave must be always greater than the velocity of the physical wave during a computational cycle, as discussed later. The solution is highly unstable during the first computational steps because of the magnitude of the unbalanced forces. Damping is introduced in order to achieve a rapid convergence to a stable solution. The damping algorithms implemented in FLAC are described in the following section. The stability criterion, which controls the state of equilibrium of the system, is based on the maximum unbalanced force which is a user defined criterion in the code. Overall, the explicit solution method implemented in FLAC leads to a high number of computational steps, which is not an issue in the analysis of non-linear and dynamic problems in which material properties change with time.

5.2. Interface elements in FLAC

FLAC provides interfaces that model sliding and/or tensile separation. The properties of interfaces that have to be defined are friction, cohesion, dilation, normal and shear stiffness, and tensile strength. Although there is no restriction on the number of interfaces or the complexity of their intersections, it is generally not feasible to model more than a few simple interfaces with FLAC because it is awkward to specify complicated interface geometry.

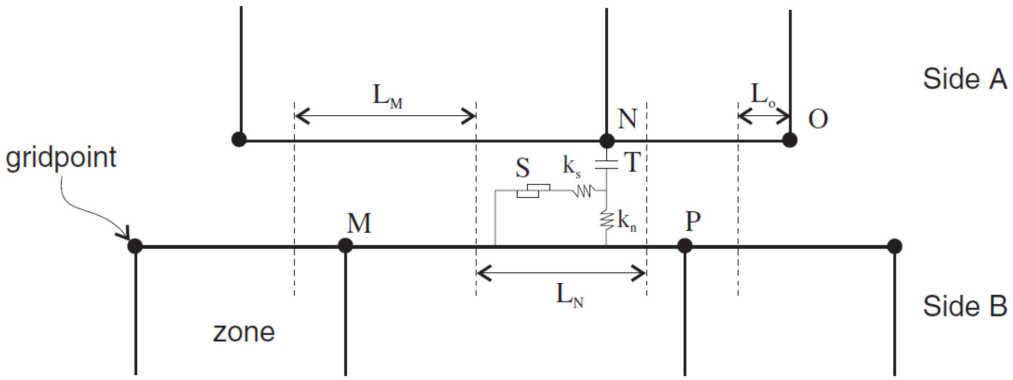

Figure 5.3. Schematic of the FLAC interface element (from Itasca 2011).

Figure 5.3 is a schematic of an interface in FLAC. An interface is represented as normal and shear stiffness between two planes which may contact one another. Where S is the slider; T is the tensile strength; k_n is the normal stiffness; k_n is the shear stiffness; L_n is the length associated with gridpoint N; is the length associated with gridpoint M; and "---" denotes limits for joint segments (placed halfway between adjacent gridpoints) FLAC uses a contact logic, which is similar in nature to that employed in the distinct element method, for either side of the interface (e.g., Cundall and Hart 1992). The code keeps a list of the grid points *(i,j)* that lie on each side of any particular surface. Each point is taken in turn and checked for contact with its closest neighboring point on the opposite side of the interface. Referring to Figure 5.3, grid point N is checked for contact on the segment between grid points M and P. If contact is detected, the normal vector, n, to the contact grid point, N, is computed. A "length," *L*, is also defined for the contact at N along the interface. This length is equal to half the distance to the nearest grid point to the left of N plus half the distance to the nearest grid point to the right, irrespective of whether the neighboring grid point is on the same side of the interface or on the opposite side of N. In this way, the entire interface is divided into contiguous segments, each controlled by a grid point.

During each timestep, the velocity Δu_i, of each grid point is determined. Since the units of velocity are displacement per timestep, and the computational timestep has been scaled to unity to speed convergence (see Itasca 2011), then the incremental displacement for any given timestep is:

$$\Delta u_i \equiv \dot{u}_\iota \tag{5.3}$$

The incremental relative displacement vector at the contact point is resolved into the normal and shear directions, and total normal and shear forces are determined by:

$$F_n^{(t+\Delta t)} = F_n^{(t)} - k_n \Delta u_n^{(t+1/2\Delta t)} L \tag{5.4}$$

$$F_s^{(t+\Delta t)} = F_s^{(t)} - k_s \Delta u_s^{(t+1/2\Delta t)} L \tag{5.5}$$

where k_n and k_s are respectively the normal and shear stiffness module.

To model an interface, FLAC offers two types of models: (a) an interface that is stiff enough compared to the surrounding material, but which can slip and perhaps open in response to the anticipated loading; or (b) an interface that is soft enough to influence the behavior of the system. In the latter case, properties should be derived from tests on real joints (suitably scaled to

account for size effect), or from published data on materials similar to the material being modeled to model the interface as close as possible as the real one, these last model were chosen.

5.2.1. Normal stiffness k_n

Itasca (2011) recommends as a rule of thumb that k_n be set to ten times the equivalent stiffness of the stiffest neighboring zone, i.e.,

$$k_n \approx 10.max\left[\frac{K+\frac{4}{3}G}{\Delta z_{min}}\right] \quad (5.6)$$

In this relation, K and G are shear and bulk modulus and Δz_{min} is the smallest width of a zone in the normal direction of the interfacing surface. The max[ ] notation indicates that the maximum value over all zones adjacent to the interface is used. The FLAC Arbitrarily large values r k_n should be avoided as is commonly done in finite element analyses, since this results in an unnecessarily small time-steps and, therefore, unnecessarily long computational times.

5.2.2. Shear stiffness k_s

The determination of k_s required considerably more effort than the determination of the other interface element parameters. In shear, the interface element in FLAC essentially is an elasto-plastic model with an elastic stiffness of k_s and yield strength S. k_s values were selected such that the resulting elasto-plastic model gave an approximate fit of the realistic soil-structure interface behavior.

The model parameters used in this research simulation are based in part on the laboratory experiment of sand, and partly from the experimental test conducted on soil-structure interface involving the same type of material. There are many studies that are dedicated to studying the behavior of the sand (Shahrour and Rezaie, 1997).

5.3. Dimensions of the finite difference zones

As mentioned previously, proper dimensioning of the finite difference zones is required to avoid numerical distortion of propagating ground motions, in addition to accurate computation of model response. The FLAC manual (Itasca, 2011, Optional Features Manual) recommends that the length of the element Δl be smaller than one-tenth to one-eighth of the wavelength λ associated with the highest frequency f_{max} component of the input motion. The basis for this recommendation is a study by Kuhlemeyer and Lysmer (1973). Interestingly, the FLUSH manual (Lysmer et al. 1975) recommends Δl be smaller than one-fifth the λ associated with f_{max}, also referencing Kuhlemeyer and Lysmer (1973) as the basis for the recommendation,

$$\Delta l \leq \frac{\lambda}{10} \quad (5.7)$$

i.e., λ is related to the shear wave velocity of the soil v_s and the frequency f of the propagating wave by the following relation:

$$\lambda = \frac{v_s}{f} \quad (5.8)$$

Assuming that the response of the retaining wall will be dominated by shear waves, substitution of Equation 5.8 into the FLAC expression for Δl in Equation 5.7 gives:

$$\Delta l \leq \frac{v_s}{10.f_{max}} \tag{5.9}$$

$$f_{max} \leq \frac{v_s}{10.\Delta l} \tag{5.10}$$

As may be observed from these expressions, the finite difference zone with the lowest v_s and a given Δl will limit the highest frequency that can pass through the zone without numerical distortion. For the FLAC analyses performed in this study, maximum sizes of 1-ft by 1-ft (0.3-m by 0.3-m) zones were used in both models.

5.4. Damping

FLAC allows mass proportional, stiffness proportional, and Rayleigh damping to be specified, where the latter provides relatively constant level of damping over a restricted range of frequencies. Use of either stiffness proportional or Rayleigh damping results in considerably longer run times than either no damping or mass proportional damping. For the analyses performed herein, Rayleigh damping was specified, for which the critical damping ratio ξ may be determined by the following relation:

$$\xi = \frac{1}{2}.\left(\frac{\alpha}{\omega} + \beta.\omega\right) \tag{5.11}$$

where

α = the mass-proportional damping constant

β = the stiffness-proportional damping constant

ω = angular frequency associated with ξ

For Rayleigh damping, the damping ratio and the corresponding central frequency need to be specified. Judgment is required in selecting values for both parameters. In most attempts to match laboratory and numerical damping curves, it is noted that the damping provided by the hysteretic formulation at low cyclic strain levels is lower than that observed in the laboratory. This may lead to low-level noise, particularly at high frequencies. Although such noise hardly affects the essential response of the systems, for cosmetic reasons it may be removed by adding a small amount of Rayleigh damping. It is found that 0.5-1% Rayleigh damping (at an appropriate center frequency) is usually sufficient to remove residual oscillations without affecting the solution timestep.

5.5. User defined constitutive models

The FLAC code allows the user to write new constitutive models. This can be done by using a special internal programming language called FISH (FlacISH), or by means of a DLL library written with the C++ language. The first method is simpler, because of the simplicity of the scripting language, but computationally it is much slower, because the script code is not compiled. The procedure consists of the following steps:

1. Initialization of the variables. It is executed only once for each element and for each solution.
2. Determination of the new stress. This e is the core of the implementation, and consists in evaluating the new state of stress starting from the strain increments $\Delta\varepsilon_{ij}$ and from the internal hardening parameters. It is called four times for each element (one for each sub zone) and for time step.
3. Evaluation of the maximum modulus. This step consists in defining the maximum shear modulus and the maximum oedometer modulus in order to permit the FLAC code to evaluate the admissible time step.
4. Thermo-mechanics coupling. This part of the code is executed only during thermal analysis and permits the thermo-mechanical coupling. The constitutive law is written for each sub-zone (with a number of 2 or 4 depending on the geometry of the element). Therefore the state parameters and the hardening parameters are determined as the averages of these quantities for all the sub-zones, by considering the area or the volume of each sub-zone.

5.6. Soil constitutive model

When a soil mass is subjected to earthquake shaking the primary loading is cyclic shearing in the horizontal plane. The cyclic shear induces stress-strain behavior that is hysteretic in nature with characteristics as discussed follow:

- Increasing hysteresis and reduction in secant modulus with greater strain.
- Increasing hysteresis and reduction in secant modulus with number of cycles.
- Permanent strains bias “ratcheting” when loaded with a static bias.
- Pore pressure generation that is a function of soil properties, cycle amplitude and/or number of loading cycles. Increased pore pressure results in increasing hysteresis, modulus reduction, and in the limiting condition soil liquefaction.
- Permanent secant modulus reduction with “damage” and pore pressure build-up
- Strength reduction with plastic strain.

A robust, relatively simple, total stress model, UBCHYST (Byrne and Naesgaard 2010) that has been developed at University of British Columbia for dynamic analyses of soil subjected to earthquake loading. The model is intended to be used with “undrained” strength parameters in low permeability clayey and silty soils, or in highly permeable granular soils where excess pore water would dissipate as generated. The model has been implemented to be used in the two dimensional finite difference program FLAC (Itasca, 2011).

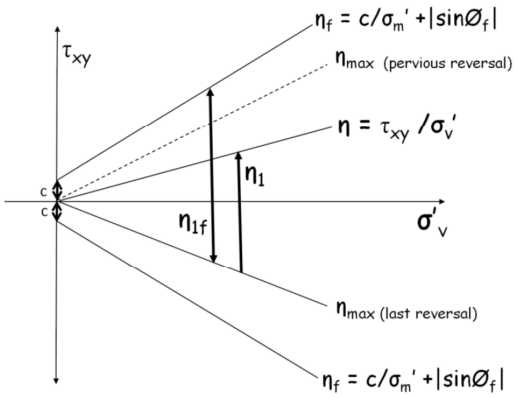

Figure 5.4. UBCHYST model key variables (from Byrne and Naesgaard 2010).

The essence of this hysteretic model is that the tangent shear modulus (G_t) is a function of the peak shear modulus (G_{max}) times a reduction factor that is a function of the developed stress ratio and the change in stress ratio to reach failure. This function is as shown in equation (5.12) and illustrated in Figure 5.4.

$$G_t = G_{max} \times \left(1 - \left(\frac{\eta_1}{\eta_{1f}}\right)^{n_1} \times R_f\right)^n \times mod1 \times mod2 \times mod3 \quad (5.12)$$

Where

η stress ratio $\left(\tau_{xy}/\acute{\sigma_V}\right)$

η_1 = stress ratio η $\left(\tau_{xy}/\acute{\sigma_V}\right)$ since last reversal $(\eta - \eta_{max})$

η_{max} = maximum stress ration (η) at last reversal

η_{1f} = change in stress ratio to reach failure envelope in direction of loading $\left(\eta_f - \eta_{max}\right)$

η_f = $\left(\sin(\varphi_f) + Cohesion \times \cos(\varphi_f)/\acute{\sigma_V}\right)$

τ_{xy} = developed shear stress in horizontal plane

$\acute{\sigma_V}$ = vertical effective stress

φ_f = peak friction angle

n_1, R_f and n are calibration parameters with suggested default values 1, 1 and 2 respectively.

$mod1$= a reduction factor for first-time or virgin loading (typically 0.6 to 0.8)

$mod2$= optional function to account for permanent modulus reduction with large $strain = \left(1 - \left|\frac{\eta_1}{\eta_{1f}}\right|^{n_1}\right) \times dfac \geq 0.1$

$mod3$= optional function to account for cyclic degradation of modulus with strain or number of cycles, etc.

Stress reversals occur if the absolute value of the mobilized stress ratio (η) is less than the previous value and a cross-over occurs if τ_{xy} changes sign. A stress reversal causes η_1 to be reset

to 0 and η_{1f} to be recalculated. However, the program retains the previous reversals (η_{1old} and η_{1fold}) so that small hysteretic loops that are subsets of larger loops do not change the behavior of the large loop (Figure 5.4). With the above equation the tangent shear modulus varies throughout the loading cycle to give hysteretic stress-strain loops with the characteristics illustrated in Figure 5.4.

5.7. Implementation

The UBCHYST's FISH source code was generously provided by Byrne and Naesgaard (Byrne and Naesgaard 2010). In order to speed up the computations the FISH source code was converted to C++ and compiled as a DLL as a part of this research effort. This approach significantly speeded up the dynamic analyses performed in this study. In this section the numerical implementation of the UBCHYST constitutive model into the FLAC code is described briefly.

The input variables for the UBCHYST model are:

- The tensor of the increments of the total strains $\Delta\varepsilon_{ij}$, which is determined by the solver for each computational step by means of the equation of motion and by means of the stress state σ_{ij}, which has been evaluated using the constitutive law in the previous step.
- The tensor of the stresses σ_{ij} which has been evaluated in the previous step.
- The stress ration parameters such as η, η_1, η_{max}, η_{1f} and η_f which have been evaluated in the previous step.

The output variables are:

- The new tensor of the stresses σ_{ij}.
- The new stress ration parameters η, η_1, η_{max}, η_{1f} and η_f.
- The shear modulus using equation 5.12.

The numerical implementation of the UBCHYST model can be subdivided into three principal blocks:

- evaluation of the first trial elastic stresses;
- evaluation of plastic corrections;
- update of the stress ratio parameters;
- update the moduli (i.e. shear and bulk).

It is important to remember that the FLAC uses the mechanics sign convention in which tensile stress as positive.

A new DLL library has been written, optimized, and compiled using the C++ language in order to obtain the maximum computational speed as possible. It is in fact very important to remember that for complex analyses and for back analyses the required time is extremely important and must be reduced to a minimum.

List of the parameters associated with UBCHYST model and their corresponding symbols in the DLL version is illustrated in Table 5.1.

Table 5.1. UBCHYST input parameters.

Parameter description	Symbol used in constitutive model
Cohesion	hcoh
Friction angle	hfric
Dilation angle	hdil
Tensile strength	hten
Small strain max. shear modulus	hgmax
Bulk modulus	hk
Hysteretic parameter	hn
Hysteretic parameter	hrf
Hysteretic parameter	hrm
Hysteretic parameter	hdfac
Atmospheric pressure	hpa

In order to compare the DLL library and original FISH model an identical model (i.e. ROOZ02) has been conducted using both FISH and CPP-UDM version. The result shows that DLL version is almost 11 time faster than the FISH model and running time reduced from 7 days to 15 hours in this particular modeling. This was a significant achievement in this research study since dynamic modeling are very time consuming and this speed up could save a lot times.

5.8. Soil parameter calibration

The calibration of the UCHYST model was conducted in two stages:

1) The model was calibrated by comparing uniform cyclic response to that inferred from published modulus reduction and damping curves (i.e. Darendeli, 2001) as shown in Figure 5.6 and/or by comparison to the results of cyclic simple shear laboratory tests. The simple shear test is preferred over triaxial loading because the loading path with rotation of principal axes, etc. more closely resembles the stress path from earthquake loading. As Show in in Figure 5.6a The UBCHYST model displayed the best match to the Darendeli (2001) modulus reduction curves. However, the model did overestimate the damping response at medium to large (>0.1%) shear strains (Figure 5.6b). The reason for this overestimation of damping factor appeared to be due to fatness of hysteresis loop using UBCHYST model. The calibrated parameters have been used for next step of calibration as described below.
2) A 1-D soil column was used to approximate semi-infinite layer in the laminar container in centrifuge test. The grid points at the same level are allowed to displace by the same amount. A static analysis was performed to determine the initial stress state of the model before applying dynamic excitation. Thereafter, the chosen acceleration time history was applied at the base of the model. Model conditions are prescribed to simulate the free-field motion of a layered soil deposit with a rigid base. The UBCHYST parameters have been adjusted to get a good agreement between free field response of centrifuge test and FLAC. The peak shear modulus of soil is defined by $G_{max} = G_{ref}\left(\frac{P\prime}{P_A}\right)^{n_e}$ where P_A is the atmosphere pressure, P' is the mean effective stress, n_e is the elastic bulk modulus exponent. A FISH function is being prepared to automatically estimates the G_{max} for

each zone for given initial stress state after static analysis. G_{ref}, n_e and P_A are treated as new input variables in the model that need to be calibrated.

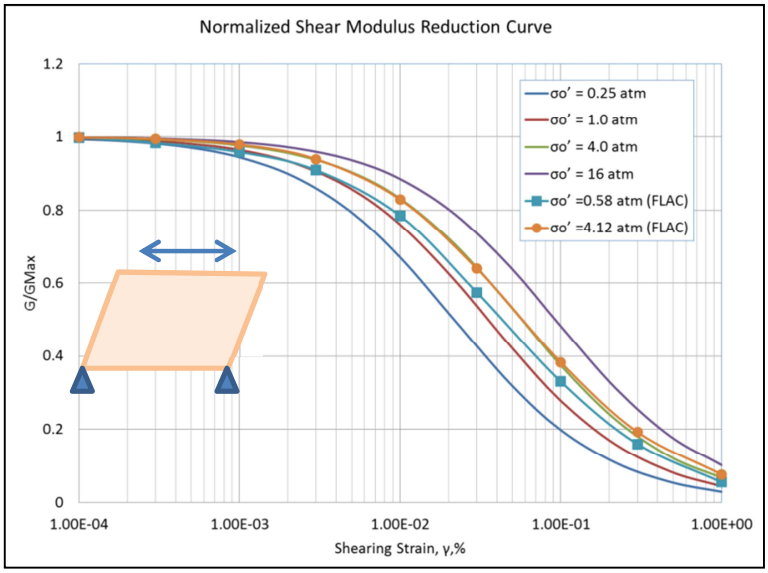

(a)

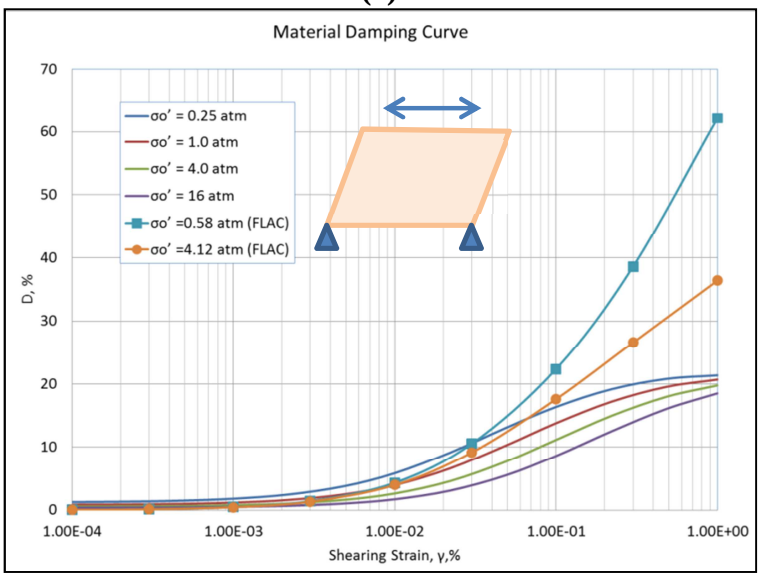

(b)

Figure 5.6. (a) Modulus reduction and **(b)** Damping ratio curve estimated by FLAC using UBCHYST model.

Figures 5.7 and 5.8 show the comparison of the horizontal acceleration and pseudo-acceleration response spectra at the base (Bedrock) and top (Free Field) of the FLAC model and centrifuge data. Here the damping ratio, minimum period and maximum period of interest are 5%, 0.001 and 4 seconds, respectively. Fairly reasonable fits to the data from centrifuge tests were obtained with the calibrated parameters for sand. The 1D wave propagation simulation was repeated for selected events and the calibrated parameters are summarized at Table 5.2.

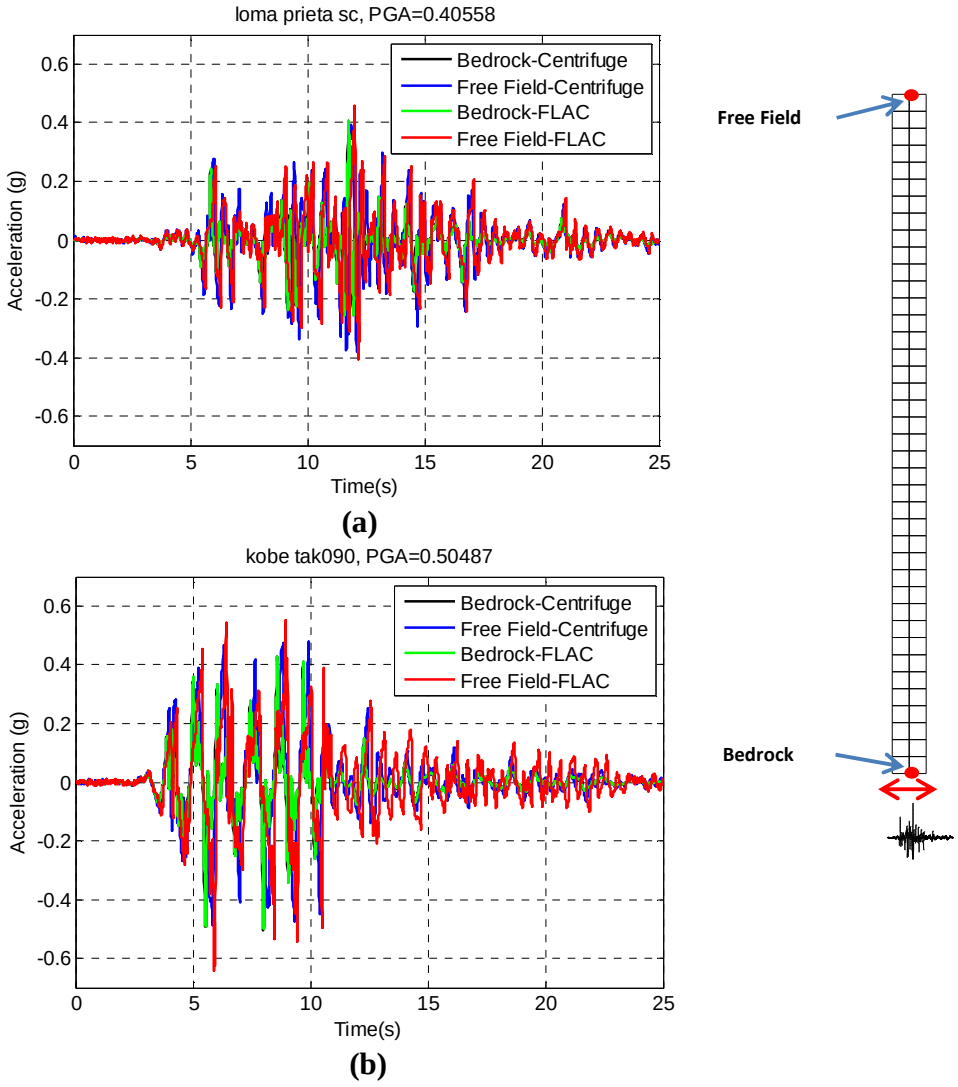

Figure 5.7. Comparison of recorded (centrifuge) and computed (FLAC) accelerations at the bedrock and top of the soil in the free field during **(a)** Loma Prieta-SC-1 and **(b)** Kobe TAK-090-2.

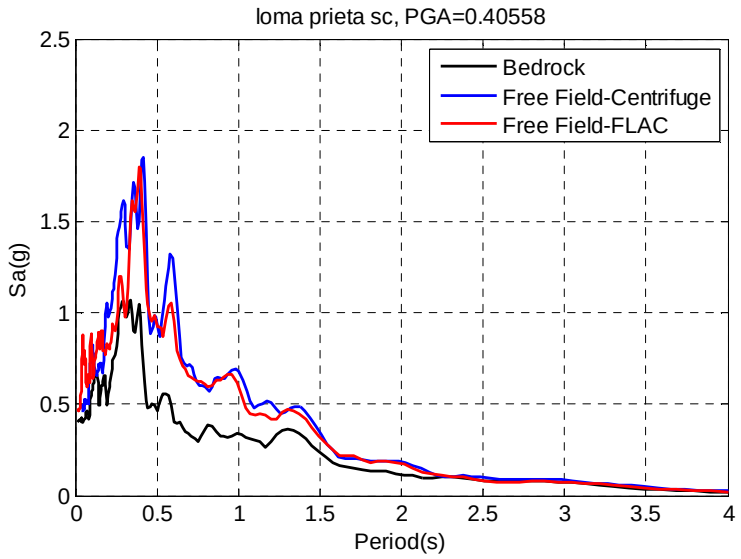

(a)

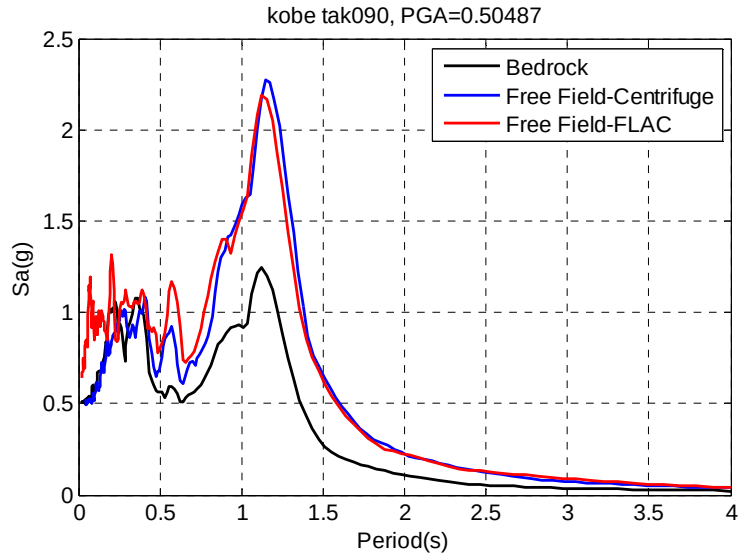

(b)

Figure 5.8. Comparison of recorded (centrifuge) and computed (FLAC) acceleration response spectra at 5% damping at the bedrock and top of the soil in the free field during **(a)** Loma Prieta-SC-1 and **(b)** Kobe TAK-090-2.

Table 5.2. Initial input parameters for the UBCHYST soil properties in the FLAC model.

Model Parameters	Initial input
hcoh (kPa)	0
hfric (deg.)	35
hdil (deg.)	0
hten (kPa)	0
ne	0.5
hgref (kPa)	1.5E05
hgmax (kPa)	Based on **hgref**, **hpa** and **ne**
hk (kPa)	3.0E05
hn	2.1-3
hrf	0.98
hrm	1.2
hdfac	0.8
hpa (kPa)	100
density (tons/m^3)	1.695

5.9. Development of the finite difference model

The 2-D plane strain FD model of the non-displacing basement structures and the backfill and base soil for experiment ROOZ01 are presented in Figure 5.9. The centrifuge model configuration for experiment ROOZ02 was presented in profile view and model scale in Figure 5.10. The FD models have the same prototype configuration as that of experiment ROOZ01 and ROOZ02.

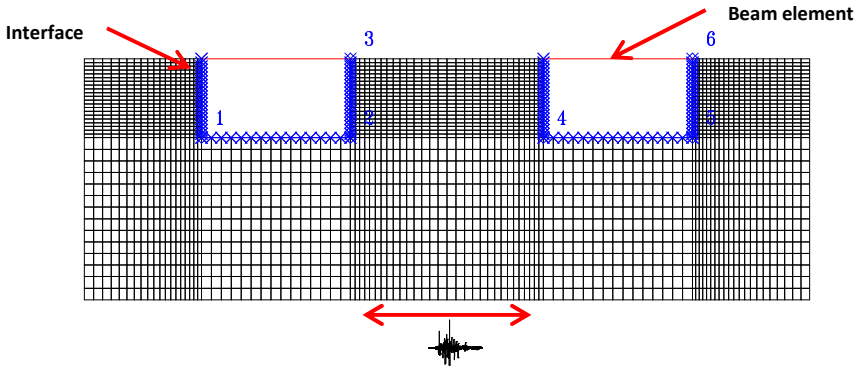

Figure 5.9. Two-dimensional, plane strain, FD mesh developed by FLAC for ROOZ01.

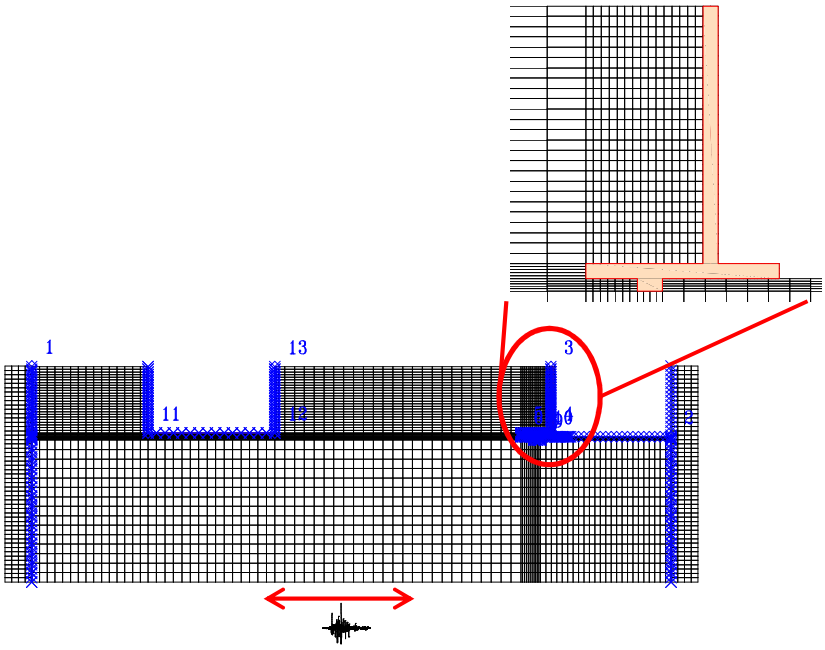

Figure 5.10. Two-dimensional, plane strain, FD mesh developed by FLAC for ROOZ02.

The non-displacing basement structures and non-displacing cantilever wall (U-shape wall) were modeled using linear elastic elements. The displacing retaining wall was modeled by a solid element as shown in Figure 5.10. The structures used in the FD model had the same prototype dimensions, mass, and properties as the aluminum structures used in the centrifuge experiments. The FD model parameters of the structures are given in Tables 5.3 through 5.6. The connections between the wall and the base of each structure were modeled as rigid moment connections in FLAC, which means that no rotational flexibility was allowed at the connections. The calibrated UBCHYST constitutive model was used to model the nonlinear response of the dry Nevada sand. Linear elastic interface elements governed by Mohr-Coulomb failure model were used to simulate soil-structure interaction as discussed in section 5.2.

Table 5.3. FLAC model properties for the stiff basement structure.

	Walls	**Roof**	**Base**
Height (m)	6.50	-	-
Width (m)	-	10.87	10.87
Thickness (m)	0.46	0.46	0.82
Density (tons/m^3/m)	4.10	15.37	3.74
Area (m^2/m)	0.46	1.75E-02	0.82
E (kPa)	6.89E07	2.06E08	6.89E07
I (m^4/m)	7.97E-03	2.29E-04	4.64E-02

Table 5.4. FLAC model properties for the flexible basement structure.

	Walls	**Roof**	**Base**
Height (m)	6.50	-	-
Width (m)	-	10.87	10.87
Thickness (m)	0.46	0.46	0.82
Density (tons/m^3/m)	6.04	15.37	3.74
Area (m^2/m)	0.26	1.75E-02	0.82
E (kPa)	6.89E07	2.06E08	6.89E07
I (m^4/m)	1.40E-03	2.29E-04	4.64E-02

Table 5.5. FLAC model properties for the displacing retaining structure.

	Walls	**Base**
Height (m)	6.14	-
Width (m)	-	4.57
Thickness (m)	0.34	0.34
Density (tons/m^3/m)	2.70	3.06
E (kPa)	6.89E07	6.89E07

Table 5.6. FLAC model properties for the Non-displacing cantilever structure.

	Walls	**Base**
Height (m)	6.50	-
Width (m)	-	10.87
Thickness (m)	0.46	0.82
Density (tons/m^3/m)	4.10	3.74
Area (m^2/m)	0.46	0.82
E (kPa)	6.89E07	6.89E07
I (m^4/m)	7.97E-03	4.64E-02

The interface model parameters used in these simulations are based on the experimental test conducted on soil-structure interface on sand presented by Shahrour and Rezaie (1997). The list of interface parameters used in this research study is given in Table 5.7.

Table 5.7. FLAC model basic data of the interface.

Parameters	**Values**
K_n (KPa/m)	5.0E05
K_s (KPa/m)	4.0E05
φ (deg.)	10

In case of simulation of ROOZ02 experiment due to the using of large number of interface and zone element the running time was inevitably large and therefore this made the debugging procedure very difficult. So in order to save some time, a Matlab (2010) code was developed to create the soil, structures as well as interface nodes and elements automatically. The m-file script was written to input the total number of zones created by Matlab (2010) as

shown in Figure 5.11. The assigning of boundary conditions, several history points to record different responses, as well as material parameters has been assigned to the model automatically. This way the model has been calibrated and debugged using smaller number of zones and after making sure that everything is in place the number of zone has been increased to achieve zone size criteria explained in section 5.3.

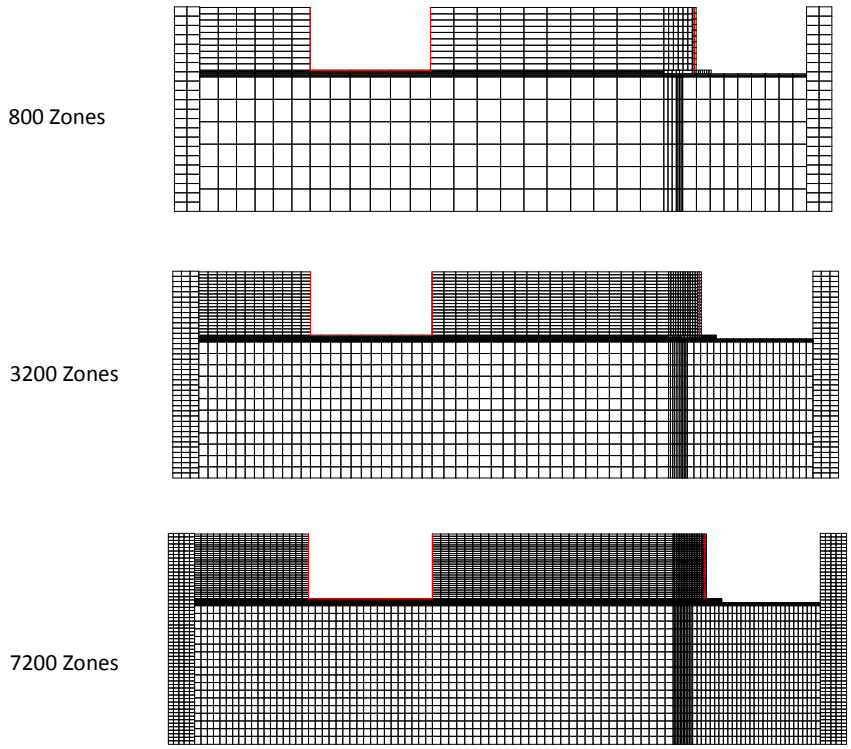

Figure 5.11. FD meshes with different resolutions.

Centrifuge models ROOZ01 and ROOZ02 were tested in a laminar container (FSB2), which consists of an aluminum base plate and a series of five stacked aluminum rings separated by soft neoprene rubber providing lateral flexibility. To minimize boundary effects, the container was designed such that its natural frequency is less than the initial natural frequency of the soil (Kutter, 1995). The behavior of flexible shear-beam model containers was evaluated in Wilson et al. (1997), Lai et al. (2004), Yang et al. (2004) and Hankatharan and Kutter (2008). Although Ilankatharan and Kutter (2008) observed that more accurate 2-D modeling of the container boundary conditions results in a more accurate numerical simulation of dynamic centrifuge experiments, researchers agree that flexible model containers do not have a significant impact on the experimental results. Flexible containers are typically regarded as representative of field conditions.

Boundary conditions in the 2-D FD mesh used herein consisted of: 1) base nodes of the soil continuum were fixed both horizontally and vertically to reproduce the fixed-base conditions of the model container in the static analysis, 2) displacement degrees of freedom of the lateral

boundary grids of the soil continuum were tied together both horizontally and vertically using the ATTACH command 3) the surface was traction free, and 4) dynamic excitation was defined as the recorded base acceleration applied to the base of the model.

For experiment ROOZ02, due to unsymmetrical geometry a virtual column of zones with similar material as soil assigned on them are utilized to preserve the symmetrical boundary as shown in Figure 5.10 then the displacement degrees of freedom of the these soil column were tied together both horizontally and vertically using the ATTACH command.

5.10. Input Earthquake Motions

Accelerations recorded during centrifuge testing at the base of the model container were used as input accelerations to the 2-D FD model using the Apply command in FLAC. The simulated input earthquakes included input acceleration time series recorded during the Kocaeli-YPT330-2, Loma Prieta-WVC270-1, Kocaeli-YPT330-3 and Kobe-TAK090-2 shaking events in experiment ROOZ01 and Kocaeli-YPT330-1, LomaPrieta-SC-1, Kobe-TAK090-1 as well as LomaPrieta-SC-2 in experiment ROOZ02. Peak accelerations varied from 0.25 to 0.85 g. The input acceleration time series and characteristics of the different shaking events used for the FD model can be found in Appendix A.

5.11. Earth pressure from numerical analysis

Computed earth pressure time series were obtained using the normal force histories in FLAC. The recorded lateral force for each contact point was divided by a contributing area to obtain corresponding lateral earth pressures. A FISH function has been written to repeat this sequence every step and calculate the normal stress automatically.

Results obtained from FLAC were processed using Matlab codes to plot different computed responses and compare them to recorded values shown in the following sections.

5.11.1. Static earth pressure

Figures 5.12 and 5.13 show the calculated distribution of static lateral earth pressure in retaining structures before and after shaking events. The at-rest and classical Coulomb active pressure profiles are also shown.

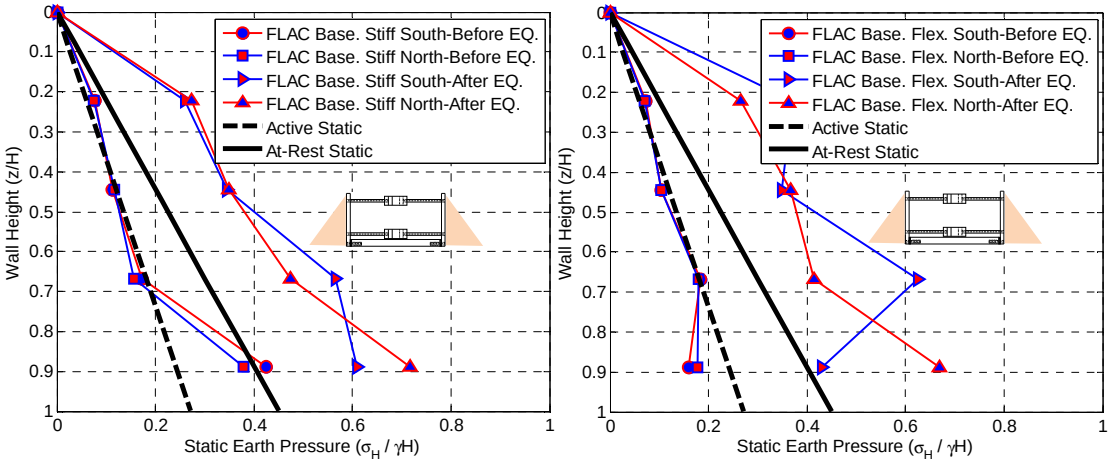

(a) **(b)**

Figure 5.12. Static lateral earth pressure profiles computed by FLAC before and after shaking events in ROOZ01 experiment on **(a)** Stiff Basement and **(b)** Flexible Basement.

In all cases, the computed static lateral earth pressures before shaking fall between the at-rest and active pressure lines. The computed profiles of static earth pressure after shaking show a that the earth pressures increase to the at-rest condition in the case of non-displacing cantilever walls and in the case of the cross-braced structures the earth pressures increase above the at-rest pressure by as much as 50%. The observed and computed increment between the static earth pressures before and after shaking appear to be due to densification of the sand in the experiments and due to irrecoverable strain in the soil elements in the numerical solution.

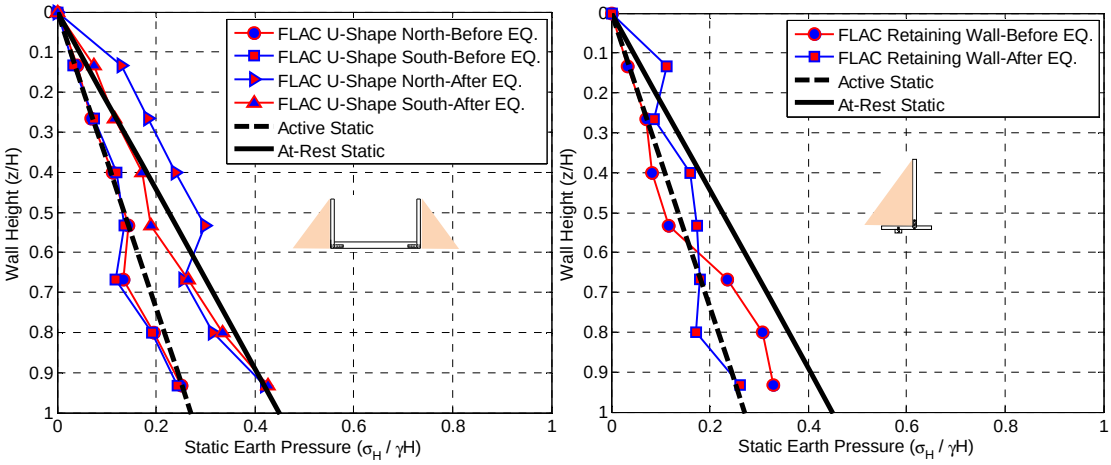

(a) **(b)**

Figure 5.13. Static lateral earth pressure profiles computed by FLAC before and after shaking events in ROOZ02 experiment on **(a)** Non-displacing cantilever wall and **(b)** Displacing retaining wall.

5.11.2. Total earth pressure

Figures 5.14 – 5.20 present a computed total lateral earth pressures at various locations on the basement, non-displacing U-shape and retaining structures the different analyzed shaking scenarios.

The computed total earth pressure profiles consistently increase monotonically downward in the manner that is typically observed and assumed under static conditions and consistent with recorded total earth pressures in the centrifuge experiments.

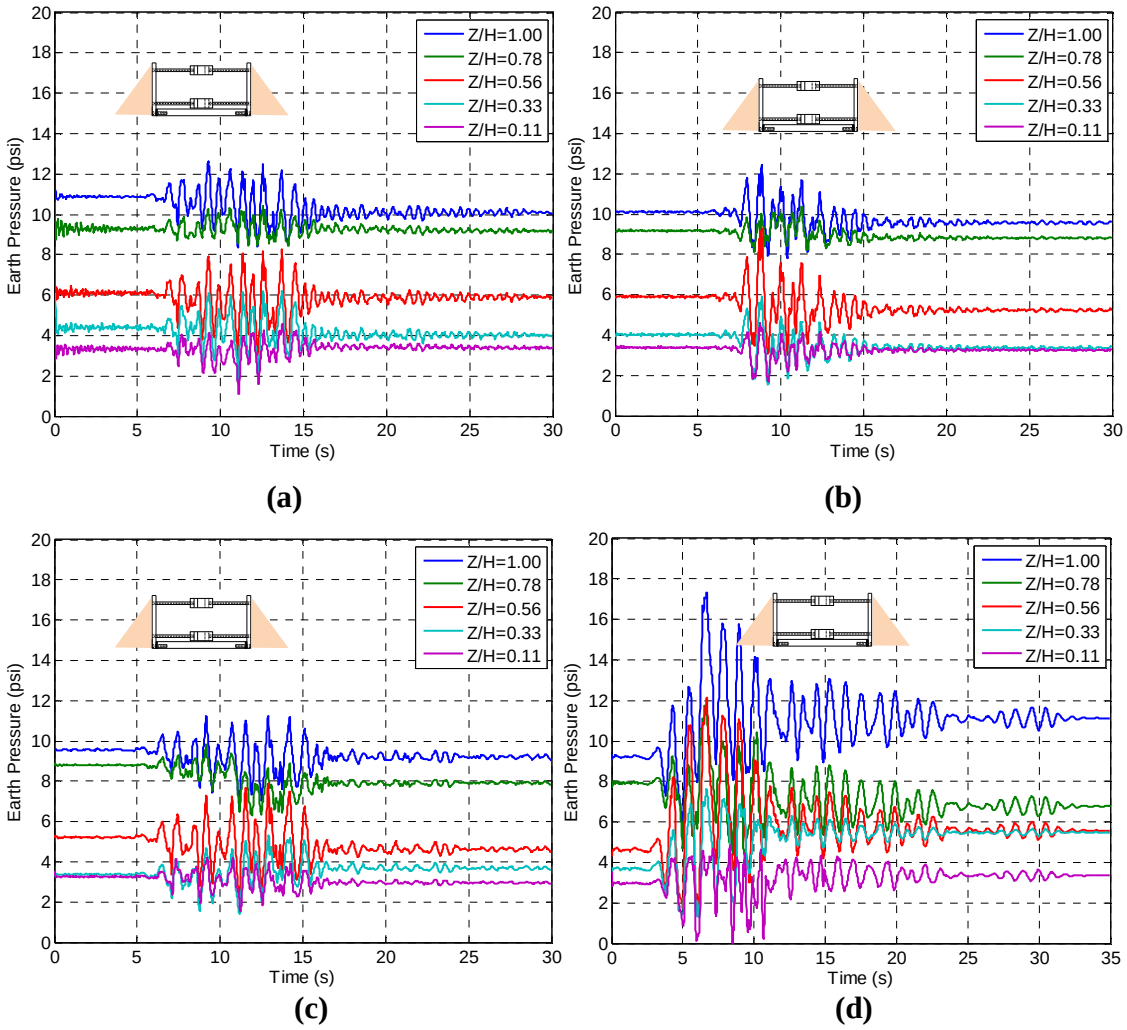

Figure 5.14. Total earth pressure time series computed by FLAC on South side of Stiff Basement wall during **(a)** Kocaeli-YPT330-2, PGA_{ff}=0.41 **(b)** Loma Prieta-WVC270-1, PGA_{ff}=0.49 **(c)** Kocaeli-YPT330-3, PGA_{ff}=0.51 and **(d)** Kobe-TAK090-2, PGA_{ff}=0.72.

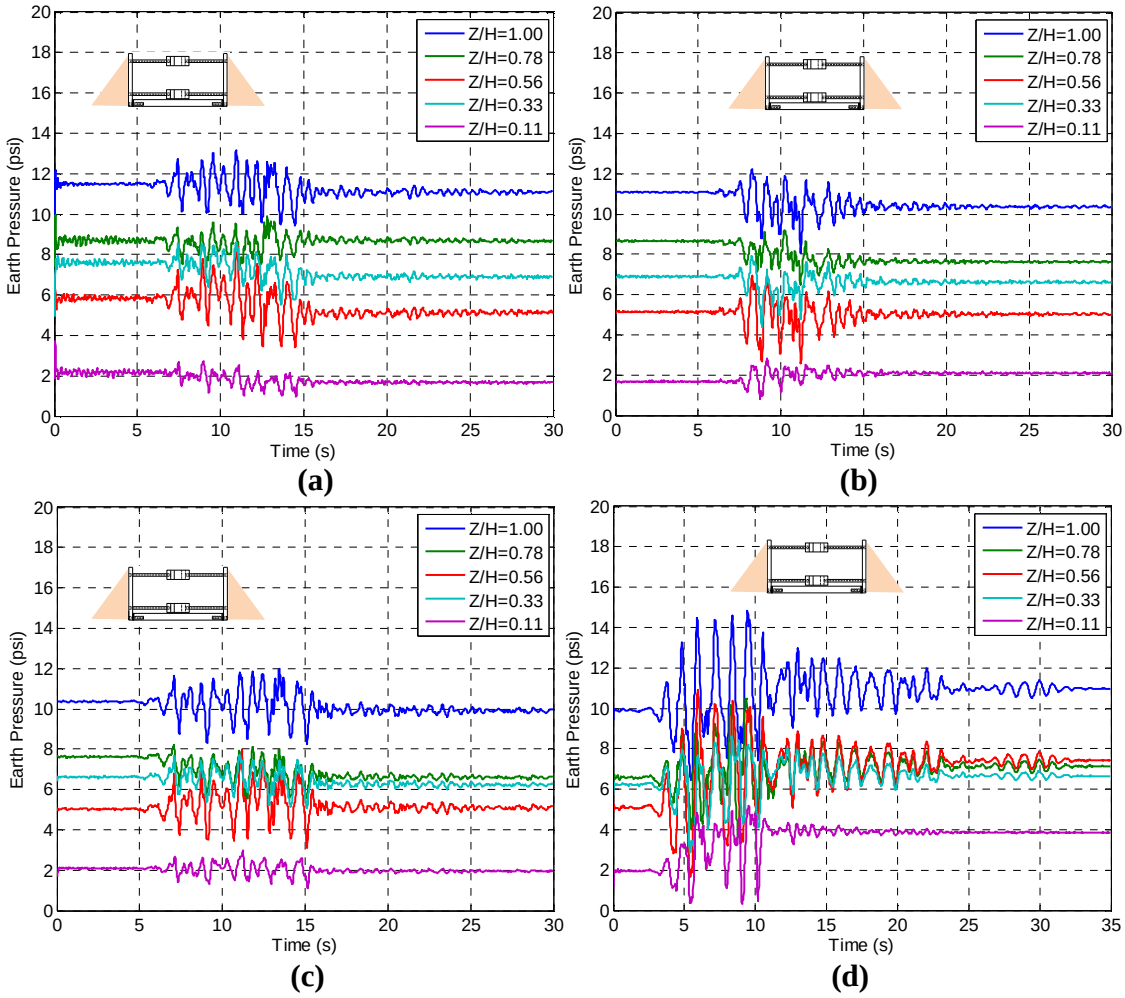

Figure 5.15. Total earth pressure time series computed by FLAC on North side of Stiff Basement wall during **(a)** Kocaeli-YPT330-2, PGA_{ff}=0.41 **(b)** Loma Prieta-WVC270-1, PGA_{ff}=0.49 **(c)** Kocaeli-YPT330-3, PGA_{ff}=0.51 and **(d)** Kobe-TAK090-2, PGA_{ff}=0.72.

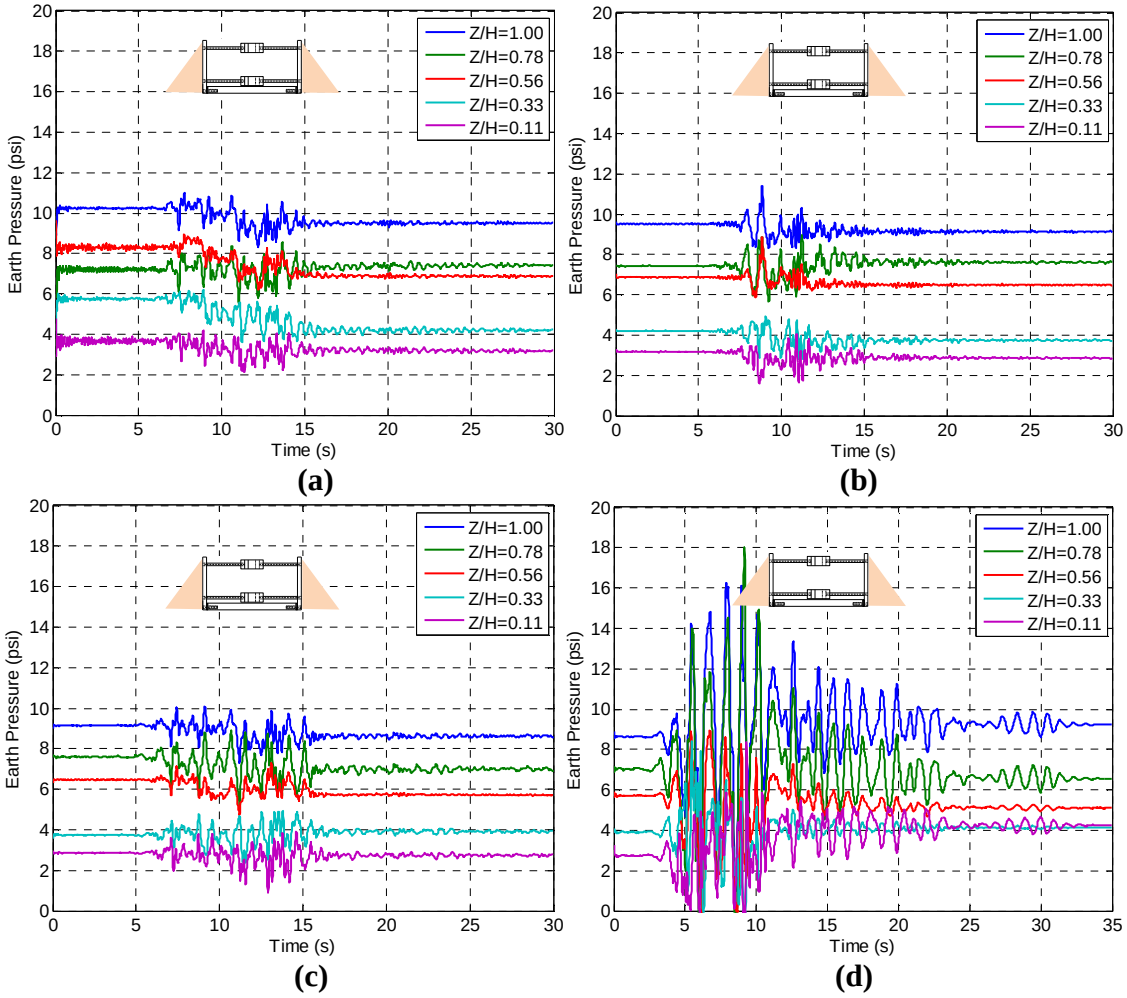

Figure 5.16. Total earth pressure time series computed by FLAC on South side of Flexible Basement wall during **(a)** Kocaeli-YPT330-2, PGA_{ff}=0.41 **(b)** Loma Prieta-WVC270-1, PGA_{ff}=0.49 **(c)** Kocaeli-YPT330-3, PGA_{ff}=0.51 and **(d)** Kobe-TAK090-2, PGA_{ff}=0.72.

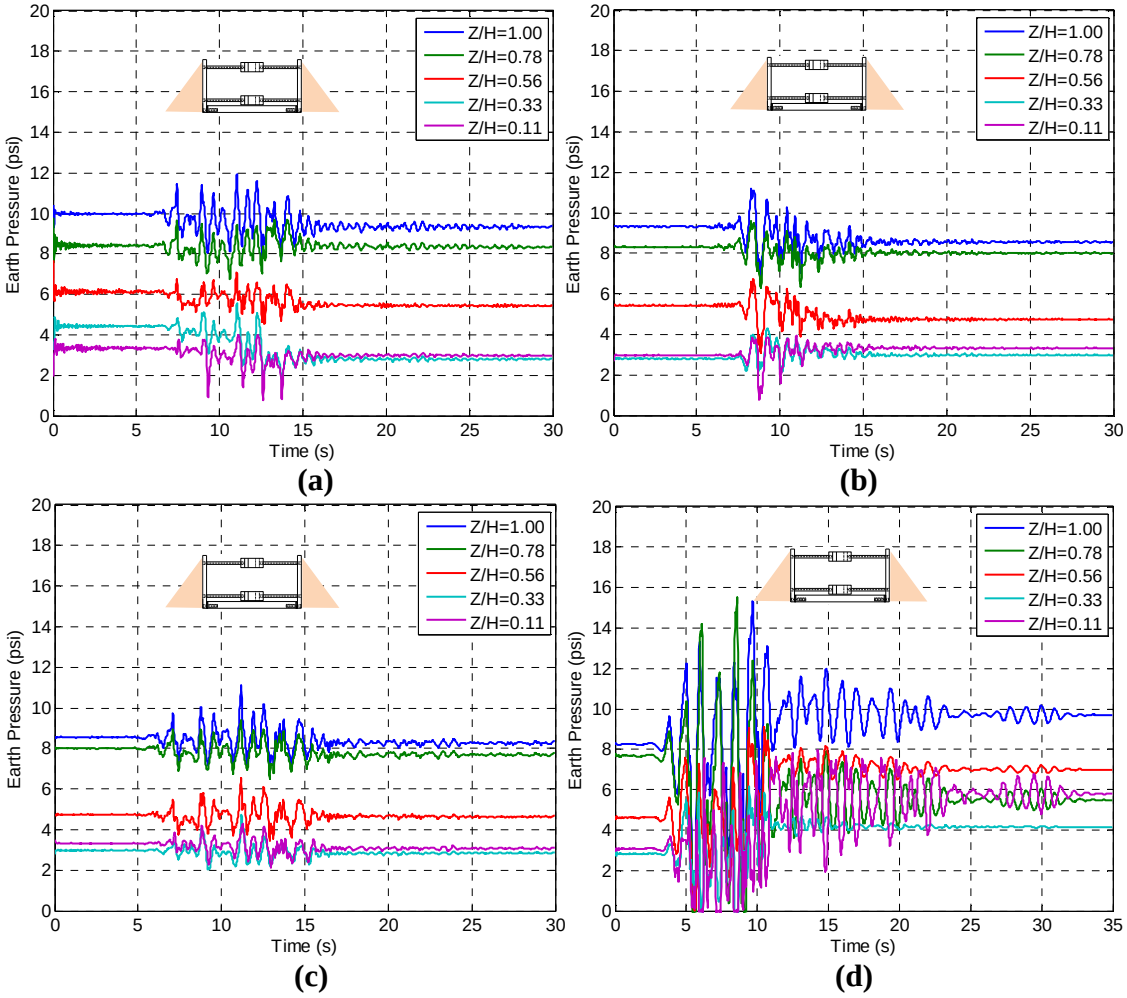

Figure 5.17. Total earth pressure time series computed by FLAC on North side of Flexible Basement wall during **(a)** Kocaeli-YPT330-2, PGA_{ff}=0.41 **(b)** Loma Prieta-WVC270-1, PGA_{ff}=0.49 **(c)** Kocaeli-YPT330-3, PGA_{ff}=0.51 and **(d)** Kobe-TAK090-2, PGA_{ff}=0.72.

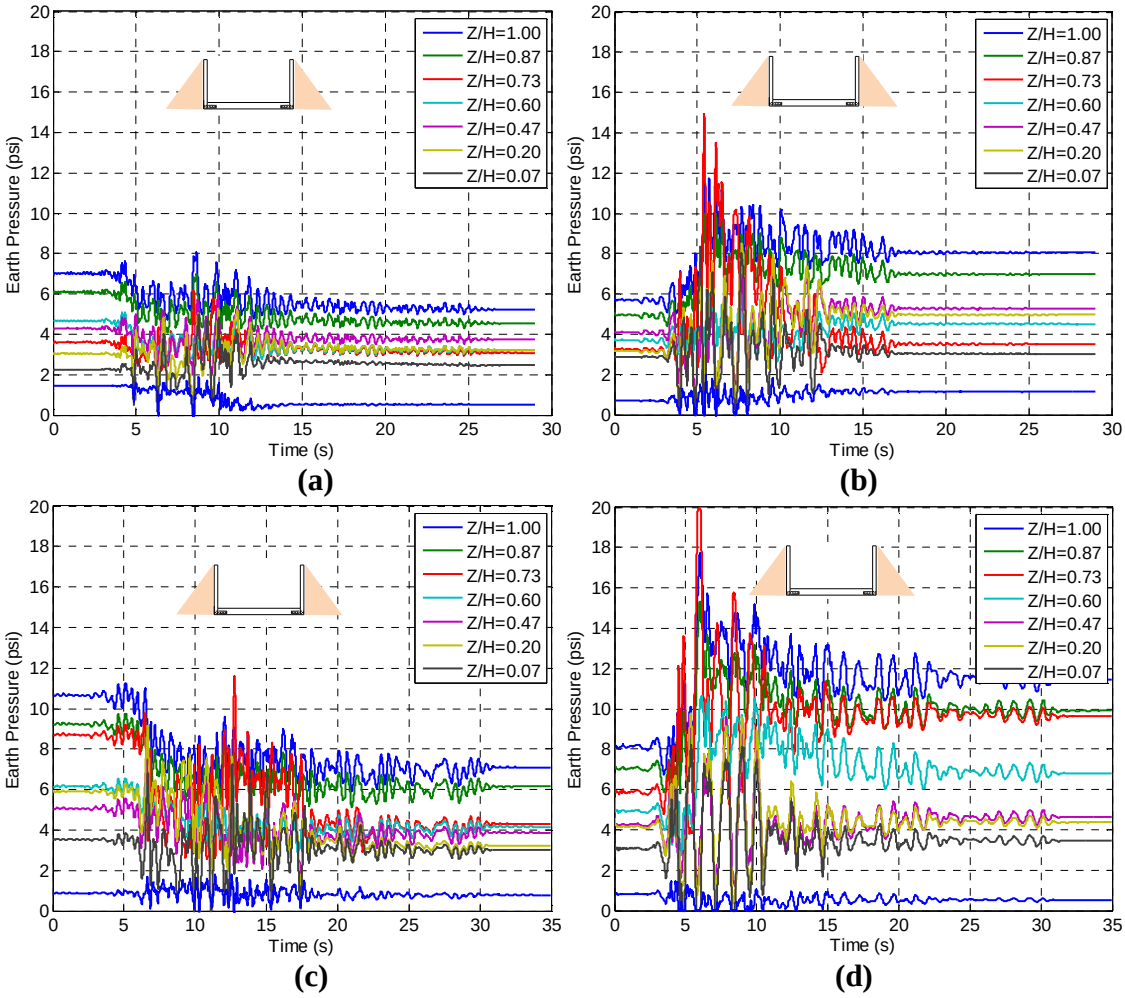

Figure 5.18. Total earth pressure time series computed by FLAC on North side of Non-Displacing Cantilever wall during **(a)** Kocaeli-YPT330-1, PGA_{ff}=0.26 **(b)** LomaPrieta-SC-1, PGA_{ff}=0.62 **(c)** LomaPrieta-SC-2, PGA_{ff}=0.48 and **(d)** Kobe-TAK090-1, PGA_{ff}=0.87.

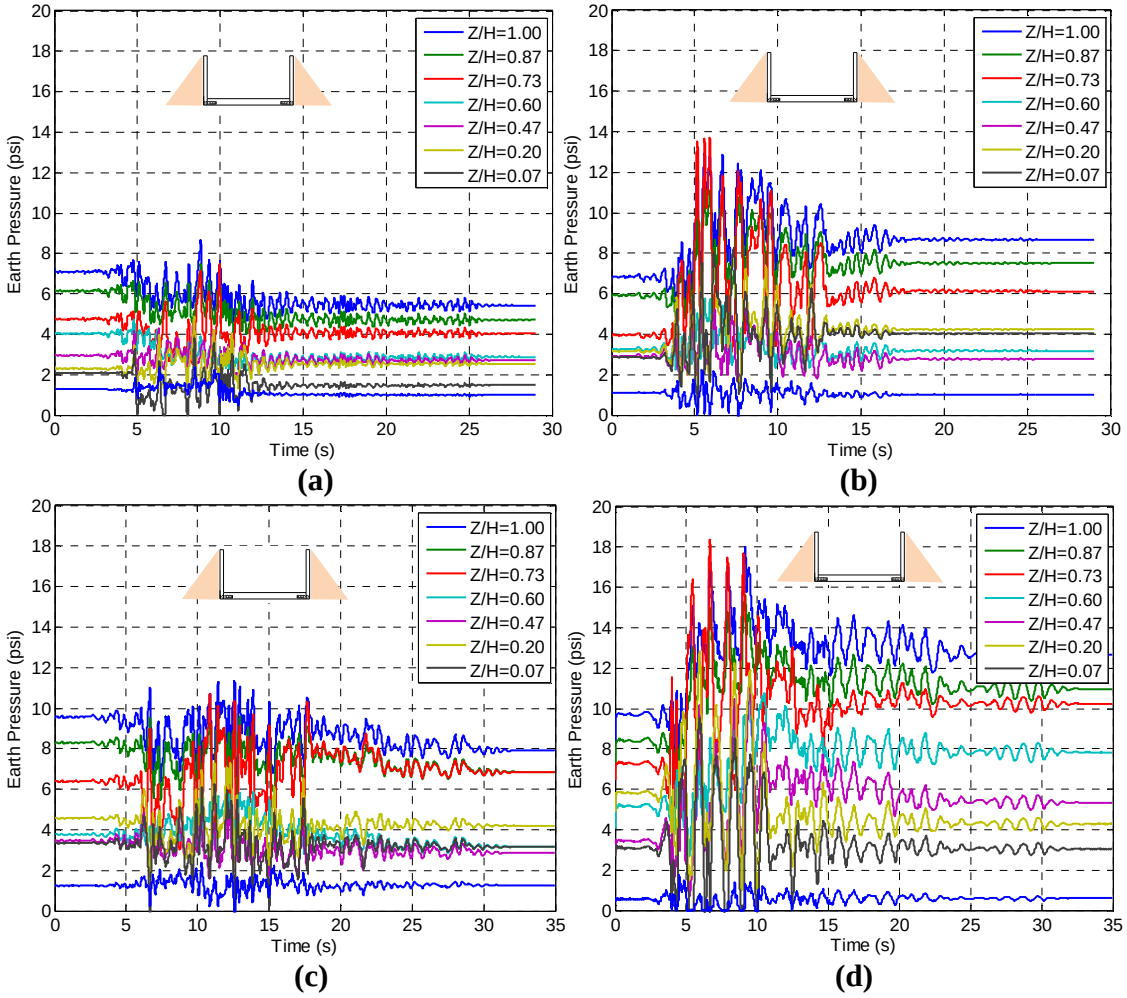

Figure 5.19. Total earth pressure time series computed by FLAC on South side of Non-Displacing Cantilever wall during **(a)** Kocaeli-YPT330-1, PGA_{ff}=0.26 **(b)** LomaPrieta-SC-1, PGA_{ff}=0.62 **(c)** LomaPrieta-SC-2, PGA_{ff}=0.48 and **(d)** Kobe-TAK090-1, PGA_{ff}=0.87.

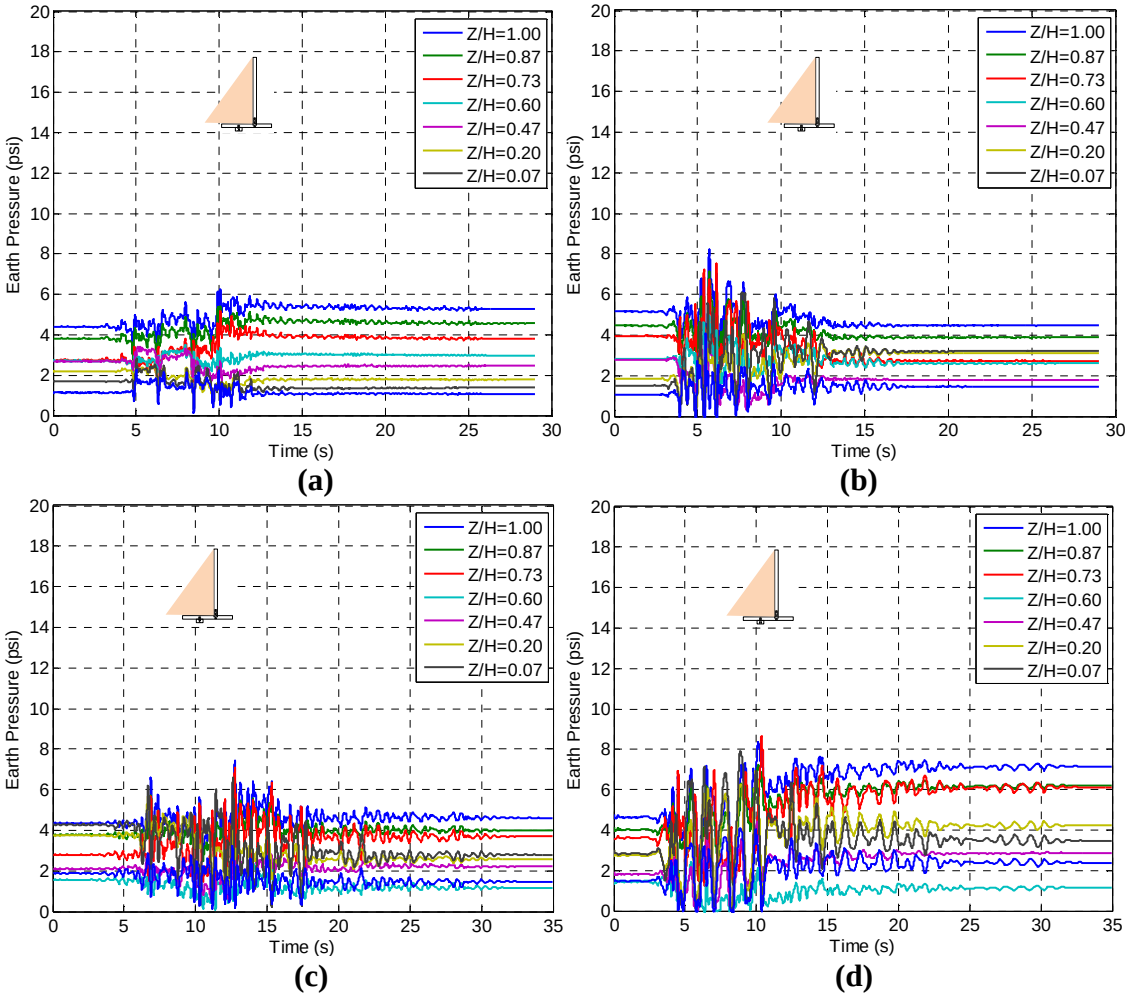

Figure 5.20. Total earth pressure time series computed by FLAC on Displacing Retaining wall during **(a)** Kocaeli-YPT330-1, PGA_{ff}=0.26 **(b)** LomaPrieta-SC-1, PGA_{ff}=0.62 **(c)** LomaPrieta-SC-2, PGA_{ff}=0.48 and **(d)** Kobe-TAK090-1, PGA_{ff}=0.87.

5.11.3. Incremental Dynamic earth pressure

Figures 5.21 – 5.23 present the incremental dynamic earth pressure time series computed by FLAC on different walls and different shaking events on ROOZ01 and ROOZ02 experiments. Total earth pressure moment estimates using the M-O (1926, 1929), Seed and Whitman (1970) and Wood (1973) methods using the free field total peak ground accelerations (PGA_{ff}) are also presented in the figures at the corresponding locations on the walls. As explained in Chapter 2, Seed and Whitman (1970) and Wood (1973) methods compute the incremental dynamic earth pressure as opposed to the M-O method which produces the total, static and dynamic, earth pressure. Therefore, Coulomb (1776) static earth pressure has been subtracted from total earth pressure given by M-O (1929) method in order to obtain the corresponding dynamic earth pressure increment.

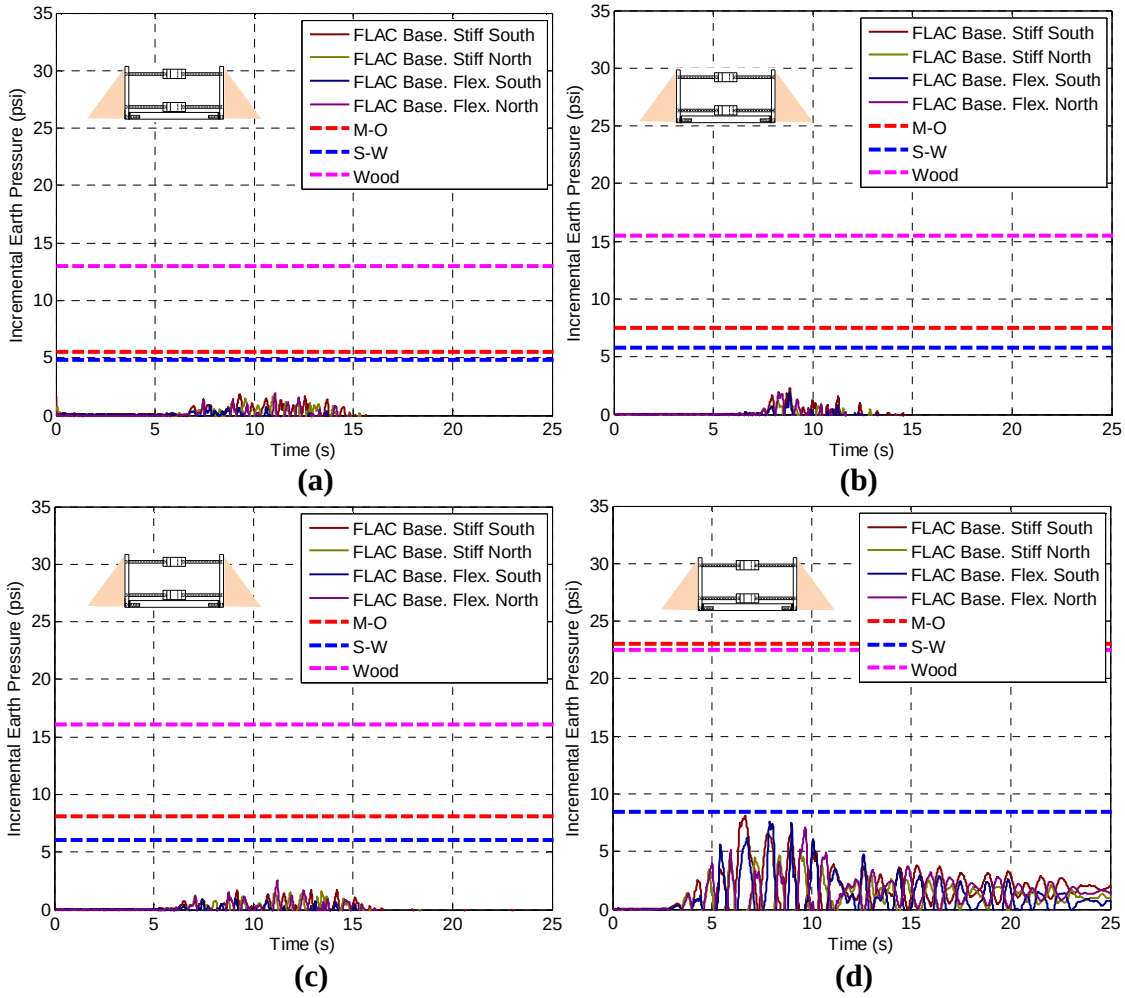

Figure 5.21. Incremental earth pressure time series computed by FLAC on South and North sides of Both Stiff and Flexible Basement wall during **(a)** Kocaeli-YPT330-2, PGA_{ff}=0.41 **(b)** Loma Prieta-WVC270-1, PGA_{ff}=0.49 **(c)** Kocaeli-YPT330-3, PGA_{ff}=0.51 and **(d)** Kobe-TAK090-2, PGA_{ff}=0.72.

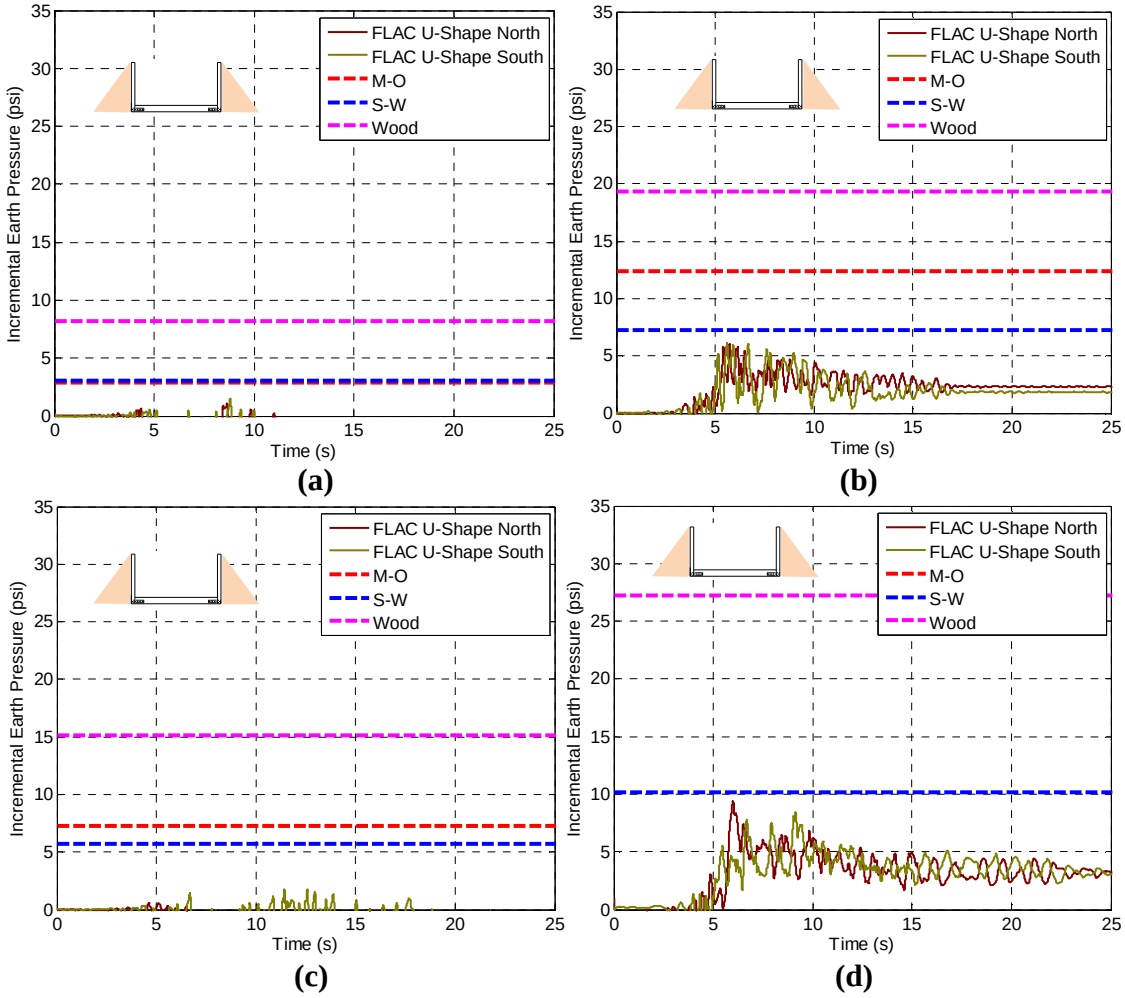

Figure 5.22. Incremental earth pressure time series computed by FLAC on Non-Displacing Cantilever wall during **(a)** Kocaeli-YPT330-1, PGA_{ff}=0.26 **(b)** LomaPrieta-SC-1, PGA_{ff}=0.62 **(c)** LomaPrieta-SC-2, PGA_{ff}=0.48 and **(d)** Kobe-TAK090-1, PGA_{ff}=0.87.

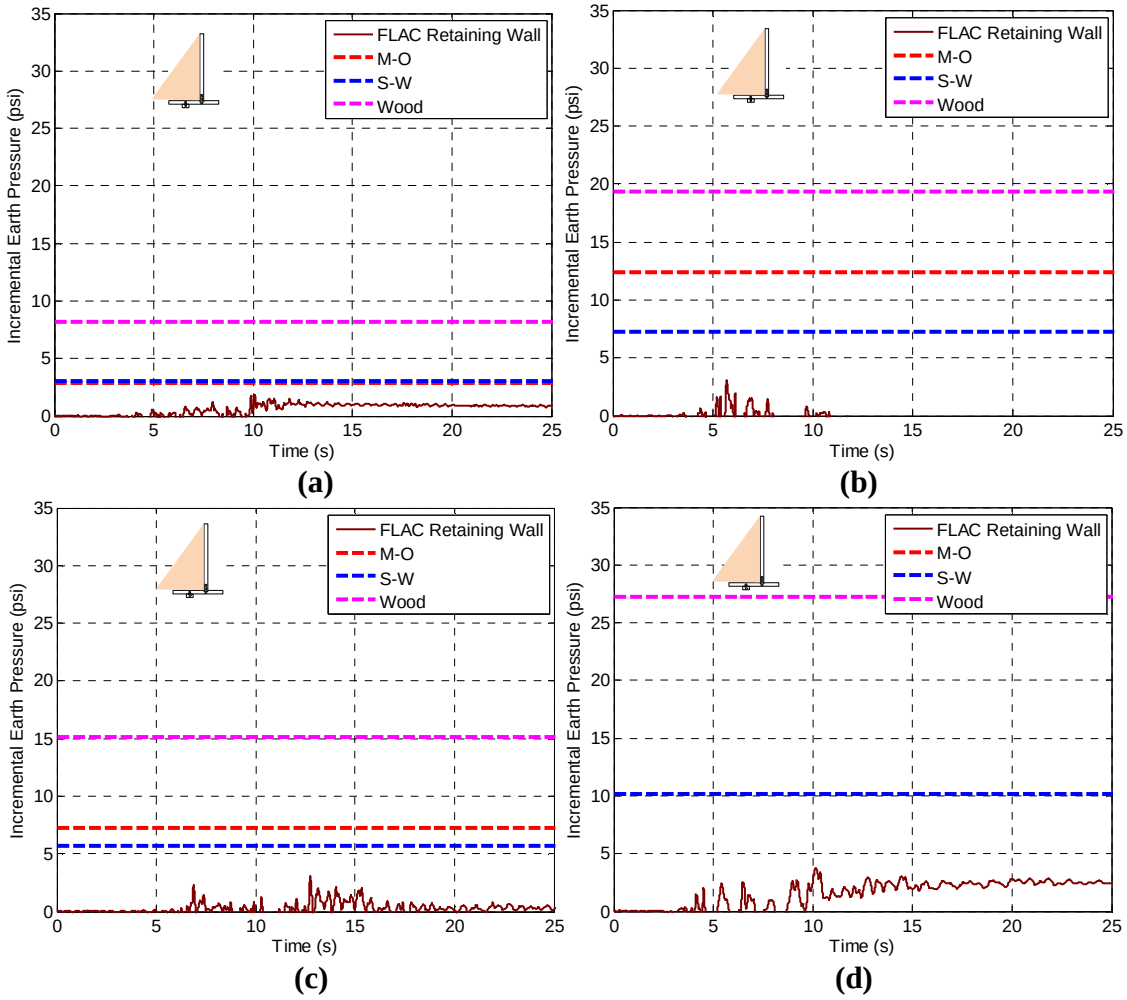

Figure 5.23. Incremental earth pressure time series computed by FLAC on Displacing Retaining wall during **(a)** Kocaeli-YPT330-1, PGA_{ff}=0.26 **(b)** LomaPrieta-SC-1, PGA_{ff}=0.62 **(c)** LomaPrieta-SC-2, PGA_{ff}=0.48 and **(d)** Kobe-TAK090-1, PGA_{ff}=0.87.

As shown in Figure 5.21 the dynamic earth pressure measured at the base of the non-displacing basement never exceed the dynamic earth pressure estimated by M-O and S-W methods. It is important to note that, theoretically, the dynamic earth pressure on non-displacing basement should be compared with the Wood method, however, as already seen the Wood solution highly overestimates the dynamic earth pressure.

Similarly, the M-O and S-W methods overestimate the dynamic earth pressure at all times for all shaking events for non-displacing cantilever and displacing retaining walls as shown in Figures 5.22 and 5.23.

Overall, the time series show that the dynamic earth pressure rarely exceed the design criteria and the maximum dynamic earth pressure are generally significantly overestimated by current design criteria.

5.12. Summary

Numerical simulations using a 2-D plane strain finite difference program, FLAC 2D, were performed to simulate the seismic earth pressure on retaining structures in centrifuge tests (ROOZ01 and ROOZ02). The UBCHyst model was used to model the behavior of the soil layers during cyclic loading. The FISH routine of UBCHYST algorithm (Byrne and Naesgaard 2010) has been converted to DLL in order to decrease the computational effort/time. The model was calibrated by comparing uniform cyclic response to response inferred from published modulus reduction and damping curves and by comparison with results of cyclic simple shear laboratory tests.

The time series plots show that the computed dynamic earth pressures generally fall well below values that would be obtained analytically using both the Seed and Whitman (1970) and the Mononobe-Okabe method and are consistent with the results of the centrifuge tests.

5.13. References

- Billaux, D. and Cundall, P. (1993). Simulation des g´eomat´eriaux par la m´ethode des ´el´ements lagrangiens. Revue Francaise de G´eotechnique, 63, 9–21.
- Byrne, P.M. and Naesgaard, E., 2010. Personal Communications.
- Cormeau, I. (1975). Numerical stability in quasi-static elasto/viscoplasticity. Int. J. Num. Methods in Engng, 9(1), 109–127.
- Coulomb, CA. "Essai sur une application des regies des maximis et minimis a quelques problemes de statique relatifs a 1'architecture," Memoires de I'Academie Royale pres Divers Savants, Vol. 7, 1776.
- Cundall, P. A., and R. D. Hart. “Numerical Modeling of Discontinua,” Engr. Comp., 9, 101-113 (1992).
- Itasca Consulting Group, Inc. (2011). FLAC (Fast Lagrangian Analysis of Continua) user's manuals, Minneapolis, MN.
- Kuhlemeyer, R. L., and J. Lysmer. “Finite Element Method Accuracy forWave Propagation Problems,” J. Soil Mech. & Foundations, Div. ASCE, 99(SM5), 421-427 (May 1973).
- Lysmer, J., et al. “FLUSH – A Computer Program for Approximate 3-D Analysis of Soil-Structure Interaction Problems,” University of California, Berkeley, Earthquake Engineering Research Center, Report No. EERC 75-30 (1975).
- Seed, HB, and Whitman, RV. "Design of Earth Retaining Structures for Dynamic Loads," ASCE Specialty Conference, Lateral Stresses in the Ground and Design of Earth Retaining Structures, Cornell Univ., Ithaca, New York, 103-147, 1970.
- Shahrour I., Rezaie. F. “An elastoplastic constitutive relation for the soil–structure interface under cyclic loading”, Comput. Geotech., 21 (1) (1997), pp. 21–39.
- MATLAB, (2010), The MathWorks Inc., Natick, Massachusetts, 7.10.0 (R2010a).
- Mononobe, N. Matsuo, M. 1929. On the determination of earth pressures during earthquakes, Proceedings, World Engineering Conference, Japan, Vol. 9.
- Okabe S. "General Theory of Earth Pressure," Journal of the Japanese Society of Civil Engineers, Tokyo, Japan, Vol. 12 , No. 1, 1926.
- Wood, JH. "Earthquake induced soil pressures on structures," PhD Thesis, California Institute of Technology, Pasadena, CA, 1973.

Chapter 6

Comparison of the Results of Centrifuge Experiments to Numerical Analyses and Existing Design Methods

The ultimate goal of this research is to develop predictive models and relationships that would be suitable for use in the design of future retaining structures. To this end the lateral earth pressures and moments observed during centrifuge experiments ROOZ01 and ROOZ02 are compared to estimates obtained using the most commonly applied dynamic earth pressure theories and with the results of numerical analyses. The combined results of experimental observation and numerical analyses are then used to develop recommendations for the seismic design of retaining structures with dry medium dense sand backfill.

6.1. Dynamic lateral earth pressures observed in centrifuge experiments

Figures 6.1, 6.2 and 6.3 are plots of the results obtained in the centrifuge experiments in terms of the normalized resultant dynamic force on the wall due to earth pressure, or dynamic earth thrust ($\Delta P_{ae}/\gamma H^2$). The curves of dynamic thrust obtained using the most common currently used analytical solutions against free field PGA are also plotted for comparison. All the data points correspond to the point of maximum measured moment on the respective structures plotted against the peak PGA.

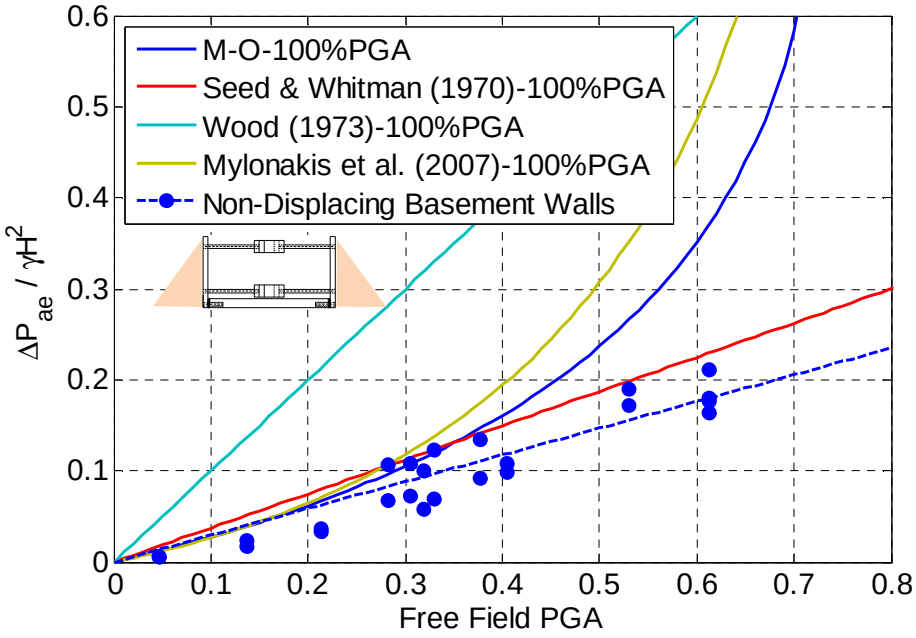

Figure 6.1. Normalized seismic earth pressure as a function of PGA for non-displacing basement structures with medium dense sand backfill.

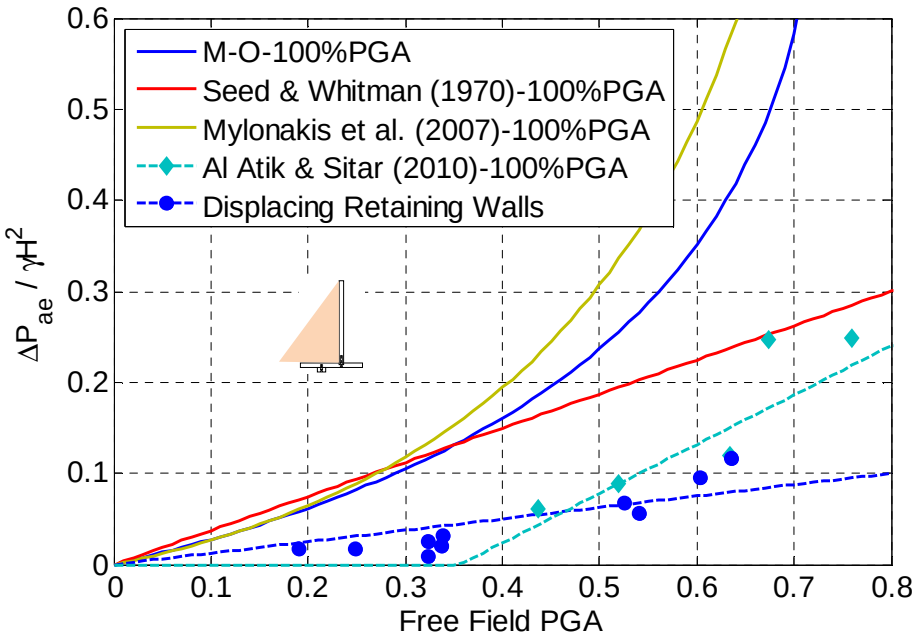

Figure 6.2. Normalized seismic earth pressure as a function of PGA for displacing retaining walls with medium dense sand backfill.

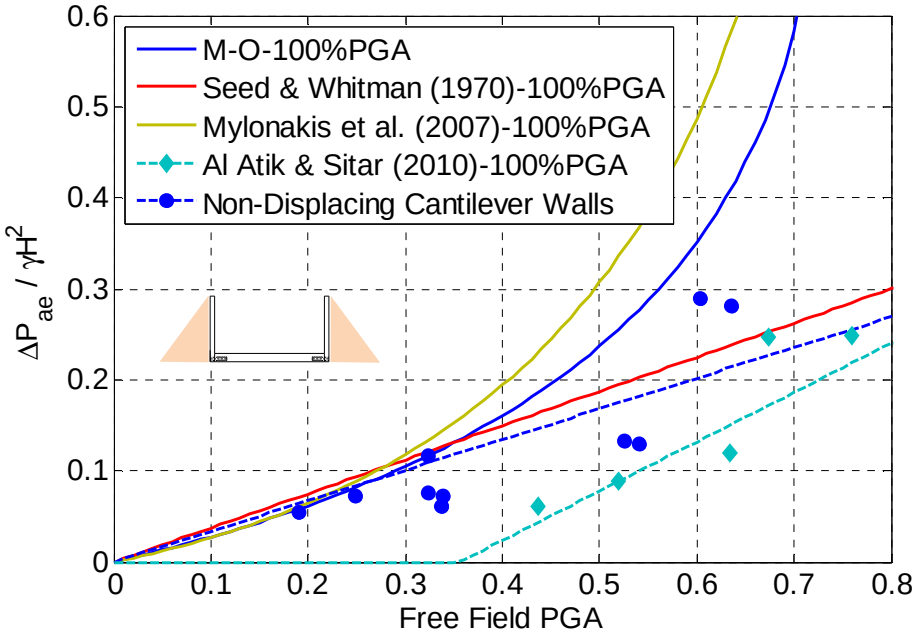

Figure 6.3. Normalized seismic earth pressure as a function of PGA for non-displacing U- shaped cantilever walls with medium dense sand backfill.

The plots show that the experimental data exhibit considerable scatter with increasing PGA and duration of the input ground motion. The scatter is particularly large for the models with the non-displacing U-shaped cantilever structures and is most likely related to a

combination of factors, including slight variations in relative density of the models and possible boundary effects that become more pronounced at higher accelerations. Therefore, additional data at high accelerations may be desirable to achieve greater level of confidence. Overall, however, the trends in the data show that the Seed and Whitman (1970) approximation, using the peak PGA, represents a reasonable upper bound for the value of the seismic earth pressure increment for both fixed base cantilever structures (U-shaped walls, Figure 6.3) and cross-braced, basement type, walls (Figure 6.1). Similarly, the envelope suggested by Al-Atik and Sitar (2010) represents a reasonable upper bound for dynamic earth pressure increment on displacing, cantilever retaining walls. In comparison, the M-O solution and the Mylonakis et al. (2007) solution are considerably higher than measured values at accelerations above about 0.4 g. The equivalent Wood (1973) seismic earth pressure, computed using the prototype structure dimensions, clearly exceeds all other results by a considerable margin, as would be expected based on the assumptions used in deriving this solution which were discussed at section 2.5.1.

The most significant difference between the analytically predicted seismic earth pressure increment and the observed data is for the free standing cantilever walls. The fact that a small amount of rotation and translation can significantly decrease the forces acting in a retaining structure have been well recognized previously (e.g. Anderson et al., 2008, Bray at al., 2010) and the data presented in Figure 6.2 clearly show this to be the case.

Finally, it is important to note that while the data from the tests on the cross-braced and U-shaped cantilever walls are quite similar, two of the data points from the tests on the U-shaped cantilever wall for the Kobe-TAK090-2 input motion plot well above the rest. This outcome is inconsistent with the conceptual notion that dynamic earth pressures on a deflecting wall should be less than those on a stiff or rigid wall. One possible explanation is that in this particular test the pressure cells were mounted on the walls closest to the walls of the container and, therefore, the high observed earth pressures are the result of interaction with the container wall. This issue deserves additional scrutiny in further studies.

6.2. Dynamic Moments

Dynamic moments are ultimately the quantities that dictate the structural design of the retaining structures. Clearly, the magnitude of the seismic earth pressure increment is very important in this regard. However, even more important is the point of application of the resultant, since the decision whether to apply the resultant at 0.6H versus 0.3H immediately changes the computed moment by a factor of about 2, as discussed at Chapter 2. The significance of this effect is illustrated in Figures 6.4-6.6 showing the normalized dynamic moment increment ($\Delta M_{ae}/\gamma H^3$) plotted against PGA for the three cases: non-displacing basement, non-displacing cantilever and displacing cantilever retaining structures. These results show that applying the moment at 0.33H, as recommended in the M-O method, gives amply conservative results over the full range of accelerations and that applying the seismic earth pressure increment at 0.6H, as recommended by Seed and Whitman (1970) and many others, leads to a significant, if not unnecessary, overdesign.

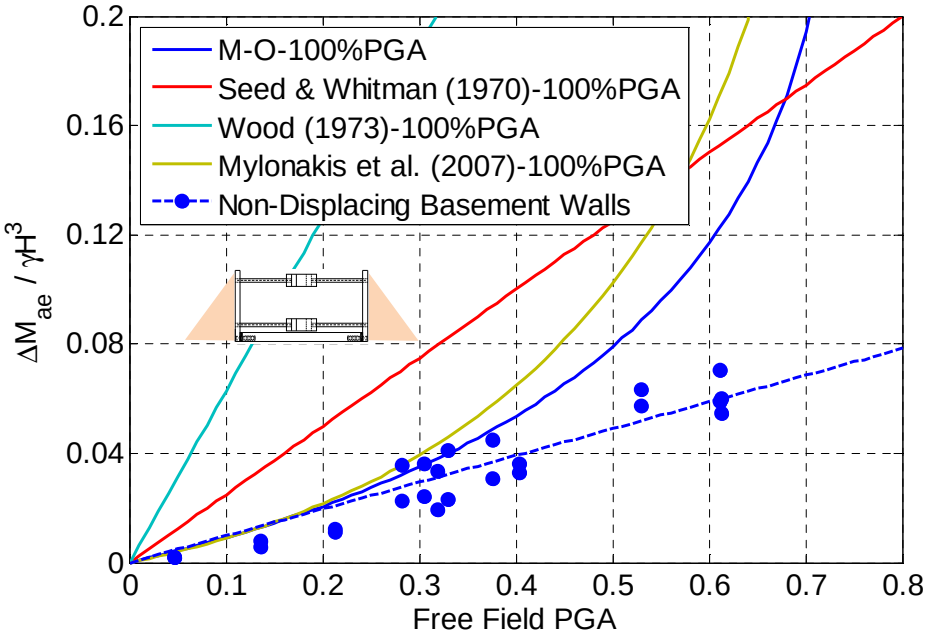

Figure 6.4. Maximum dynamic moment increment as a function of PGA for non-displacing basement structures with medium dense sand backfill.

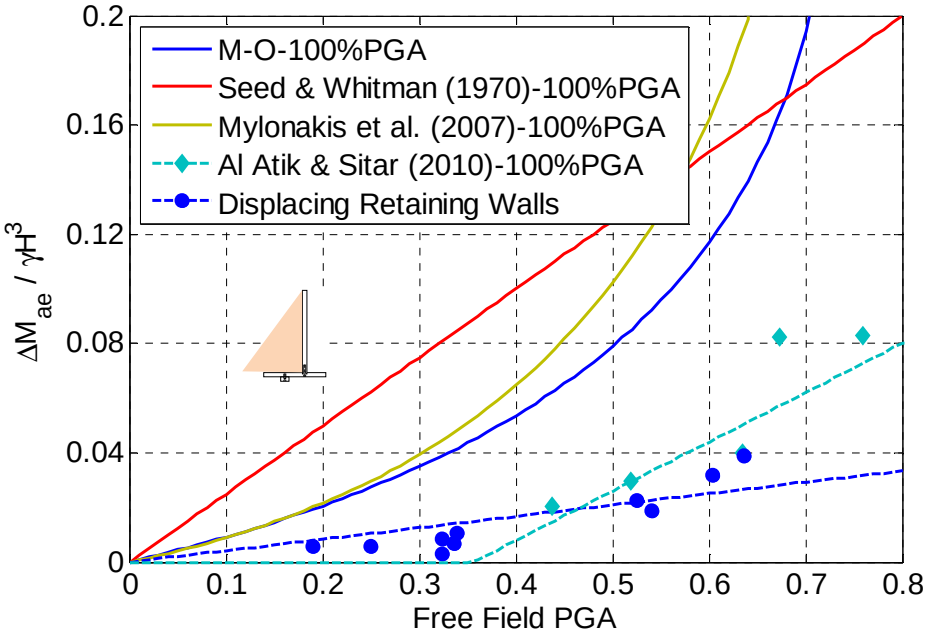

Figure 6.5. Maximum dynamic moment increment as a function of PGA for displacing retaining walls with medium dense sand backfill.

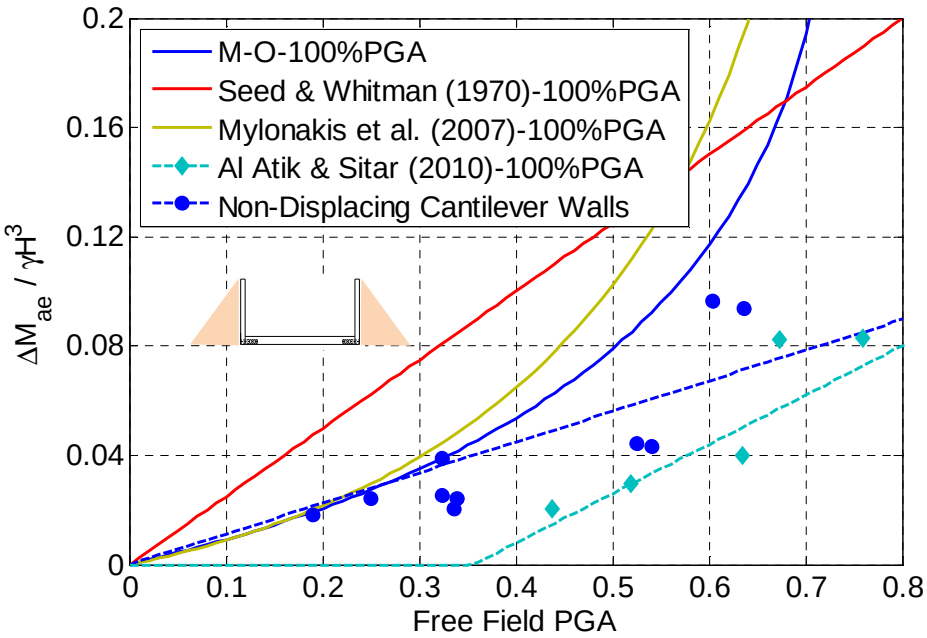

Figure 6.6. Maximum dynamic moment increment as a function of PGA for non-displacing U- shaped cantilever walls with medium dense sand backfill.

Overall, the data show that the seismic earth pressure increments increase with depth consistent with static earth pressure distribution and consistent with the M-O solution which represents the upper bound for the experimental results. In contrast, applying the dynamic earth pressure increment at 0.6H ("the inverted triangle"), as suggested by Seed and Whitman (1970), leads to a significant over estimate of the dynamic moments. These results are quite consistent with the results previously obtained by Ortiz et al. (1983), Stadler (1996) and Al-Atik and Sitar (2010).

6.3. Dynamic Earth Pressure Coefficients

The dynamic earth pressures interpreted from the strain gage and load cell measurements were used to back-calculate ΔK_{ae} for the shaking events in experiments ROOZ01 and ROOZ02. Figures 6.7-6.9 present ΔK_{ae} relationships for the non-displacing basement, non-displacing cantilever and displacing retaining walls as a function of the peak ground acceleration measured at the top of the soil in the free field. The maximum ΔK_{ae} values corresponding to maximum dynamic moment computed using the most commonly used methods are also presented in Figures 6.7-6.9 for comparison. It should be noted that using maximum ΔK_{ae} values for design purposes is over-conservative when added to the maximum wall inertial response. It is also important to note that the back calculated ΔK_{ae} values presented in Figures 6.7-6.9 do not include any factor of safety that would normally be incorporated in seismic designs.

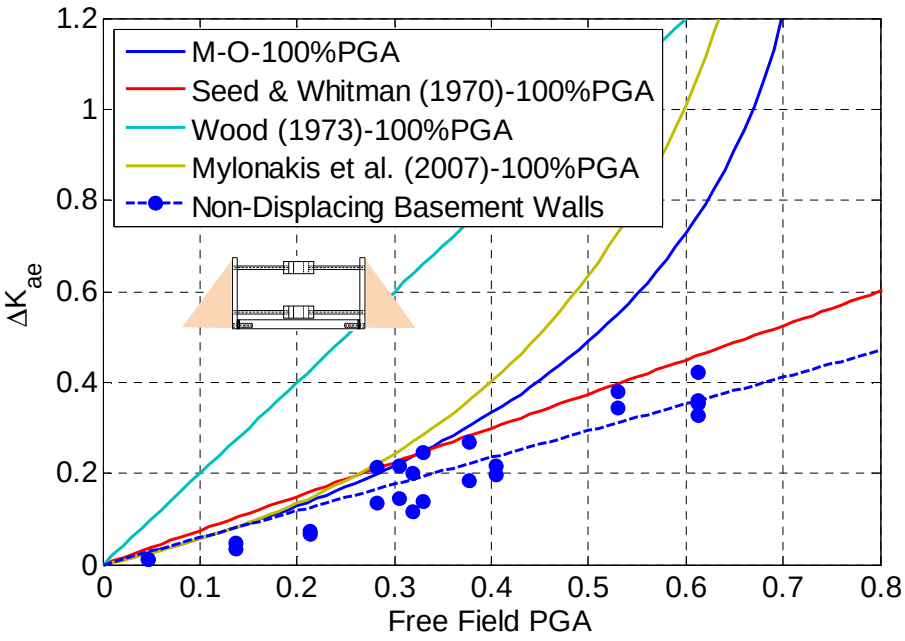

Figure 6.7. Dynamic earth pressure coefficient as a function of PGA for non-displacing basement structures with medium dense sand backfill.

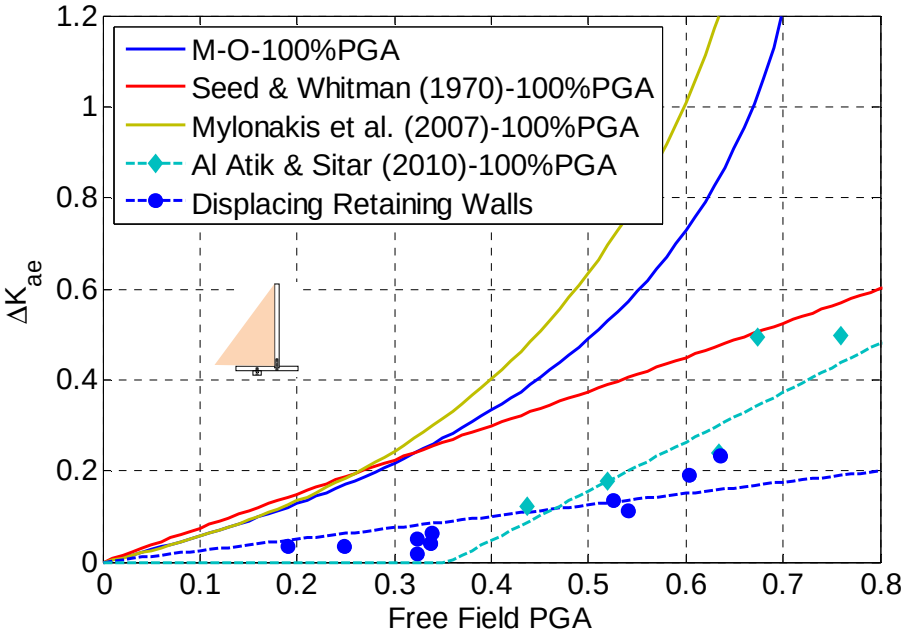

Figure 6.8. Dynamic earth pressure coefficient as a function of PGA for displacing retaining walls with medium dense sand backfill.

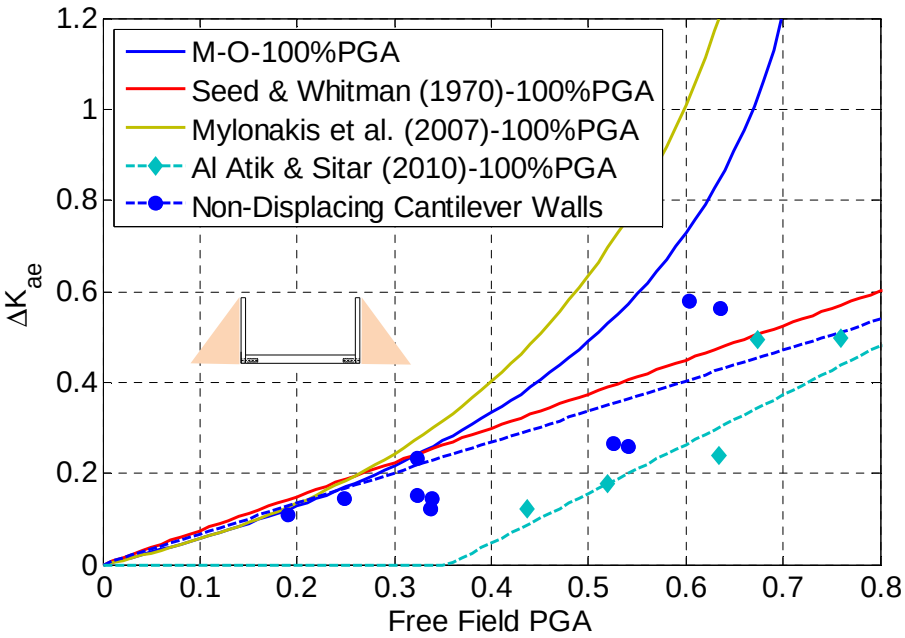

Figure 6.9. Dynamic earth pressure coefficient as a function of PGA for non-displacing U- shaped cantilever walls with medium dense sand backfill.

6.4. Effect of Static Factor of Safety

In accordance with allowable static lateral earth pressure, it is common practice to calculate the design capacity (allowable earth pressure) of a retaining wall by applying a factor of safety (FS) to the ultimate static force. The purpose of the FS is to incorporate the effect of various factors including but not limited to variability of the soil, lack of confidence in developing input parameters such as soil properties, construction control, and limitation of the method used for estimating ultimate capacity. Design and allowable capacity of retaining wall can be calculated by:

$$Q_{allowable} = \frac{Q_{ult}}{FS} \tag{6.1}$$

The Coulomb lateral earth pressure theory gives the resultant static force acting on the retaining wall as (allowable capacity):

$$P_{Static} = \frac{1}{2} K_h \gamma H^2 \tag{6.2}$$

where:
P_{Static} = Lateral static earth pressure
K_h = Lateral earth pressure coefficient
γ = Unit weight of soil
H = Depth from ground surface

The value of K_h used for design depends on the soil properties and the displacement of the structure (i.e., whether soil loading is at-rest, active or passive). So the design capacity can be expressed as below:

$$Q_{ult} = \left(\frac{1}{2} K_h \gamma H^2\right) \times FS \tag{6.3}$$

The above equation can be rewritten to reflect the design load with factor of safety of one (FS=1) and an additional design load due to the added margin of safety:

$$Q_{ult} = \left(\frac{1}{2} K_h \gamma H^2\right) + \left(\frac{1}{2} K_h \gamma H^2\right) \times (FS - 1) \tag{6.4}$$

Typically, a factor of safety on the order of 1.5 is used for the lateral load, depending on the level of confidence in the geotechnical design. In general, however, the overall factor of safety is higher due to accumulation of factors of safety at different stages of design (i.e. structural design) and, therefore, significantly exceeds 1.5.

The second term of equation 6.4 can be interpreted in terms of the dynamic earth pressure increment, as suggested by Seed and Whitman (1970) and it is plotted versus free field PGA for both non-displacing and displacing structures in Figures 6.10-6.12. These plots show that at PGA values less that 0.3 the dynamic earth pressure increment does not exceed the static design capacity for a design with a static factor of safety of 1.5 for both non-displacing basement walls and for non-displacing U-shaped cantilever structures. This effect is even more pronounced for free standing cantilever structures.

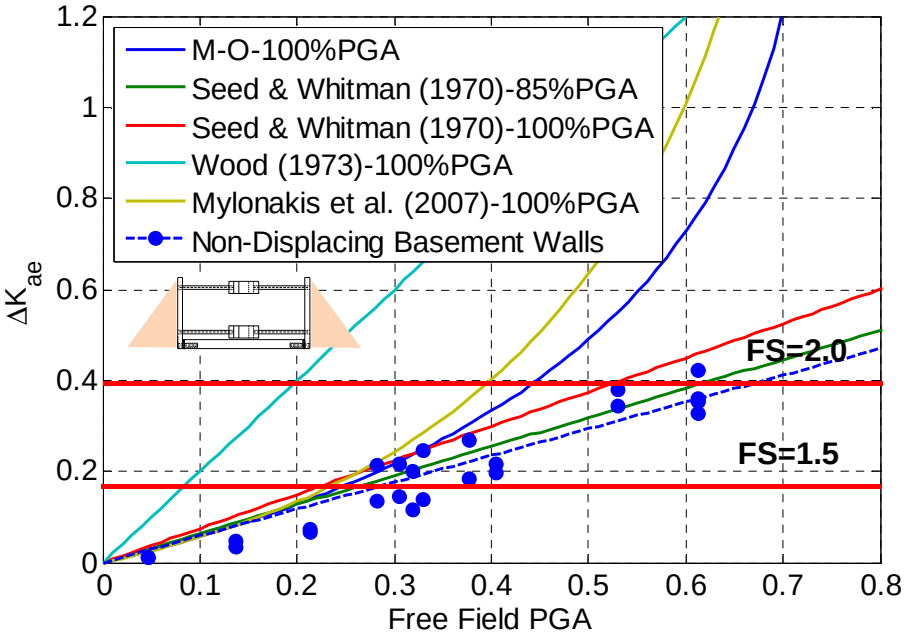

Figure 6.10. Dynamic earth pressure coefficient as a function of PGA for non-displacing basement structures with medium dense sand backfill.

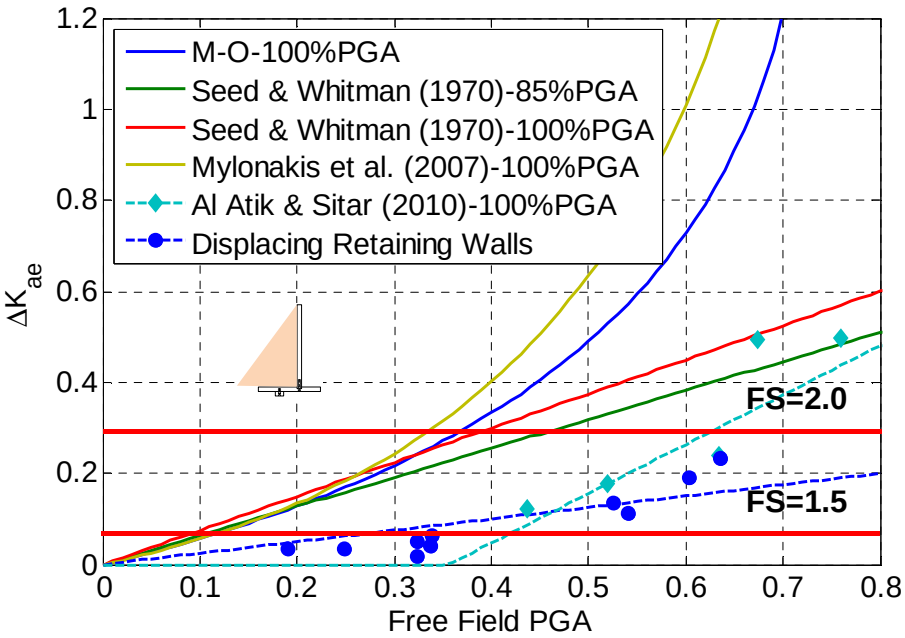

Figure 6.11. Dynamic earth pressure coefficient as a function of PGA for displacing retaining walls with medium dense sand backfill.

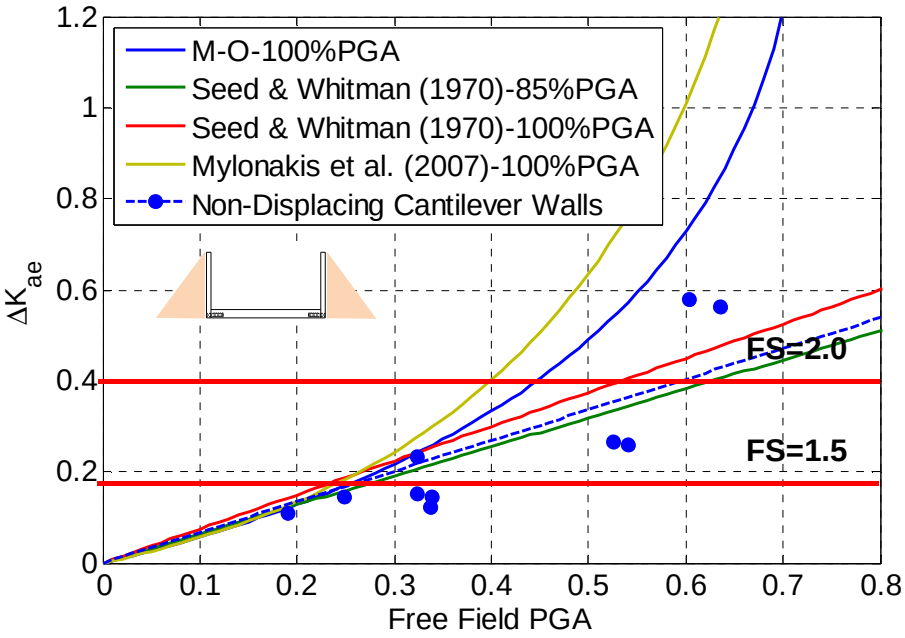

Figure 6.12. Dynamic earth pressure coefficient as a function of PGA for non-displacing U- shaped cantilever walls with medium dense sand backfill.

Similar conclusions were reached by Seed and Whitman (1970) who observed that a wall designed to a reasonable static factor of safety should be able to resist seismic loads up of 0.3 g. This is consistent with the observations and analyses performed by Clough and Fragaszy (1977)

and Al-Atik and Sitar (2010), who concluded that conventionally designed cantilever walls with granular backfill could be expected to resist seismic loads at accelerations up to 0.4 g.
Finally, there is also a question which acceleration quantity should be used in the analyses. Seed and Whitman (1970) suggested the use of 0.85 PGA to represent the multiple cycles of loading during an earthquake. More recently, NEHRP (FEMA 750) guidelines suggested that PGA be used in the Seed and Whitman type analysis. The results presented herein show that the using the PGA leads to a reasonable upper bound for non-displacing U-shaped and cross-braced structures. The use of 0.85 PGA, on the other hand, essentially matches the mean dynamic earth pressure increment observed in the experiments. In the case of displacing cantilever walls, the dynamic earth pressure increment is significantly smaller and corresponds to 0.35 PGA in the Seed and Whitman (1970) analysis.

6.5. Dynamic Wall Deflections in the Centrifuge Tests

As discussed in Chapter 2, the minimum active pressure which can be exerted against a wall occurs when the wall moves sufficiently far outwards for the soil behind the wall to expand laterally and reach a state of plastic equilibrium. The amount of movement necessary to reach these conditions is dependent primarily on the type of backfill material (seeTable 6.1). Figure 6.13 shows the typical variation in wall pressure with movement. For a rigid wall, free to translate or rotate about its base, the active or passive condition occurs if sufficient movement can take place, and the pressure distribution remains approximately triangular for uniform sloping ground.

Table 6.1. Wall displacements required to develop active and passive earth pressures (after Canadian geotechnical society 1992).

Soil type and condition	Rotation, Y/H	
	Active	Passive
Dense cohesionless	0.001	0.02
Loose cohesionless	0.004	0.06
Stiff cohesive	0.010	0.02
Soft cohesive	0.020	0.04

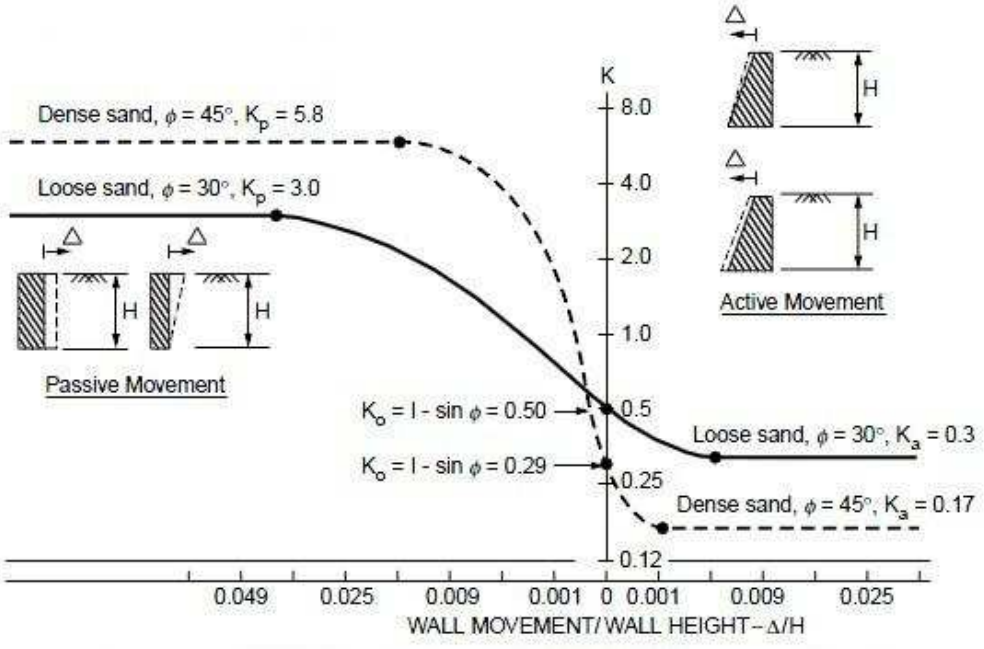

Figure 6.13. Effect of wall movement on earth pressure.

Figures 6.14 and 6.15 show the rigid body translation and transient deflection of the both non-displacing cantilever and displacing retaining walls derived from LVDT and strain gage measurements in the experiments.

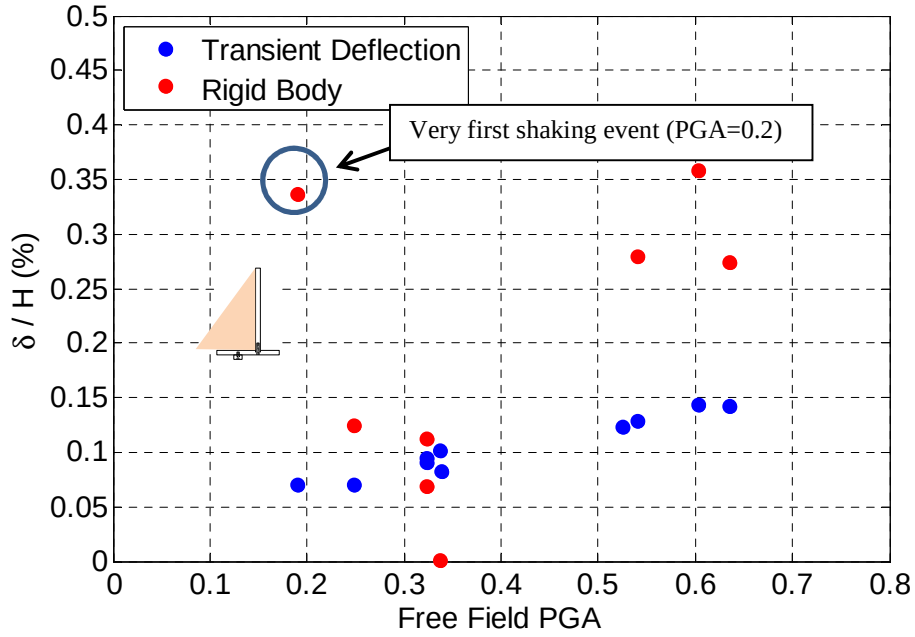

Figure 6.14. Transient deflection and rigid body translation of displacing cantilever wall.

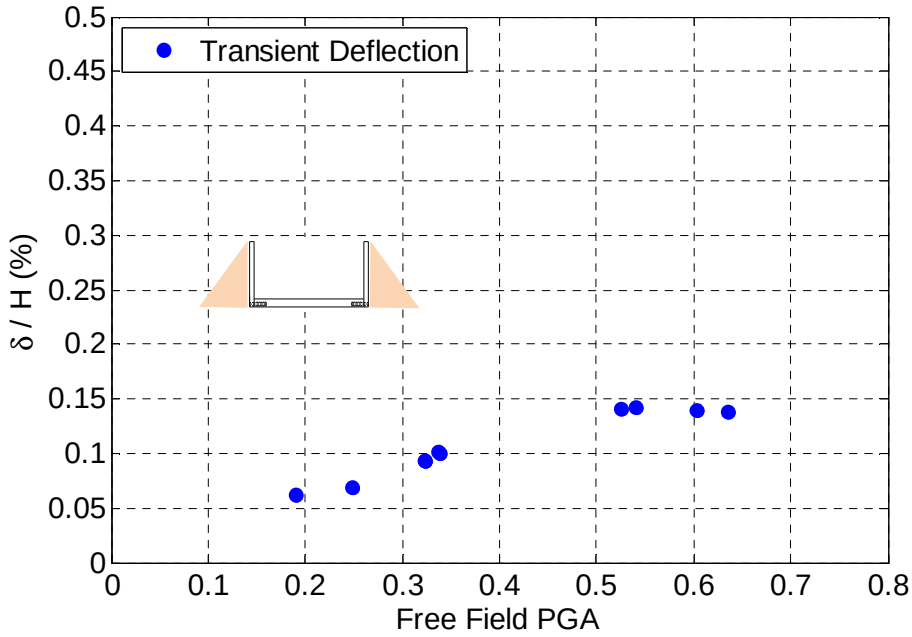

Figure 6.15. Transient deflection of non-displacing retaining wall.

As can be seen, the transient deflection measured by strain gages passed the necessary displacement (i.e. 0.001H) to produce active earth pressure after 0.3 free field PGA. In case of non-displacing cantilever wall the rigid body translation is slightly scattered as opposed to transient deflection. It is important to note that in Figure 6.14 the first data point in rigid body given at 0.2 PGA happens to be for the first shaking event in which the sand was not yet densified due to shaking. As a result the rigid body transient is estimated to be so high, but other than that both transient and rigid body translation increases with increasing free field PGA, as shown in Figures 6.14 and 6.15.

6.6. Comparison of Dynamic Earth Pressure Coefficients from Centrifuge and FLAC

The dynamic earth pressure coefficients calculated from FLAC were used to back-calculate ΔK_{ae} for the shaking events and plotted in the same graph as described in section 6.3. Figures 6.16 through 6.18 present ΔK_{ae} relationships for the non-displacing basement, non-displacing cantilever and displacing retaining walls as a function of the peak ground acceleration measured at the top of the soil in the free field.

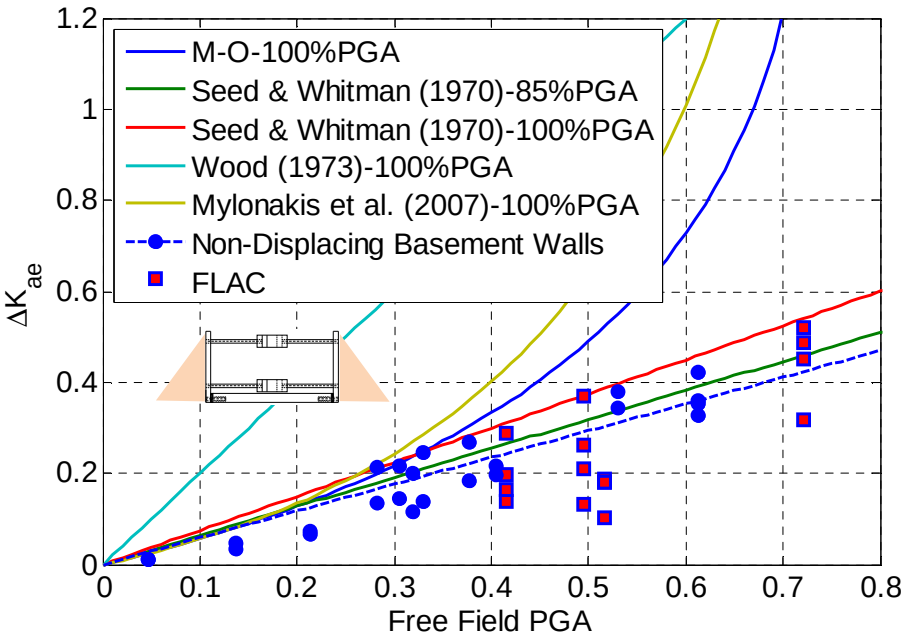

Figure 6.16. Dynamic earth pressure coefficient as a function of PGA for non-displacing basement structures with medium dense sand backfill.

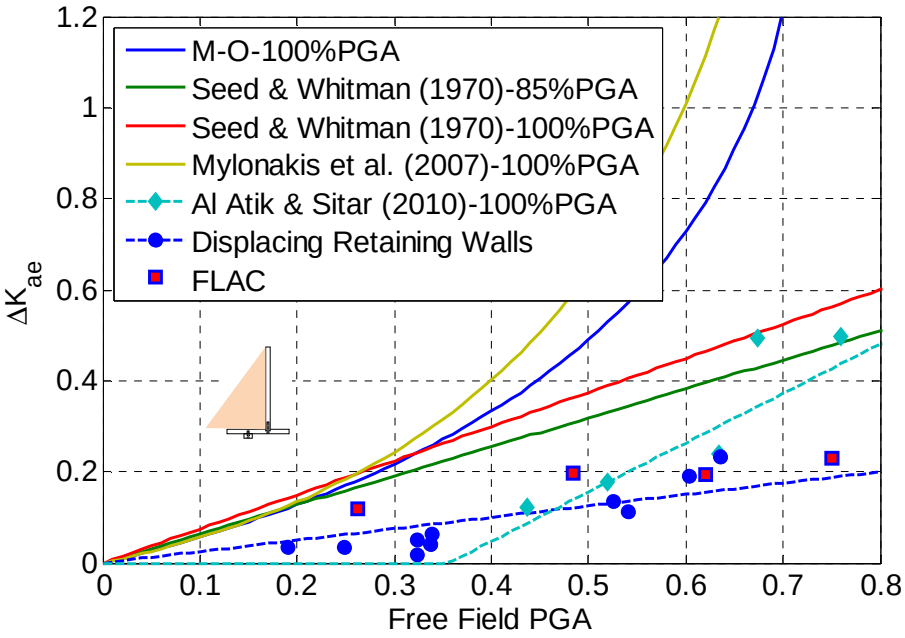

Figure 6.17. Dynamic earth pressure coefficient as a function of PGA for displacing retaining walls with medium dense sand backfill.

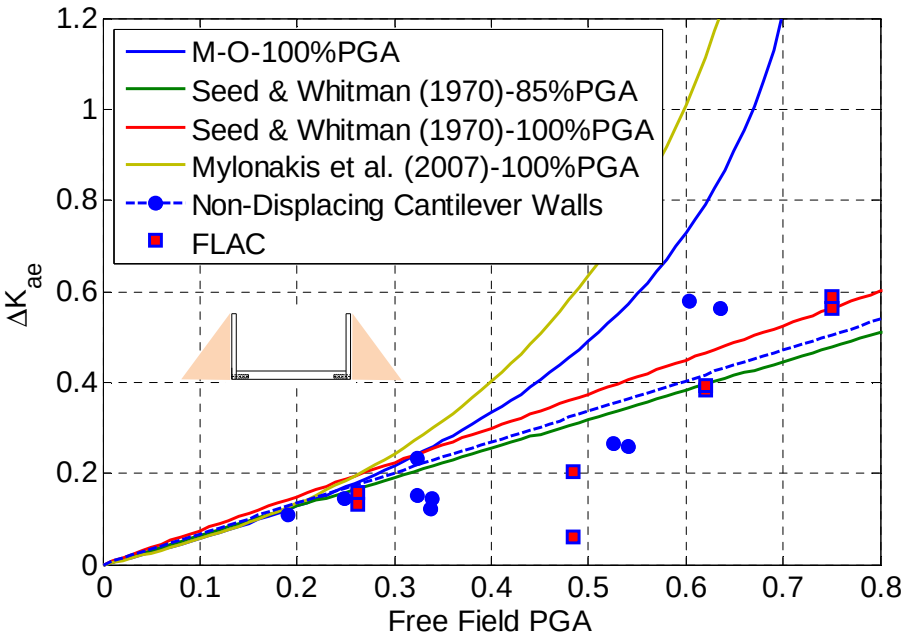

Figure 6.18. Dynamic earth pressure coefficient as a function of PGA for non-displacing U- shaped cantilever walls with medium dense sand backfill.

As shown in Section 5.11.2, the total earth pressure profiles calculated from numerical analysis, consistently increase monotonically downward in the manner that is typically observed and assumed under static conditions. Therefore, the point of application of the incremental dynamic earth pressure in retaining wall was estimated to be at 0.3H.

Although overall there was a good agreement between the dynamic earth pressure coefficient calculated using FLAC and the data given by centrifuge test, there is still some scatter in the data from the numerical analyses and the match is not perfect. The differences between the numerical results and the centrifuge experiments may be attributable to the fact that UBCHyst is a simple constitutive model that does not fully capture the dynamic behavior of cohesionless material such as densification due to shaking. In addition, a linear interface element used in this study may not be able to capture the nonlinearity of soil-structure interaction. Overall, however, the numerical models captured the observed static and dynamic behavior quite satisfactorily.

6.7. Summary

The overall trends in the incremental dynamic earth pressure data show that the Seed and Whitman (1970) approximation using PGA represents a reasonable upper bound for the value of the seismic earth pressure increment for both fixed base cantilever structures (U-shaped walls) and cross-braced, basement type, walls. In comparison, the M-O solution and the Mylonakis et al. (2007) solutions are considerably higher than measured values at accelerations above about 0.4 g. The equivalent Wood (1973) seismic earth pressure, computed using the prototype structure dimensions, clearly exceeds all other results by a considerable margin, as would be expected based on the assumptions used in deriving this solution , as discussed in section 2.5.1.

The data also show that the seismic earth pressure increments increase with depth consistent with static earth pressure distribution and consistent with that implicit in the M-O solution which forms the upper bound for the experimental results. The Seed and Whitman (1970) solution with PGA produces a reasonable upper bound over a range of experimental results for both non-displacing cantilever and for cross-braced U-shaped structures. The use of 0.85 PGA in the same analysis produces values very close to the mean of the experimental data. In contrast, the dynamic earth pressure increment on free standing cantilever walls are significantly smaller and correspond to using 0.35 PGA in the Seed and Whitman approximation. These results are quite consistent with the results previously obtained by Ortiz et al. (1983), Stadler (1996) and Al-Atik and Sitar (2010). The experimental and analytical results also show that applying the moment at 0.33H, as recommended in the M-O method, gives amply conservative results over the full range of accelerations and that applying the seismic earth pressure increment at 0.6H, as recommended by Seed and Whitman (1970) and many others, leads to a significant overestimate.

Moreover, at PGA values less that 0.3 the dynamic earth pressure increment does not exceed the static design capacity for a design with a static factor of safety of 1.5 for both non-displacing basement walls and for non-displacing U-shaped cantilever structures. This effect is even more pronounced for free standing cantilever structures. Similar conclusions were reached by Seed and Whitman (1970) who observed that a wall designed to a reasonable static factor of safety should be able to resist seismic loads up of 0.3 g. These results are consistent with the observations and analyses performed by Clough and Fragaszy (1977) and Al-Atik and Sitar (2010), who concluded that conventionally designed cantilever walls with granular backfill could be expected to resist seismic loads at accelerations up to 0.4 g.

Finally, the results of numerical modeling using FLAC were quite consistent with the data obtained from the centrifuge experiments. These results demonstrate that numerical models are quite capable of capturing the observed response within the level of accuracy sufficient for typical design.

6.8. References

- Al-Atik, L. and Sitar, N. (2010), "Seismic Earth Pressures on Cantilever Retaining Structures," Journal of Geotechnical and Geoenvironmental Engineering, October, (136) 10, pp. 1324-1333.
- Anderson, D.G., Martin, G.R., Lam, I.P. and Wang, J.N. (2008). "Seismic Design and Analysis of Retaining Walls, Buried Structures, Slopes and Embankments", *NCHRP Report 611. Transportation Research Board, National Cooperative Highway Research Program*, Washington, D.C.
- Bray, J.D., Travasarou, T. and Zupan, J. (2010). "Seismic Displacement Design of Earth Retaining Structures," Earth Retention Conference, ER 2010, ASCE, Seattle, pp. 638-655.
- Canadian Foundation Engineering Manual (1992) Third Edition, Canadian Geotechnical Society. Technical Committee on Foundations, BiTech Publishers Ltd.
- Clough, G.W. and Fragaszy, R.F. (1977). "A Study of Earth Loadings on Floodway Retaining Structures in the 1971 San Fernando Valley Earthquake," Proceedings of the Sixth World Conference on Earthquake Engineering, Vol. 3.
- Mylonakis, G., Kloukinas, P. and Papatonopoulos, C. (2007). "An Alternative to the Mononobe-Okabe Equation for Seismic Earth Pressures", Soil Dyn. and Earthquake Eng., (27) 10, 957-969.
- Seed, H.B. and Whitman, R.V. (1970). "Design of Earth Retaining Structures for Dynamic Loads," ASCE Specialty Conference, Lateral Stresses in the Ground and Design of Earth Retaining Structures, Cornell Univ., Ithaca, New York, 103–147.
- Wood, J.H. (1973). "Earthquake Induced Soil Pressures on Structures," PhD Thesis, California Institute of Technology, Pasadena, CA.

Chapter 7

Conclusions and Recommendations

The research contained in this dissertation was composed of two parts: (1) physical modeling of seismically induced earth pressure on retaining structures and braced wall using centrifuge tests, and (2) numerical modeling of these centrifuge tests. Specifically, two sets of centrifuge experiments were performed on scaled model U-shaped cantilever, free-standing cantilever and braced walls with medium dense sand backfill. The retaining structures were densely instrumented with accelerometers, pressure transducers and strain gauges, and subjected to a series of shaking events. The recorded data were then used to obtain dynamic moment, pressure, strain and displacement distributions (static, dynamic) for the different structures.

The centrifuge experiments results and observations were then used to develop and calibrate two-dimensional finite difference, FLAC^{2D}, models. The purpose of the numerical analysis of this study was to evaluate the ability of FD models to capture the essential features and response characteristics of the retaining wall-backfill system under seismic loading.

7.1. Seismic Earth Pressure Distribution

The centrifuge data consistently showed that for the height of structures considered herein, i.e. in the range of 20-30 ft, the maximum dynamic earth pressures increase with depth and can be reasonably approximated by triangular distribution analogous to that used to represent static earth pressures. This result is contrary to the assumption made by Seed and Whitman (1970), which based their approach on the experimental work of Matsuo (1941) and other similar type of experiments. Matsuo's experiments were on dry, relatively loose sand in a rigid shaking table container up to 6 ft deep. While these experiments were performed meticulously and were pioneering in their scope at the time, they cannot be simply scaled to capture the response of taller structures. More importantly, the observed amplification of ground motion and the observed increase in earth pressure upwards appear to be a direct result of the physical layout of the geometry of the shaking table box and properties of the sand. In that sense, Matsuo's results are correct for the given geometry and material and are directly applicable to walls up to 6 ft in height with relatively loose granular backfill.

7.2.Seismic Earth Pressure Magnitude and Factor of Safety

A very significant aspect of the data obtained in this work is the relationship between the magnitude of the seismic earth pressure increment and the corresponding ground motion. The data show (Figures 6.11-6.13) that overall, the Seed and Whitman (1970) approximation to the Mononobe-Okabe solution provides a reasonable upper bound for the observed data when using peak PGA for non-displacing cantilever and cross-braced, stiff, structures in level ground. Alternatively, representing the ground motion time history by 0.85 PGA, as suggested by Seed and Whitman (1970), gives a solution that closely matches the mean trends in the data. In comparison to the structures with limited ability to rotate and with a fixed base, free-standing cantilever walls experience a much lower dynamic earth pressures corresponding to about 0.35 PGA.

Another important aspect of the results presented herein is the observation that stiff, embedded structures do not seem to experience substantial increase in seismic earth pressure over that experienced by cantilever structures with fixed base. In this regard, the centrifuge experiment data shows that the Wood (1973) solution for a rigid structure on a rigid foundation is not representative of the most common conditions and unnecessarily overestimates the actual earth pressure by a very large factor.

An important issue in seismic design is the consideration of the inherent capacity of a structure to resist seismic loads. The results presented in Section 6.4. and Figures 6.10-6.12 suggest that non-displacing U-shaped cantilever and cross-braced structures tested perform well at accelerations up to 0.3 g, if designed for a static factor of safety of at least 1.5. Similar conclusions and recommendations were made by Seed and Whitman (1970). Their approach assumed that a wall designed to a reasonable static factor of safety should be able to resist seismic loads up 0.3 g. In the present study, experimental data suggest that seismic loads up to and even slightly over 0.4 g could be resisted by cantilever walls designed to a factor of safety of at least 1.5. These observations are consistent with the observations and analyses performed by Clough and Fragaszy (1977) and Fragaszy and Clough (1980) and Al-Atik and Sitar (2010) who concluded that conventionally designed cantilever walls with granular backfill could be reasonably expected to resist seismic loads at accelerations up to 0.4 g.

7.3.Dynamic Moments on Retaining Walls

As discussed in Section 6.2, the dynamic moments measured by the strain gages and in the centrifuge experiments represent the combined effects of both dynamic earth pressures and wall inertial forces. An important contribution to the overall dynamic wall moments is the mass of the wall itself as pointed out by Richards and Elms (1979 and 1980) in their recommendation for the seismic design of gravity walls. Al-Atik and Sitar (2010) similarly concluded that the inertial forces should not be neglected. They recommended that the dynamic earth pressures and wall inertial effects on the wall moments should be estimated separately and this conclusion is supported by the results presented herein. Current results show that the wall inertial moments contribution to the overall dynamic wall moments should be accounted for separately and superimposed.

As already discussed above, the dynamic earth pressure is increasing with depth and earth pressure distribution can be reasonably approximated by triangular distribution. This suggests that the point of application of the resultant force of the dynamic earth pressure increment is around 0.33H above the base of the wall. The most direct impact of the recognition that the point of application of the seismic earth pressure increment can be reasonably placed at 0.33H is the reduction in the computed design moments for the structure as shown in Figure 7.1.

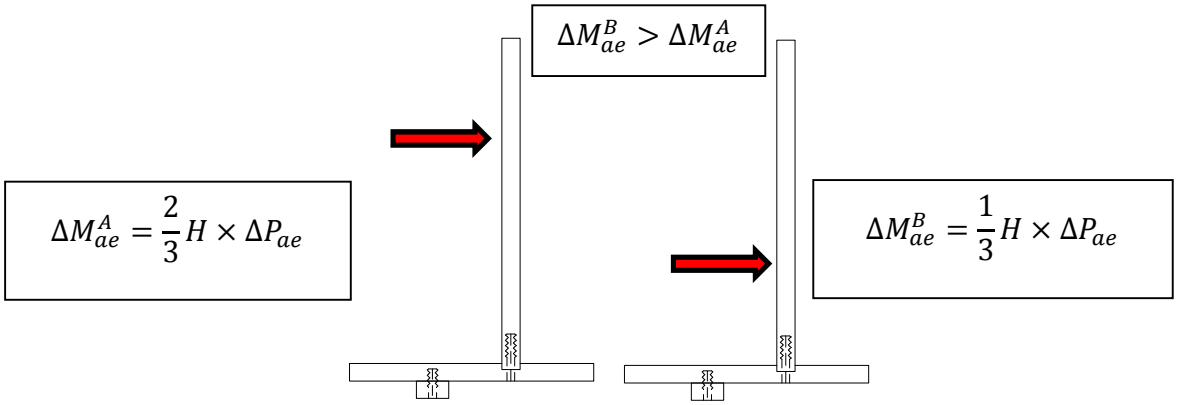

Figure 7.1. Effect of point of application of the seismic earth pressure increment on dynamic moment of retaining walls.

7.4.Numerical Modeling Results

Numerical simulation using a finite difference program, FLAC^{2D}, was performed to simulate the seismically induced earth pressure on retaining structures centrifuge. The UBCHyst Sand model was used to model the behavior of the medium dense dry sand during cyclic loading.

The FD model was calibrated and evaluated against a set of centrifuge results for four shaking events from each series of experiments. Computed and centrifuge recorded results consisting of acceleration, response spectra, bending moments, earth pressures time series were compared. Despite the simplifications and inherent limitations in the model, as well as the uncertainties in the input parameters, computed results show that, the FD analysis is able to capture reasonably well the essential system responses observed in the centrifuge experiments.

However, calibrating the FD model with real data is essential for the validation of the computed results. Results from the FD model are sensitive to input soil properties and constitutive models used. Therefore, the reliability of analytical seismic earth pressures and moment results is subject to having reliable estimates of soil properties, good soil constitutive models that are able to capture the nonlinear soil response under seismic loading and a set of experimental or field data for the calibration of the model.

7.5.Limitations and Recommendations for Future Work

From the information acquired from the experimental tests, the following limitations and recommendations can be made.

1. As shown in Table 3.1, the dynamic frequency is scaling up with N, scaling factor, which means an earthquake with maximum frequency of 25 Hz is going to have N×25 Hz frequency in the centrifuge world. So in order to monitor the dynamic response of a structure in the centrifuge, instruments with high level of frequency response range are essential. As shown in Table 3.3 the Tactilus earth pressure transducers have a nominal frequency response maximum of 100 Hz. This frequency response is sufficient for sampling static earth pressures, but unfortunately is likely under sampling the dynamic

earth pressures. Therefore, in this study, the earth pressure transducers were used to identify behavioral trends and to support measurements made by gages such as load cells and strain gages which respond in a higher frequency range. Pressure transducers with higher frequency response are clearly desirable, if not essential; in future studies that include earth pressure measurements.

2. The current experimental study has been conducted on retaining walls in the range of 20-30 ft in prototype scale and further experimental studies are needed on walls with different heights to study the effect of fundamental frequency on dynamic earth pressures and moments.
3. The results of the centrifuge experiments and FD modeling presented herein are limited to retaining structures with dry medium dense sand backfill and level ground surface.
4. The data presented in this study clearly show an approximate triangular distribution of seismic earth pressures increasing with depth, and it would appear reasonable to consider the point of application of the resultant seismic force on cantilever retaining walls at 0.33H above the base of the wall.
5. The numerical simulations were generally capable of reproducing the primary features of the observed responses in the four tests, including dynamic earth pressure as well as earth pressure distribution, although there were some differences between the computed and observed results. Some of these differences between measurement and prediction were likely due to three-dimensional effects in the centrifuge model as discussed by Lai et al (2002). Therefore, three dimensional analyses are recommended to evaluate fully this effect.
6. There is also need to develop a more accurate constitutive model that can handle change on shear strength due to densification and dynamic frequency.
7. One of the challenges in the evaluation of the experimental data and in the numerical modeling is the evaluation of the influence of the container response on the observed behavior. In future experiment the rings of the container and the soil adjacent to the ring should be instrumented in the direction of the shaking in order to better constrain the boundary effects as shown in Figure 7.2.

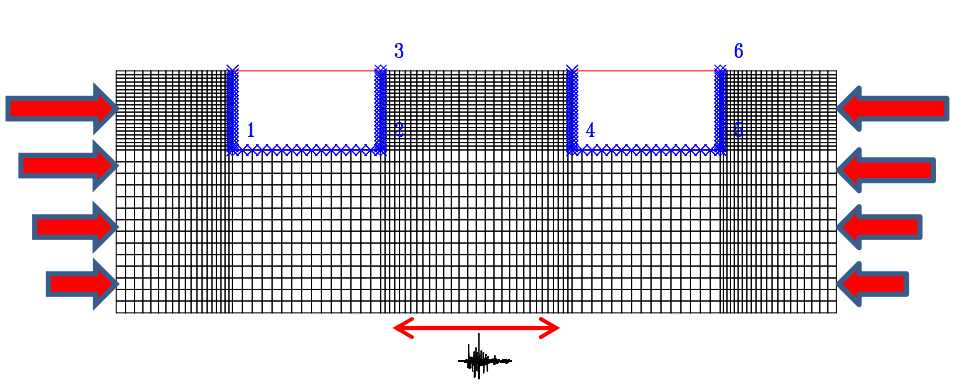

Figure 7.2. Schematic of the proposed mesh and boundary treatment to reduce the uncertainty due to the container behavior during shaking.

8. Finally, field instrumentation of a variety of retaining structures should be undertaken in a systematic manner. The data from such instrumented structures would be an invaluable

resource in improving our understanding of the behavior of prototype structures and, hence, improve our ability to arrive at the safe and economic designs.

7.6.References

- Al-Atik, L. and N. Sitar, 2010. Seismic Earth Pressures on Cantilever Retaining Structures, Journal of Geotechnical and Geoenvironmental Engineering, Vol. 136, No. 10, pp. 1324-1333, doi: 10.1061/(ASCE)GT.1943-5606.0000351.
- Clough, GW, and Fragaszy, RF. "A study of earth loadings on floodway retaining structures in the 1971 San Fernando Valley earthquake," Proceedings of the Sixth World Conference on Earthquake Engineering, Vol. 3, 1977.
- Fragaszy, RF, and Clough, GW. "Seismic Behavior of Gravity Retaining Walls - Discussion," Journal of the Geotechnical Engineering Division, ASCE, 106 (GT6), 734-735, 1980.
- Lai, T., Elgamal, A., Wilson, D.W. and Kutter B.L. (2002). “Three-dimensional Modeling for Site Seismic Response in Laminated and Rigid Centrifuge Containers,” Int. Conf. on Physical Modeling in Geotechnics, Canada, July 10-12.
- Matsuo, H. "Experimental Study on the Distribution of Earth Pressures Acting on a Vertical Wall during Earthquakes," Journal of the Japanese Society of Civil Engineers, Vol. 27, No. 2, 1941.
- Mononobe, N, and Matsuo M. "On the Determination of Earth Pressures during Earthquakes," Proceedings, World Engineering Congress, Vol. 9, 179-187, 1929. Okabe S. "General Theory of Earth Pressure," Journal of the Japanese Society of Civil Engineers, Tokyo, Japan, Vol. 12 , No. 1, 1926.
- Seed, HB, and Whitman, RV. "Design of Earth Retaining Structures for Dynamic Loads," ASCE Specialty Conference, Lateral Stresses in the Ground and Design of Earth Retaining Structures, Cornell Univ., Ithaca, New York, 103-147, 1970.
- Richards, R, and Elms, DG. "Seismic Behavior of Gravity Retaining Walls," Journal of the Geotechnical Engineering Division, ASCE, 105, (GT4), 449-64, 1979.
- Richards, R, and Elms, DG. "Seismic Behavior of Gravity Retaining Walls - Closure," Journal of the Geotechnical Engineering Division, ASCE, 106 (GT6), 737-738, 1980.

Appendix A

Figures

APPENDIX A

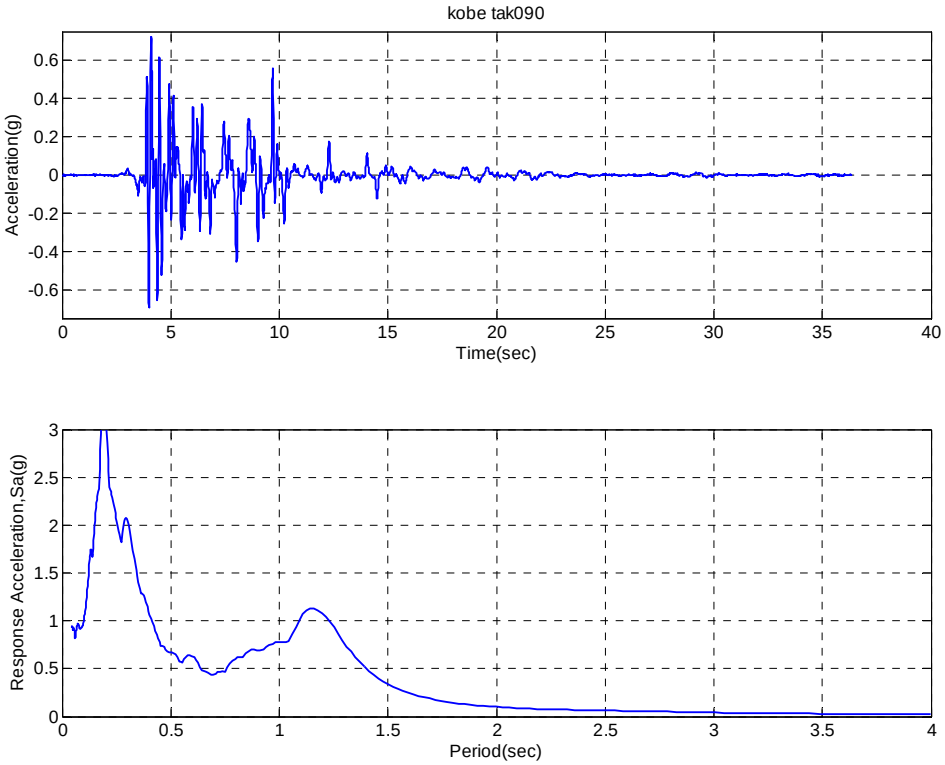

Figure A.1. Horizontal acceleration, response spectrum (5% damping) of Kobe-TAK090-1 input ground motion for ROOZ01.

APPENDIX A

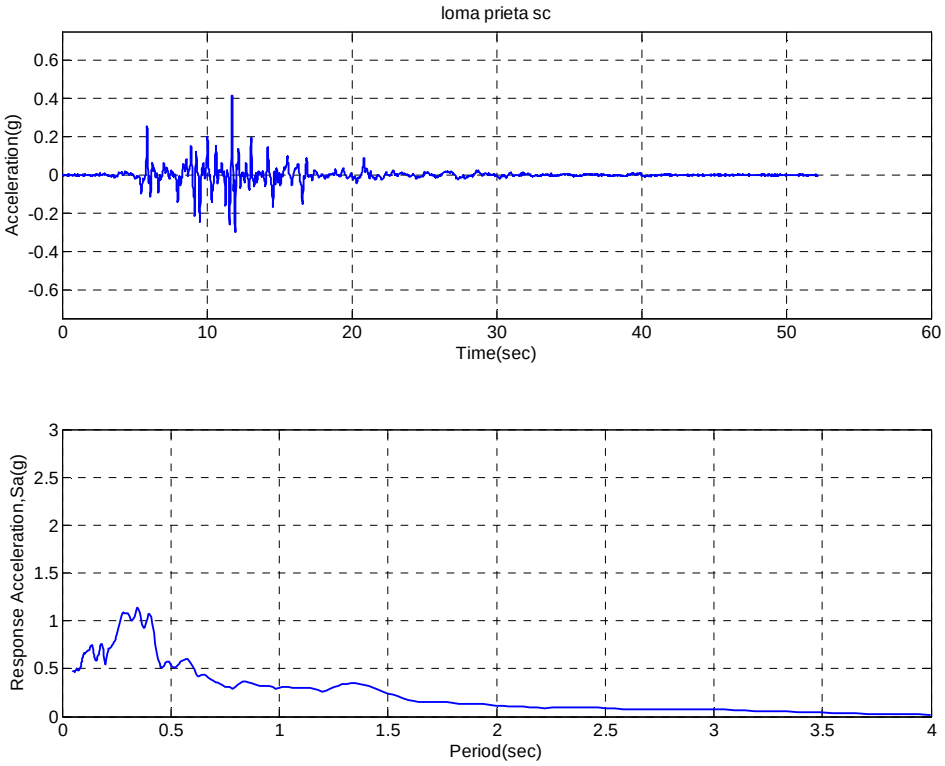

Figure A.2. Horizontal acceleration, response spectrum (5% damping) of Loma Prieta-SC-1 input ground motion for ROOZ01.

APPENDIX A

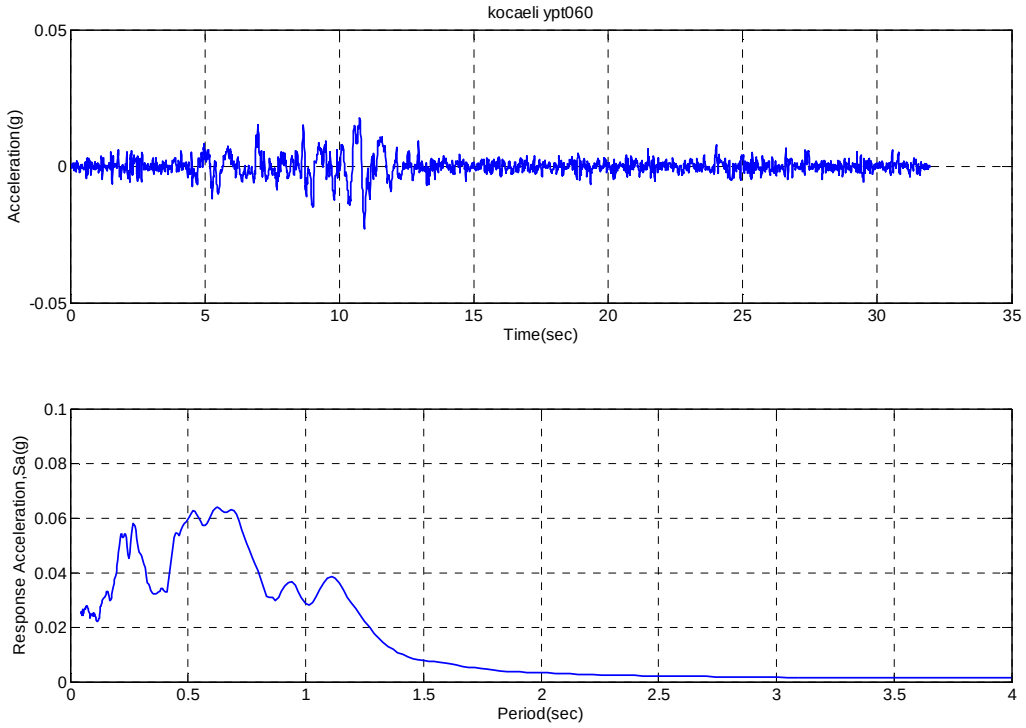

Figure A.3. Horizontal acceleration, response spectrum (5% damping) of Kocaeli-YPT060-1 input ground motion for ROOZ01.

APPENDIX A

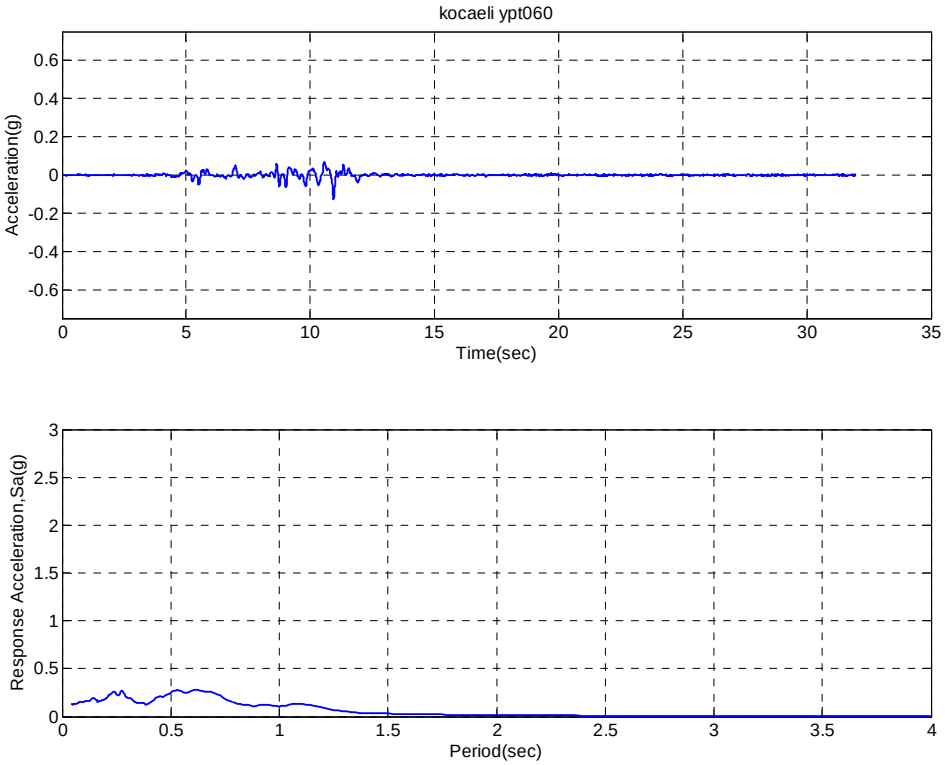

Figure A.4. Horizontal acceleration, response spectrum (5% damping) of Kocaeli-YPT060-2 input ground motion for ROOZ01.

APPENDIX A

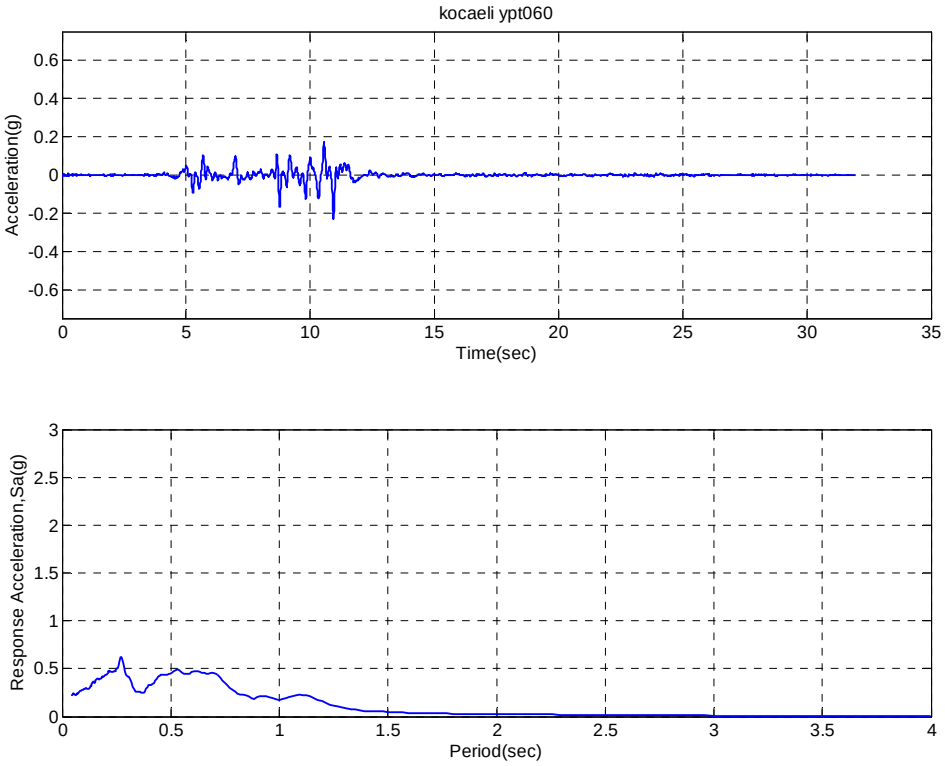

Figure A.5. Horizontal acceleration, response spectrum (5% damping) of Kocaeli-YPT060-3 input ground motion for ROOZ01.

APPENDIX A

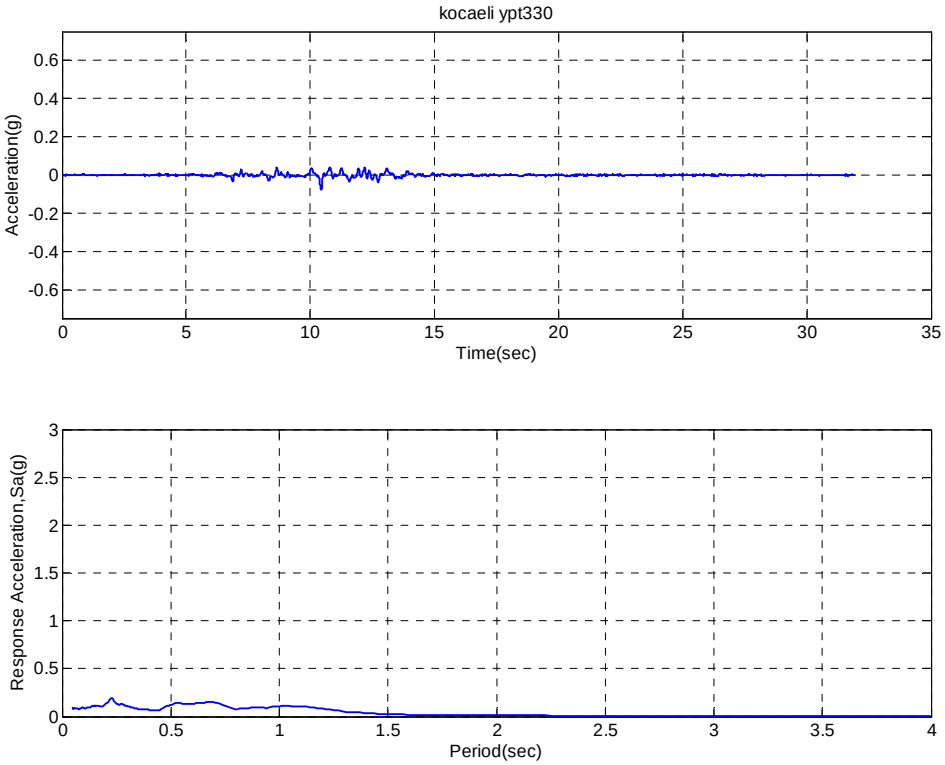

Figure A.6. Horizontal acceleration, response spectrum (5% damping) of Kocaeli-YPT330-1 input ground motion for ROOZ01.

APPENDIX A

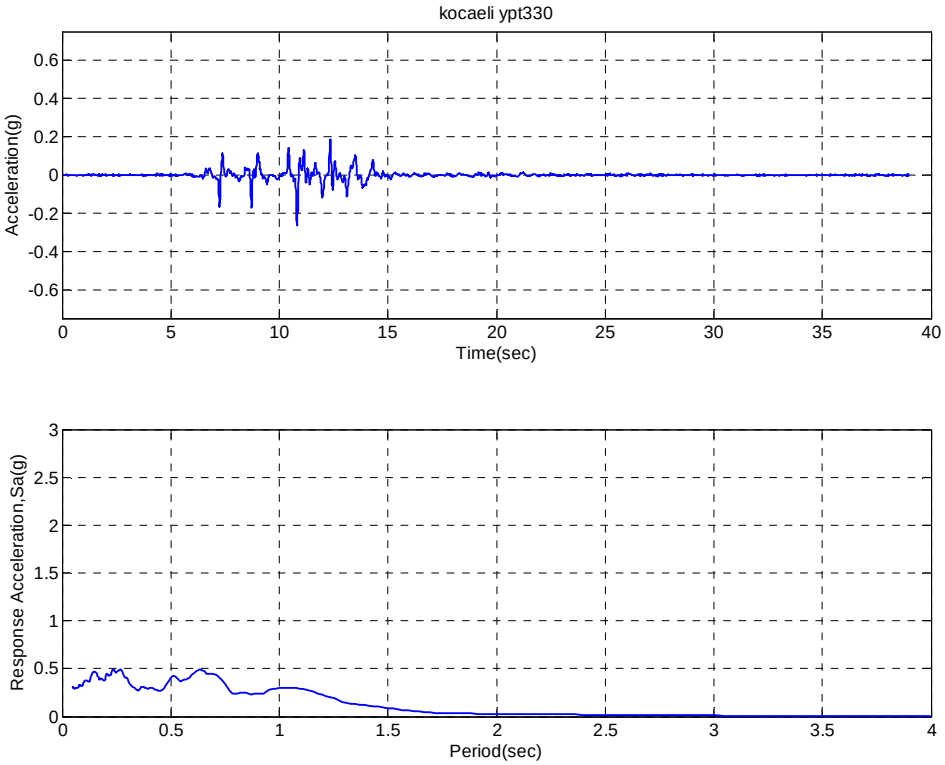

Figure A.7. Horizontal acceleration, response spectrum (5% damping) of Kocaeli-YPT330-2 input ground motion for ROOZ01.

APPENDIX A

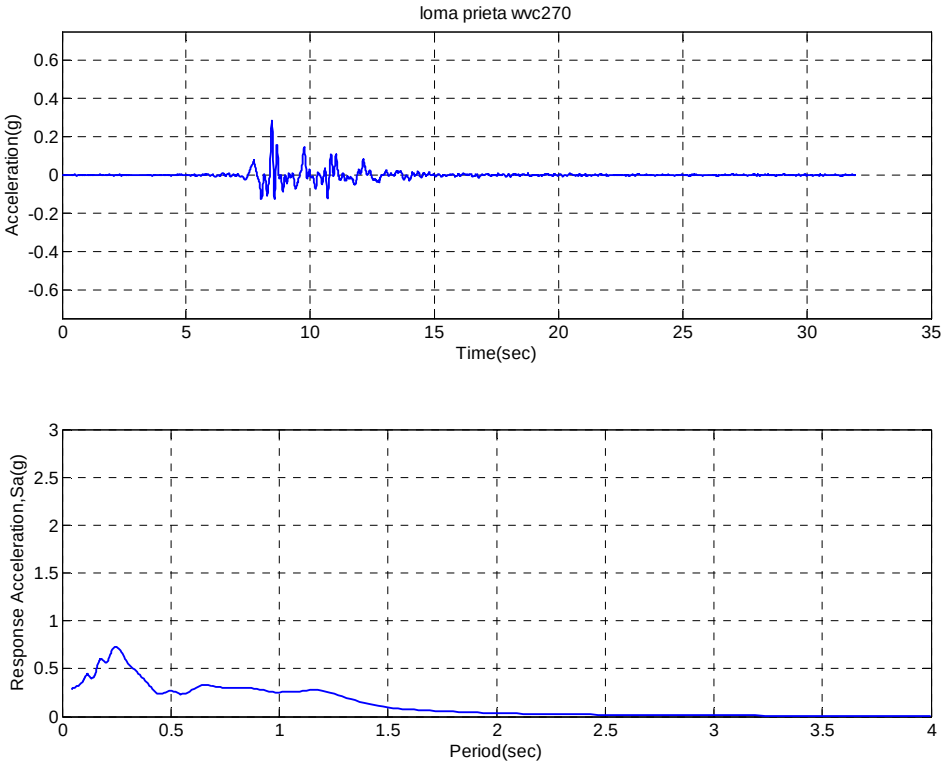

Figure A.8. Horizontal acceleration, response spectrum (5% damping) of Loma Prieta-WVC270-1 input ground motion for ROOZ01.

APPENDIX A

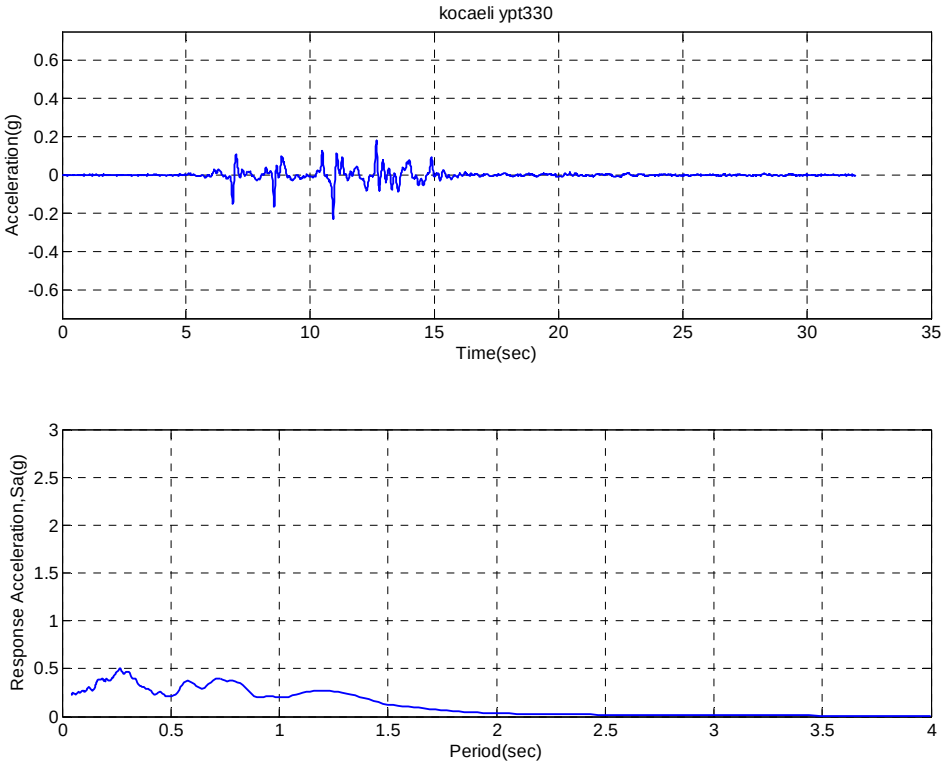

Figure A.9. Horizontal acceleration, response spectrum (5% damping) of Kocaeli-YPT330-3 input ground motion for ROOZ01.

APPENDIX A

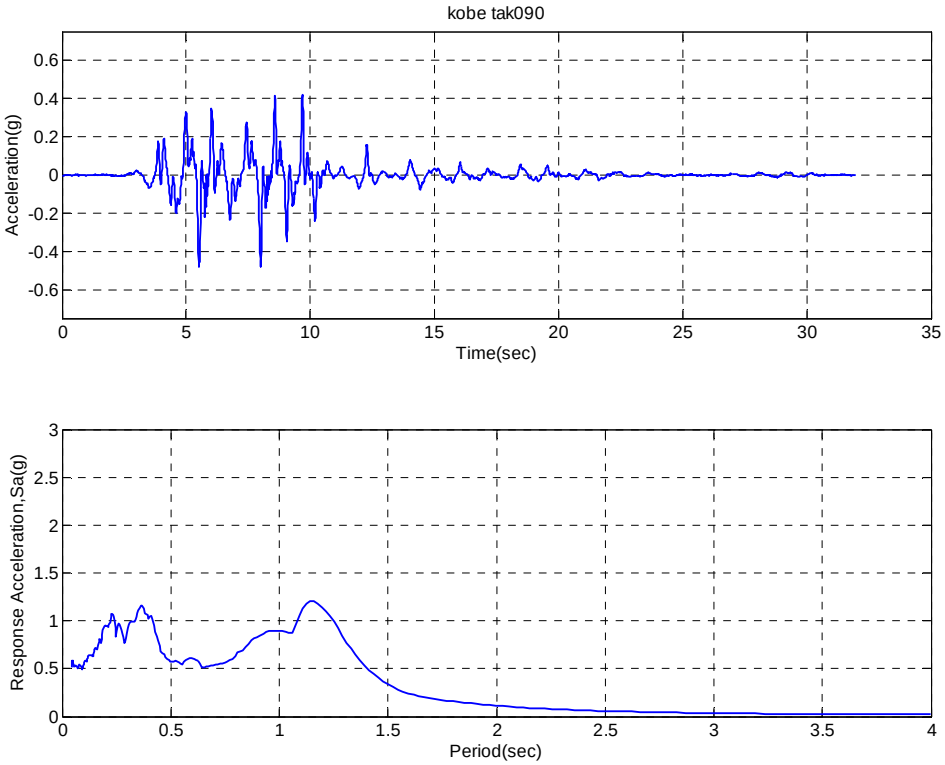

Figure A.10. Horizontal acceleration, response spectrum (5% damping) of Kobe-TAK090-2 input ground motion for ROOZ01.

APPENDIX A

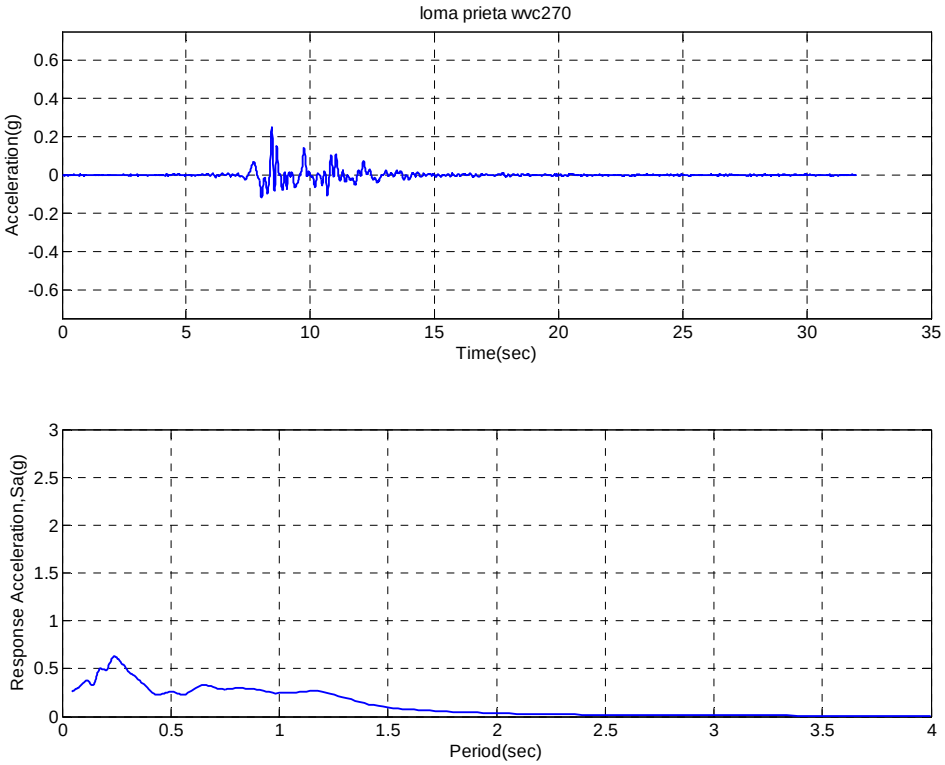

Figure A.11. Horizontal acceleration, response spectrum (5% damping) of Loma Prieta-WVC270-2 input ground motion for ROOZ01.

APPENDIX A

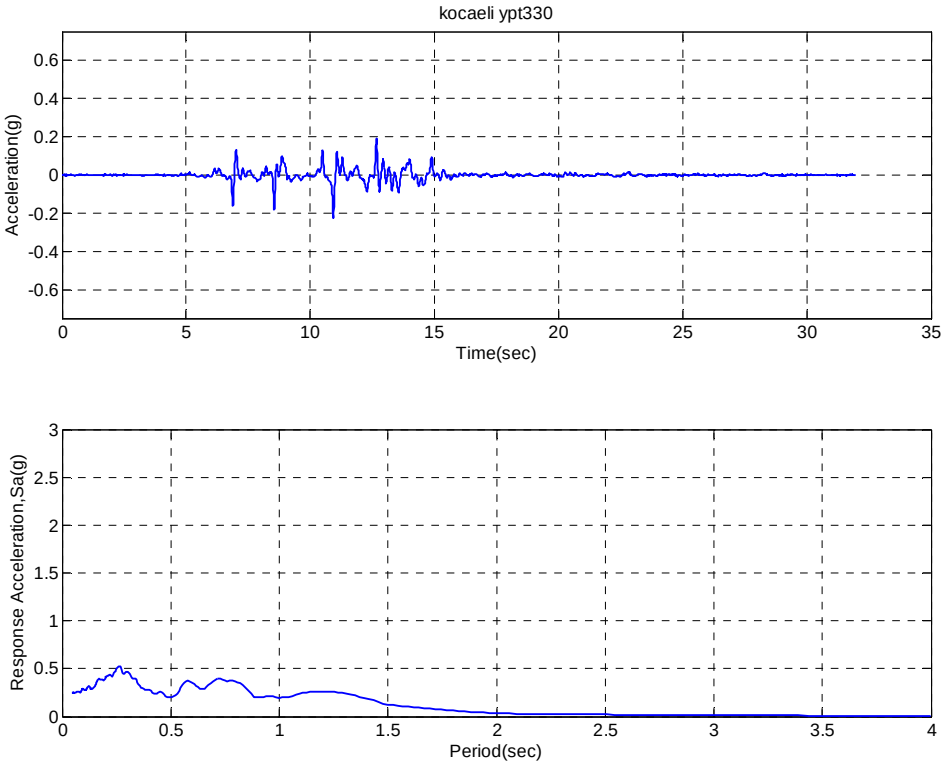

Figure A.12. Horizontal acceleration, response spectrum (5% damping) of Kocaeli-YPT330-3 input ground motion for ROOZ01.

APPENDIX A

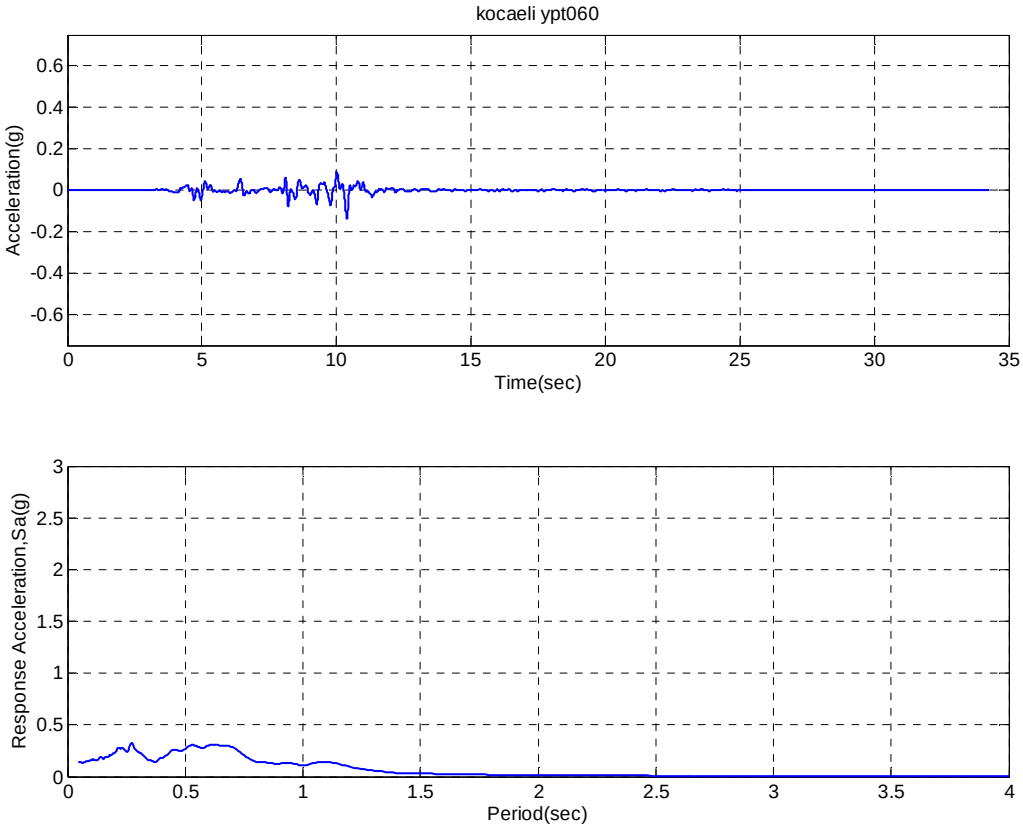

Figure A.13. Horizontal acceleration, response spectrum (5% damping) of Kocaeli-YPT060-1 input ground motion for ROOZ02.

APPENDIX A

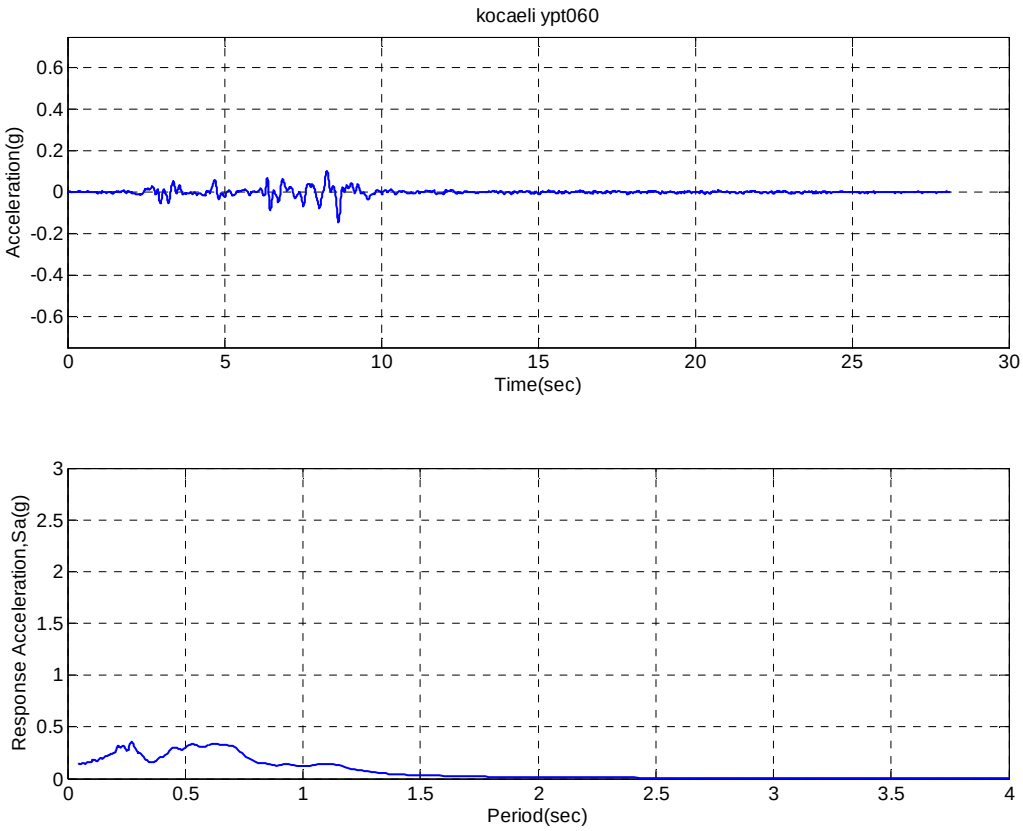

Figure A.14. Horizontal acceleration, response spectrum (5% damping) of Kocaeli-YPT060-2 input ground motion for ROOZ02.

APPENDIX A

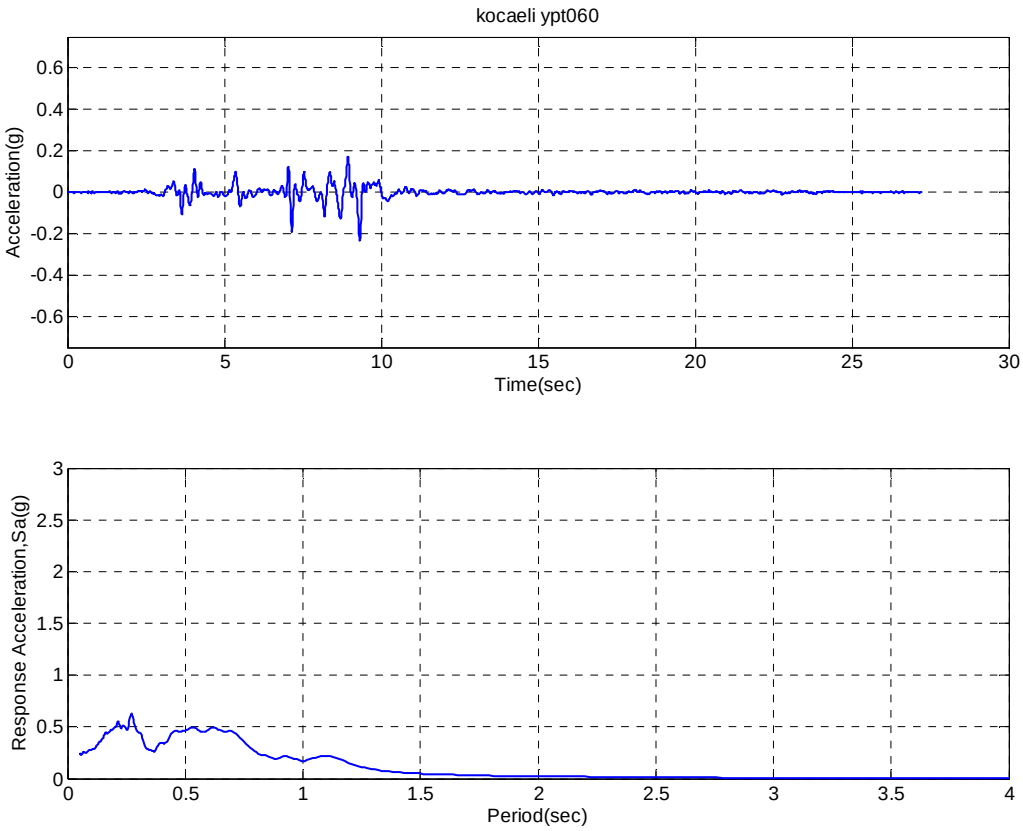

Figure A.15. Horizontal acceleration, response spectrum (5% damping) of Kocaeli-YPT060-3 input ground motion for ROOZ02.

APPENDIX A

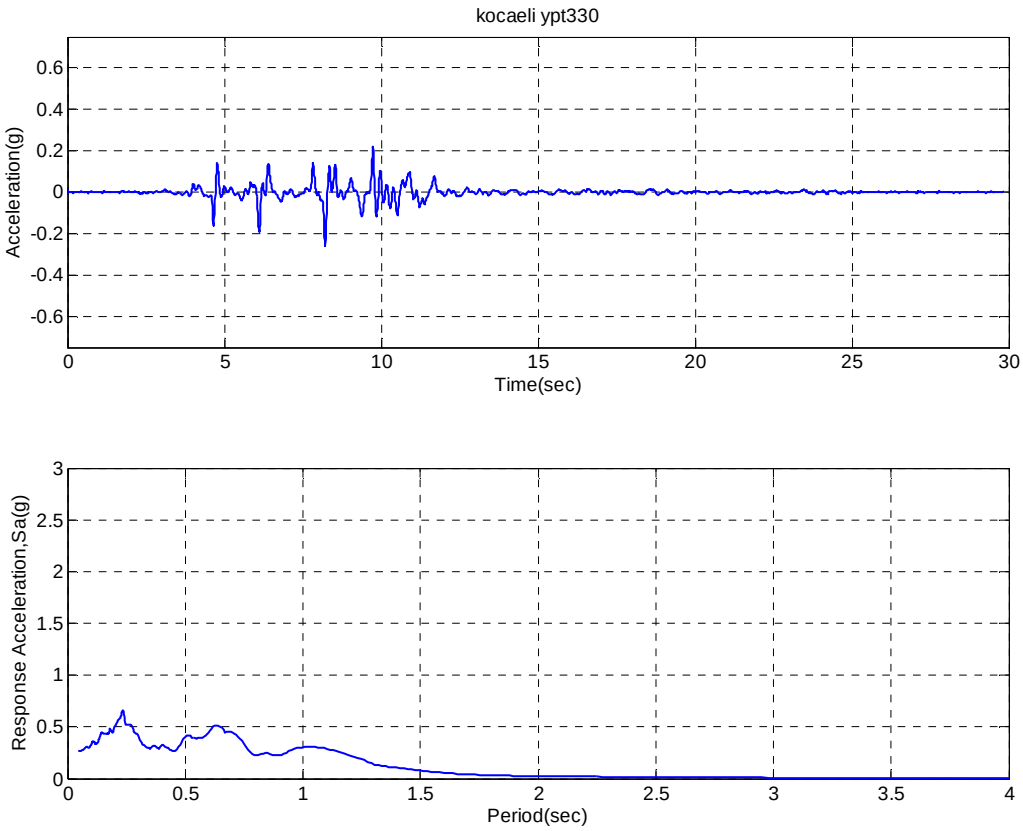

Figure A.16. Horizontal acceleration, response spectrum (5% damping) of Kocaeli-YPT330-1 input ground motion for ROOZ02.

APPENDIX A

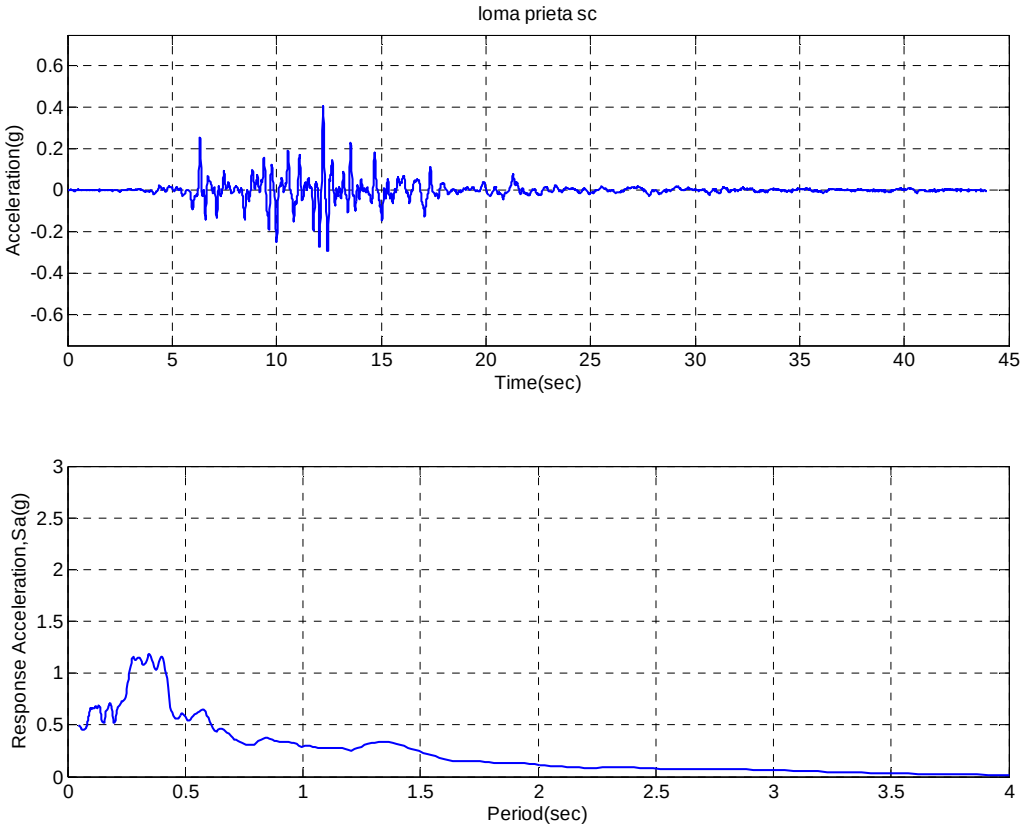

Figure A.17. Horizontal acceleration, response spectrum (5% damping) of Loma Prieta-SC-1 input ground motion for ROOZ02.

APPENDIX A

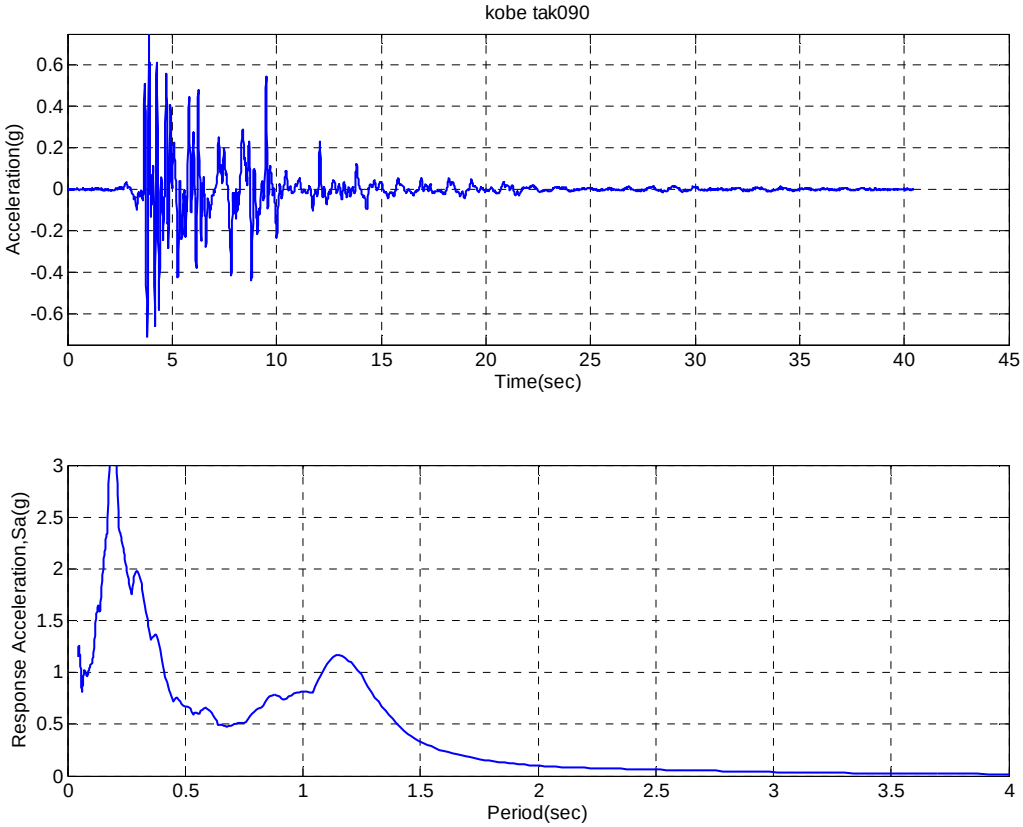

Figure A.18. Horizontal acceleration, response spectrum (5% damping) of Kobe-TAK090-1 input ground motion for ROOZ02.

APPENDIX A

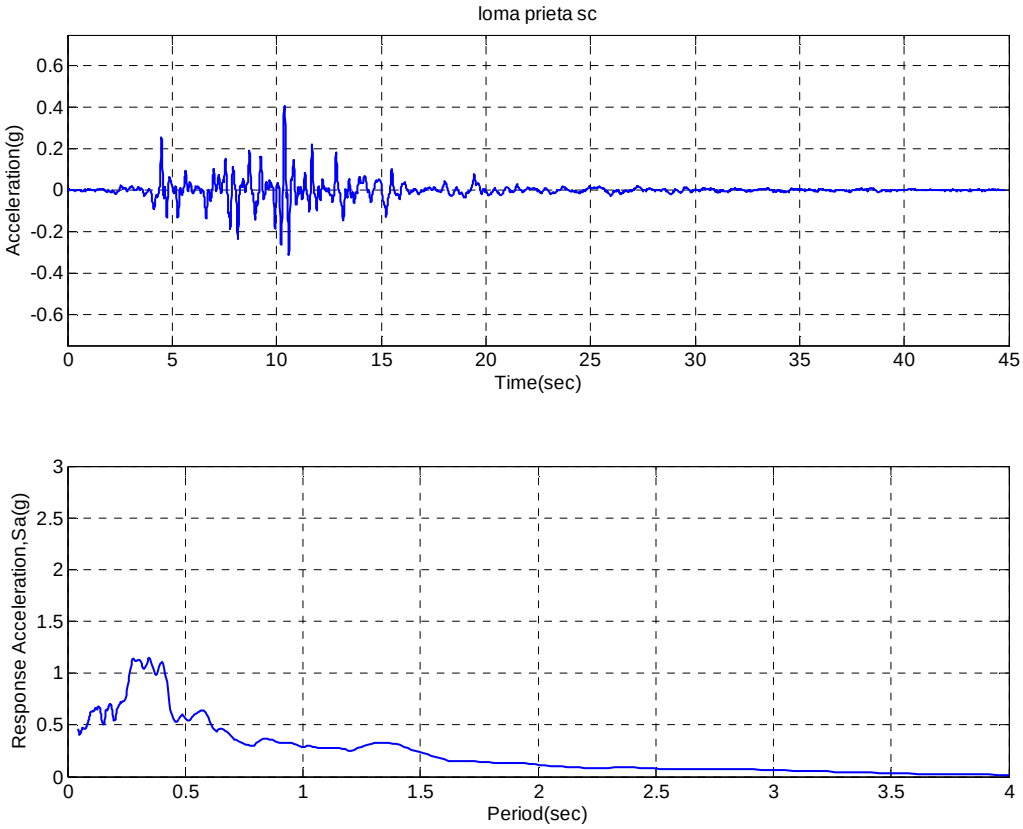

Figure A.19. Horizontal acceleration, response spectrum (5% damping) of Loma Prieta-SC-2 input ground motion for ROOZ02.

APPENDIX A

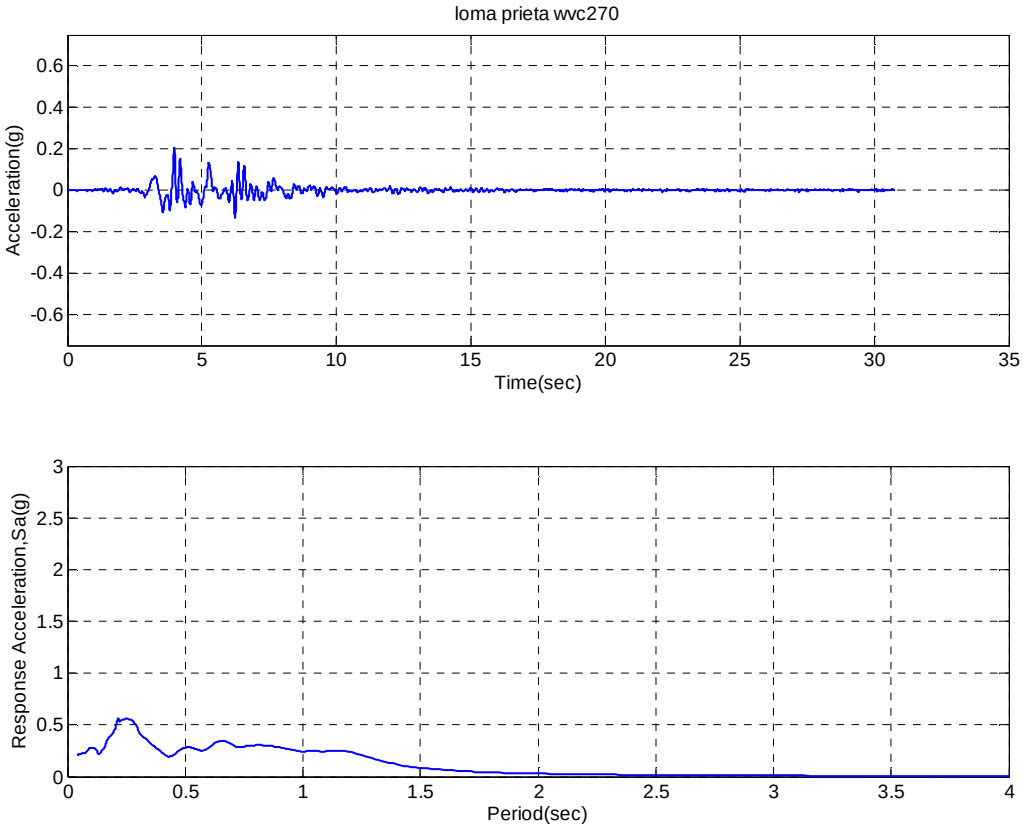

Figure A.20. Horizontal acceleration, response spectrum (5% damping) of Loma Prieta-WVC270-1input ground motion for ROOZ02.

APPENDIX A

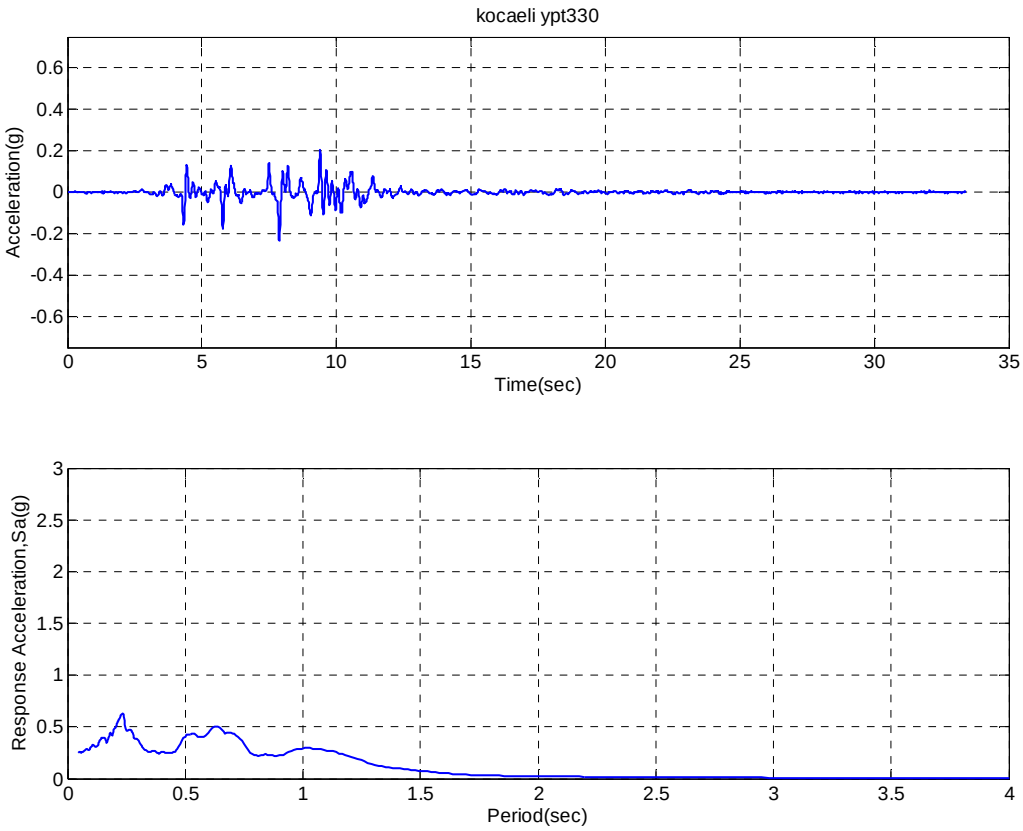

Figure A.21. Horizontal acceleration, response spectrum (5% damping) of Kocaeli- YPT 330-2 input ground motion for ROOZ02.

APPENDIX A

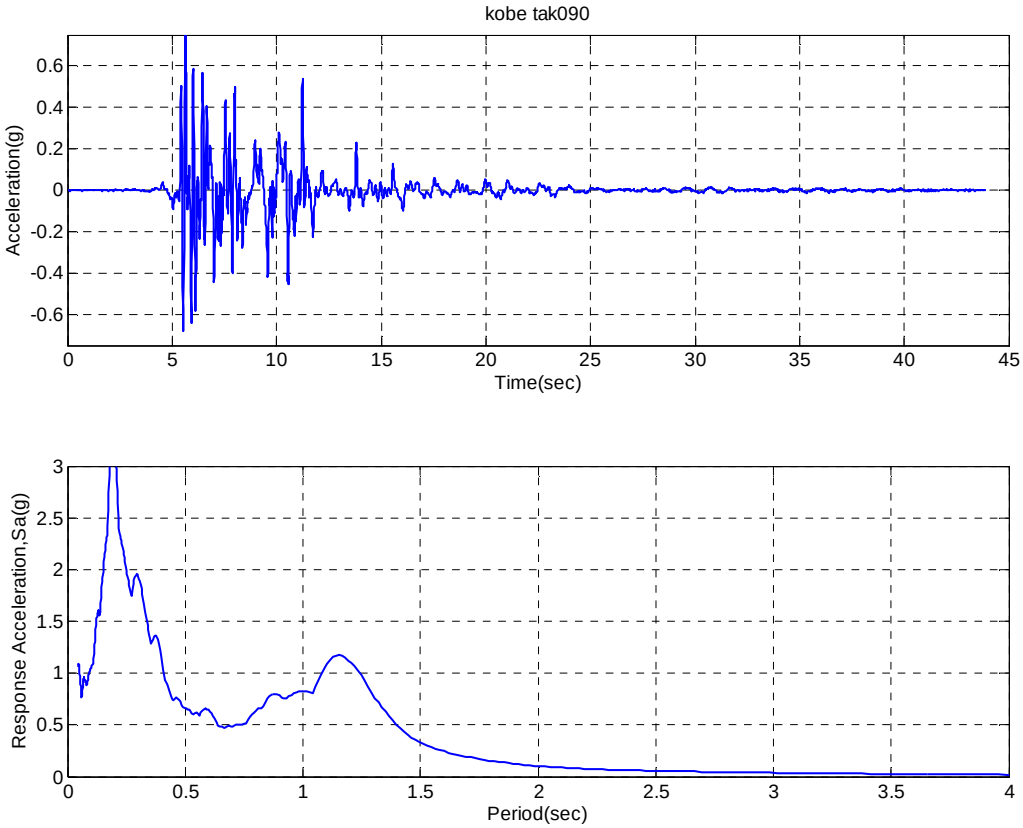

Figure A.22. Horizontal acceleration, response spectrum (5% damping) of Kobe-TAK090-2 input ground motion for ROOZ02.

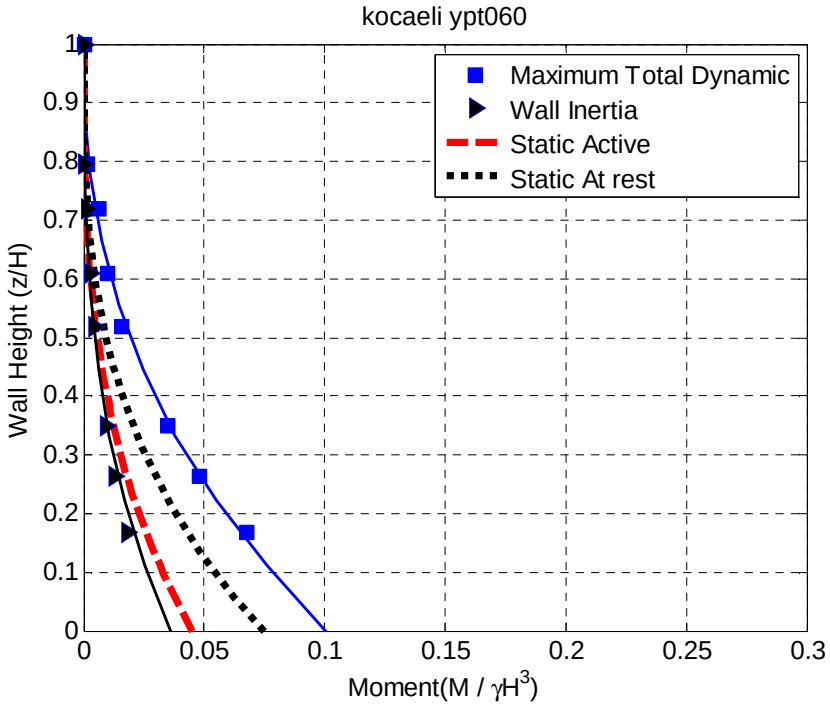

Figure A.23. Maximum total wall moment profiles measured by strain gages and static active and at rest moment estimates on the non-displacing cantilever wall for Kocaeli-YPT060-1 for ROOZ02.

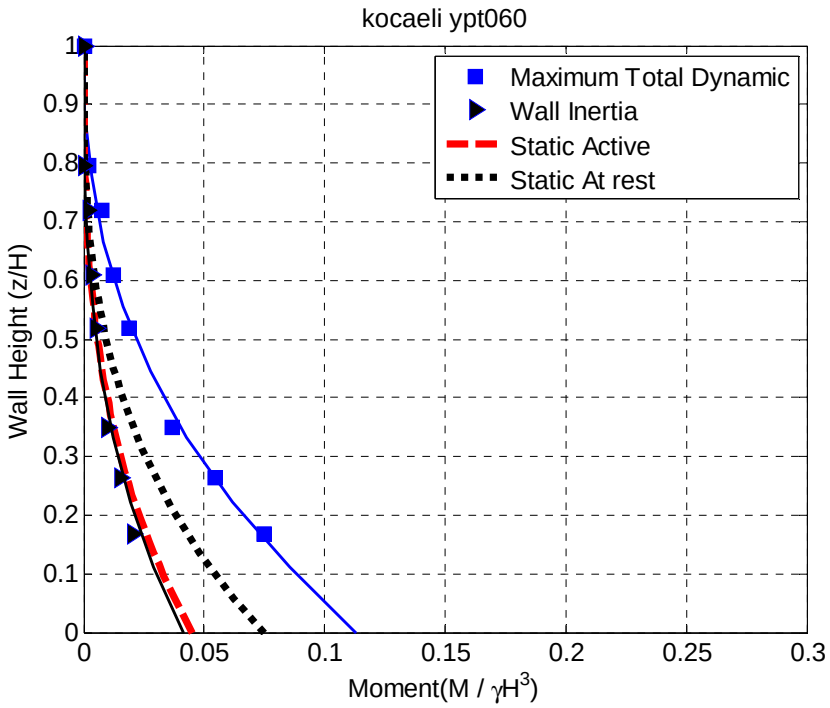

Figure A.24. Maximum total wall moment profiles measured by strain gages and static active and at rest moment estimates on the non-displacing cantilever wall for Kocaeli-YPT060-2 for ROOZ02.

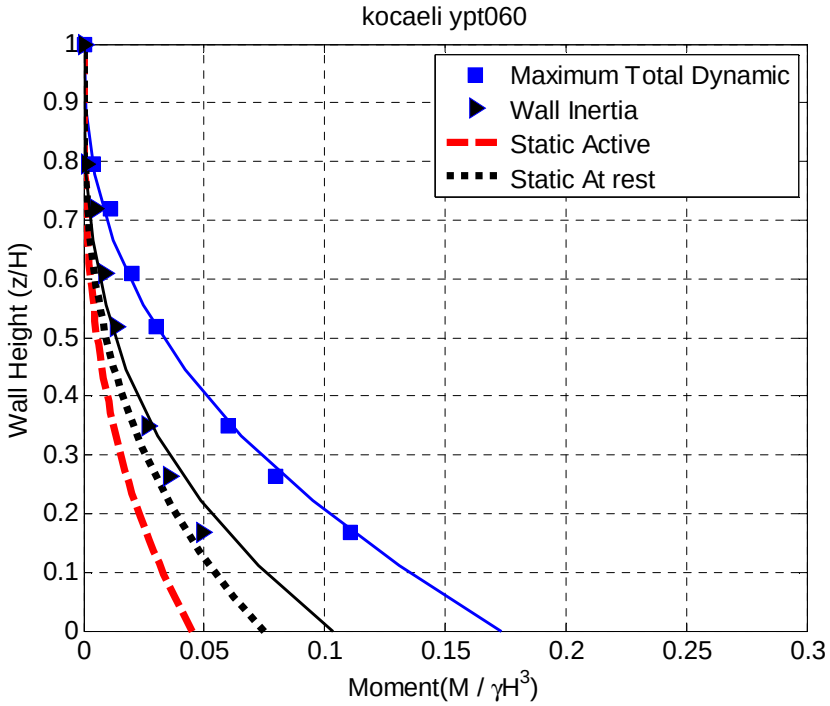

Figure A.25. Maximum total wall moment profiles measured by strain gages and static active and at rest moment estimates on the non-displacing cantilever wall for Kocaeli-YPT060-3 for ROOZ02.

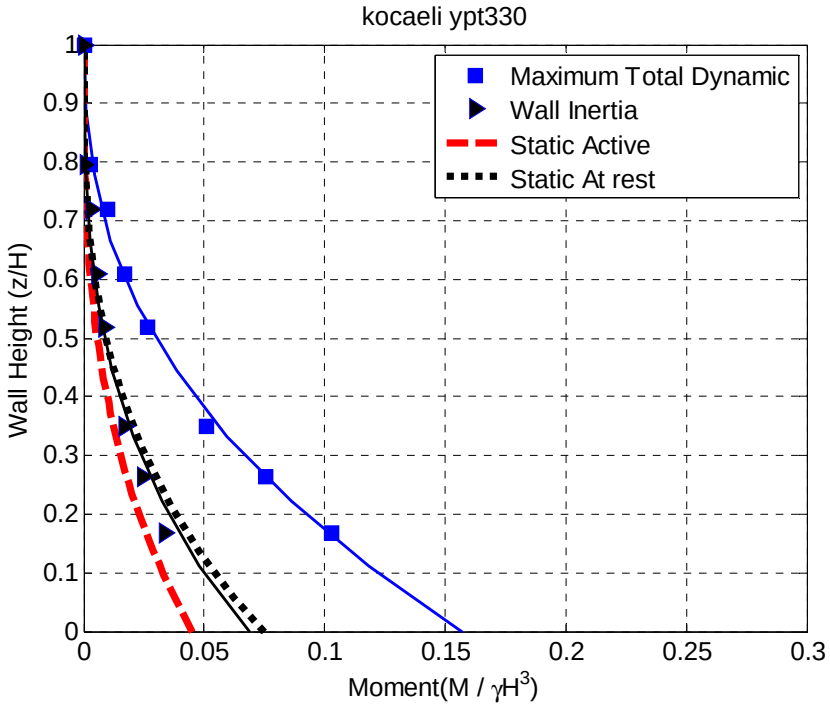

Figure A.26. Maximum total wall moment profiles measured by strain gages and static active and at rest moment estimates on the non-displacing cantilever wall for Kocaeli- YPT 330-1 for ROOZ02.

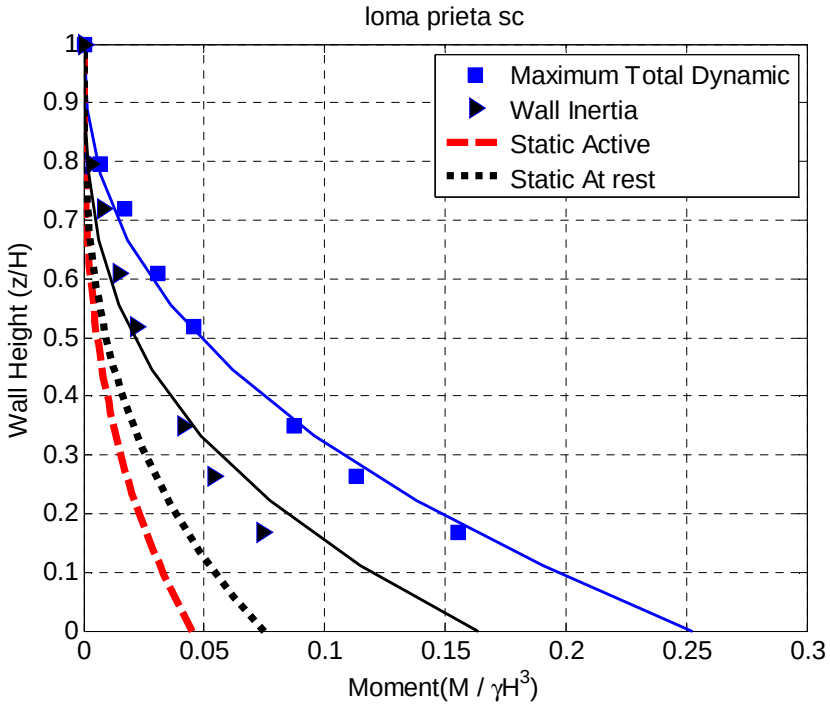

Figure A.27. Maximum total wall moment profiles measured by strain gages and static active and at rest moment estimates on the non-displacing cantilever wall for Loma Prieta-SC-1 for ROOZ02.

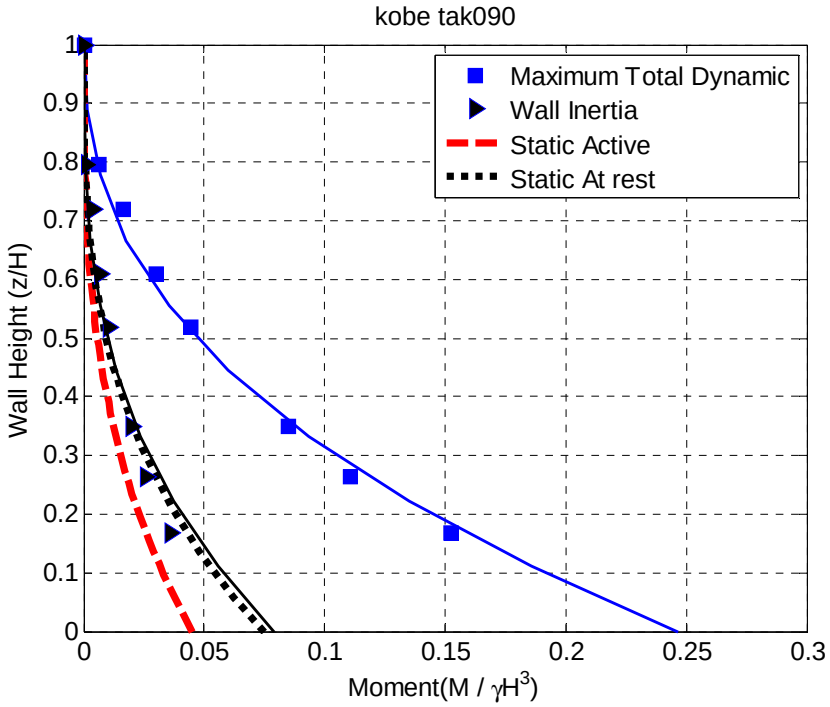

Figure A.28. Maximum total wall moment profiles measured by strain gages and static active and at rest moment estimates on the non-displacing cantilever wall for Kobe-TAK090-1 for ROOZ02.

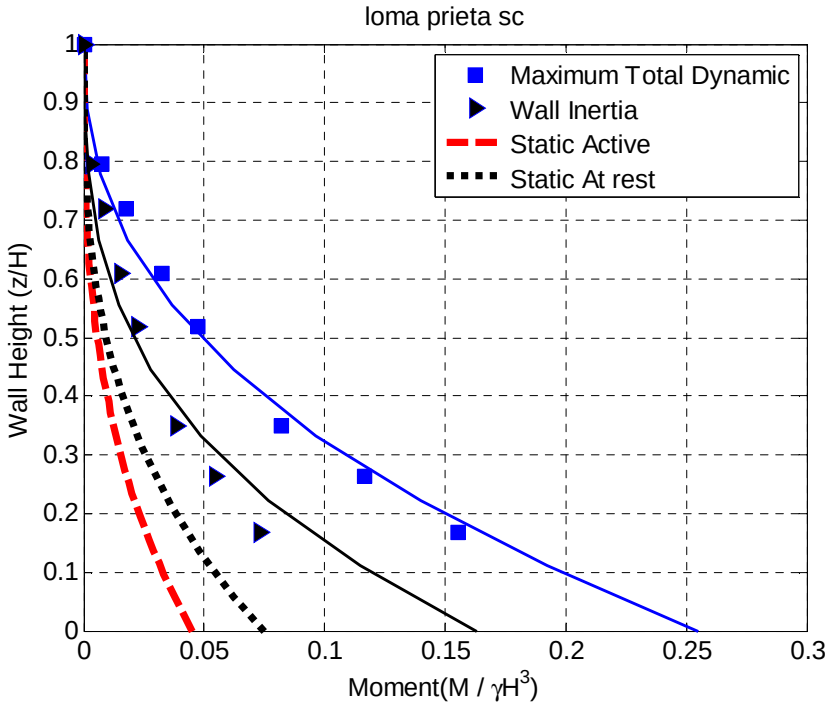

Figure A.29. Maximum total wall moment profiles measured by strain gages and static active and at rest moment estimates on the non-displacing cantilever wall for Loma Prieta-SC-2 for ROOZ02.

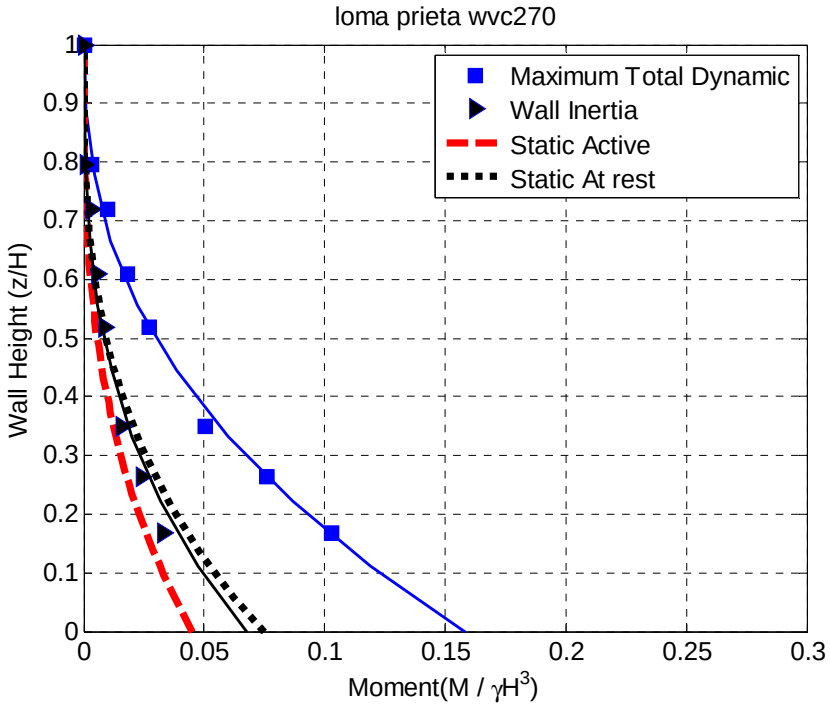

Figure A.30. Maximum total wall moment profiles measured by strain gages and static active and at rest moment estimates on the non-displacing cantilever wall for Loma Prieta-WVC270-1 for ROOZ02.

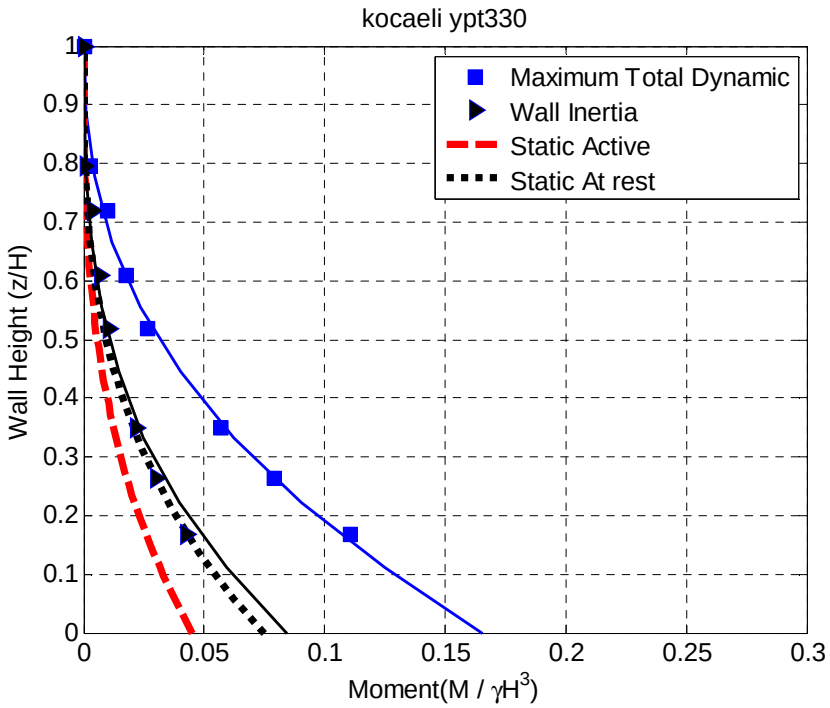

Figure A.31. Maximum total wall moment profiles measured by strain gages and static active and at rest moment estimates on the non-displacing cantilever wall for Kocaeli- YPT 330-2 for ROOZ02.

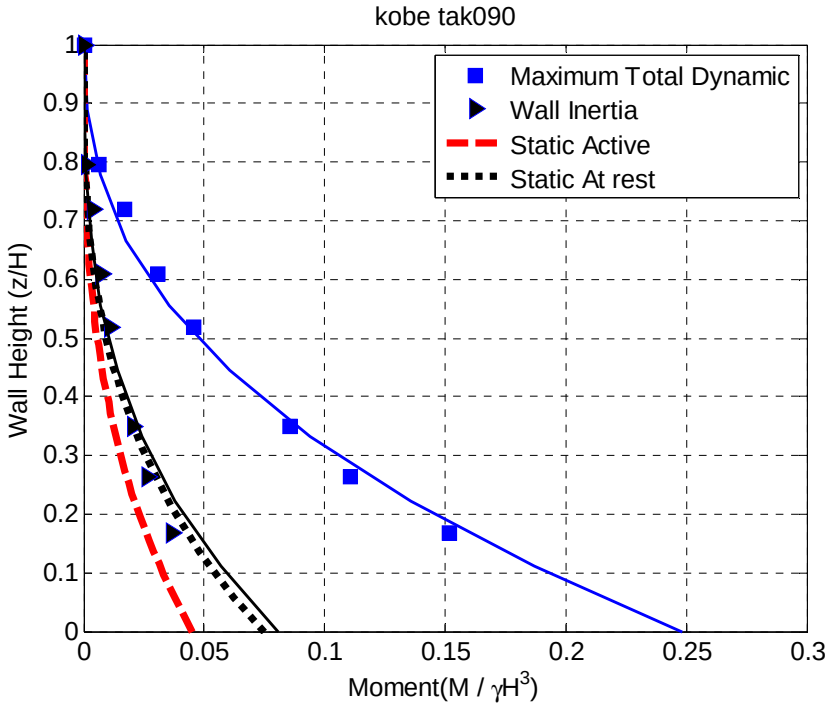

Figure A.32. Maximum total wall moment profiles measured by strain gages and static active and at rest moment estimates on the non-displacing cantilever wall for Kobe-TAK090-2 for ROOZ02.

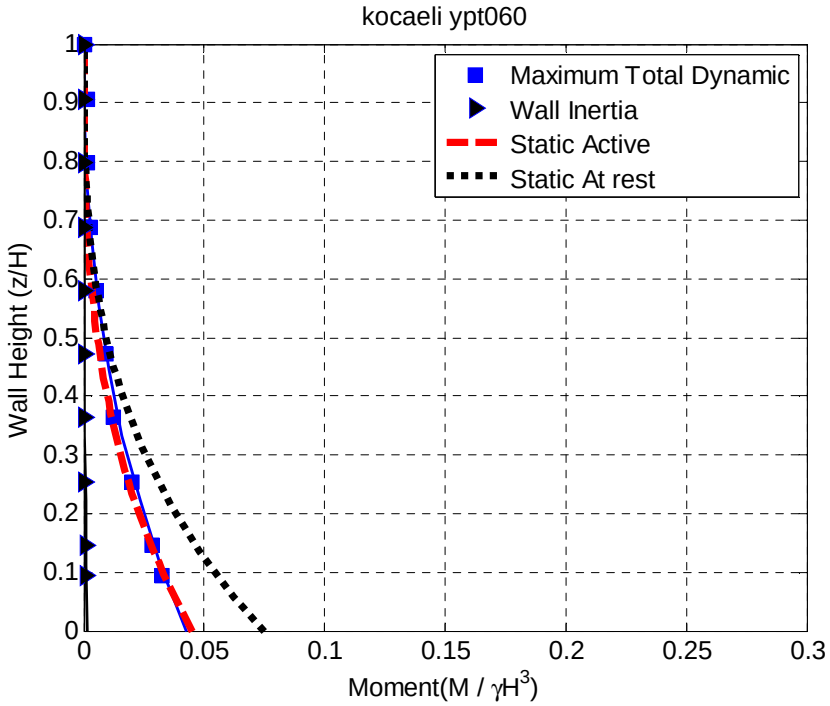

Figure A.33. Maximum total wall moment profiles measured by strain gages and static active and at rest moment estimates on the displacing retaining wall for Kocaeli-YPT060-1 for ROOZ02.

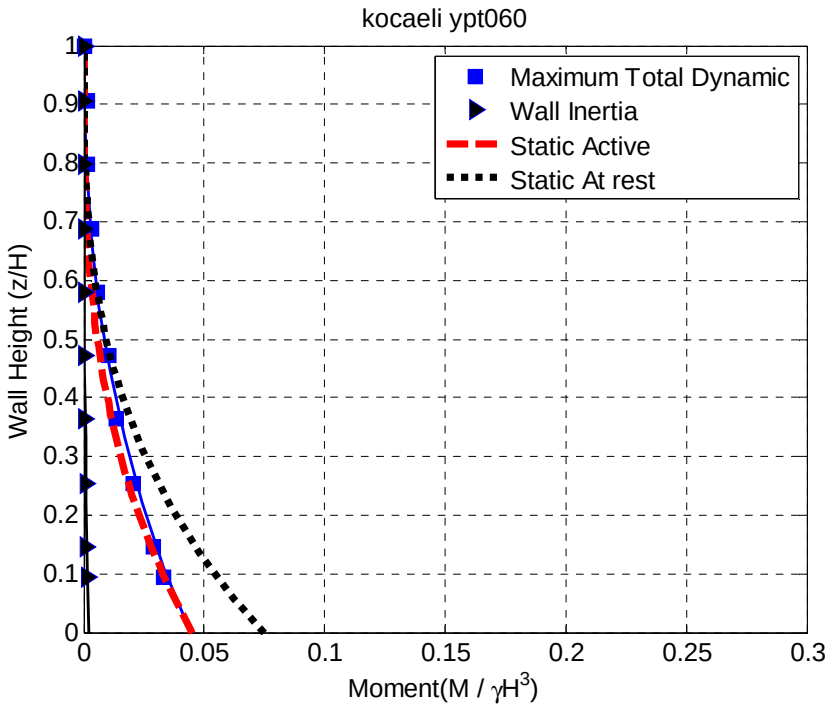

Figure A.34. Maximum total wall moment profiles measured by strain gages and static active and at rest moment estimates on the displacing retaining wall for Kocaeli-YPT060-2 for ROOZ02.

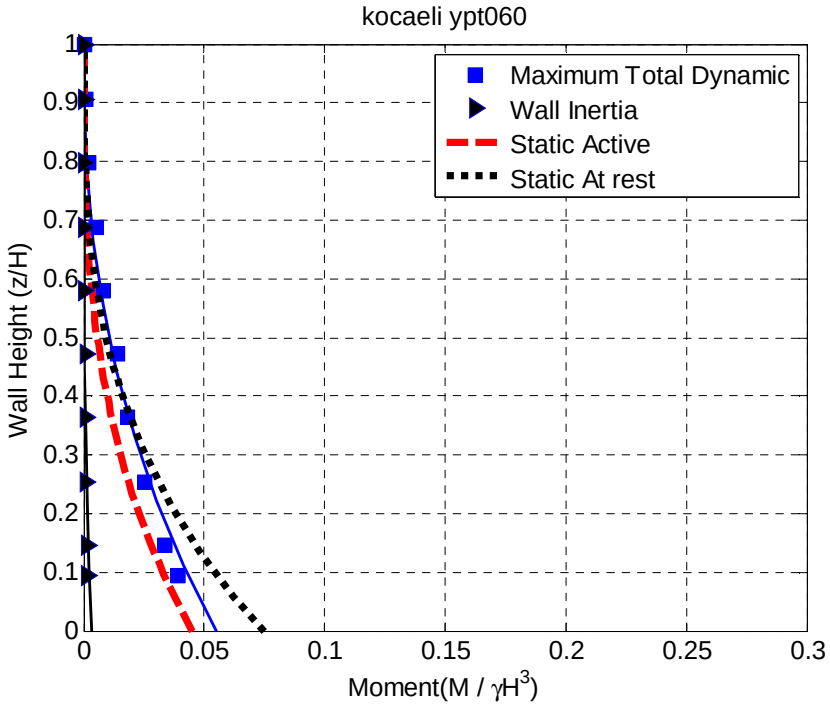

Figure A.35. Maximum total wall moment profiles measured by strain gages and static active and at rest moment estimates on the displacing retaining wall for Kocaeli-YPT060-3 for ROOZ02.

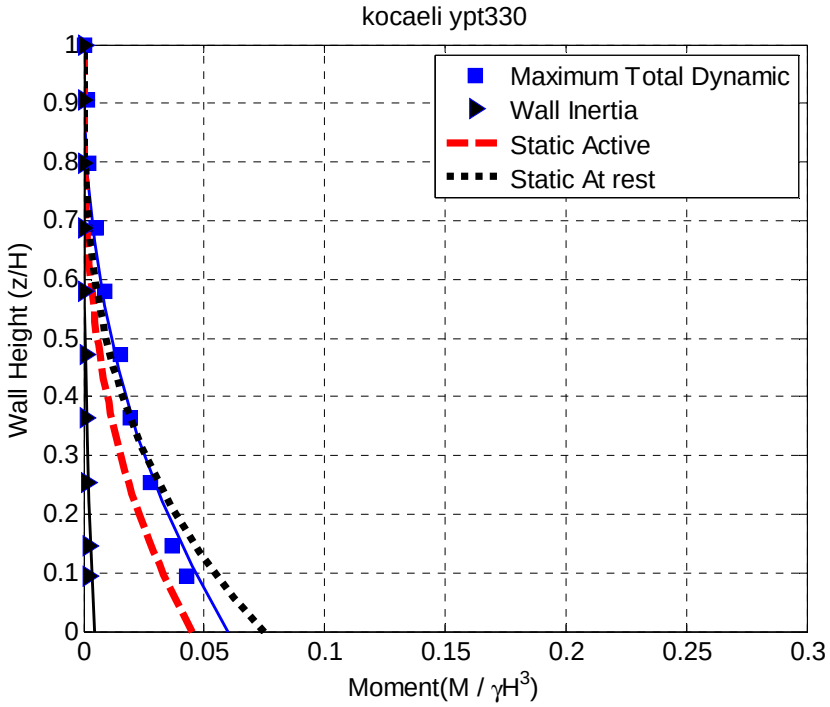

Figure A.36. Maximum total wall moment profiles measured by strain gages and static active and at rest moment estimates on the displacing retaining wall for Kocaeli- YPT 330-1 for ROOZ02.

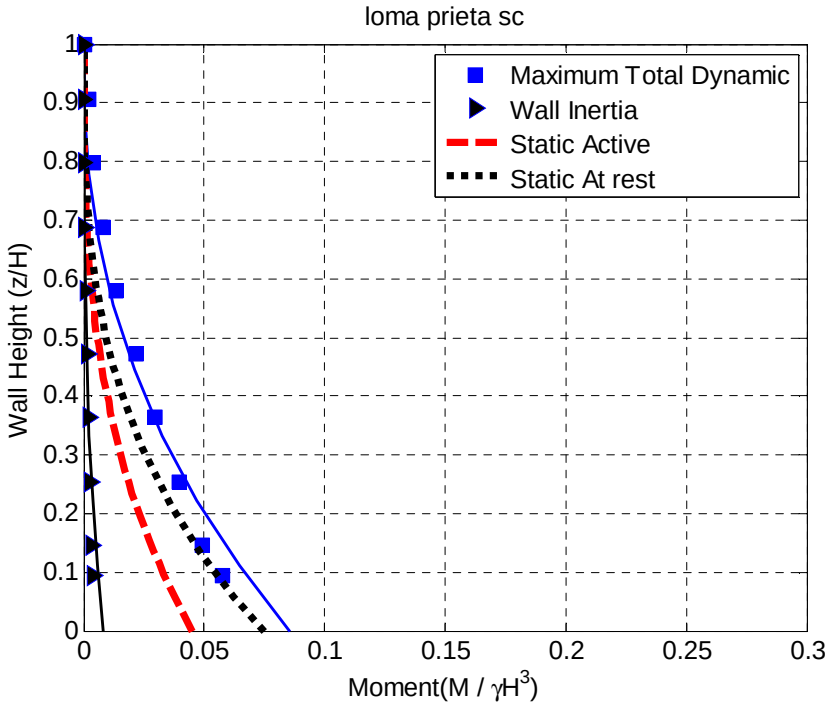

Figure A.37. Maximum total wall moment profiles measured by strain gages and static active and at rest moment estimates on the displacing retaining wall for Loma Prieta-SC-1 for ROOZ02.

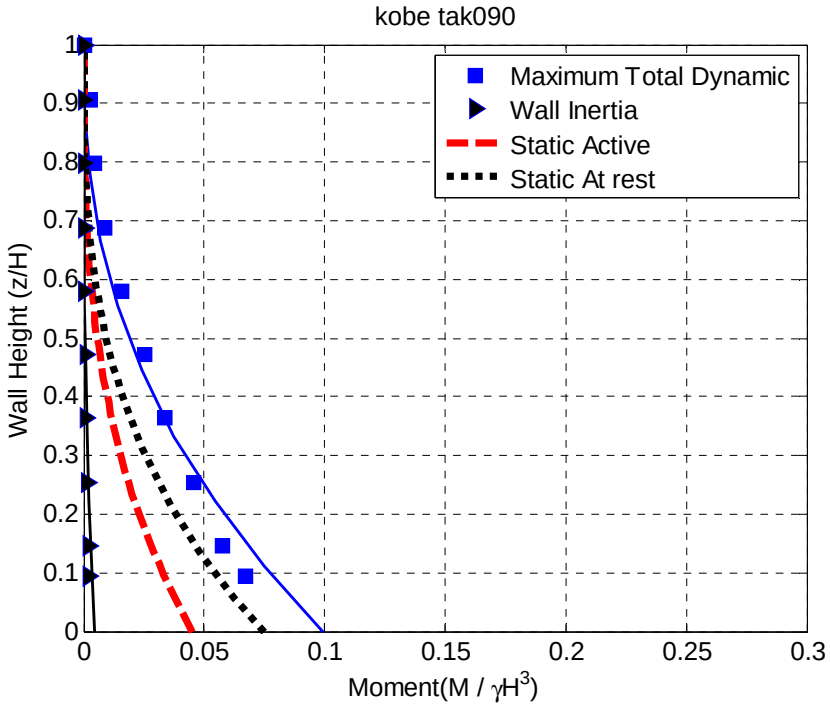

Figure A.38. Maximum total wall moment profiles measured by strain gages and static active and at rest moment estimates on the displacing retaining wall for Kobe-TAK090-1 for ROOZ02.

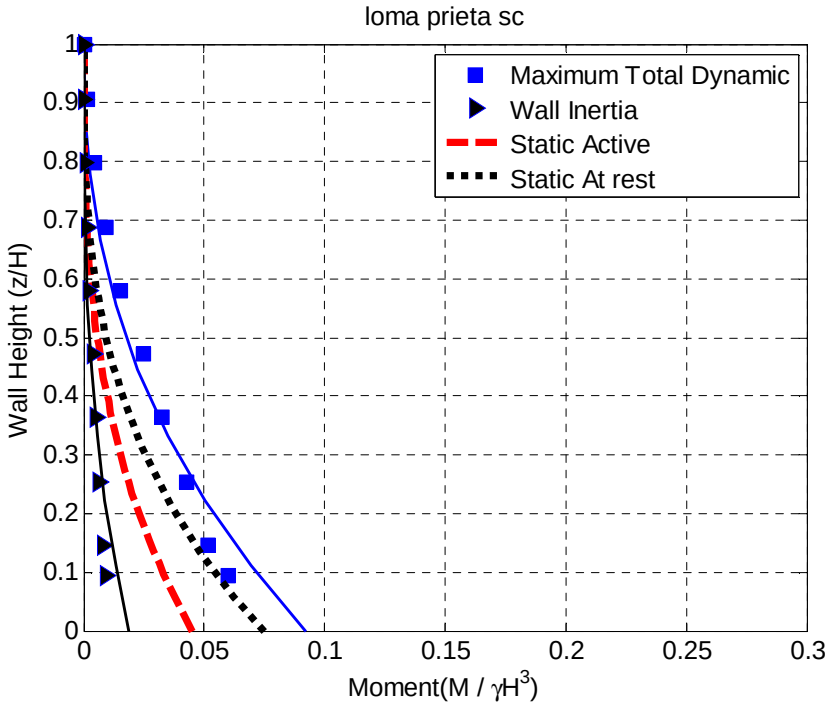

Figure A.39. Maximum total wall moment profiles measured by strain gages and static active and at rest moment estimates on the displacing retaining wall for Loma Prieta-SC-2 for ROOZ02.

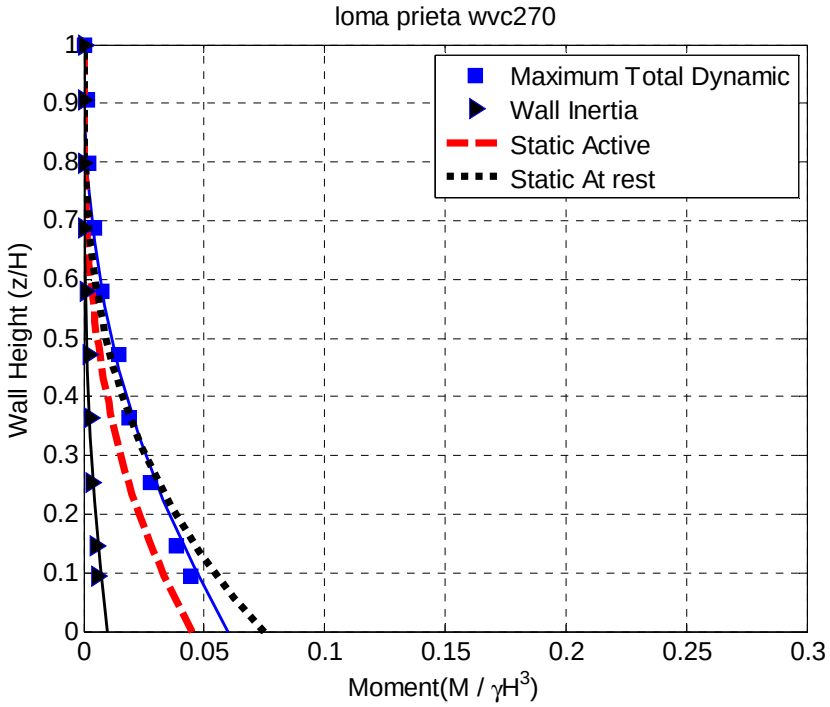

Figure A.40. Maximum total wall moment profiles measured by strain gages and static active and at rest moment estimates on the displacing retaining wall for Loma Prieta-WVC270-1 for ROOZ02.

APPENDIX A

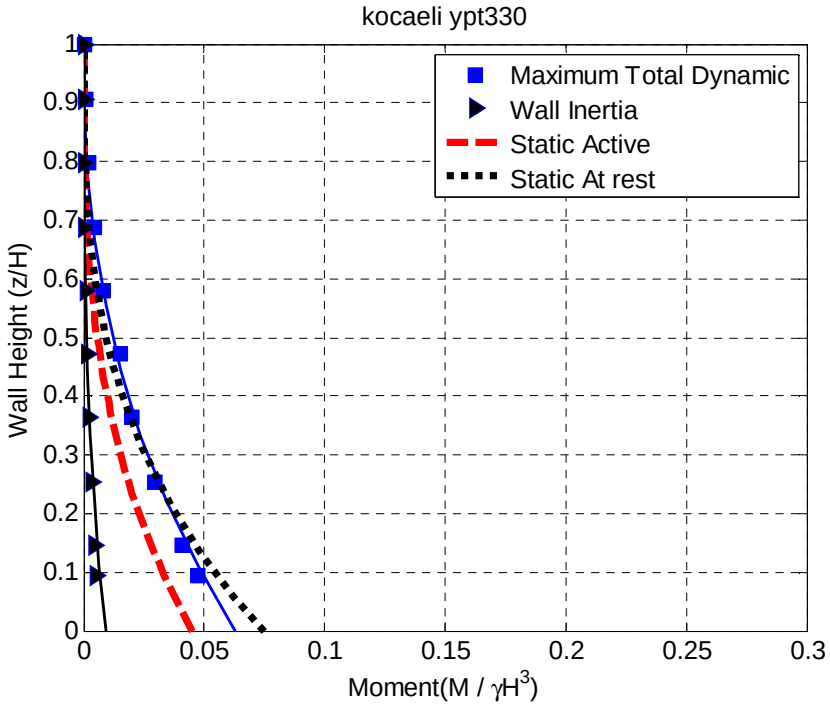

Figure A.41. Maximum total wall moment profiles measured by strain gages and static active and at rest moment estimates on the displacing retaining wall for Kocaeli- YPT 330-2 for ROOZ02.

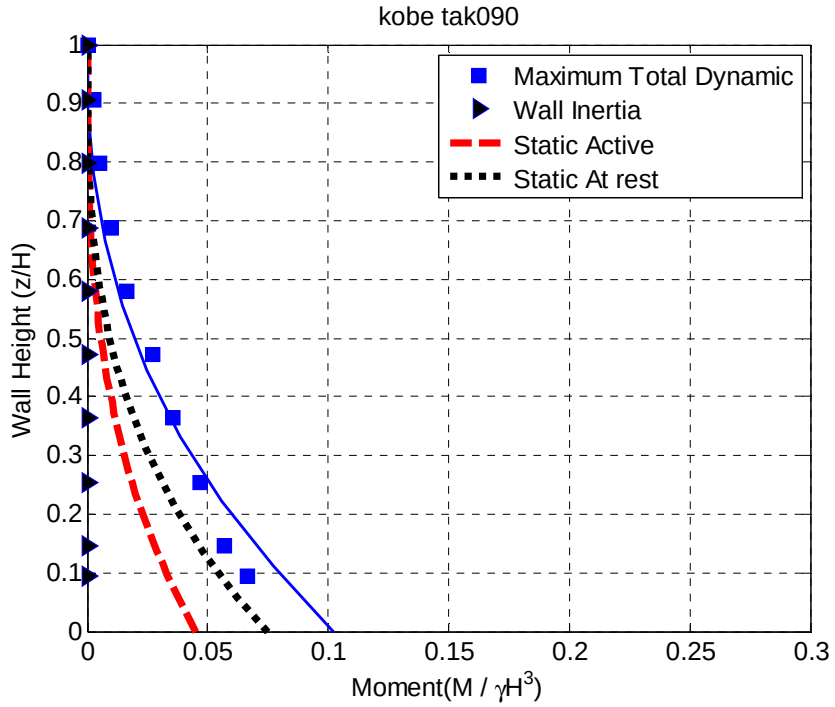

Figure A.42. Maximum total wall moment profiles measured by strain gages and static active and at rest moment estimates on the displacing retaining wall for Kobe-TAK090-2 for ROOZ02.

APPENDIX A

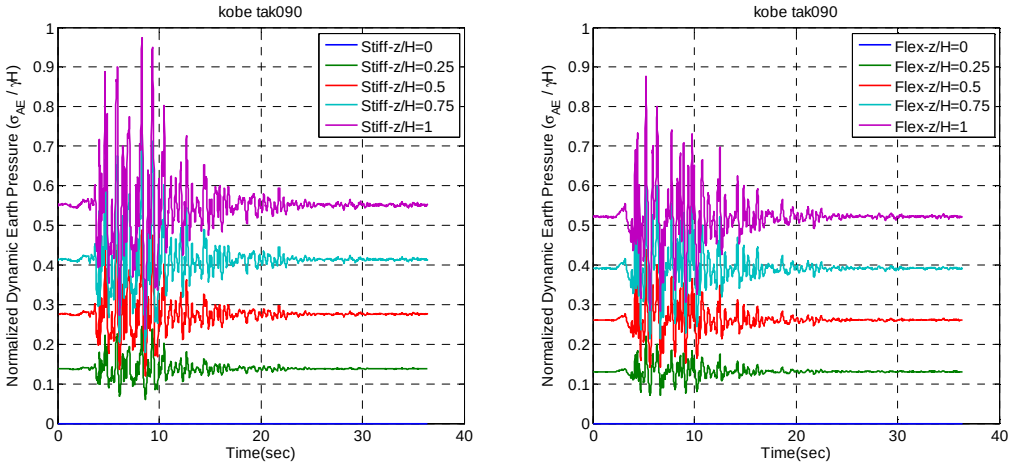

Figure A.43. Total earth pressure time series interpreted from load cell data on both stiff and flexible non-displacing basement walls for Kobe-TAK090-1 for ROOZ01.

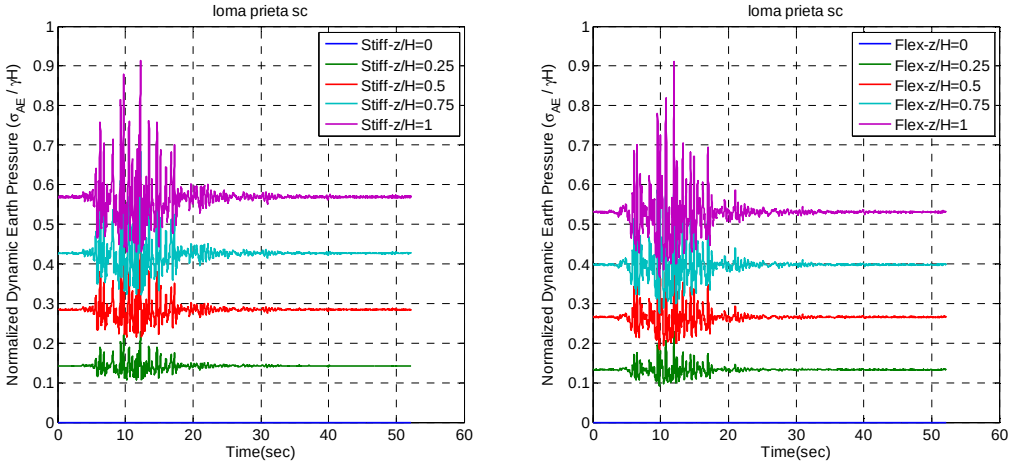

Figure A.44. Total earth pressure time series interpreted from load cell data on both stiff and flexible non-displacing basement walls for Loma Prieta-SC-1 for ROOZ01.

APPENDIX A

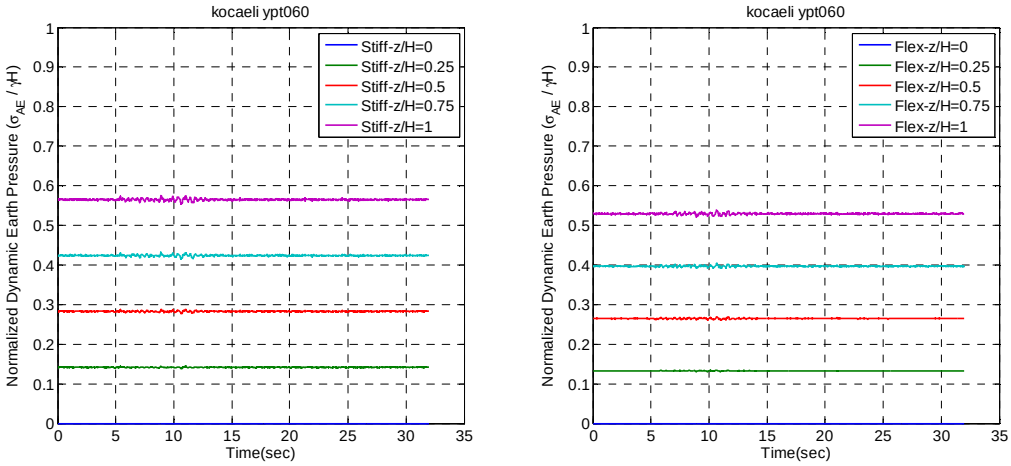

Figure A.45. Total earth pressure time series interpreted from load cell data on both stiff and flexible non-displacing basement walls for Kocaeli-YPT060-1 for ROOZ01.

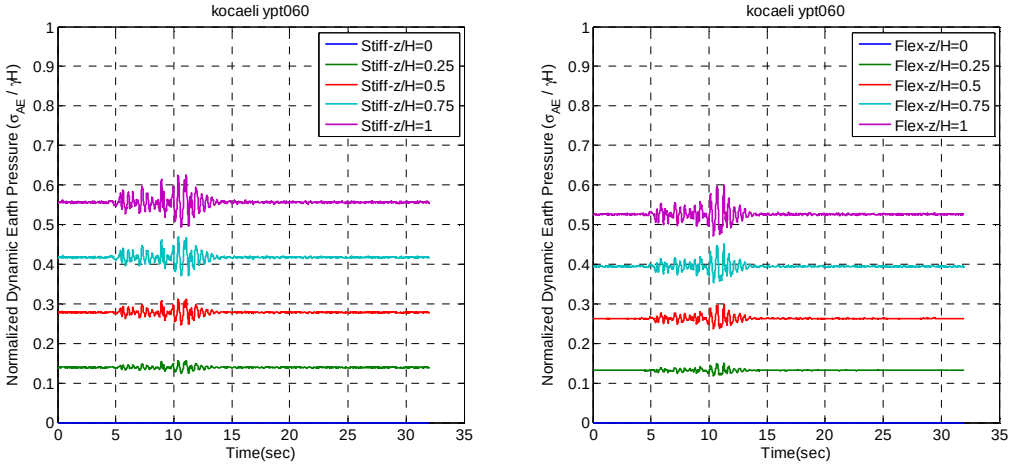

Figure A.46. Total earth pressure time series interpreted from load cell data on both stiff and flexible non-displacing basement walls for Kocaeli-YPT060-2 for ROOZ01.

APPENDIX A

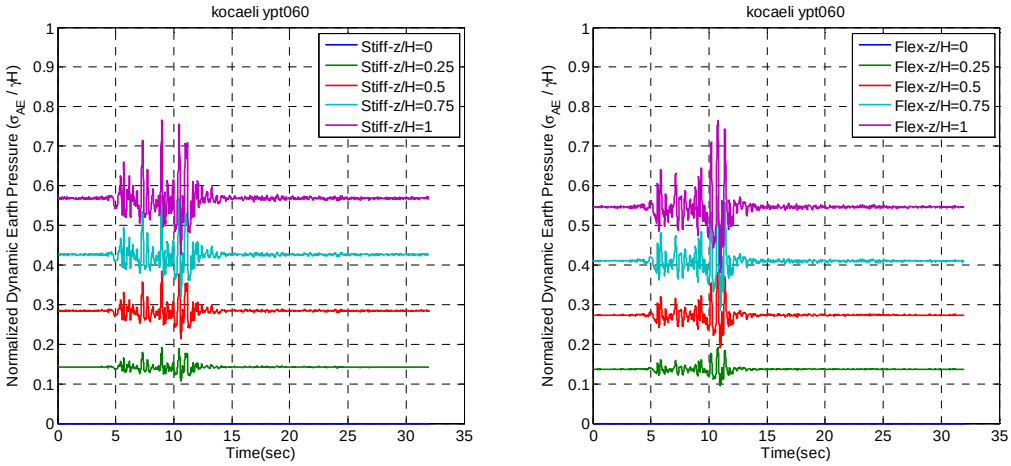

Figure A.47. Total earth pressure time series interpreted from load cell data on both stiff and flexible non-displacing basement walls for Kocaeli-YPT060-3 for ROOZ01.

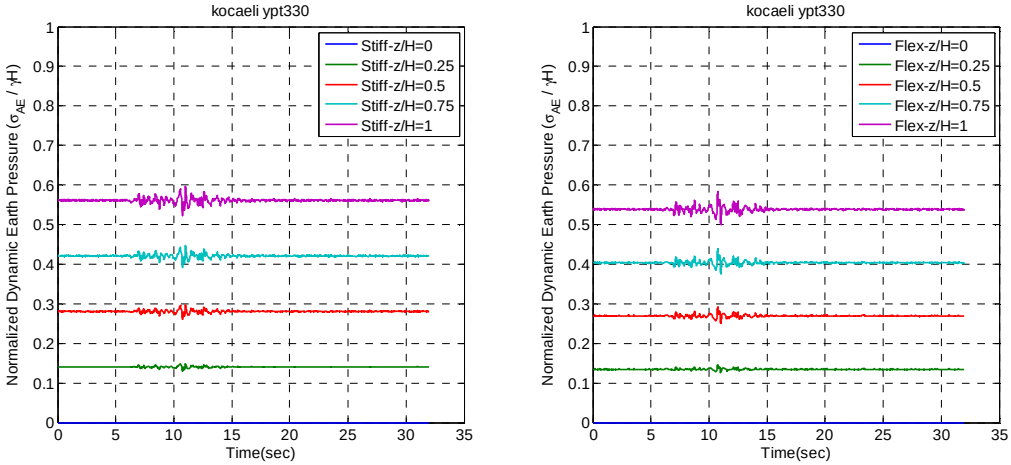

Figure A.48. Total earth pressure time series interpreted from load cell data on both stiff and flexible non-displacing basement walls for Kocaeli-YPT330-1 for ROOZ01.

APPENDIX A

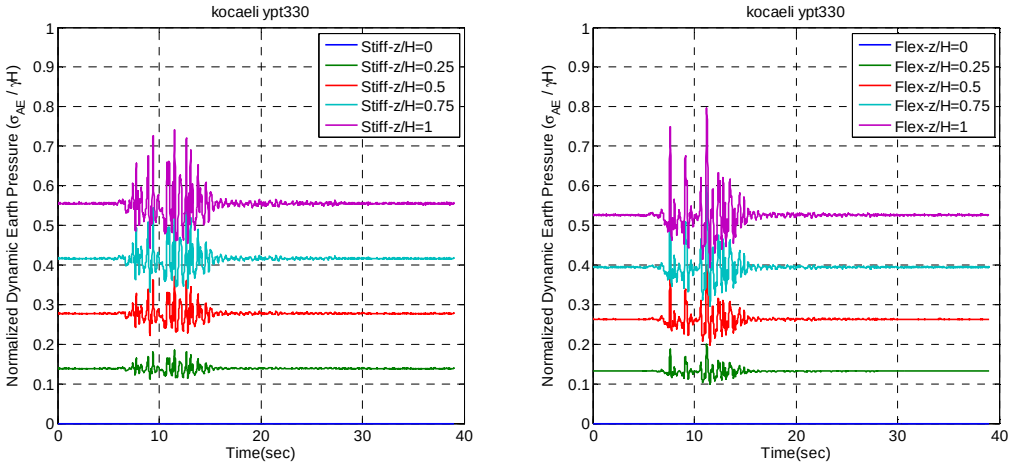

Figure A.49. Total earth pressure time series interpreted from load cell data on both stiff and flexible non-displacing basement walls for Kocaeli-YPT330-2 for ROOZ01.

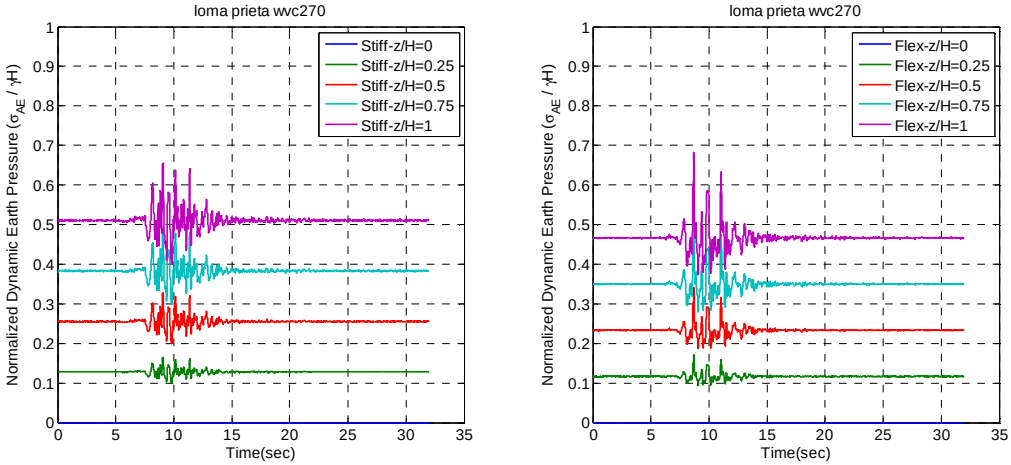

Figure A.50. Total earth pressure time series interpreted from load cell data on both stiff and flexible non-displacing basement walls for Loma Prieta-WVC270-1 for ROOZ01.

APPENDIX A

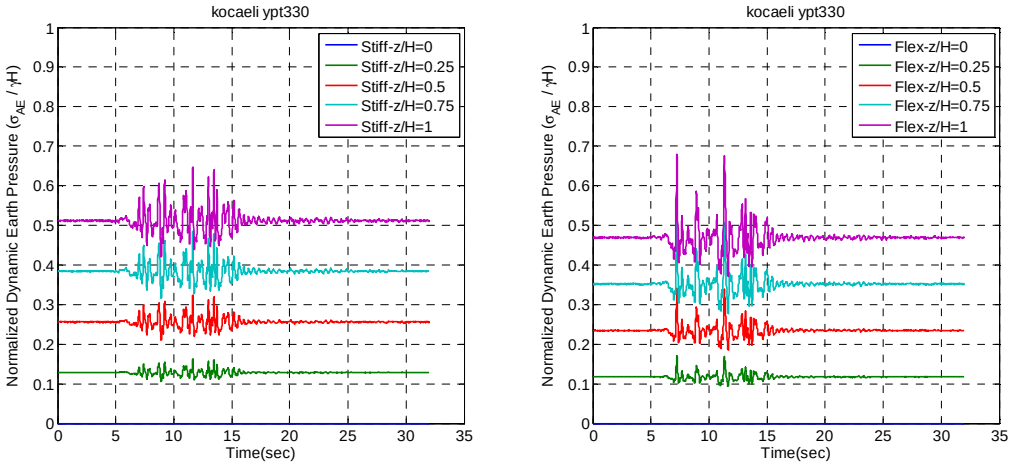

Figure A.51. Total earth pressure time series interpreted from load cell data on both stiff and flexible non-displacing basement walls for Kocaeli-YPT330-3 for ROOZ01.

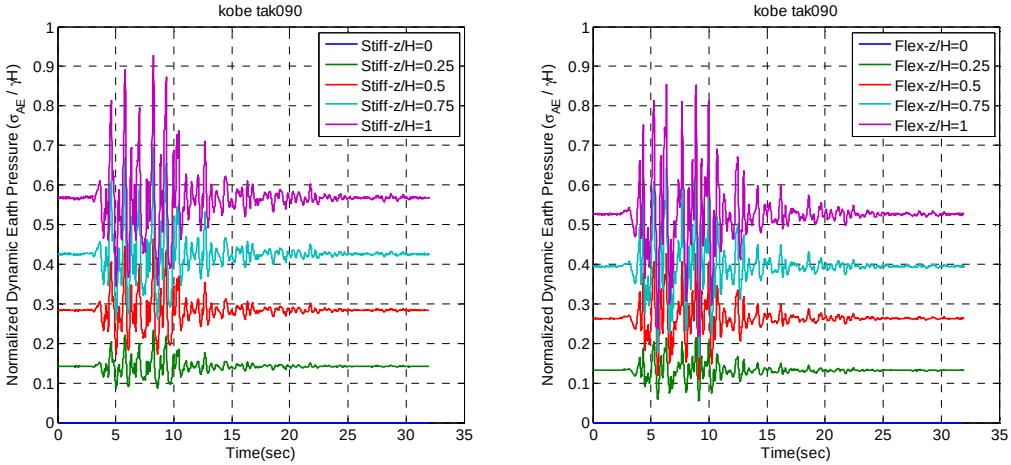

Figure A.52. Total earth pressure time series interpreted from load cell data on both stiff and flexible non-displacing basement walls for Kobe-TAK090-2 for ROOZ01.

APPENDIX A

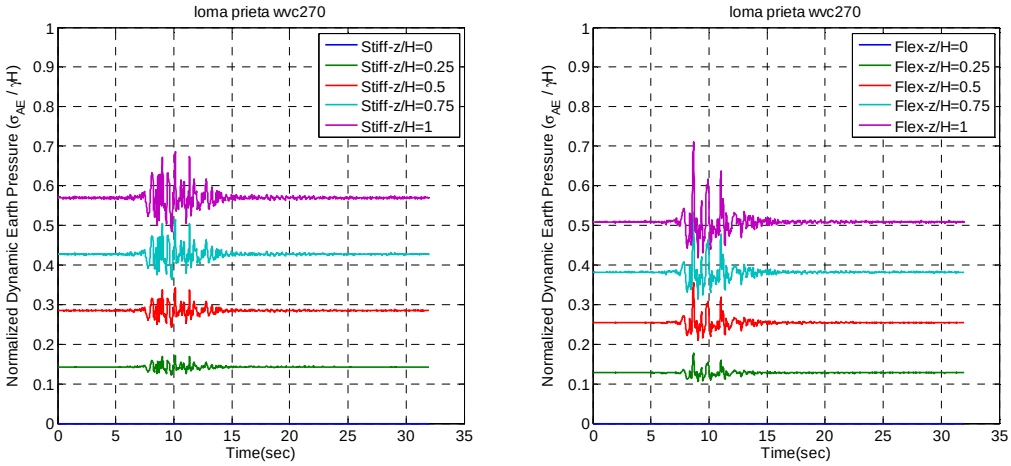

Figure A.53. Total earth pressure time series interpreted from load cell data on both stiff and flexible non-displacing basement walls for Loma Prieta-WVC270-2 for ROOZ01.

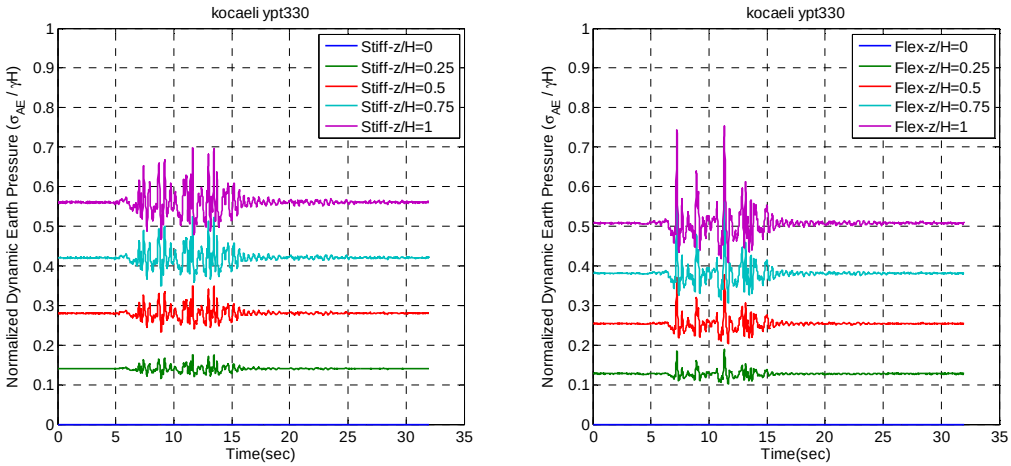

Figure A.54. Total earth pressure time series interpreted from load cell data on both stiff and flexible non-displacing basement walls for Kocaeli-YPT330-3 for ROOZ01.

APPENDIX A

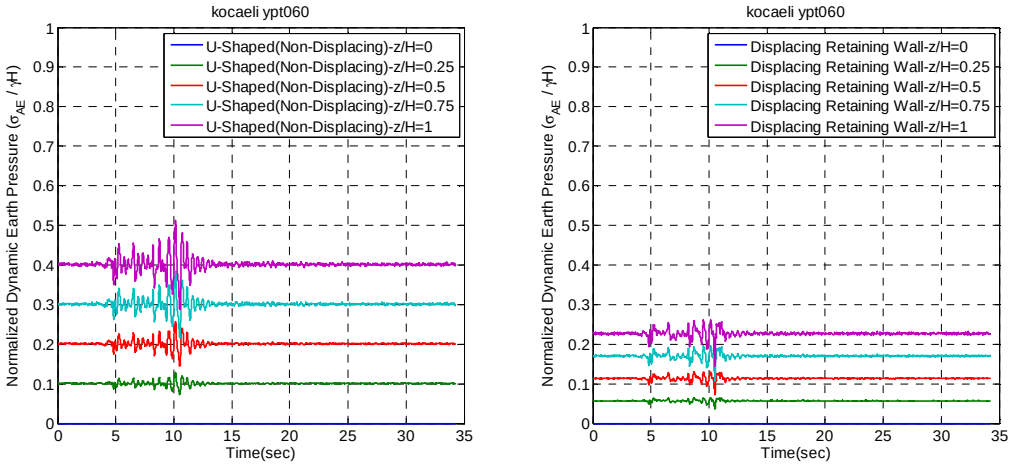

Figure A.55. Total earth pressure time series interpreted from strain gage data on both non-displacing and displacing retaining walls for Kocaeli-YPT060-1 for ROOZ02.

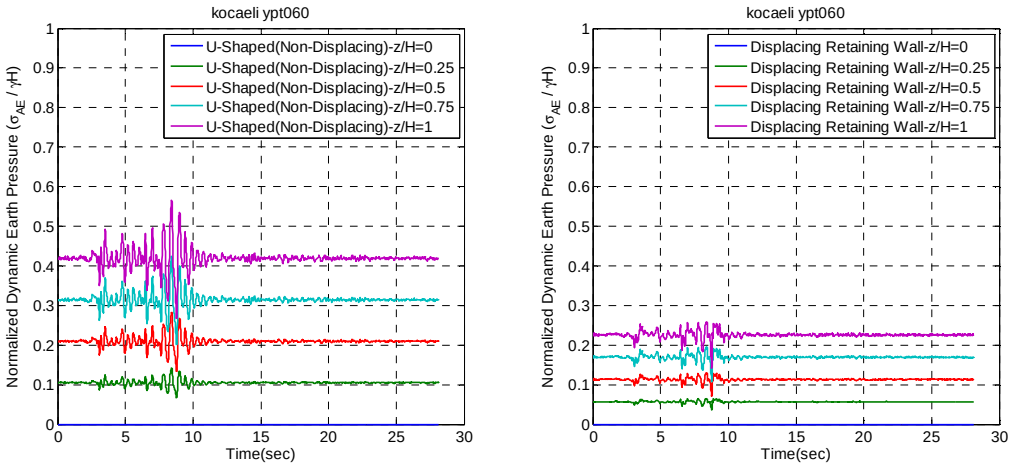

Figure A.56. Total earth pressure time series interpreted from strain gage data on both non-displacing and displacing retaining walls for Kocaeli-YPT060-2 for ROOZ02.

APPENDIX A

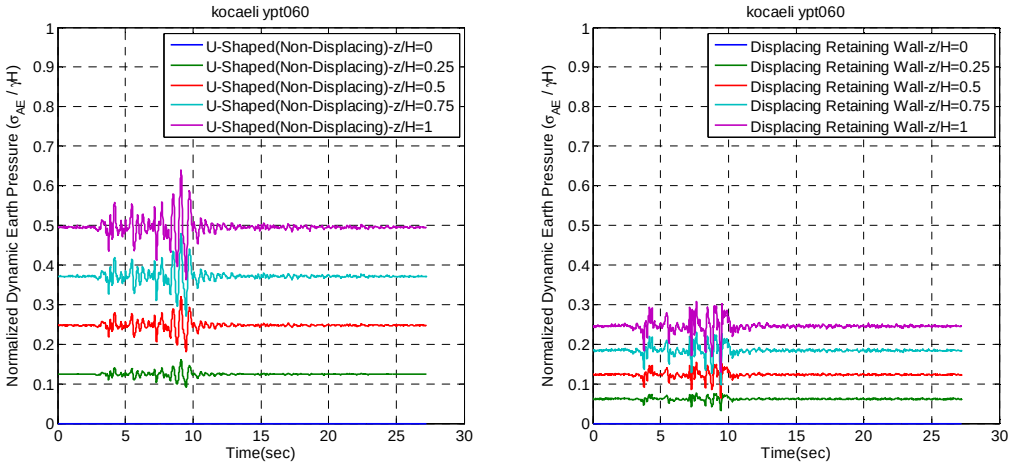

Figure A.57. Total earth pressure time series interpreted from strain gage data on both non-displacing and displacing retaining walls for Kocaeli-YPT060-3 for ROOZ02.

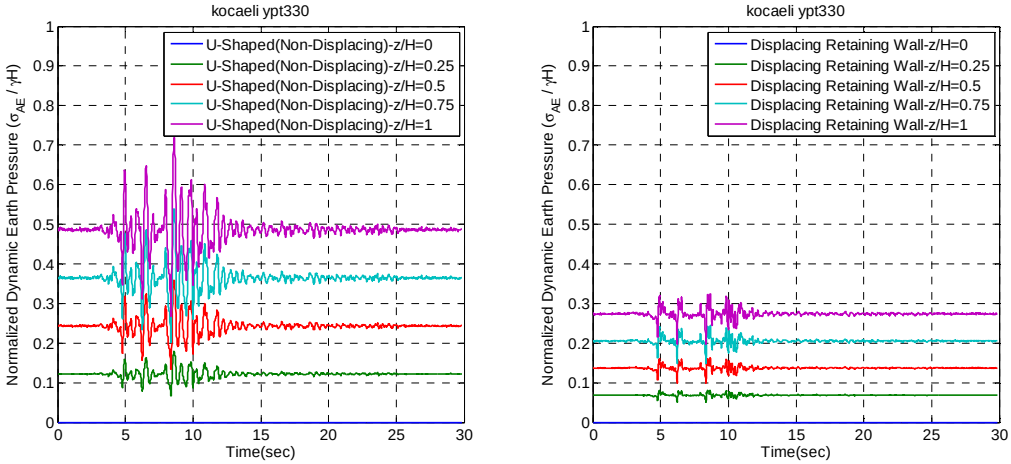

Figure A.58. Total earth pressure time series interpreted from strain gage data on both non-displacing and displacing retaining walls for Kocaeli-YPT330-1 for ROOZ02.

APPENDIX A

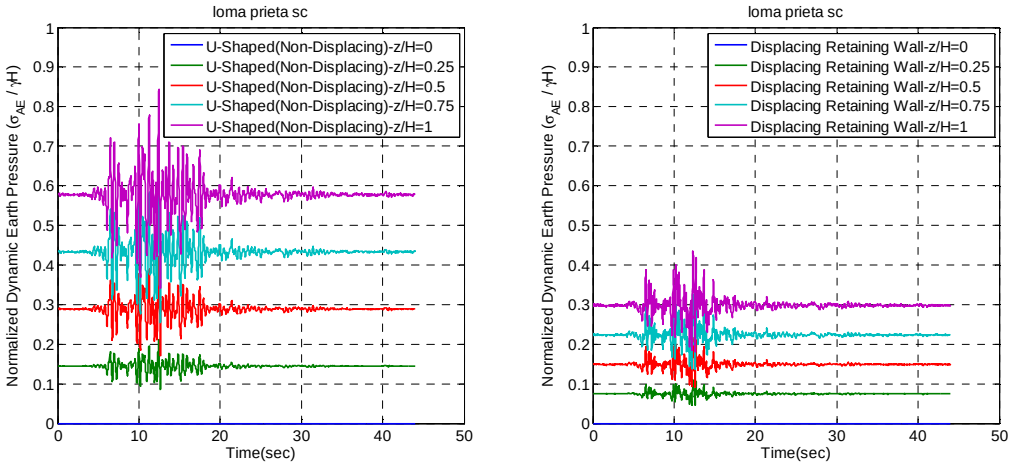

Figure A.59. Total earth pressure time series interpreted from strain gage data on both non-displacing and displacing retaining walls for Loma Prieta-SC-1 for ROOZ02.

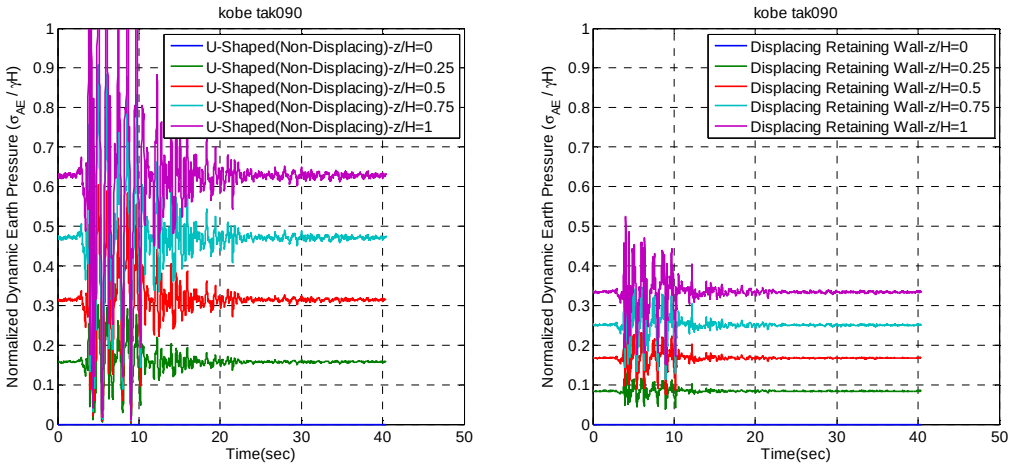

Figure A.60. Total earth pressure time series interpreted from strain gage data on both non-displacing and displacing retaining walls for Kobe-TAK090-1 for ROOZ02.

APPENDIX A

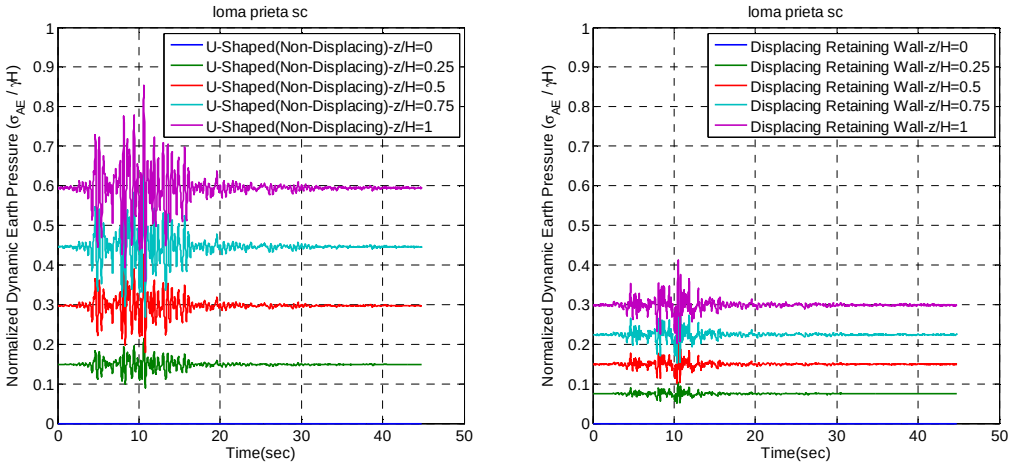

Figure A.61. Total earth pressure time series interpreted from strain gage data on both non-displacing and displacing retaining walls for Loma Prieta-SC-2 for ROOZ02.

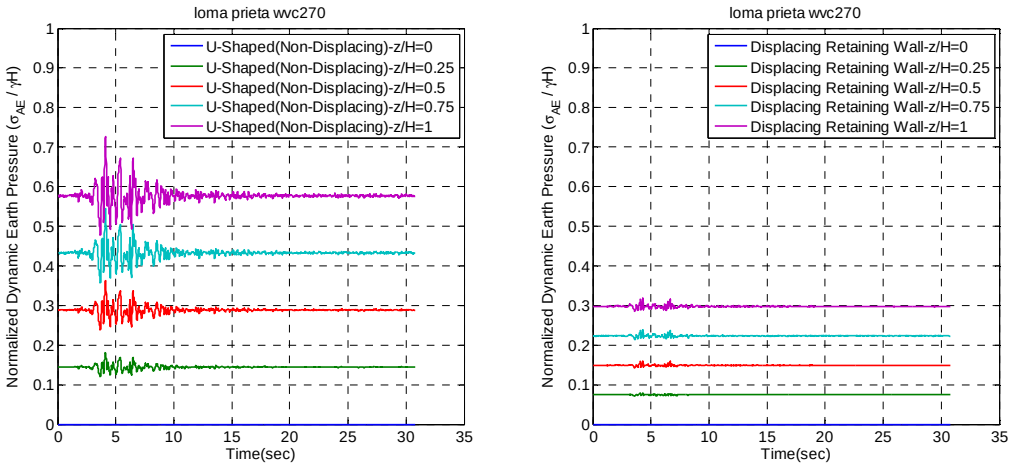

Figure A.62. Total earth pressure time series interpreted from strain gage data on both non-displacing and displacing retaining walls for Loma Prieta-WVC270-1 for ROOZ02.

APPENDIX A

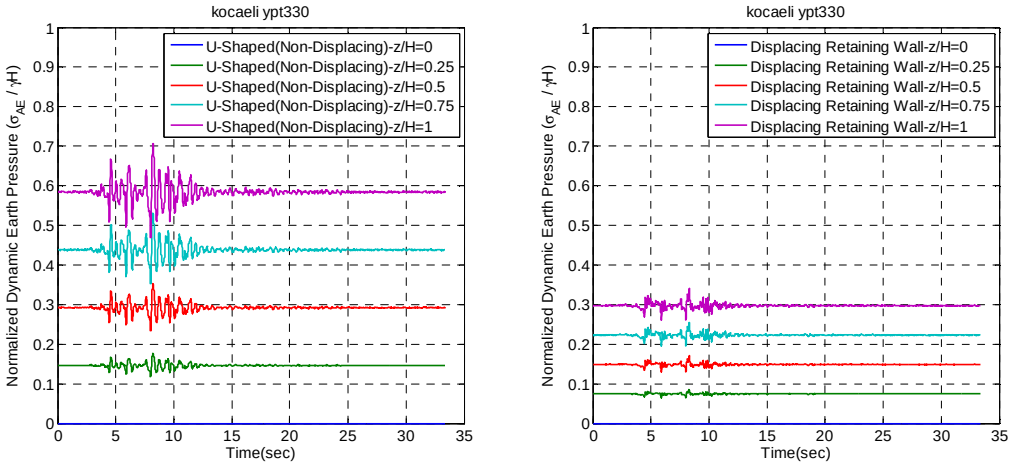

Figure A.63. Total earth pressure time series interpreted from strain gage data on both non-displacing and displacing retaining walls for Kocaeli- YPT 330-2 for ROOZ02.

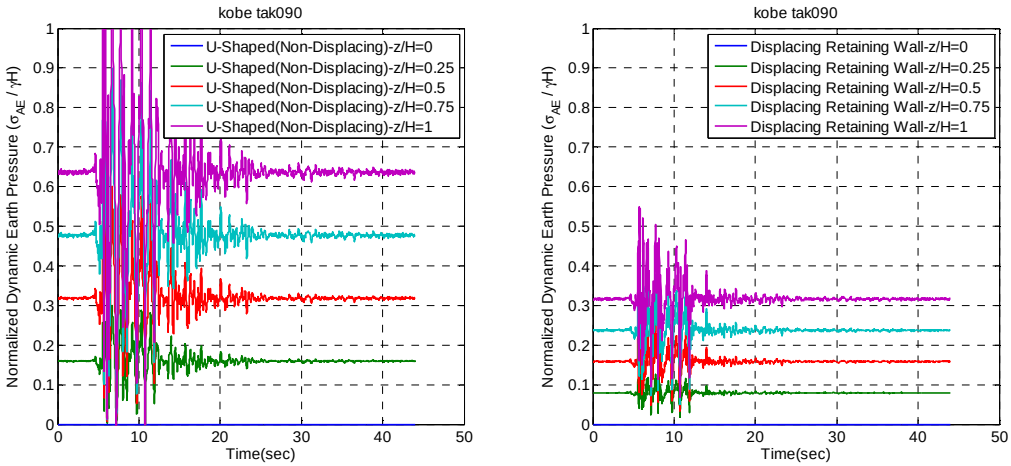

Figure A.64. Total earth pressure time series interpreted from strain gage data on both non-displacing and displacing retaining walls for Kobe-TAK090-2 for ROOZ02.